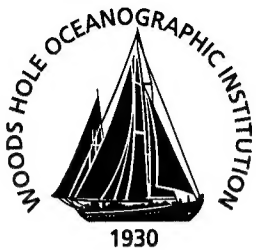


Woods Hole Oceanographic Institution



The 1998 WHOI/IOS/ONR Internal Solitary Wave Workshop: Contributed Papers

Edited by

Timothy F. Duda
Woods Hole Oceanographic Institution

and

David M. Farmer
Institute of Ocean Sciences, Canada

July 1999

Technical Report

Funding was provided by the Office of Naval Research
under Contract Nos. N00014-95-1-0633 and N00014-99-1-0126.

Approved for public release; distribution unlimited.

DTIC QUALITY INSPECTED 4

19991004 220

**The 1998 WHOI/IOS/ONR Internal Solitary Wave Workshop:
Contributed Papers**

edited by

Timothy F. Duda
Woods Hole Oceanographic Institution
and

David M. Farmer
Institute of Ocean Sciences, Canada

Woods Hole Oceanographic Institution
Woods Hole, Massachusetts 02543

July 1999

Technical Report

Funding was provided by the Office of Naval Research
under Contract Nos. N00014-95-1-0633 and N00014-99-1-0126.

Reproduction in whole or in part is permitted for any purpose of the United States
Government. This report should be cited as Woods Hole Oceanog. Inst. Tech. Rept.,
WHOI-99-07.

Approved for public release; distribution unlimited.

Approved for Distribution:



Timothy K. Stanton

Department of Applied Ocean Physics and Engineering



THE 1998 WHOI/IOS/ONR INTERNAL SOLITARY WAVE WORKSHOP: CONTRIBUTED PAPERS

Timothy F. Duda¹ & David M. Farmer²
Editors

¹ Applied Ocean Physics & Engineering Dept., MS 11
Woods Hole Oceanographic Institution
Woods Hole, MA 02543, USA

² Acoustical Oceanography Research Group
Institute of Ocean Sciences
9860 West Saanich Road
Sidney, BC, V8L 4B2, Canada

Abstract

A workshop entitled *Internal Solitary Waves in The Ocean: Their Physics and Implications for Acoustics, Biology, and Geology* was held during October, 1998 in Sidney, British Columbia, Canada. It was jointly organized by the Woods Hole Oceanographic Institution (MA, USA), the Institute of Ocean Sciences (Sidney, BC, Canada), and the U.S. Office of Naval Research. More than 60 scientists from seven countries attended. Participants contributed papers prior to the meeting which were published on the internet at the Woods Hole web site. Those papers are reproduced here.

Table of Contents

Preface.....	9
--------------	---

I. Acoustics

Realistic Simulation Studies of Acoustic Signal Coherence in the Presence of an Internal Soliton Wavepacket.....	12
<i>C.-S. Chiu</i>	
Some Thoughts on the Outstanding Acoustical and Oceanographic Issues Concerning "Solibore" Internal Waves.....	18
<i>J. A. Colosi and J. F. Lynch</i>	
Acoustic Mode Coupling Within Internal Solitary Waves and Wave Groups.....	22
<i>T. F. Duda and J. C. Preisig</i>	
Acoustic Field Fluctuations Caused by Internal Wave Soliton Packets.....	29
<i>S. Finette, M. Orr and J. Apel</i>	
Acoustical Impacts and Inversion Scheme of Internal Solitary Waves.....	33
<i>E. C. Shang, Y. Y. Wang and L. Ostrovsky</i>	
Contributions of the Turbulence Field and Zooplankton to Acoustic Backscattering by an Internal Wave.....	36
<i>T. K. Stanton, J. D. Warren, P. H. Wiebe, M. C. Benfield and C. H. Greene</i>	
Effects of Internal Waves and Bores on Acoustic Transmissions in the Strait of Gibraltar.....	46
<i>C. O. Tiemann, P. F. Worcester, B. D. Cornuelle and U. Send</i>	
Modeling the Effects of Solitons on Acoustics.....	52
<i>A. C. Warn-Varnas, S. A. Chin-Bing, D. B. King, S. A. Piascek and A. MacNaughton</i>	

II. Biology

Preliminary Observations of Optical Variability Associated with Internal Solitary Waves During the Coastal Mixing and Optics Experiment.....	65
<i>G. C. Chang and T. D. Dickey</i>	
Phytoplankton Patchiness and High-Frequency Internal Waves.....	69
<i>C. E. Lennert-Cody and P. J. S. Franks</i>	
Issues in Larval Transport by Internal Tidal Bores.....	73
<i>J. Pineda</i>	

III. Waves and Flows with Regional Constraints

Observations of Isolated Waves in Two-Layer Downslope Flows.....	78
<i>P. G. Baines, D. Murray and T. Ruchon</i>	
Intrusive Solibores in Knight Inlet.....	83
<i>E. A. D'Asaro</i>	
Fully Nonlinear Simulations of Upstream Waves at a Topography.....	89
<i>J. Grue</i>	
Flows in Rotating Channels: Hydraulic Adjustment, Jumps and Shocks.....	95
<i>K. R. Helfrich and L. J. Pratt</i>	
Nonlinear Internal Wave Observations on the Continental Shelf.....	101
<i>M. Levine and T. Boyd</i>	
Internal Solitary Waves in the Western Tropical Pacific.....	107
<i>R. Pinkel</i>	
Internal Wave Induced Variability in the Vicinity of Steep Island Flanks.....	110
<i>D. Vithanage and P. K. Sullivan</i>	

IV. Dissipation

A Study of Dissipative, Shoaling High-Frequency Internal Waves in Shallow Water.....	116
<i>J. Lerczak, C. Winant and M. Hendershott</i>	
Turbulent Mixing in Solitons.....	123
<i>N. S. Oakey and N. A. Cochrane</i>	
Observations of Turbulence Associated with Highly Nonlinear, Near-Surface Solitons Over the Continental Shelf.....	128
<i>T. P. Stanton</i>	

V. Remote Sensing

Relationships Between Strong Internal Waves and Their Surface Signatures.....	133
<i>R. A. Kropfli, L. A. Ostrovsky, T. P. Stanton, E. A. Skirta, A. N. Keane and V. G. Irisov</i>	
Nonlinear Internal Wave Interaction in the China Seas.....	140
<i>A. K. Liu and M.-K. Hsu</i>	
Continental Shelf Parameters Inferred from SAR Internal Wave Observations.....	143
<i>D. L. Porter and D. R. Thompson</i>	
Internal Solitons in the Ocean: Prediction from SAR.....	147
<i>J. Small, R. Hornby, M. Prior and J. Scott</i>	

VI. Sediments and Optics

A Mechanism for Sediment Resuspension by Internal Solitary Waves.....	156
<i>D. J. Bogucki and L. G. Redekopp</i>	
The Massachusetts Bay Internal Wave Experiment - 1998:	
Do Solitons Resuspend the Bottom Sediments?	162
<i>B. Butman, S. P. Anderson, A. Scotti, R. C. Beardsley, R. P. Trask, R. A. Weller</i>	
Internal Tides and Sedimentation on Continental Slopes.....	169
<i>D. A. Cacchione</i>	

VII. Wave Physics

Are Strongly Sheared Baroclinic Currents Sources for Internal Solitons?	172
<i>J. Apel</i>	
On the Maximal Form of Internal Solitary Waves.....	176
<i>W. A. B. Evans</i>	
Solitary Waves Formed Over Topography.....	188
<i>D. Farmer and L. Armi</i>	
Modeling Internal Solitary Waves in the Ocean.....	193
<i>R. Grimshaw and E. Pelinovsky</i>	
Strongly Nonlinear Internal Waves on the Australian North West Shelf.....	197
<i>P. E. Holloway, E. Pelinovsky and T. Talipova</i>	
Preliminary Results from Observations of Internal Tides and Solitary Waves in the Bay of Biscay.....	203
<i>F.-P. A. Lam, T. Gerkema and L. R. M. Maas</i>	
Theoretical Descriptions of Shallow-Water Solitary Internal Waves: Comparisons with Fully Nonlinear Waves.....	209
<i>K. G. Lamb</i>	
Numerical Modeling of Internal Wave-Wave Interactions.....	218
<i>P. Lynett and P. L.-F. Liu</i>	
How to Describe Strong Internal Waves In Coastal Areas.....	224
<i>L. A. Ostrovsky</i>	
Numerical Modelling of the Evolution of Internal Bores and Generation of Internal Solitons at the Malin Shelf.....	229
<i>E. Pelinovsky, T. Talipova and J. Small</i>	
Cross-Shelf Mass Transport by Non-Linear Internal Waves.....	237
<i>G. I. Shapiro, M. E. Inall and T. J. Sherwin</i>	
An Investigation of the Temporal Variability of a Non-Linear Internal Wave Field on the Portuguese Shelf.....	240
<i>T. J. Sherwin and D. R. G. Jeans</i>	
VIII. WHOI/IOS/ONR Internal Solitary Wave Workshop Attendees.....	246

Preface

This volume contains papers contributed by participants in a workshop entitled "Internal Solitary Waves in the Ocean: Their Physics and Implications for Acoustics, Biology and Geology." The meeting was organized by the Woods Hole Oceanographic Institution (MA, USA) and the Institute of Ocean Sciences (BC, Canada). It was held at Dunsmuir Lodge, Sidney, BC, Canada, 27-29 October 1998. Participants were requested to submit short papers, covering either research results or research issues, to be made available to attendees prior to the meeting. The request was met with enthusiasm, resulting in this diverse set of forty papers. Only the papers are published here. The proceedings and results of the workshop will appear elsewhere.

The energetic and ubiquitous nature of internal solitary waves forces researchers in all disciplines of coastal oceanography to consider their effects. For example, the waves strongly influence acoustics, organisms, the sea surface, the seafloor, turbulent mixing, momentum flux, and mass flux. The purpose of the workshop was to bring together an international and interdisciplinary group of nonlinear wave and solitary wave investigators. Many of the physical oceanographic participants in this workshop attended the internal solitary wave special session of the February 1998 AGU Ocean Sciences Meeting, but that session lacked the interdisciplinary nature we strove for and was enveloped by the other diverse and interesting sessions of the meeting. The AGU meetings also do not fully represent research outside of North America, although ironically a few Asian February AGU participants could not attend in October.

First and foremost, these are internet (web) publications, accessible from the web site <http://www.whoi.edu/science/AOPE/ISW98workshop/>. For the purposes of citation and browsing they have been reproduced in this printed Technical Report format. However, note that many of the figures were created for viewing on video monitors and are best examined online. Some (but not exhaustive) efforts have been made to improve their appearance here.

The papers are grouped into seven categories. Many alternative groupings would have been sensible. Many of the papers concern more than one topic, so please don't let the organization limit your survey. Papers are alphabetized within each group by first author. The topics of the papers are described here; to avoid adding personal bias the conclusions are not.

Group 1, Acoustics (eight papers), contains seven papers concerned with propagation of 200-2000 Hz signals through wave-riddled coastal environments. The eighth paper (*Stanton et al.*) examines 43-1000 kHz water-column backscatter obtained from a platform towed through waves. Of the others, *Tiemann et al.* present signal fluctuations at Gibraltar. *Shang et al.* present an inversion scheme. *Chiu, Duda and Preisig*, *Finette et al.* and *Warn-Varnas et al.* discuss modeling of signal variations from internal solitary waves. *Colosi and Lynch* describe some experimental results, discuss the knowledge of the community at this time, and list open issues. The *Oakey and Cochrane* paper of group 4 compares acoustic backscatter to turbulent dissipation and could very well have been placed in this group.

Group 2, Biology (three papers), contains two papers (*Lennert-Cody and Franks, Pineda*) dealing with planktonic transport by internal solitary waves and bores, including organism distribution and response. Each examines observations. The other paper (*Chang and Dickey*) discusses optical signal variability (chlorophyll and sediment) observed during solitary wave events.

Group 3, Waves and Flows with Regional Constraints (seven papers), contains one paper on thermocline waves observed in the shallow zone of very deep water (*Pinkel*) and one covering wave observations over a flat bottom on the shelf (*Levine and Boyd*). Three papers are on nonlinear waves and flows in confined regions: *D'Asaro*, observations at a sill; *Grue*, modeling at a sill; and *Helfrich and Pratt*, modeling in a channel. The *Baines et al.* paper discusses theory and experiments on unstable waves in downslope flow of a dense bottom layer. *Vithanage and Sullivan* present observations of strong vertical motion near an island.

Group 4, Dissipation (three papers), contains one paper on observed wave-amplitude decay at a shoaling site (*Lerczak et al.*), one paper comparing turbulent dissipation to acoustic backscatter (*Oakey and Cochrane*), and one paper on the topic of dissipation observed in high-amplitude solitary waves (*Stanton*).

Group 5, Remote Sensing (four papers), includes three papers which discuss satellite synthetic aperture radar (SAR) images of internal solitary waves, including inversion for wave and water column parameters. *Liu and Hsu* discuss China Sea waves, *Porter and Thompson* discuss inversion in the Mid-Atlantic Blight, and *Small et al.* consider waves north west of the United Kingdom. The fourth paper by *Kropfli et al.* covers Doppler radar and microwave radiometer signals from coastal internal waves.

Group 6, Sediments and Optics (three papers) includes one paper concerning nonlinear internal wave effects at continental slopes (*Cacchione*). *Bogucki and Redekopp* model a mechanism enabling internal solitary waves to resuspend sediment. *Butman et al.* describe a field program to study coastal internal waves and resuspension. The paper by *Chang and Dickey* (group 2) could also have been in this group.

Group 7, Wave Physics (twelve papers) is made up of papers concerned with wave dynamics and wave properties rather than with the geophysical or biological ramifications of their presence. The group 3 papers belong here in principle but were separated because they focus on particular topographic or forcing structures. This group is very diverse. *Apel* shows evidence for a new and not-understood generation mechanism involving large-scale currents. *Evans* examines theoretically-derived wave shapes. *Farmer and Armi* show observations and suggest that shear-flow instability may contribute to generation. *Grimshaw and Pelinovsky* discuss a wave evolution equation which includes shear, topography, dissipation, rotation, and cubic nonlinearity. Three papers (*Holloway et al., Lam et al.* and *Pelinovsky et al.*) compare wave observations to model predictions. *Lamb* compares wave shapes from weakly and fully-nonlinear wave theories. *Lynett and Liu* models waves and crossing wave-wave interactions. *Ostrovsky* discusses various wave evolution equations. *Shapiro et al.* examine mass transport by internal solitary waves analogous to the Stokes drift of surface waves. *Sherwin and Jeans* critically examine compatibility of observed waves with wave propagation theories.

I would like to dedicate this report to Michelle Yachnik at Dunsmuir Lodge who did a fine job of helping us organize the meeting. She passed away unexpectedly just prior to the meeting.

Finally, the papers appearing here and at the web site are copyrighted material. Please contact the authors for copyright information.

Tim Duda
Woods Hole Oceanographic Institution

Realistic Simulation Studies of Acoustic Signal Coherence in the Presence of an Internal Soliton Wavepacket

Ching-Sang Chiu

Department of Oceanography, Naval Postgraduate School, Monterey, CA 93943

Abstract: Based on moored Acoustic Doppler Current Profiler (ADCP) data obtained during the 1995 Shallow Water Acoustic Random Media Experiment (SWARM), the temporal and spatial fluctuations in the sound-speed field associated with the passage of an internal soliton wavepacket were synthesized. Using a coupled normal-mode sound propagation model and the synthesized sound-speed variations, the variability of sound pressure and of the acoustic modal amplitudes for a 224-Hz CW transmission were simulated. The auto and cross-correlations of sound pressure at different depths, and of the acoustic modal amplitudes at a fixed range, were computed for estimating the vertical and temporal scales of the fluctuating sound field. The results of the correlation analysis are presented and discussed. [The research is partially sponsored by the Office of Naval Research.]

1. Introduction

As part of the environmental monitoring network in the 1995 Shallow-Water Acoustic Random Media Experiment (SWARM), the Naval Postgraduate School (NPS) provided two self-contained Acoustic Doppler Current Profilers (ADCPs). They were moored 4 m above the seafloor, facing upward, at two separate locations, 16.5 km apart, along the experimental track. The resultant ADCP data set comprises a time series of depth profiles of three-dimensional current velocities with a sampling time interval of 90 s and a depth interval of 4 m over a three-week period. A detailed oceanographic analysis of the ADCP time-series has been performed by NPS, and the subsequent results were reported in Ref. 1 along with the initial acoustic findings obtained by the other SWARM investigators. The ADCP data analysis has provided a far-reaching physical understanding as well as a high-quality characterization of the medium fluctuations which were produced predominately by the large-amplitude, nonlinear, internal soliton wavepackets that propagated shoreward from the shelfbreak. The generation mechanism, vertical structure, evolution behaviors and spectral characteristics of these soliton wavepackets, as observed by the ADCPs, were discussed in Ref. 1.

Moving forward from the oceanographic findings, the focus of this paper is on estimating (or predicting) the properties of the fluctuating sound field. Our method of estimation uses the ADCP observations in conjunction with an acoustic model. Based on the analyzed ADCP results, the internal displacement structure of a soliton wavepacket was developed to realistically synthesize the temporal and spatial fluctuations in the sound-speed field. Using a coupled normal-mode model for sound propagation and the synthesized sound-speed variations, the variability of sound pressure and of the acoustic modal amplitudes along a SWARM acoustic transmission path were simulated. The auto and cross-correlations of sound pressure at different depths, and of the acoustic modal amplitudes at fixed ranges, were then computed for estimating the vertical and temporal scales of the fluctuating sound field. In this paper, we report the simulated acoustic variability as well as the results of the correlation analysis for a 224-Hz CW transmission.

2. Acoustic Modeling

The inferred displacements of the isotherms were used to empirically model the sound-speed perturbations. In Fig. 1, the inferred displacements of the first baroclinic mode of internal waves at JD (Julian day) 211.3 is shown, revealing the presence of a large-amplitude soliton wavepacket. (Hereafter, range is the distance toward the shelfbreak from a 224-Hz sound source and time is relative to JD 211.3.) These internal-wave modal displacements were derived from the ADCP data using an empirical orthogonal function analysis, a nonlinear relation between current and displacement, and a time-to-space mapping based on observed phase speeds of the wavepackets [Ref. 1]. The shape of the first baroclinic mode is shown in Fig. 2., which accounts for most of the observed temperature fluctuations.

The coupled normal-mode model of Chiu et al. [Ref. 2] was employed to calculate the fluctuating sound field for a 224-Hz CW sound source located at a depth of 50 m,. At the initial time, i.e., $t = 0$, the leading edge of the soliton wavepacket was approximately 2 km from the source. The movement of the wavepacket was simulated by translating the wavepacket with an observed phase speed of 0.8333 m/s. "Snap-shots" of the soliton wavepacket were taken at every 5 seconds to create the sound speed perturbations at those instances. The sound speed perturbations were simply the products of the displacements in first baroclinic internal-wave mode and the vertical sound speed gradients of the mean profile. With such an evolution model of the sound speeds, the fluctuating acoustic wavefield within a range of 10 km from the sound source was then calculated at a geophysical time-step of five seconds over a period of half an hour. This produced time series of sound pressure at various ranges and depths, as well as time series of the modal amplitudes at various ranges.

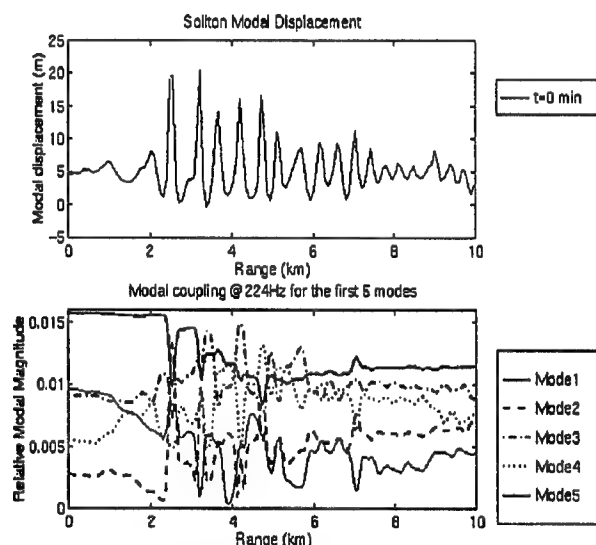


Figure 1. Soliton modal displacement (top) and the relative magnitudes of the first five acoustic normal modes (bottom).

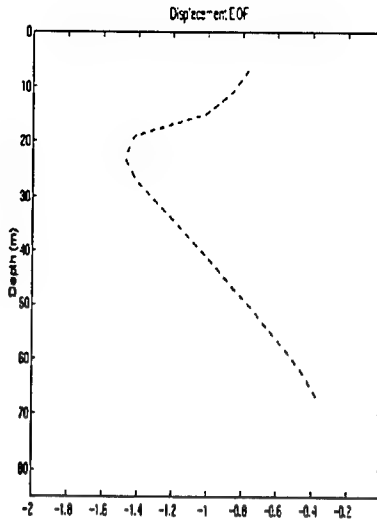


Figure 2. The 1st baroclinic internal-wave mode.

3. Results and Discussion

Figure 3 shows the temporally and spatially varying transmission loss (TL) calculated by the coupled normal-mode model. Only the TL at every 90 seconds is displayed although it was calculated at a 5-second interval. Given the large displacements produced by the soliton wavepacket, the large fluctuations in the calculated transmission loss are expected. At ranges longer than 0.5 km, there are rampant abrupt variations in the TL of up to 20 dB over short distances of 50-100 m out to the 10-km range. These spatial changes, i.e., highs and lows, are due to the interference of the different acoustic normal modes. Of interest is the shifting of the locations of the highs and lows in the TL as the soliton wavepacket evolves in time. These shifts, or changes in the interference pattern, are due to small but different changes in the phases of the different normal modes. These shifts result in a temporal variability in the TL that has a time scale of approximately 10 minutes as displayed in Figure 3.

To illustrate the significance of mode coupling, the calculated magnitudes of the first five acoustic modes versus range at $t = 0$ are displayed in the bottom panel of Fig. 1. Note that the internal soliton displacements for the same time is shown on the top. Energy transfer between modes is evident. For example, Modes 1 and 2 as well as Modes 3 and 5 are easily seen to be tightly coupled. As energy in one mode increases, the energy in the other mode decreases. It can also be seen that mode coupling takes place as soon as the sound energy passes the leading edge of the soliton wavepacket, particularly in the vicinity of the local peaks in the wavepacket. Where the internal displacements are small, i.e., at the back of the leading portion of the wavepacket, the coupling between modes is mild. Active energy exchange between modes, thus largely occurs within the leading portion of the wavepacket. Figure 4 shows the variability of the magnitudes of Mode 1 and Mode 2 over the modeled duration of 30 min. Again, it is seen that the modal magnitudes change abruptly at the leading edge of the soliton wavepacket as the wavepacket propagates toward the sound source. The fluctuations in the modal amplitudes have the same time-scale as the TL, which is about 10 min.

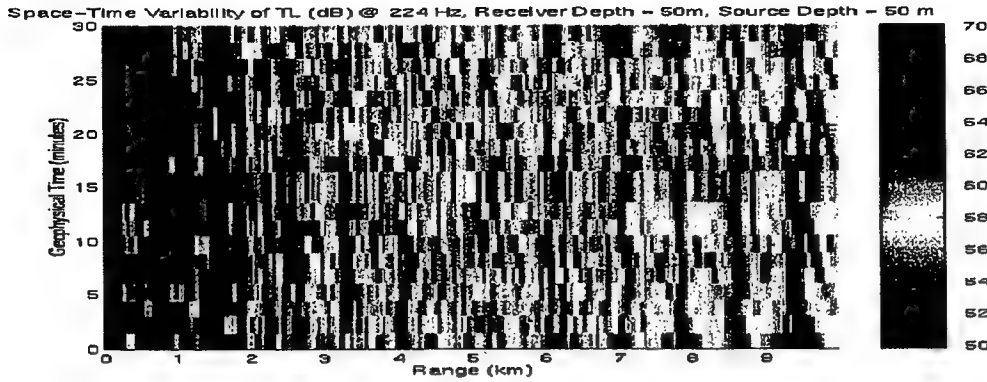


Figure 3. Space-time variability of transmission loss.

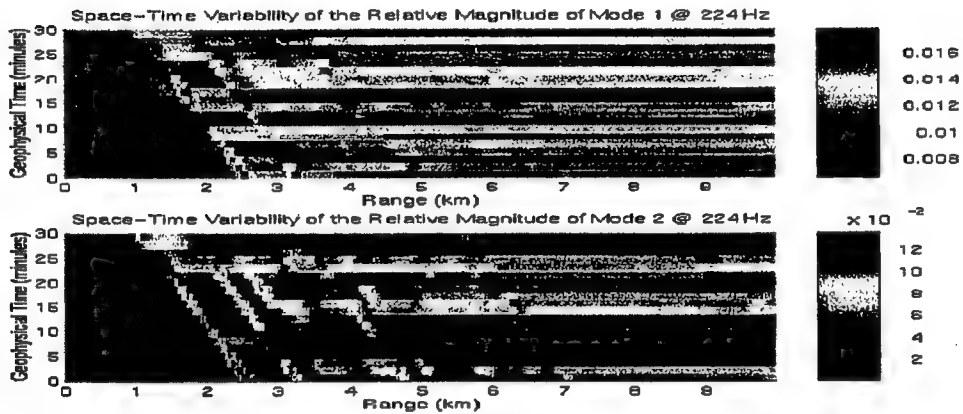


Figure 4. Space-time variability of the relative magnitudes of Mode 1 (top) and Mode 2 (bottom).

To investigate the correlation (vertical) distance and time of the sound pressure field, the receptions by seven hydrophones representing a vertical line array (VLA) located at 10 km from the 224-Hz CW sound source were synthesized. The top phone is located at a depth of 10-m and the bottom phone at 70 m. These hydrophones are labeled as Phone 1 to 7 from top to bottom. The depth spacing between adjacent hydrophones is 10 m. Table 1 shows the auto and cross-correlation coefficients (at zero lag) of the synthesized time records of complex sound pressure perturbation at the seven depths. For all the cross-correlation functions computed, the peaks occur at zero lag. This indicates that the sound field is dominated by the low modes or the low grazing-angle acoustic energy. High correlations of the sound pressure perturbations over the entire VLA (or the entire water depth) are obtained. This outcome is expected because the large-amplitude soliton wavepacket affects a major portion of the shallow water column producing sound speed fluctuations that are in phase at all depths.

Table 2 shows the de-correlation times estimated from the auto-correlation functions of the sound pressure perturbation time series. The de-correlation time is taken to be the lag at which the correlation coefficient drops to a value of 0.3679, i.e., e^{-1} . A de-correlation time of 50-60 seconds is found at all the hydrophones. The sound pressure perturbations at the various depths along the VLA are likely to have similar structure again due to the shallow water depth and the large-amplitude and vertically in-phase sound-speed changes.

The de-correlation times of the various acoustic modes are tabulated in Table 3. A value of 0.3679 is again used to determine these modal de-correlation times. There are considerable variability in the de-correlation times of the various modes. Mode 1 has the longest de-correlation time. Given a negative sound speed profile in the SWARM site, the soliton wavepackets are expected to have a lesser impact on Mode 1, since the span of Mode 1 is well below the depths of maximal sound speed perturbation. Due to the larger vertical spans of the higher modes, they are likely to be more affected by the soliton wavepacket. Since the de-correlation times of the modal amplitudes are longer than the sound pressure observed by a single phone, the use of VLAs in shallow water can be more advantageous. A shorter de-correlation time in the single-phone measurements is due to the interference of the multi-modes.

Table 1: Cross-correlation coefficients of the sound pressure perturbations at the seven depths.

Phone	1	2	3	4	5	6	7
1	1						
2	0.9310	1					
3	0.9061	0.8432	1				
4	0.9296	0.8535	0.9385	1			
5	0.8934	0.8276	0.9773	0.9558	1		
6	0.7599	0.6765	0.8229	0.8277	0.8436	1	
7	0.8745	0.8387	0.9679	0.9030	0.9730	0.7720	1

Table 2: De-correlation times of the sound pressure perturbations at seven depths.

Phone	1	2	3	4	5	6	7
De-correlation time (s)	60	60	50	55	50	55	55

Table 3: De-correlation times of the amplitudes of acoustic normal modes.

Mode	1	2	3	4	5
De-correlation time (s)	300	75	112	90	83

4. Conclusions

From the modeling investigations carried out thus far, the following conclusions for a 224-Hz signal transmission can be drawn:

- The modal magnitudes change abruptly at the leading edge of the soliton wavepacket as the wavepacket propagates toward the sound source. Coupling between the modes takes place

immediately after their initial contact with the wavepacket. Active coupling occurs within the front portion (approximately the first half) of the wavepacket where the sound-speed perturbations are large. At the downstream of the wavepacket, the coupling of modes is significantly lessened. The time scale of the variability of both the modal magnitudes as well as transmission loss is approximately 10 minutes.

- There is a high correlation between the sound pressure changes at different depths over the entire water column. This outcome is expected because the large-amplitude soliton wavepackets affect a major portion of the shallow-water column producing sound speed fluctuations that are in phase at all depths. The de-correlation times of sound pressure are about one minute, independent of depth.
- There are large differences in the de-correlation times of various acoustic modes. Mode 1 has the longest de-correlation time of about 300 s. The higher modes have de-correlation times on the order of 100 s. With a negative sound-speed profile in the SWARM site, the effects of the soliton wavepacket on Mode 1 are minimized because the vertical span of Mode 1 is well below the depths of maximal sound speed perturbation. Higher modes are likely to be affected more by the soliton wavepacket due to their larger vertical spans.

References

1. SWARM Group (J. Apel, M. Badiey, C.-S. Chiu, R. Headrick, J. Kemp, J. Lynch, M. Orr, A. Turgot and S. Wolf), "An overview of the 1995 SWARM shallow water internal wave acoustic scattering experiment," IEEE Journal of Oceanic Engineering, July issue, 1997.
2. Chiu, C.-S., J. H. Miller and J. F. Lynch, "Forward coupled-mode propagation modeling for coastal acoustic tomography," J. Acoust. Soc. Am. 99(2), Feb. 1996.

Some thoughts on the outstanding acoustical and oceanographic issues concerning “solibore” internal waves

John A. Colosi and James F. Lynch

Woods Hole Oceanographic Institution, Woods Hole, MA 02543

During the past few years much attention has been paid to nonlinear continental shelf internal waves. This focus has been driven by the important oceanographic, acoustic, optical, geological, and biological interest related to this phenomenon. Since these strongly nonlinear continental shelf internal waves are generated by barotropic tidal interactions with bathymetry and since the resulting internal tide evolves into an internal bore with trailing soliton-like waves; we generically call this entity a solibore. Solibores are extremely common throughout the world's shallow seas, straight, Fjords, and continental shelves and so in studying their behavior we are not looking at an isolated curiosity. During the past few years our acoustical oceanography group here at WHOI has been involved in studying the acoustical and oceanographic properties of solibores on the New Jersey and New England continental shelves via the SWARM (Shallow Water Acoustic Random Media) and Shelfbreak front PRIMER experiments. In these experiments large arrays of acoustical and oceanographic instrumentation were deployed giving us a first exciting look at this natural phenomenon. We discuss here some of the important scientific issues raised by this field work which we will break up into acoustical and oceanographic issues even though the two are closely related.

I. Acoustical Issues

Our SWARM [1] and PRIMER [2] experiments concentrated acoustically on broadband, transmissions in the 50 to 500 Hz range, which are crudely ideal frequencies for optimizing transmission range in shallow water (water depth less than about 500 m) given the competing effects of lossy bottom interactions which are larger with lower frequencies and chemical attenuation which is larger at higher frequencies. SWARM and PRIMER also transmitted about perpendicular to the iso-baths so that the transmission direction and the direction of solibore propagation were roughly the same (i.e. within 45 deg.). Using controlled sources at 200 and 400 Hz and using moored vertical receiving arrays we have studied the time and depth variability of the acoustic signals which had propagated over distances of 30 to 40km. In terms of the low order acoustic normal mode arrivals we have measured time spread, travel time bias, and intensity fluctuations and we have attempted, with mixed success, to correlate these measurements with in-situ solibore observations [3,4].

The main acoustical issues raised by these experiments center around the idea of the predictability of the acoustical field, that is how well do we need to know the mean state of the ocean, and/or the statistics of the ocean (not withstanding questions of seabed geology) to predict the acoustic field or the statistics of the acoustic field to some level of accuracy. This problem is a function of acoustic frequency, transmission range, and transmission direction relative to the solibore propagation. We have concentrated our efforts at 200 and 400 Hz center frequencies and ranges of 30 to 40 km but we need to explore lower frequencies and longer/shorter ranges. Lower frequencies are interesting since they are

less sensitive to small-scale oceanographic variations and they show less chemical absorption but they suffer from increased lossy seabed interactions. Longer and shorter ranges are interesting because we do not know the range scaling for any of the acoustic observables. Predictions for mode spread and bias in a deep water waveguide with Garrett-Munk internal waves indicate spread scales like $R^{3/2}$ and bias scales like R^2 [5]. Furthermore mode intensity variability saturates at 1000km range showing an exponential probability density function [5]. Information like this is not known for a shallow water situation.

In addition, with the exception of Worcester's and Send's Strait of Gibraltar experiment, there is no moored acoustic transmission data for sound propagation perpendicular to the solibore propagation direction. Acoustic scattering in this cross-wave geometry can be severe since the acoustic energy is propagating along the crests or troughs of the solibore. Therefore more work in this geometry is well justified.

Of central importance for signal processing are the acoustic coherence limits that are imposed by solibores. More work is needed on the temporal, spatial and frequency coherence of the field in the presence of solibore internal waves. In particular, no data exists for the spatial coherence of a horizontal line array. This is an important geometry for Navy systems particularly towed arrays.

Another acoustic issue is the forward scattering of sound by solibores at 1 to 10 kHz frequencies. Simple theory would suggest that such scattering would respond to small scale ocean variability of order 10 to 100 m. However spatial structures that small in the solibore have not been routinely measured, and so both first order oceanography and acoustics measurements are needed here. Also in experimental situations where there is acoustic bottom interaction there may be a coupling between volumetric acoustic effects caused by solibores and ocean seabed scattering; that is, the solibore will change how the seabed is ensonified.

There is also the issue of 3-D propagation effects caused by solibores. Transverse gradients of sound speed can cause 3-D scattering of acoustic energy and these gradients become more important as one looks at the cross wave propagation situation[6]. Theoretically we have always treated the propagation, as 2-D and horizontal coherence calculations are generally Nx2D. The use of dense horizontal arrays in future experiments could indicate whether horizontal multipathing is significant and therefore if 3-D effects need to be considered in our theoretical formulations of acoustic wave propagation through solibores.

Finally, we have a wealth of theoretical machinery for calculating acoustic fluctuation quantities like coherence, but what we are lacking are the oceanographic models to be used as inputs to our acoustic fluctuation calculations to test their capabilities in the shallow-water environment. This was the situation in deep-water acoustics nearly 30 years ago before the successful Garrett-Munk internal wave model was used. The key piece of information from an acoustic fluctuation standpoint is the correlation function of the sound speed fluctuations or equivalently the sound speed fluctuation spectrum. Significant simplifications can be made if there is a dispersion relation to link the spatial and temporal scales of the solibore internal wave. Because of the strong non-linearity of the solibore a dispersion relation may not be simply attainable.

Coming full circle to our main issue of the predictability of the acoustic field, we see that this issue is centrally linked to the predictability of the solibore field that is addressed in the next section.

II. Oceanographic Issues

Oceanographically there are many loose ends to tie up on solibore physics. There are three convenient main categories for which the solibore phenomenon can be broken down: generation, propagation, and dissipation. All three of these have been worked on through out the years, but by and large, the propagation problem seems to be the best understood. However, even there, the understanding via mathematical and computer models is far ahead of the field work: In our opinion there is an urgent need for more field work in all three categories of solibore physics. Based on our fieldwork from SWARM and PRIMER, which focuses on continental shelf solibores instead of solibores in straits, we find the following issues to be of major importance.

Concerning the tidal generation of these waves from bathymetry we have an understanding of the lee wave situation where the tidal flow is super-critical for the internal tide but in many cases we see solibores in strongly sub-critical conditions (PRIMER is one example). One possible mechanism for the sub-critical generation is the Rattray-Baines critical slope mechanism but this has not been studied in detail. In addition there is the issue of the effects of the shelfbreak front (and its associated jet), slope-shelf eddies, and wind stresses on the generation of solibores. In the shelfbreak PRIMER we observed a great deal of variability in solibore generation which must be associated with interactions with the rapidly changing shelfbreak front. In addition we observed the interaction of a Gulf Stream eddy with the shelf region which resulted in no solibore generation. Further there is the issue of the evolution of internal tides into solibores. In general the barotropic tide interaction with the bathymetry results in a symmetric linear-looking internal tide which subsequently through non-linear steepening and some other mechanisms evolves into an asymmetric bore with solitons being generated at the bore face. Since the solitons have a smaller horizontal wavelength than the internal tide they fall behind and therefore a train of solitons develops behind the bore. In shelfbreak PRIMER we observed rapid solibore evolution from the internal tide approximately over 1/8 of an internal tide period. Using fully non-linear models with average stratification profiles we are unable to simulate this rapid development; we find that approximately $\frac{1}{2}$ a tidal cycle is needed for solibore development.

Once a solibore is generated it will propagate up-shelf transferring its energy more and more from a bore-like internal tide to a train of high wavenumber solitons. Proceeding to this propagation the following issues arise. What is the dominant cause of fluctuations in the solibore group velocity, high wavenumber content, energy, and duration? What is the connection between the stochastic background internal wave field and the solibore field? Why are the widths and amplitudes of the solitons on the solibore not related by the simple KDV formulae? What is the significant of dissipation, bathymetric steering, scattering and horizontal refraction in solibore dynamics? Can we treat these waves as essentially 2-D waves? What is the best combination of deterministic and stochastic descriptions of the solibore field?

Turning to dissipation, the first order question is how do solibores break-up? Generally once the solibore is near its break-up point it is more soliton-like than bore-like. Likely candidates for the soliton break-up mechanisms are wave breaking when the thermocline has shoaled to where the solitons cannot exist as waves of depression but must rapidly evolve into waves of elevation, bottom friction, shear dissipation, or interactions with a mixing front. Does the relative importance of these processes shift from site to site? Another big question related to soliton breaking is that we do not know what exactly happens when the solitons rapidly evolve from waves of depression to waves of elevation. Do they break immediately, or do they flip over and break later?

III. Summary

Based on this discussion of the basic acoustical and oceanographic issues it is our opinion that there are a number of desirable measurements that need to be made. From an acoustic standpoint a fixed acoustic range containing a diversity of frequencies, source receiver ranges and both vertical and horizontal array types is a necessity. Transmissions both along and across internal wave crests are needed to test the anisotropy of the acoustic environment. Propagation through the generation region of the internal waves should be explored as this measurement has been largely ignored to date. What is clearly essential here is that we collect the essential oceanographic data with our acoustic observations so that we can make the key links between the oceanic variability and the acoustic variability.

Turning to the oceanography, we advocate an experiment, which would follow a solibore internal wave from its generation through to its break-up or dissipation. We advocate a dense line of moorings extending up-slope from the generation region on the continental slope to the dissipation region. A few moorings could be placed out of the line plane to look at 3-D effects. The moorings ideally would be equipped with temperature and conductivity sensors, temperature only sensors, a few micro-structure probes, and upward looking ADCP. Sea Soar, SAR, acoustic backscatter, and other measurements would complement the mooring line.

Bibliography

1. The SWARM Group, "An overview of the 1995 SWARM shallow water internal wave acoustic scattering experiment", IEEE J. Oceanic Eng., V 22(3), pp465-500, (1997)
2. The shelfbreak PRIMER Group, "Shelfbreak PRIMER - An integrated acoustic and oceanographic field study in the middle Atlantic bight", In Shallow-Water Acoustics, Editors Rehne Zhang and Jixun Zhou
3. R. H. Headrick, J. F. Lynch, and the SWARM Group, "Acoustic normal mode fluctuation statistics in the 1995 SWARM internal wave scattering experiment", submitted to J. Acoust. Soc. Am., 1997
4. R. H. Headrick, J. F. Lynch, and the SWARM Group, "Modeling mode arrivals in the 1995 SWARM acoustic transmission experiment", submitted to J. Acoust. Soc. Am., 1997
5. J. A. Colosi and S. M. Flatte, "Mode coupling by internal waves for multimegamerter acoustic propagation in the ocean", J. Acoust. Soc. Am., V 100 (6), pp3607-3620, (1996)
6. J. C. Preisig and T. F. Duda, "Coupled acoustic mode propagation through continental-shelf internal solitary waves", IEEE J. Oceanic Eng., V22(2), (1997).

Acoustic Mode Coupling Within Internal Solitary Waves and Wave Groups

Timothy F. Duda and James C. Preisig

*Applied Ocean Physics and Engineering Department
Woods Hole Oceanographic Institution, Woods Hole, MA 02543*

Abstract: Propagation of sound through continental shelf internal solitary waves and wave groups (packets) is shown to be strongly influenced by coupling of the acoustic normal modes. Transfer of energy between modes (coupling) is caused by strong lateral gradients of sound speed in the waves. In the simplified situation of a symmetric individual soliton of lateral scale 50 to 400 m in 50-m deep water, the coupling behavior mimics that from a square-well thermocline displacement. The more realistic case of a wave group, coupling is controlled by the modal input conditions, the dimensions of each wave and of the group, and the ambient depth structures of temperature and salinity. In the case of a moving packet, changing relative mode phasing alters the coupling and the resultant signal properties as the packet moves. The mode phasing within the packet varies with time scales of minutes for a moving packet, causing coupling and signal fluctuations at comparable time scale.

Introduction

Energetic baroclinic tides and waves are a common feature of continental slope regions during stratified periods [Huthnance, 1989]. These often have characteristics comparable to internal solitary wave (ISW) or "soliton" mathematical solutions for stratified systems. The large vertical water displacements of these waves cause significant perturbation of the acoustic waveguide, making them important contributors to fluctuations of low-frequency acoustic signals. By low frequencies, we mean those having less than 15 propagating modes in the water-column waveguide, usually less than 1000 Hz on the continental shelf. The short scale (less than 200 m) of the solitary waves and the large displacements suggest that adiabatic mode propagation (independently propagating normal modes) criteria [Milder, 1969] may be violated and energy may scatter between modes. A few studies of this coupled-mode effect in the shallow-water waveguide have been published in the last decade, starting with Zhou, Zhang and Rogers, 1991.

We have completed two studies on this topic, Preisig and Duda 1997; Duda and Preisig, 1999. The results are restricted to acoustic propagation within 65 degrees of the direction of soliton propagation. Attenuation of acoustic energy in the bottom does not influence the mode coupling behavior in ISW's. On the other hand, attenuation plays a very important role in the acoustic energy far downstream of ISW mode-coupling events. This is because the high-order modes tend to suffer more attenuation than low-order modes, and a varying blend of modes arising from coupling can lead to strong energy fluctuations.

Analysis of horizontal mode refraction within ISWs for acoustic paths oblique to the ISW troughs shows that the modeling should work for paths at angles up to 65 degrees from a path normal to the solitary wave crests. Therefore, a stretching of the effective horizontal scale of the ISW (L) by a factor of $\cos^{-1} \theta$, allows the results to be applied to a wide range of incidence angles.

This numerical work was motivated in part by the SWARM acoustic experiment east of New Jersey [Apel et al., 1997; Headrick 1997].

Single-Wave Coupling

Our initial study was of coupling within individual solitary waves. With numerically simulation of 200 and 400 Hz sound in a waveguide of 50 m depth, it was shown that the energy modal energy distribution changes rapidly at the steep faces of internal solitary waves having vertical displacement shape $\eta(x, t) = a \operatorname{sech}^2((x - ct)/L)$. The coupling occurs over propagation ranges of tens of meters (Figure 1),

small in comparison to the so-called mode cycle distance, defined as the scale of the difference of the wavenumbers of a pair of interacting modes. For L less than about 200 m, the coupling at each face is well approximated by a sharp-interface approximation (SIA), meaning that the effect of the entire wave can be approximated well by coupling at a pair of interfaces separated by approximately L , a square-well.

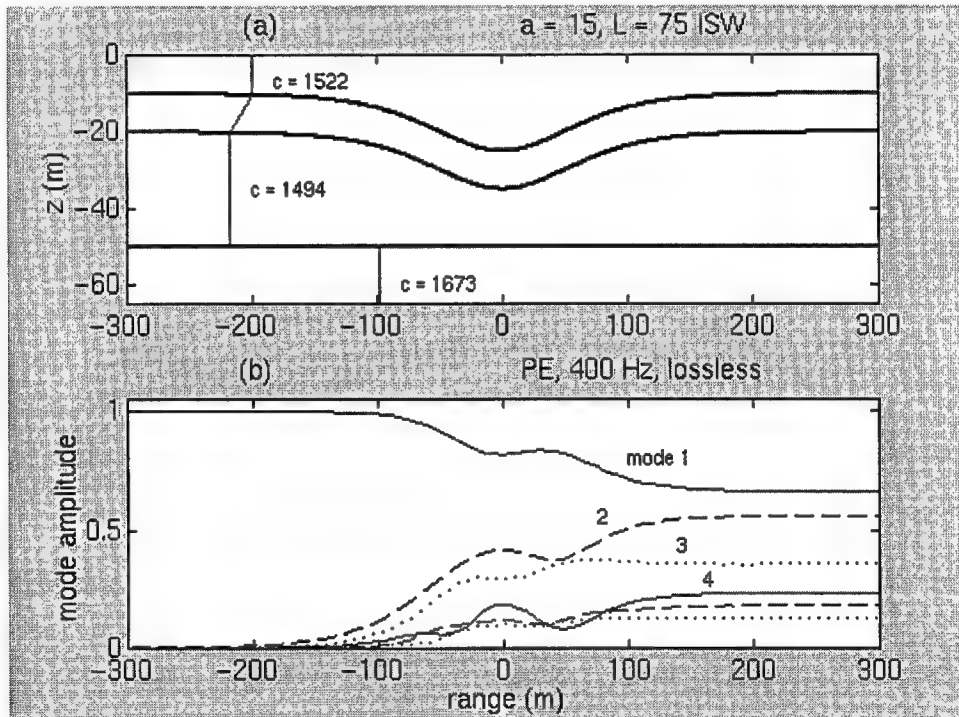


Figure 1. The model sound-speed profile and an example soliton are shown in the upper frame. Below, amplitudes of modes as a function of position within the wave are shown. Only mode 1 energy comes into the wave from the left, whereas many modes contain energy after the wave is encountered.

Using the SIA, which involves simple propagation of normal modes except at the coupling locations, the relative phases of modes propagating through the troughs of ISW's were shown to control the amount of net mode coupling induced by the ISW. For the case examined, 400 Hz and a three-layer system, this generally holds for horizontal ISW scales of less than 200 meters (Figure 2).

The relative phase changes in the modes can be used to predict the existence of four physical regimes. ISW's of small L are in the **cancellation** regime of little net coupling. The **net coupling** regime appears for longer waves, as do periodically occurring regimes of little net coupling referred to as **transparent resonances** which are determined by interference of energetic modes in the trough. The fourth regime is **adiabatic propagation**, the long-ISW limiting case, which occurs for L above a limit which varies with mode number, stratification, etc. The cases of cancellation and transparent resonance have little or no net coupling after energy completely traverses the wave, but are distinct from the adiabatic situation because they exhibit strong coupling within the ISW.

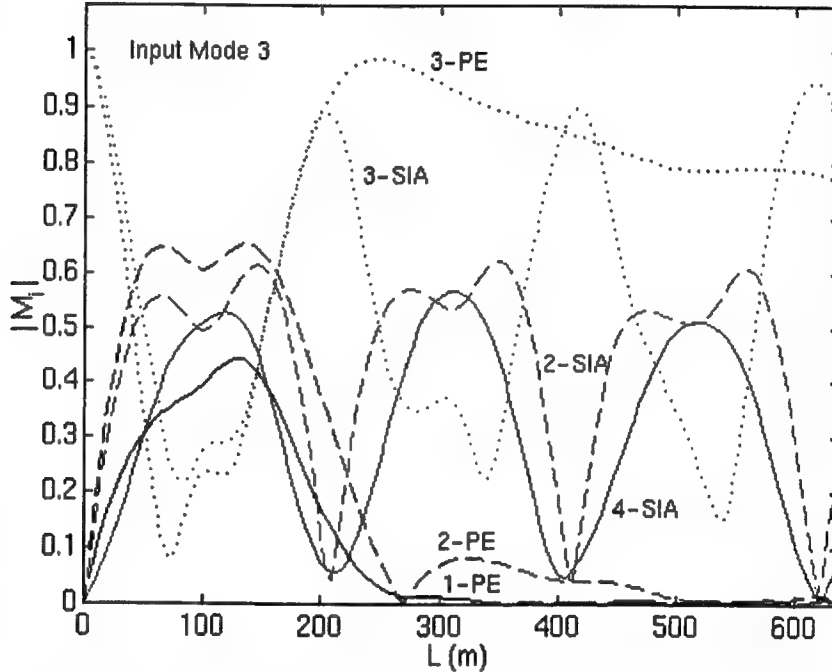


Figure 2: Sharp interface (SIA) numerical solutions agree well with Parabolic Equation solutions (PE) for internal waves shorter than 250 m. The mode amplitudes after traversing single solitons of amplitude 15 m and variable L are shown, with energy coming into the wave only in mode 3.

Coupling in Moving Wave Packets

Since solitary waves generally appear in packets rather than individually [Fu and Holt, 1984; Liu, 1988; Sandstrom and Oakey, 1995] our understanding must be extended to the effects of packets of waves. An insight from the sharp interface approximation single-wave study is that the relative phasings of the dominant modes at the scattering interfaces are the most significant factor in coupling. Earlier studies have investigated packet effects by attempting to relate the physical characteristics of packets to the induced coupling [Zhou, Zhang and Rogers, 1991; Zhou, 1993]. However, we have found that very different

coupling will result from the same packet shifted a few hundred meters, with all other parameters unchanged. We have performed detailed analysis of evolving coupling behavior in a packet as it moves through the ocean. It was shown that the relative phasing between dominant modes largely controls mode coupling and signal fluctuations caused by an entire packet, comparable to single-wave behavior, despite the added complexity of the problem.

There are two basic results: (1) Solitary wave packets can cause gain or loss of acoustic energy received at ranges of order 35 km through interaction of mode coupling and attenuation of higher modes. The net gain is dependent on packet position relative to the source and source depth. (2) Superimposed on those persistent signal gains (or losses) are fluctuations having time scales of minutes. These fluctuations are controlled primarily by the relative phasings of the dominant modes of the acoustic field as it first encounters the soliton packet.

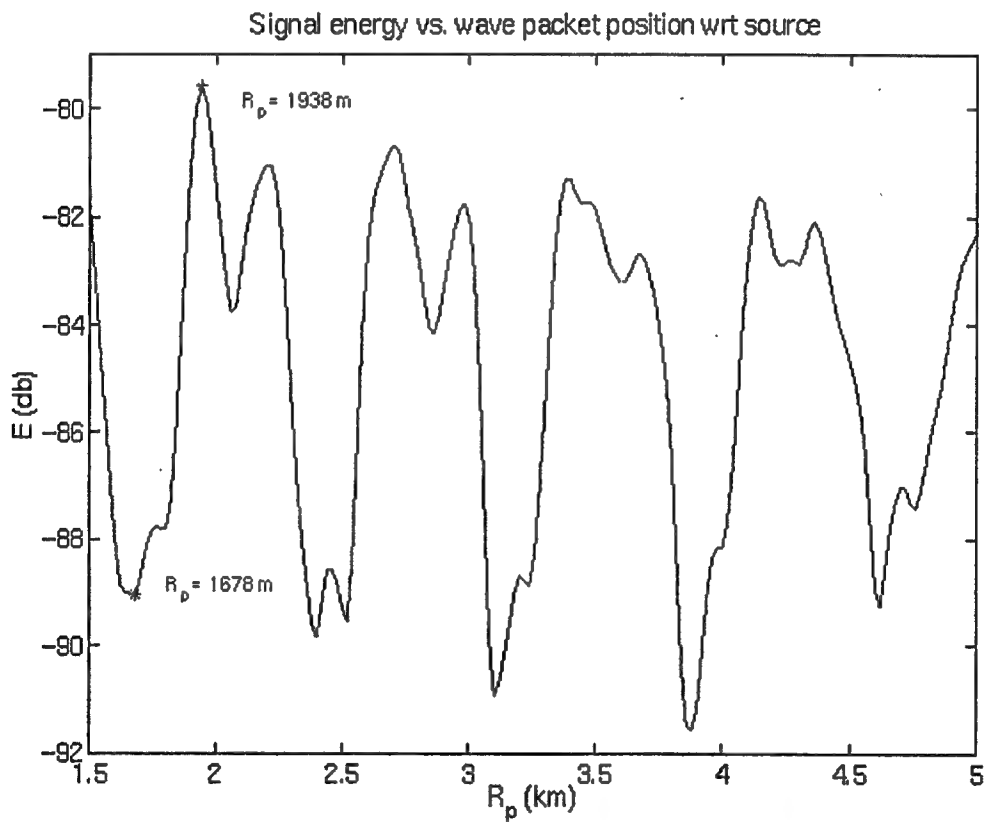


Figure 3. The signal reaching a receiver 33 m from a source is a strong function of the position of an intervening internal wave packet. At packet speed 1 m/s, this represents one hour of time.

Figure 3 shows depth-integrated acoustic energy in the water column, 400 Hz, after propagation through a set of three solitons at range of a few km from the acoustic source to a receiver at 33 km distance.

Propagation is adiabatic except in the packet. R_p is the x-position of the furthest crest from the source, which is at $x=0$. For packet speeds of roughly 1 m/s, this represents about one hour of signal fluctuation. Two situations chosen for further analysis are highlighted, one loud (position 1938 m) and one quiet (position 1678 m). Figures 4 and 5 show the level of energy in each acoustic mode between the source and the receiver. The modes are attenuated by bottom interactions at different rates. Since mode 1 propagates effectively, the loss of mode 1 energy to other modes in the $R_p = 1678$ case leads to signal loss at 33 km.

Conversely, it is useful to compare the nonlinear-wave effects to other possible effects. A single nonlinear wave packet of 10 to 15 m displacement amplitude gives signal fluctuations of order 10 dB at 33 km range. A continuous field of small (1-3 m amplitude) thermocline displacements has an effect of roughly one dB.

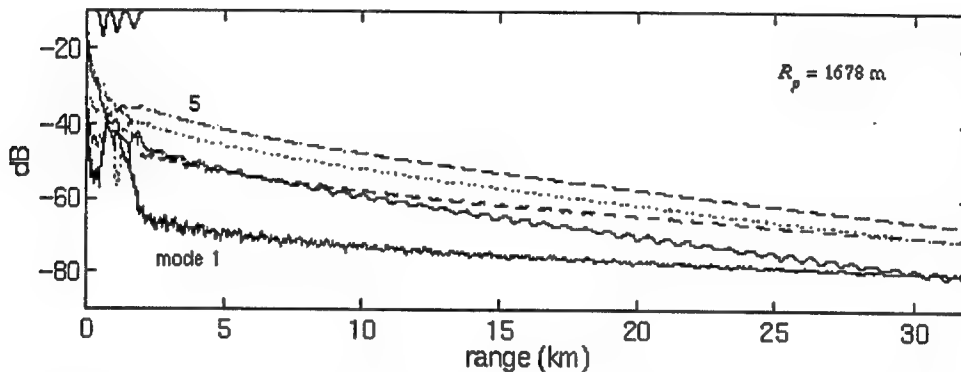


Figure 4. Mode 1 loses energy to other modes in a soliton packet at range 1678 m from the source at range 0. The energy which is transferred to the higher-order modes is attenuated to a greater extend than it would have been if it had remained in mode 1, so the signal level at 33 km is reduced by the packet.

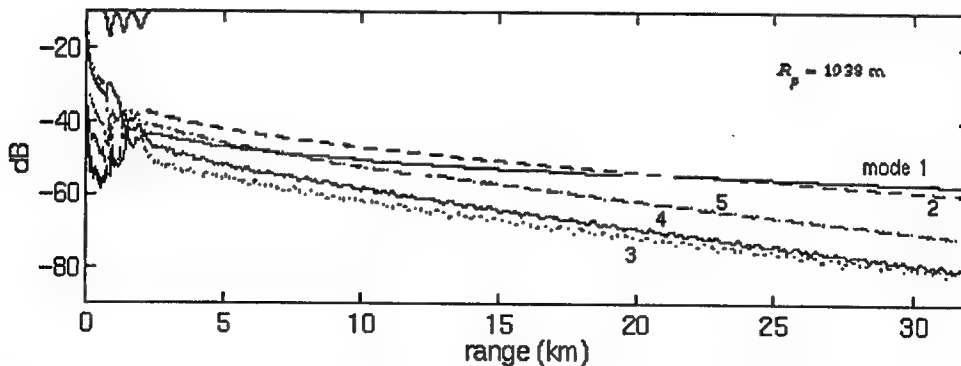


Figure 5. Mode 1 is amplified by the wave packet at range 1978 m from the source, then it propagates strongly to a receiver at 33 km range. The signal is amplified by the presence of the packet, unlike the situation with the packet at the nearby location of Figure 4.

Summary

Analysis of mode coupling within large-displacement thermocline displacements intended to mimic the behavior of nonlinear internal waves and wave groups shows that these phenomena can have strong effects on coastal acoustic signals of a few hundred Hz. Such strong fluctuations have been seen in recent acoustics experiments including SWARM (Figure 6). Our results strongly indicate that effects of nonlinear waves are at least part of the explanation.

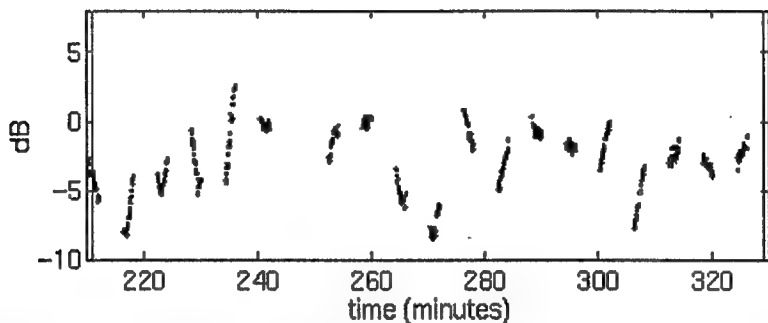


Figure 6. 400-Hz signal energy fluctuations at 33 km from the source during the SWARM experiment on the continental shelf south of New York.

References

Apel, J. R. *et al*, An overview of the 1995 SWARM shallow water internal wave acoustic scattering experiment, *IEEE J Oceanic Eng.*, **22**, 465-500, 1997.

Duda, T. F. and J. C. Preisig, Acoustic effects of moving coastal solitary wave packets, *IEEE J Oceanic Eng.*, *to appear*, 1999.

Fu, L.-L., and B. Holt, Internal waves in the Gulf of California: Observations from a spaceborne radar, *J. Geophys. Res.*, **89**, 2053-2060, 1984.

Headrick, R. H., *Analysis of Internal Wave Induced Mode Coupling Effects on the 1995 SWARM Experiment Acoustic Transmissions*, MIT/WHOI Joint Program, PhD Dissertation, 1997.

Huthnance, J. M., Internal tides and waves near the continental shelf edge, *Geophys. Astrophys. Fluid Dynamics.*, **48**, 81-106, 1989.

Lui, A. K., Analysis of nonlinear internal waves in the New York Bight, *J. Geophys Res.*, **93**, 12,317-12,329, 1988.

Milder, D. M., Ray and wave invariants for SOFAR channel propagation, *J. Acoust. Soc. Am.*, **46**,

1259-1263, 1969.

Preisig, J. C., and T. F. Duda, Coupled acoustic mode propagation through continental-shelf internal solitary waves, *IEEE J. Oceanic Eng.*, **22**, 256-269, 1997.,

Sandstrom, H., and N. S. Oakey., Dissipation in internal tides and solitary waves, *J. Phys. Oceanogr.*, **25**, 604-614, 1995.

J. Zhou, X. Zhang and P. H. Rogers, Resonant interaction of sound wave with internal solitons in the coastal zone, *J. Acoust. Soc. Am.*, **90**, 2042-2054, 1991.

- [About this document ...](#)

[Next](#) | [Up](#) | [Previous](#)

Next:[About this document ...](#)

Tim Duda

1998-10-23

Acoustic Field Fluctuations Caused by Internal Wave Soliton Packets

Steven Finette and Marshall Orr

Acoustics Division, Naval Research Lab, Washington DC 20375

John Apel

Global Ocean Associates, P.O. Box 12131, Silver Spring, MD 20908

The SWARM (Shallow Water in a Random Medium) experiment[1] performed on the continental shelf off the New Jersey Coast provided an opportunity to measure acoustic field properties in an area of intense internal wave activity. A number of oceanographic measurements made during the course of the experiment allowed us to develop a model of the internal wavefield, which consisted of both a spatially diffuse component and a spatially localized non-linear contribution from soliton packets. The latter were associated with the leading edge of the M2 internal tide. Both internal wave components evolve in space and time. Below, we briefly consider a model of the soliton packet contribution and illustrate the time-dependent effect of these soliton components on acoustic field fluctuations as the packets move in a direction anti-parallel to the direction of acoustic propagation.

Tow-yo CTD data were mapped onto the 42 Km acoustic track, and several points along the track where soliton activity was "low" were determined from a combination of ship radar images of the surface expression of the soliton internal wave field and 200 kHz acoustic backscatter measurements [Fig. 1]. Isolating regions of low soliton activity was necessary because the mode structure (depth dependence) of the internal wave field depends only on its linear (spatially diffuse) contribution. These real-time, space co-incident measurements are illustrated in the figure where the isopycnal displacements obtained from the acoustic backscatter shown as an overlay on the tow-yo CTD strips and a radar image is given in the upper right corner. Buoyancy profiles at these locations were used to compute mode one internal wave eigenfunctions. The envelope of the isopycnal displacements describing the time evolution of the soliton packet contribution was obtained from a solution to the Kortewig-deVries equation, and named the 'dnoidal' solution [2]. Specification of the solution requires estimates of the coefficients of the KdV equation (i.e. $\{a, b\}$ representing the strength of the non-linear and dispersive terms, respectively), the non-linear phase speed, amplitude and long wavelength wavenumber. These quantities were estimated by a combination of data from acoustic backscatter, tow-yo CTD and ship radar measurements as illustrated in Fig. (1), allowing one to parameterize the soliton model.

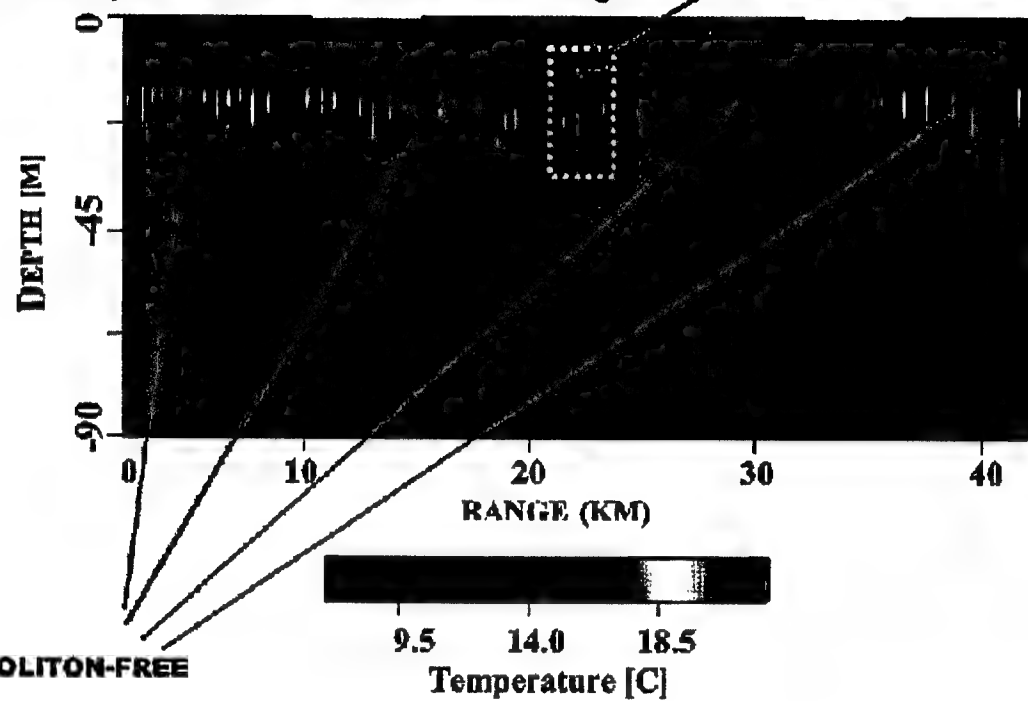
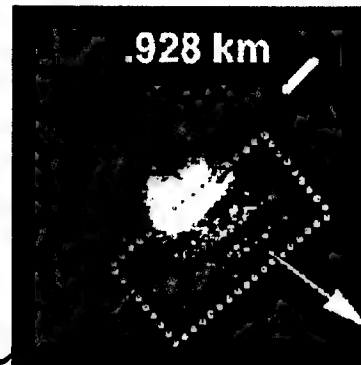
A deterministic sound speed distribution estimated from temperature and salinity profiles provided a background environment in which the sound speed variations associated with the packet propagated along the 42 km separation between a vertical line array and a 400 Hz. acoustic source. Bathymetry (shown in the figure as a red curve) and bottom/sediment properties were estimated using a chirp sonar inversion technique[1]. An elastic parabolic equation solver then computed the acoustic field at the array in one minute increments as the environment evolved due to the space-time variations in the soliton packets[3].

An example of the result of this calculation is depicted in Fig. 2, which shows the time variability of transmission loss and absolute phase at the array. The time window was approximately 12.4 hours with

EXTRACTION OF INTERNAL WAVE PARAMETERS

ship radar image of
soliton surface expression

tow-yo temperature distribution along track
with overlayed acoustic backscatter image



COMPUTE ENVIRONMENTAL

PARAMETRIZED DNOIDAL
SOLITON MODEL

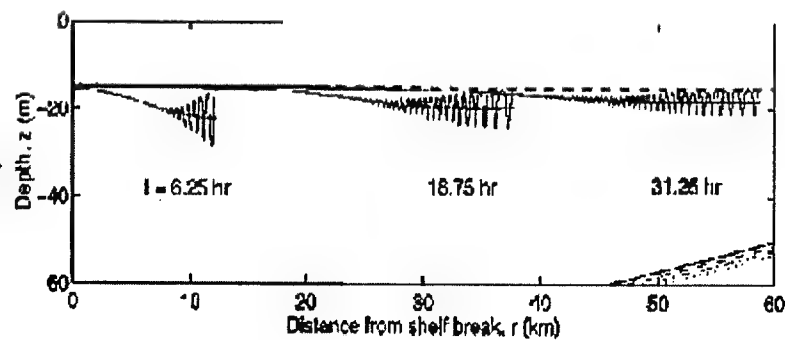
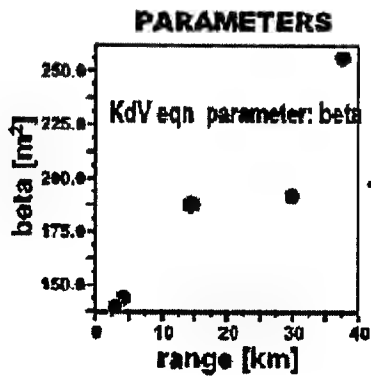


Figure 1

one minute increment updates of both soliton and acoustic fields. The upper three figures in the illustration are snapshots of the sound speed distribution along the track, showing the superposition of the solitons on the deterministic background distribution. The red lines connecting these snapshots to the intensity plot show the approximate times that the snapshots were taken within an M2 tidal cycle. The sound speed distributions show two packets traveling to the left (toward the source) in the first two snapshots, with a space separation between the packets associated with the M2 tide. The third snapshot contains a single packet, as the one near the array has now moved off the grid. Sound speed fluctuations associated with these packets can be as large as 20-30 m/sec. The corresponding transmission loss at the array as a function of depth and time has a complex structure that changes qualitatively when packets are no longer near the source and receiver. The time variations in intensity and phase are associated with acoustic mode coupling, since the received field under conditions of adiabatic propagation is not sensitive to the location of the range dependent fluctuations along the acoustic path. This is strictly true for a range-independent quiescent environment, since in a range-dependent environment the local influence of the perturbation can be range dependent. A recent analysis of mode coupling due to internal waves and its effect on modal intensity statistics is given in [4]. Temporal phase variations, particularly the phase gradient along the array, have implications for source localization schemes such as matched field processing and are under investigation.

Acknowledgement

This research was sponsored by the Office of Naval Research.

References

- [1] J.R. Apel, M. Badiey, C.S. Chiu, S. Finette, R. Headrick, J. Kemp, J.R. Lynch, A. Newhall, M.H. Orr, B.H. Pasewark, D. Tielbuerger, K. von der Heydt and S. Wolf: "An Overview of the 1995 SWARM Shallow-Water Internal Wave Acoustic Scattering Experiment", *IEEE J. Oceanic Engineering* **22** 465-500 (1997).
- [2] J. Apel, S. Finette, M.O. Orr and J.F. Lynch: "The ?Dnoidal? Model for Internal Solitons and Tides on the Continental Shelf" submitted to *J. Geophysical Research* (1998).
- [3] S. Finette, M.Orr and J.R. Apel: "Acoustic field propagation through a shallow water waveguide dominated by internal waves" *Abs. J. Acoust. Soc. Am.* **102** 3062 (1997).
- [4] D. Tielbuerger, S. Finette and S. Wolf: "Acoustic propagation through an internal wave field in a shallow water waveguide" *J. Acoust. Soc. Am.* **101** 789-808 (1997).

**INTENSITY AND PHASE VARIATIONS CAUSED BY INTERNAL WAVE
400 Hz / SOURCE DEPTH=29 M**

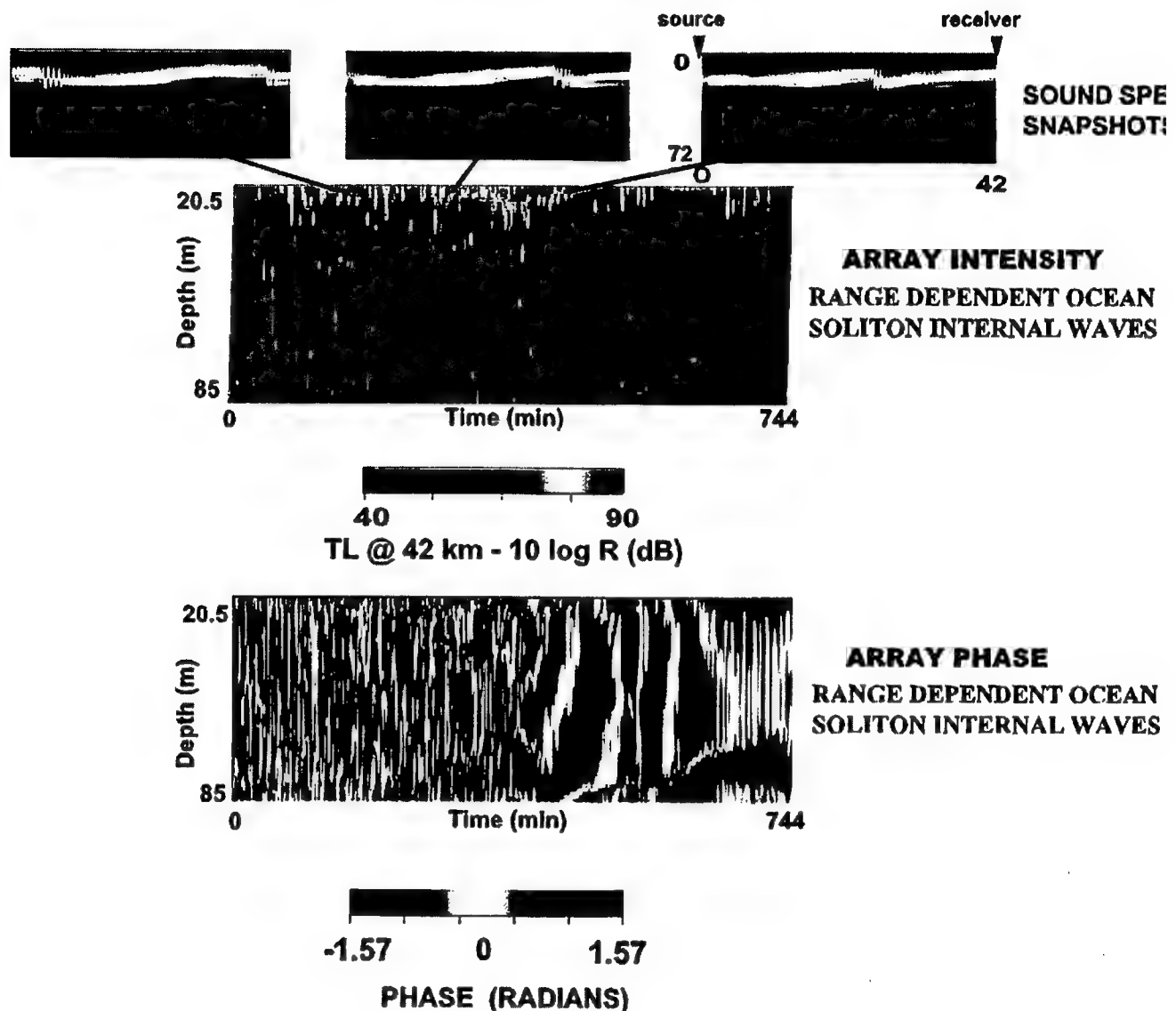


Figure 2

ACOUSTICAL IMPACTS AND INVERSION SCHEME OF INTERNAL SOLITARY WAVES

E. C. Shang, Y. Y. Wang and L. Ostrovsky

CIRES, University of Colorado/NOAA/ETL, Boulder, Colorado, USA

Abstract

Based on the internal solitary waves (ISWs) data obtained during the COPE experiment conducted from September-October, 1995 in the Oregon coastal area, numerical simulation on acoustic propagation has been performed. Frequency dependency of transmission loss (TL) is analyzed in range of 50 - 1000 Hz. It has been found that for lower frequencies (< 100 Hz) the propagation is *adiabatic*, whereas for higher frequencies (> 200 Hz) significant mode-coupling takes place which causes a 5~10 db loss increase as compared with the background case (without ISW), but no strong resonant loss appears in this case.

The tomographic inversion scheme based on modal phase tomography is proposed; the ISW parameter that can be retrieved in this scheme is the *integral depression (ID)* of the ISW.

1. Introduction

The nonlinear internal waves in the ocean have been known for over a century and extensive investigations have been made by the oceanographic community in the recent years [1,2]. The increased interest to this phenomenon in the ocean acoustic community during the 1990s, was stimulated by Zhou's paper, which considered the ISWs as possible candidates to explain the strong frequency-selected transmission loss observed in the shallow water of the Yellow Sea [3].

In this paper, the numerical simulation is performed based on the ISW data obtained in the "Coastal Probing Experiment" (COPE) which was conducted by NOAA/ETL in Sept-Oct 1995 in the Oregon coastal area [4]. Trains of extremely nonlinear tide-generated solitary waves (thermocline depressions up to 30 m on the background of 5-8 m depth thermocline) were observed. They seem to approach critical magnitudes when the Richardson number is close to 0.25, and particle velocities are close to wave velocities so that most usable models (KdV, Benjamin-Ono, Joseph) are inapplicable. Both the forward problem (acoustic propagation) and the inverse problem (parameter retrieval) are studied.

2. Forward Problem

The acoustic propagation through the ISW is calculated by using a PE code. The TL of a point source at depth $z_s=50$ m, and receiver at depth 50m (water depth is 150 m) are calculated in frequency range of 50 - 1000 Hz for the distance $R=32$ km (covered the whole ISW at the normal direction). It is found that for lower frequencies (< 100 Hz), the TL only suffered a phase shift and

there is no interference pattern change compared with the background case showing that the propagation is *adiabatic* in this case. However, for higher frequencies (> 200 Hz), the pattern of TL changed significantly and an extra 5-10 dB loss is found that shows that a significant mode-coupling takes place. The *adiabaticity* is also verified by mode repopulation by exciting a single mode as the starting field. The azimuthal dependency of the adiabatic modal phase is also investigated.

3. Tomographic Inverse Scheme

The modal phase tomography based on adiabatic mode theory has been suggested previously [5]. If we take the constant depth of the thermocline, $h_0 = 5$ m, as the background, then the perturbed modal phase shift by the ISW is given by

$$m = [k_m(r) - k_m^b] dr = [k_m^{\text{Ave}} - k_m^b] L() \quad (1)$$

where k_m^{Ave} is the range-averaged modal wavenumber over the effective length $L()$, and k_m^b is the modal wavenumber corresponding to the background. By replacing the averaged modal wavenumber with an "effective" modal wavenumber k_m^{eff} which corresponds to the effective perturbation with a constant thermocline depression h^{eff} in the same length $L()$, we have

$$m() = [k_m(h^{\text{eff}}) - k_m^b] L() \quad (2)$$

In equation (2), there are only two unknown parameters : h^{eff} and $L()$. By measuring one more modal phase perturbation, we can eliminate the parameter $L()$ and get

$$\{m / n\} = \{ [k_m(h^{\text{eff}}) - k_m^b] / [k_n(h^{\text{eff}}) - k_n^b] \} \quad (3)$$

The parameter h^{eff} can be uniquely determined by Eq.(3). After that, the parameter L can be calculated from Eq.(2). Finally, the "integral depression" (ID) of the thermocline caused by ISW (which is roughly related to the total energy stored in ISW) can be estimated. The real ID is

$$(\text{ID})^{\text{real}} = [h(r) - h_0] dr \quad (4)$$

and the effective $(\text{ID})^{\text{eff}}$ is

$$(\text{ID})^{\text{eff}} = [h^{\text{eff}} - h_0] L \quad (5)$$

Our numerical result shows that $(\text{ID})^{\text{eff}} = 1.4 \cdot 10^5$ m², that is pretty close to the real value of the depression area $(\text{ID})^{\text{real}} = 1.5 \cdot 10^5$ m².

The retrieved parameter (ID) combined with the soliton width data obtained independently by radar measurement or SAR measurement can be used for amplitude estimation.

Acknowledgment: This work was supported by the Office of Naval Research (ONR) and NOAA.

References

- [1]. L.Ostrovsky and Y. Stepanyants, "Do internal solitons exist in the ocean?", *Rev. Geophys.* 27, pp.293-310, 1989.
- [2]. J.R. Apel, L. Ostrovsky and Y. Stepanyants, "Internal solitons in the ocean," Applied Physics Lab.. Johns Hopkins University, 1997.
- [3]. Jin-Xun Zhou, Xue-zhen Zhang and P. Rogers, "Resonant interaction of sound wave with internal solitons in coastal zone," *J.Acoust.Soc.Am.*,90, pp.2042-2054, 1991.
- [4]. R. Kropfli, L. Ostrovski, T. Stanton, E. Skirta, A. Keane and V. Irosov, "Relationship between strong internal waves in the coastal zone and their radar and radiometric signatures" (accepted by *J. Geophys. Res.*)
- [5]. E.C. Shang, "Ocean acoustic tomography based on adiabatic mode theory, " *J. Acoust. Soc. Am.*, 85, pp.1531-1537, 1989.

Contributions of the Turbulence Field and Zooplankton to Acoustic Backscattering by an Internal Wave

Timothy K. Stanton*, Joseph D. Warren*, Peter H. Wiebe**,
Mark C. Benfield¹, Charles H. Greene²

* Woods Hole Oceanographic Institution, Department of Applied Ocean Physics and Engineering, Woods Hole, MA 02534;

** Woods Hole Oceanographic Institution, Department of Biology, Woods Hole, MA 02543;

¹ Louisiana State University, Coastal Fisheries Institute, Baton Rouge, LA 70803;

² Ocean Resources and Ecosystems Program, Center for the Environment, Department of Geological Sciences, Cornell University, Ithaca, NY 14853

ABSTRACT

A multifrequency acoustic backscatter survey system (BIOMAPER-II) has been used to map an internal wave in the Gulf of Maine, a shallow water coastal region north of Cape Cod, MA. The acoustic visualization of the internal wave showed the wave to consist of two scattering layers, each with a distinctly different frequency response. The response of one is consistent with the scattering by shrimp-like zooplankton while the response of the other is consistent with the scattering by turbulence-induced sound speed microstructure. Preliminary results are presented and implications for quantitative mapping of internal waves and zooplankton are discussed.

INTRODUCTION

Internal waves have long been visualized with acoustic backscattering survey systems (Munk and Garrett, 1973; Proni and Apel, 1975; Orr and Hess, 1978; Haury et al., 1983; Seim et al., 1995; Wiebe et al., 1997). The visualization has provided quantitative information on key parameters of the waves including their amplitude and wavelength. This information can be determined directly from the echograms because of the resolution of the acoustic system: the acoustic beamwidth and range resolution are small enough in comparison with the larger scale features so the acoustic system could resolve them.

Although the larger scale features of the internal wave can be directly determined from an acoustic echogram, the mechanism causing the acoustic scattering by the internal wave cannot. Intrinsic in this mechanism are parameters such as size, numerical density, material properties, and taxa of particulate scatterers that may be present (typically zooplankton) as well as parameters such as scale and dissipation rate of smaller scale features of turbulence that may be present (Goodman, 1990; Goodman et al., 1992; Stanton et al., 1994; Seim et al., 1995; Fig 1 of this paper). Understanding the scattering physics of zooplankton and turbulence will help provide methods for estimating their respective parameters.

ACOUSTIC SURVEY

A survey was made in the Gulf of Maine during a cruise in October, 1997 (Fig. 2). The site was selected because of the important biological activity in relation to the bathymetric and physical oceanographic properties of the region. A cruise track was designed so that a significant portion of the Gulf was surveyed.

The survey involved towing the BIOMAPER-II (BIO-Optical Multi-frequency Acoustical and Physical Environmental Recorder) (Austin et al., submitted; Fig. 3 of this paper). This system contains a wide suite of acoustical, optical, and environmental sensors. The acoustic sensors consist of two identical sets of transducers, one set looking upward and the other looking downward. The frequencies in each set are 43 kHz, 120 kHz, 200 kHz, 420 kHz, and 1 MHz. The optical sensors includes a high resolution underwater camera (video plankton recorder or VPR) that can resolve features of individual zooplankton. Also included in the optics package are an optical transmissometer and fluorometer, and various optical spectral devices (absorption, attenuation, down-welling irradiance, and up-welling irradiance). Depth, temperature, and conductivity sensors are included in the environmental sensor package. During the transects, BIOMAPER-II was either tow-yoed up and down throughout the water column or towed near the surface making use of only the downlooking acoustic systems.

OBSERVATION AND MEASUREMENTS OF INTERNAL WAVE

During the latter part of R/V ENDEAVOR Cruise 307, a search was made for an internal wave packet like one seen earlier in the cruise in the same area (Greene et al., 1997). In that search, a strong internal wave was observed first with the ship-board radar (Fig. 4) and then with the downlooking transducers on the BIOMAPER-II (Fig. 5) as the ship steamed in a direction parallel to the direction of propagation of the internal wave. The internal wave showed two distinct scattering layers, one centered at about 25 m depth and the other at about 50 m depth. The peak-to-peak (internal wave) amplitude of each layer was of order 25 m.

After the near-surface tow was completed, the ship was turned around and the wave was surveyed three more times, once with BIOMAPER-II lowered to the depth of 50 m which corresponded to the lower scattering layer of the wave, once at a depth of about 25-30 m depth which corresponded to the depth of the upper scattering layer, and once where the BIOMAPER-II system was towed near the surface again, but while the MOCNESS multiple net system was towed at various depths so that zooplankton could be caught. Towing BIOMAPER-II through the different scattering layers allowed the short range sensors (optics, temperature, etc.) to directly measure parameters of the wave.

The two scattering layers have a distinctly different frequency response (Fig. 6). The upper layer shows the scattering to be higher at the lower frequencies than at the higher frequencies and the lower layer is the opposite. In fact, the upper layer is barely detectable at 420 kHz and the lower layer is not at all detectable at 43 kHz.

COMPARISON WITH SCATTERING PREDICTIONS AND IMPLICATIONS

Comparison of the observed frequency response of the different layers illustrated in Fig. 6 with the predicted response for intense turbulence and zooplankton in Fig. 1 shows that the response of the upper layer is consistent with the scattering by turbulence and that the response of the lower layer is consistent with the scattering by shrimp-like zooplankton. Both responses are consistent with those corresponding types of scatterers in that the shapes of the curves are similar. However, the observed values are about 10-15 dB higher. This could easily be due to the intensity of the turbulence and size or number of

zooplankton being different in this region than what was used in the predictions. Nonetheless, it is the shape of the curves that are indicative of the scattering processes. These correlations between the respective scattering processes indicate that apparently the zooplankton are acting as tracers of the internal wave in the lower layer and are dominating the scattering. In the upper layer, it appears that turbulence is present in the internal wave and is dominating the scattering.

These observations have important implications in the use of mapping internal waves and zooplankton in the ocean:

MAPPING INTERNAL WAVES: a) Whether zooplankton, turbulence or other types of scatterers dominate the scattering, larger scale features of the internal waves can be directly measured from acoustic echograms. However, proper selection of the acoustic frequency is essential. If turbulence is present and dominates the scattering, parts or all of the wave may not be detectable at the higher acoustic frequencies (including frequencies at which certain acoustic doppler current profilers operate). b) Multifrequency acoustic systems can be used to discriminate between sources of scattering in the internal wave. c) As suggested in this and previous studies, under some conditions internal waves can dominate the acoustic scattering. When that is the case, there is potential for other parameters related to scale and dissipation rates not resolved by the echograms (ones connected with the scattering process) to be inferred from the scattering. This inference is a subject for future studies by these authors.

MAPPING ZOOPLANKTON: It is generally assumed that marine life such as zooplankton dominates the backscattering throughout most of the water column. As a result, scattering levels from the water column are usually directly converted into biomass values. For conditions under which turbulence significantly contributes to, or even dominates, the scattering, biomass estimates would be in error if the contributions due to the turbulence are not taken into account. Certainly, the rate of occurrence of turbulence with high enough levels for it to dominate the scattering is low. However, it is believed that the turbulence can play a major role in biological processes (Rothchild and Osborn, 1988; Evans, 1989; Davis et al., 1991; Yamazaki et al. 1991). As a result, regions where high levels of turbulence occur may be the focus of certain biological studies, which places importance on understanding the role of turbulence in acoustic mapping of the region.

CONCLUSIONS

In conclusion, acoustic scattering of an internal wave is a complex function of various parameters of the turbulence field and abundance and composition of the zooplankton population that may be present. These preliminary results are suggestive of the care one needs to make in quantitatively mapping the turbulence and zooplankton, especially when one is in the presence of the other. Further analysis is underway which will test these inferences by comparing the observed acoustic scattering with predictions of the scattering based upon direct measurements of the zooplankton population and estimates of the turbulence field.

ACKNOWLEDGEMENTS

The authors are grateful to the captain and crew of the RV Endeavor for their support of the cruise in 1997 as well as Shirley Barkley for preparation of the manuscript of this paper. This research was supported by the Office of Naval Research, National Science Foundation, and the Woods Hole Oceanographic Institution Graduate Education Program.

REFERENCES

Davis, C.S., G.R. Flierl, P.H. Wiebe, and P.J.S. Franks, 1991. "Micropatchiness, turbulence and recruitment in plankton," *J. Mar. Res.* 49, 109-151.

Evans, G.T., 1989. "The encounter speed of moving predator and prey," *J. Plankton Res.* 11, 415-417.

Greene, C., P. Wiebe, H. Sosik, M. Benfield, and A. Bucklin, 1997. R/V ENDEAVOR Cruise 307 to Georges Bank Report (7-17 October 1997). 47 pgs.

Haury, L.R., P.H. Wiebe, M.H. Orr and M.G. Briscoe, 1983. "Tidally generated high frequency internal wave packets and their effects on plankton in Massachusetts Bay," *J. Mar. Res.* 41, 65-112.

Munk, W.H. and J.C.R. Garrett, 1973. "Internal wave breaking and microstructure (The chicken and the egg)." *Boundary Layer Meteorol.* 4, 37-45.

Orr, M.H. and F.R. Hess, 1978. "Remote acoustic monitoring of natural suspensate distributions, active suspensate and slope/shelf water intrusions." *J. Geophys. Res.* 83, 4062-4068.

Proni, J.R. and J.R. Apel, 1975. "On the use of high-frequency acoustics for the study of internal waves and microstructure," *J. Geophys. Res.* 80, 1147-1151.

Rothschild, B.J. and T.R. Osborn, 1988. "Small-scale turbulence and plankton contact rates," *J. Plankton Res.* 80, 465-474.

Seim, H.E., M.C. Gregg, and R.T. Miyamoto, 1995. "Acoustic backscatter from turbulent microstructure," *Atmos. Ocean. Tech.* 12, 367-380

Stanton, T.K., P.H. Wiebe, D. Chu, and L. Goodman, 1994. "Acoustic characterization and discrimination of marine zooplankton and turbulence," *ICES J. Mar. Sci.*, 51, 469-479.

Wiebe, P.H., T.K. Stanton, M.C. Benfield, D.G. Mountain, and C.H. Greene, 1997. "High-frequency acoustic volume backscattering in the Georges Bank coastal region and its interpretation using scattering models," *IEEE J. Ocean. Eng.* 22, 445-464

Yamazaki, H., T.R. Osborn, and K.D. Squires, 1991. "Direct numerical simulation of planktonic contact in turbulent flow," *J. Plankton Res.* 13, 629-643.

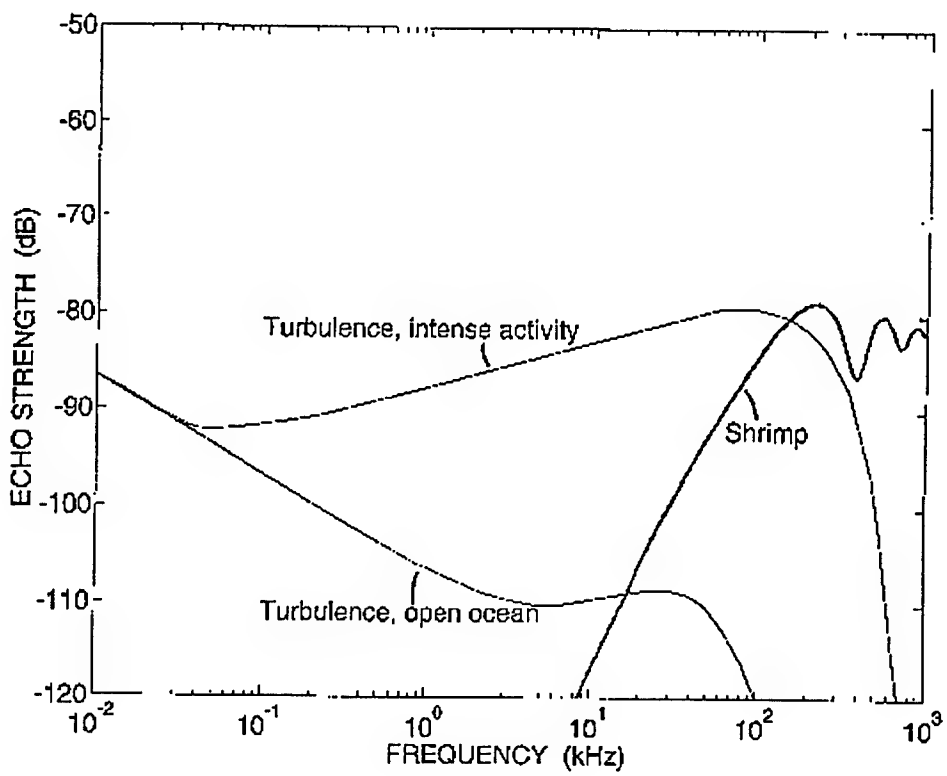


Figure 1. Acoustic scattering levels due to turbulence for intense area of the ocean such as in internal waves, turbulence in the open ocean away from intense fields, and 2-cm-long zooplankton averaged over angle of orientation. From Stanton et al. (1994).

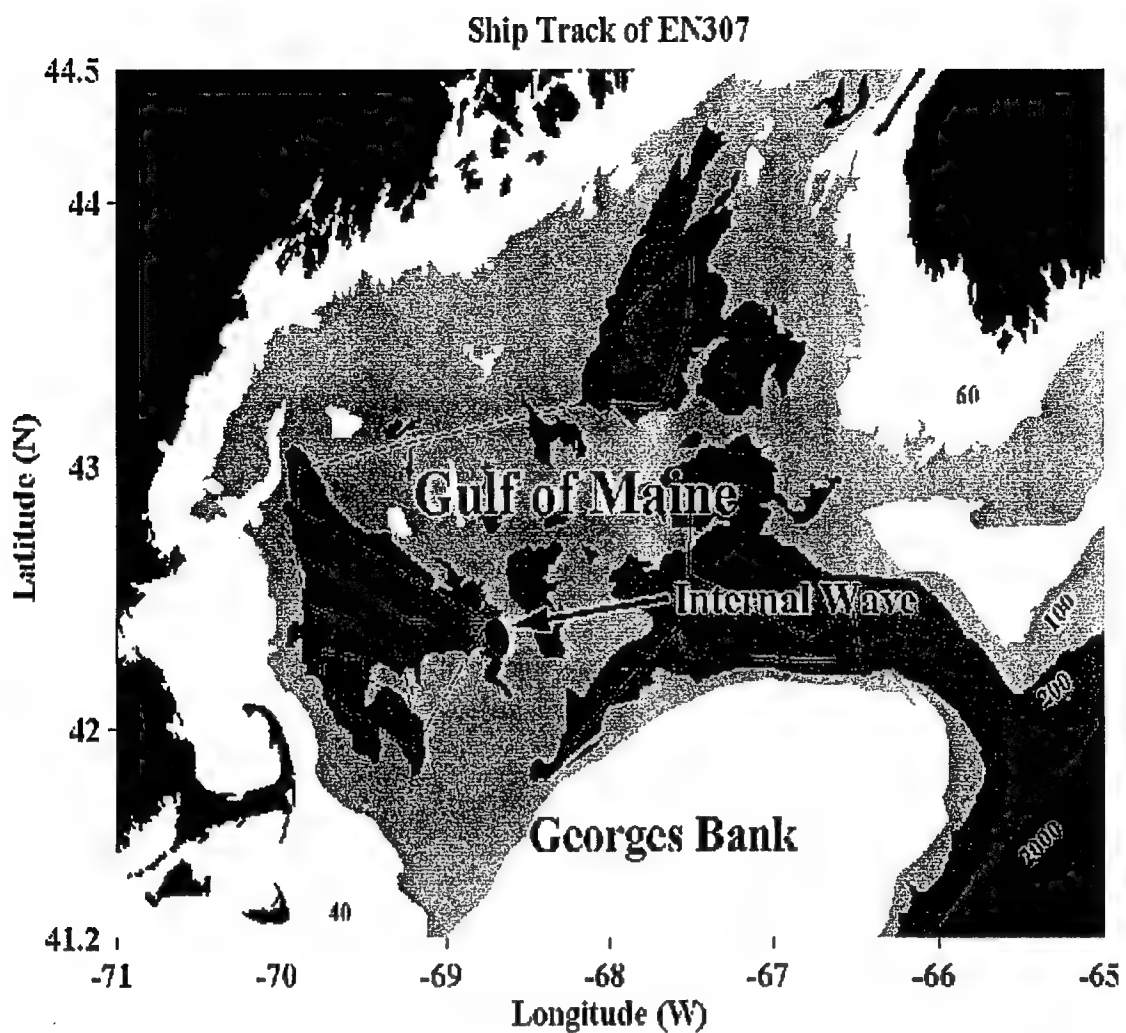


Figure 2. Cruise track in October 1997 survey of Gulf of Maine region. The section in which the internal wave was mapped is indicated.

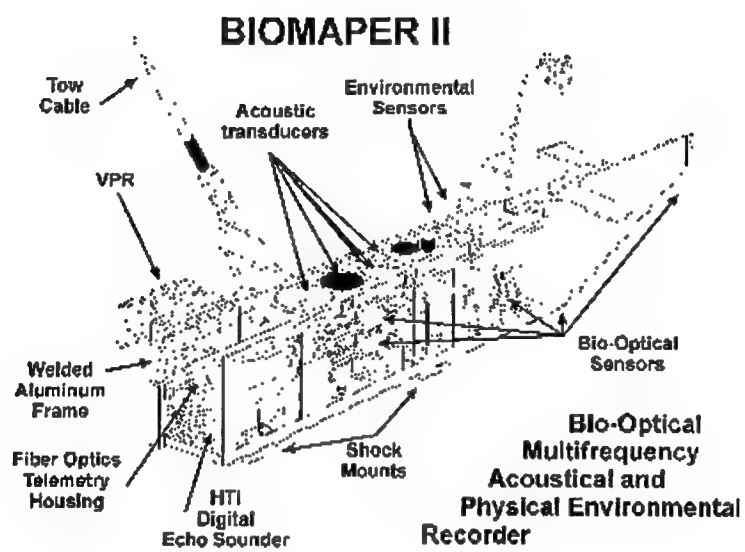
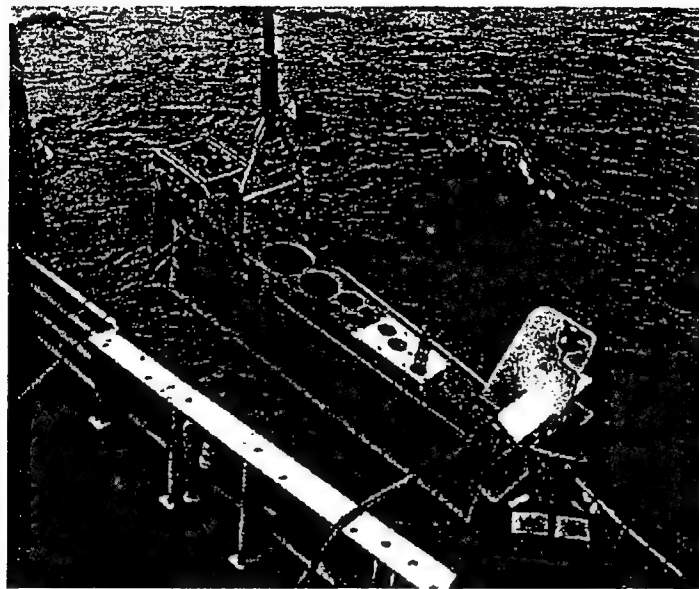


Figure 3. BIOMAPER-II towed system. The system contains five acoustic transducers looking up (43 kHz to 1 MHz) and an identical set looking down, an underwater camera system for recording images of

zooplankton, and various other optical systems and environmental sensors. Optical fibers in the core of the tow cable allow large volumes of data to be transmitted to the ship-board computers. Austin et al. (submitted).

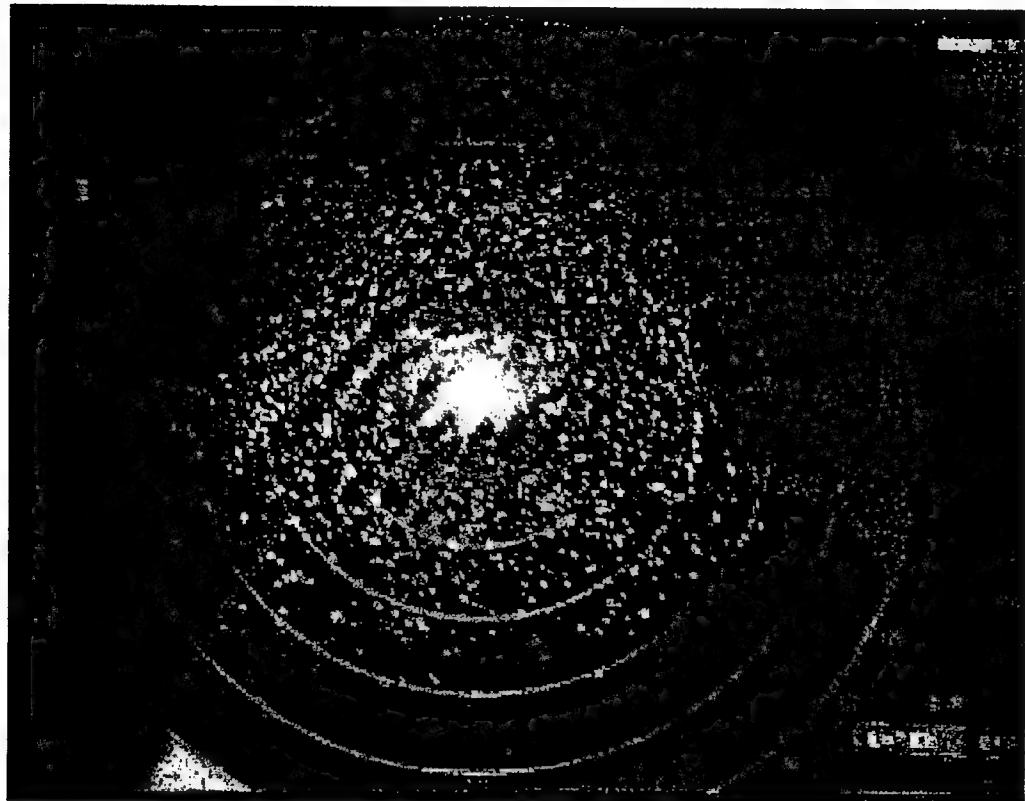


Figure 4. Radar image of internal wave as viewed from the ship's radar system at the sea surface.

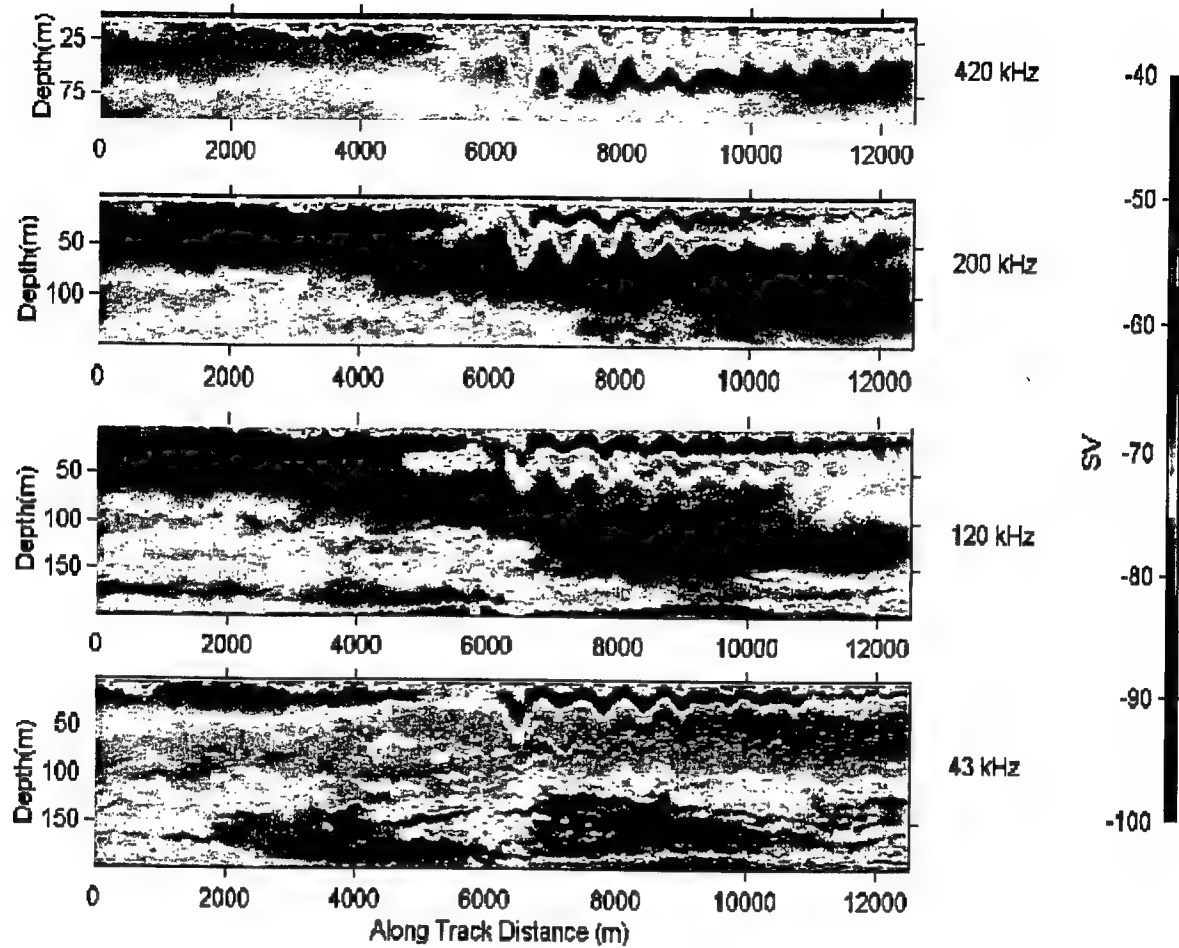


Figure 5. Acoustic image of internal wave within the ocean's interior at four acoustic frequencies. The color is modulated according to level of volume scattering strength (red corresponds to a high echo level, blue corresponds to a low level). Although the vertical dimensions of each plot are different due to the different range of each frequency, the scales are the same so that one-for-one comparisons can be made.

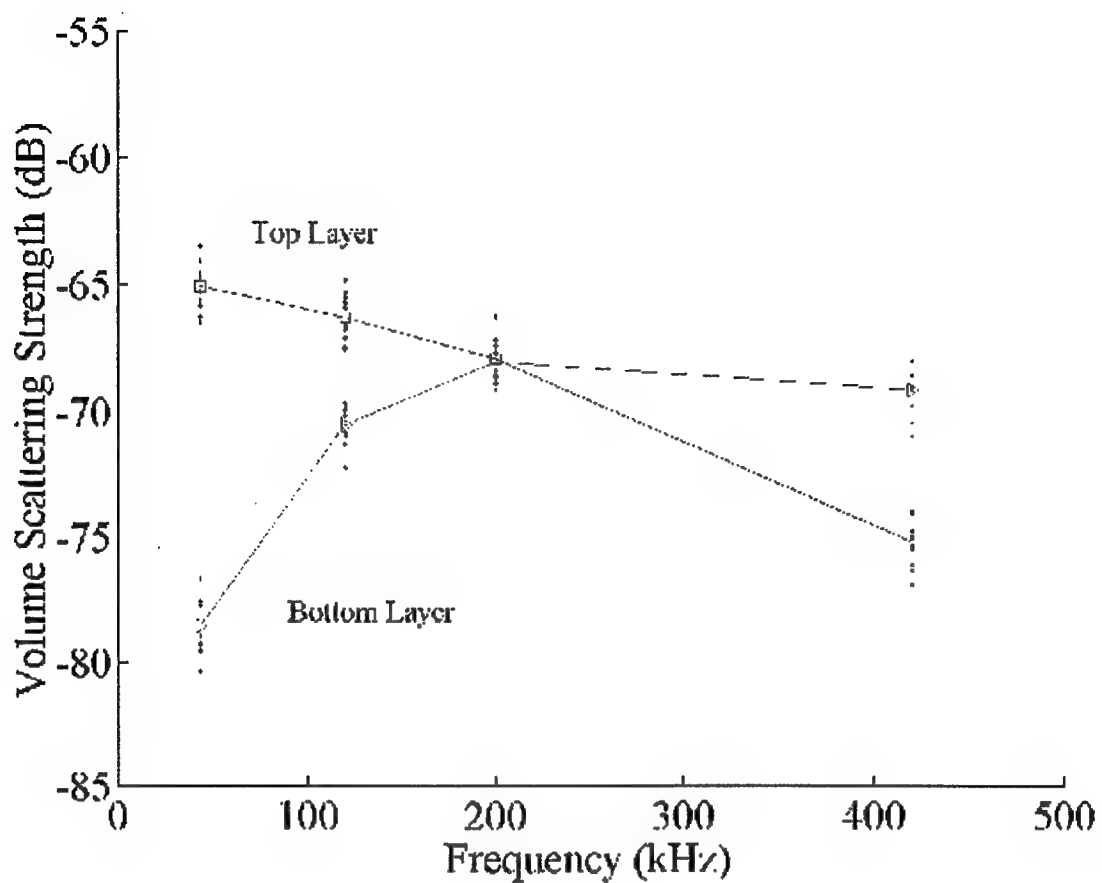


Figure 6. Acoustic volume scattering strength versus frequency as measured in a small section of the upper and lower scattering layers of the internal wave illustrated in Fig. 5. Each average scattering strength was determined by averaging the levels within a layer, first on a linear scale before the logarithm was performed. One layer was first sampled at one frequency (where the return was strongest) along its peak value at approximately one-quarter wavelength intervals (internal wave wavelengths). The layer was then sampled at precisely those locations for the other frequencies.

Effects of Internal Waves and Bores on Acoustic Transmissions in the Strait of Gibraltar

Christopher O. Tiemann, Peter F. Worcester, Bruce D. Cornuelle

Scripps Institution of Oceanography, University of California at San Diego,
La Jolla, California 92093, USA

Uwe Send

Institut fur Meereskunde, University of Kiel, 24105 Kiel, Germany

Abstract. The Strait of Gibraltar Acoustic Monitoring Experiment was conducted in April 1996 to determine the feasibility of using acoustic methods to make routine, rapidly repeated transport measurements in the Strait of Gibraltar, as well as to explore the acoustic scattering caused by the unique internal wave field in the Strait. The acoustic data from high frequency (2-kHz) reciprocal transmissions across the Strait are unique in that they clearly isolate the acoustic effects of passing internal bores without the added complexity of surface and bottom interactions. Although the acoustic scattering caused by each internal bore is different, some common characteristics can be identified.

Environment

The basic circulation in the Strait of Gibraltar is relatively simple. An upper layer of warm, fresh, Atlantic water about 100 m thick flows east into the Mediterranean Sea, and a lower layer of colder, salty Mediterranean water flows west into the Atlantic. This mean flow is modulated by large tidal flows and is also subject to hydraulic controls at the shallowest sill (Camarinal Sill on the west side of the Strait) and the narrowest constriction (Tarifa Narrows.) Furthermore, there are tidal fluctuations in the depth of the interface between the upper Atlantic and lower Mediterranean water layers.

Perhaps the most interesting feature, though, is the propagation of internal bores which are released at the Camarinal Sill at the relaxation of most high tides and propagate east down the Strait. These bores can have amplitudes as high as 100 m peak to peak and wavelengths of 1 km. They are found at the interface depth and travel with a phase speed of 1-2 m/s. The bore eventually disintegrates into a train of as many as twelve internal solitary waves. [Armi and Farmer, 1988; Farmer and Armi, 1988; Watson and Robinson, 1989]

Experimental Approach

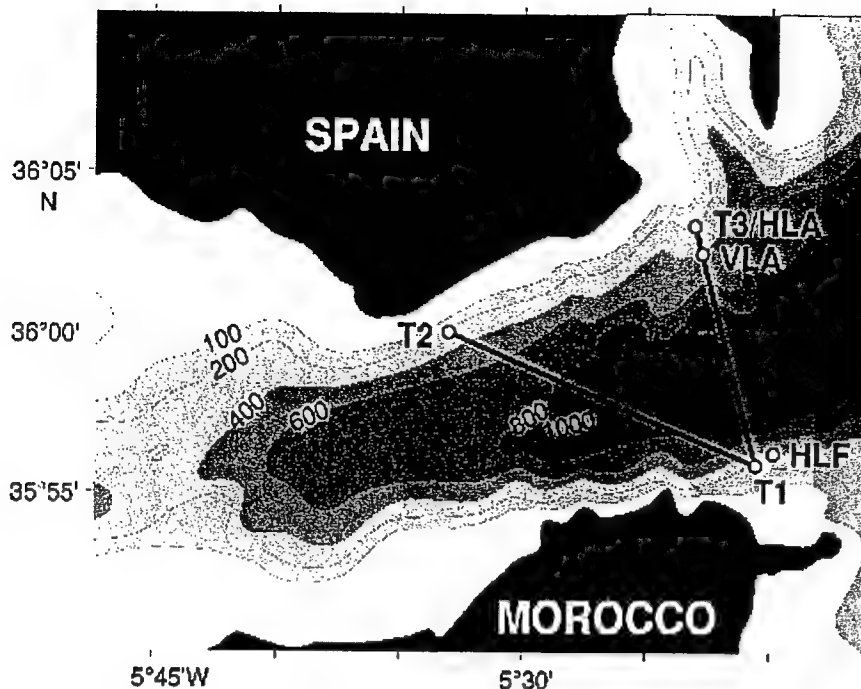


Figure 1. Instrument locations and acoustic paths in the Strait of Gibraltar.

for instrument motion. Examination of the motion data for the T1 instrument showed brief but violent kicks occurring roughly every 12 hours during spring tides. These kicks are due to the passing of an internal bore over the instrument and are now being used as a "clock" of internal bore crossings.

In addition to the acoustic data that was recorded, the tilts and orientations of the three moorings were measured as well and used to correct ray travel times

Analysis

The corrected, absolute travel times for several acoustic rays are shown as a "dot plot" in Figure 2. For each transmission from T1 to T2 occurring over the two weeks shown along the x-axis, a dot is placed along the vertical axis at each time when a peak in the acoustic amplitude occurs. The size of the dot is proportional to the signal-to-noise ratio. The times from the internal bore clock are overlaid in red, indicating the passing of an internal bore over the T1 instrument.

The transmissions through the strong tidal flows, internal bores, and trains of interfacial internal waves have complex travel time fluctuations and path structure. The dot plots for the T1-T2 path show that the earliest arrival, from a deep-going ray which samples only the lower Mediterranean water layer, was stable over the duration of the experiment and had a strong tidal signal. This early arrival was successfully tracked over all days of the experiment and is shown in green in Figure 2. The later arrivals are from shallow rays which sample the interface between the two water layers. They also show tidal variability, but the path structure is more complicated; the shallow rays are smeared into a broad cluster of arrivals that are difficult to track. Dot plots for the T1-T3 path are generally similar to those for T1-T2, but the tidal signal is much smaller for the deep ray arrivals as the acoustic path is perpendicular to the tidal currents.

A closer look at the dot plot data from Figure 2 shows an interesting effect of the passing bores on the

acoustics. The travel time of the earliest ray decreases with each passing of the bore, followed by a sudden increase in travel time shortly after the bore has passed. Because the effects are slightly different with each bore occurrence, nine examples of travel time data showing bore effects from the days of spring tides have been stacked on each other, as shown in Figure 3, in order to identify some effects common in all cases. Figure 3 shows dot plot data from T1-T2 transmissions for 5 hours before and after nine bore crossings, where each of the nine examples has been shifted to align all the green tracked paths at the time of a bore occurrence.

Figure 3 shows that the brief decrease, then increase, in lower ray path travel times is a common acoustic effect seen each time an internal bore passes over the T1 instrument. Differential travel times from reciprocal transmissions along the T1-T2 path show such travel time changes to be an effect of temperature, rather than current effects. Perhaps warm shallow water is being displaced deeper by the bore to the depths of the instruments, increasing the soundspeed near the endpoints of the deep going rays. Also note how both the shallow and deep ray arrivals show much more scattering in the hours following a bore crossing, with some shallow rays arriving at the same time as the deep rays.

Figure 4 also shows stacked dot plot data for nine bore crossings during spring tides, but now for transmissions along the other acoustic path from T1 to T3. Once again there is the common feature of a brief decrease, then increase, in lower ray travel times shown in green, as the bore passes the instrument. The cloud of shallow ray arrivals shows a very sharp decrease in travel times, and for hours after the bore has passed some shallow rays are arriving earlier than the deep rays! This may be because the interface layer is deepened behind the passing bore and is slow in restoring itself, allowing shallow rays to travel through warmer water during that time.

Conclusion

The challenge is to explain these acoustic observations in terms of the physical processes occurring. Acoustic propagation models through range- and time-dependent soundspeed fields representing the Strait of Gibraltar and perturbed by internal bore models are being used to understand these observations and answer several other questions: To what aspects of the bore are the acoustics most sensitive? How complicated of an ocean model is necessary to reproduce the observations, and are existing ray trace codes adequate? Can acoustics be used to observe a bore's direction of propagation and phase speed?

References

Armi, L., and D. M. Farmer (1988). The flow of Mediterranean Water through the Strait of Gibraltar. *Progress in Oceanography*, 21, 1-105.

Farmer, D. M., and L. Armi (1988). The flow of Atlantic Water through the Strait of Gibraltar. *Progress in Oceanography*, 21, 1-105.

Watson, G., and I. S. Robinson (1989). A Study of Internal Wave Propagation in the Strait of Gibraltar using Shore-Based Marine Radar Images. *J. Phys. Oceanogr.*, 20, 374-395.

Worcester, P., U. Send, B. Cornuelle, and C. Tiemann (1997). Acoustic monitoring of flow through the Strait of Gibraltar. *Shallow-Water Acoustics*, Proc. of the International Conference on Shallow Water Acoustics, Beijing, China, 21-25 April 1997. R. Zhang and J. Zhou, eds., 471-477, China Ocean Press.

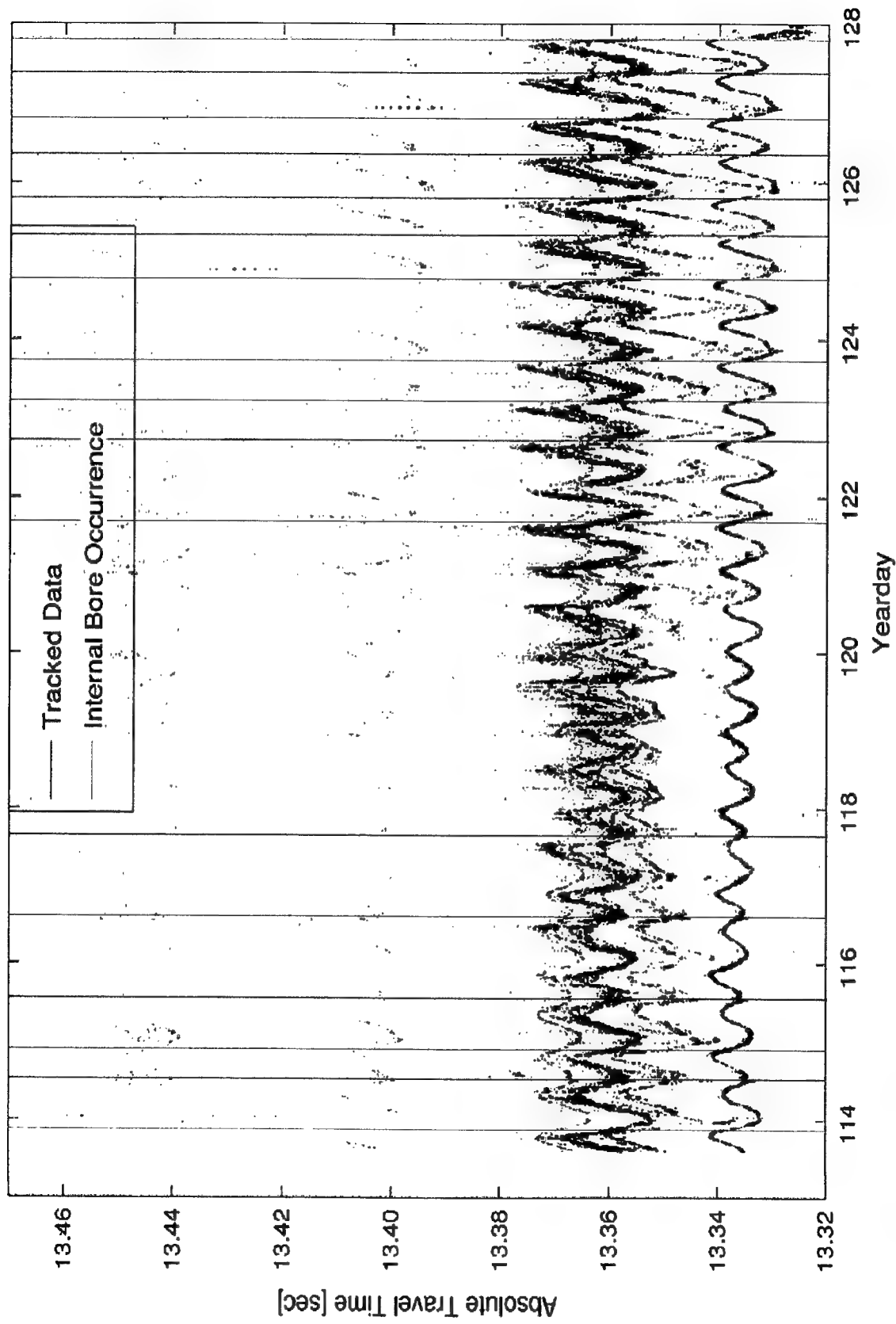


Figure 2: T2 from T1 acoustic receptions with times of bore crossings indicated.

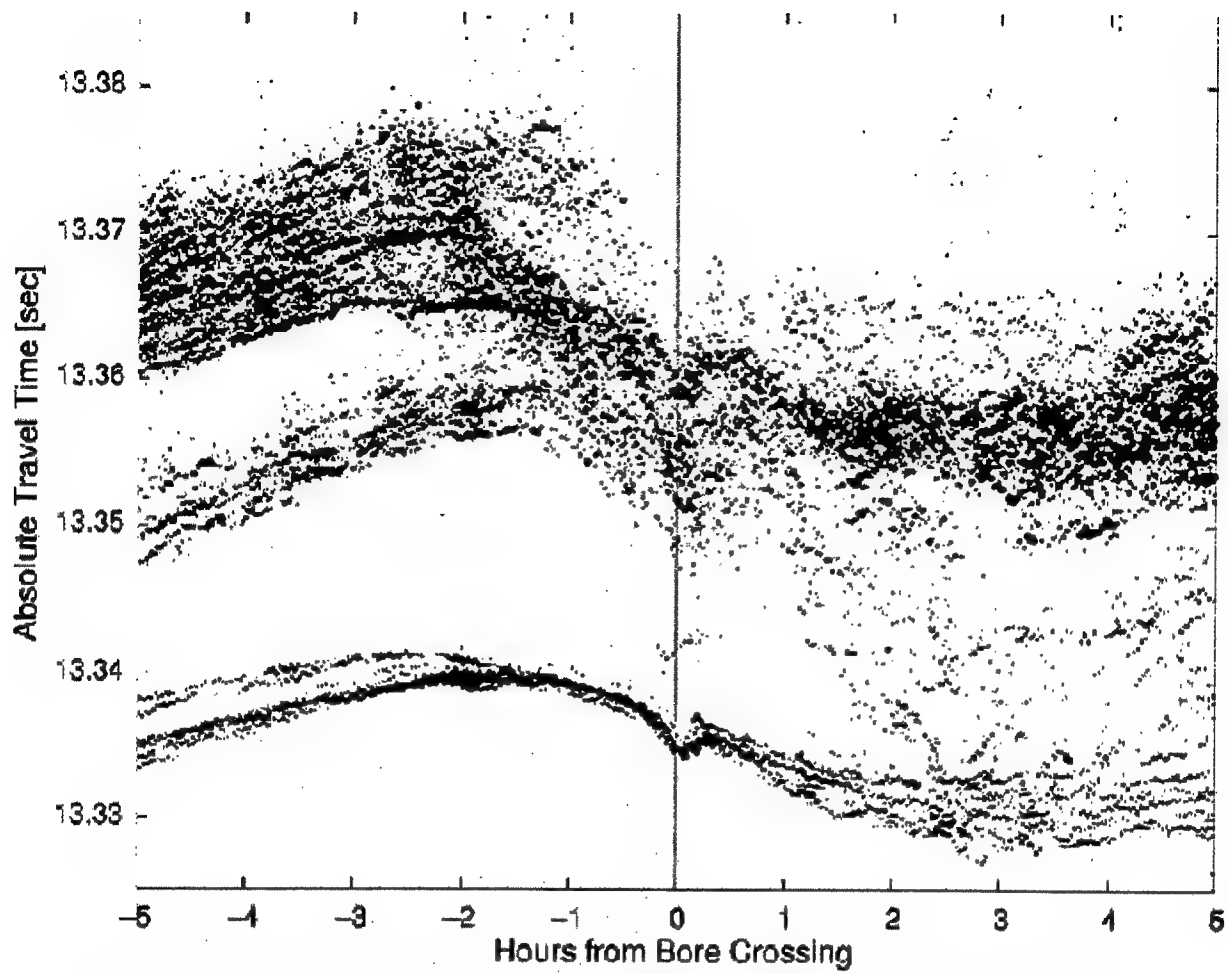


Figure 3: T2 from T1 stacked travel times, 9 bores from days 121–127.

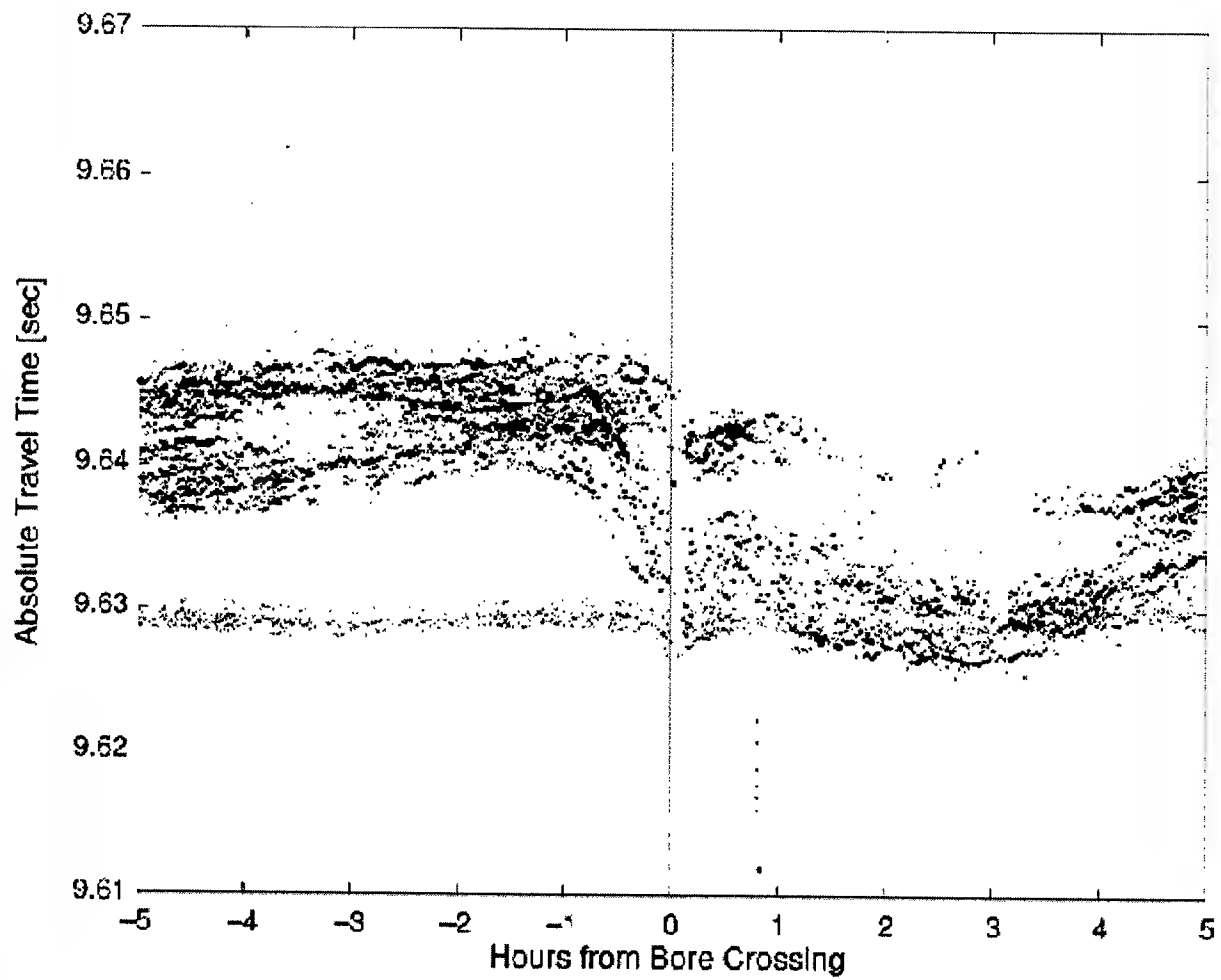


Figure 4: T3 from T1 stacked travel times, 9 bores from days 121-127.

Modeling the Effects of Solitons on Acoustics

Alex C. Warn-Varnas[¶], Stanley A. Chin-Bing[¶], David B. King[¶], Steve A. Piacsek[¶],
and Andrew MacNaughton[§]

[¶] Naval Research Laboratory, Stennis Space Center, MS 39529-5004

[§] Naval Oceanographic Office, Stennis Space Center, MS 39529-6000

Abstract. Recently shallow water solitons have become a major topic of interest to both oceanographers and ocean acousticians. Numerous research efforts are underway to identify and predict soliton properties that are unique to each scientific discipline. In this work preliminary results are presented from a cross-disciplinary study of shallow-water solitons that utilizes oceanographic models, ocean acoustic models, oceanographic data, and ocean acoustic data. It is concluded that all four entities are required to fully understand and predict the impact that shallow-water solitons have on ocean-acoustic signal transmission.

Introduction

The stimulation for our study was initiated by the observation of an anomalous frequency response in shallow-water sound propagation measurements. In particular, acoustical measurements in the Yellow Sea conducted by Zhou, Zhang and Rogers[1] showed an anomalous drop in acoustical intensity, of about 30 dB, at a range of 28 km for acoustic frequencies around 630 Hz. The measured transmission loss was found to be time and direction dependent. The authors performed transmission loss calculations using an acoustic parabolic equation (PE) model and a gated sine function representation of solitons in the thermocline. The simulation results from this hypothetical case showed that an anomalous transmission loss can occur around 630 Hz when acoustical waves and solitons interact. Computer simulations subsequently confirmed [2,3] that the resonant like transmission loss is caused by an acoustical mode coupling due to the presence of solitons, together with a corresponding larger bottom attenuation for the coupled acoustic modes. At the "resonant" frequency (~630 Hz) acoustic modes are coupled and energy is passed from one mode to another. When the acoustic mode receiving the energy has a higher bottom attenuation than the other acoustic mode, a net loss in transmitted energy occurs. Over a long distance these losses become additive and can result in a large transmission loss. The *entire process* resembles a resonance phenomenon.[2,3]

Since the Zhou, *et al.* studies, the acoustical and oceanographic properties of bores and solitons have been studied in many areas. Surveys have been performed on the New Jersey and New England continental shelves. During the summer of 1995 SWARM[4] (shallow-water acoustics in a random medium) was conducted on the continental shelf region off the New Jersey coast. The Shelfbreak PRIMER[5] experiment addresses an integrated acoustic and oceanographic field study in the middle Atlantic bight. Other acoustic predictability experiments where solitons are present have been performed.

We are presently performing studies of solitons and their anomalous effects on the intensity of the acoustical field in the Yellow Sea and the Strait of Messina regions. The Yellow Sea is a shallow sea, with a maximum depth of around 80 meters in the center. The semidiurnal tides are very strong and reach magnitudes of around 2 m/sec along sections of the Korean and Chinese coasts. Our work is

concentrated to the south of the Shan-Tung peninsula in an area where the acoustical transmission loss measurements of Zhou, *et al.*[1] were conducted. There the water depth varies from 40 to 50 meters. ERS-1 satellite SAR images suggest that solitons are present in the area. The generation mechanism of solitons in this region is under investigation at present. The objective is to provide both oceanographic and acoustic model simulations that can corroborate the assumptions and findings of Zhou, *et al.* No oceanographic data were taken by Zhou, *et al.*, thus, their assumption that solitons were the cause of the anomalous loss seen in their data remains unsupported.

In contrast to the Yellow Sea, the Strait of Messina is a narrow channel that separates the Tyrrhenian and Ionian Seas. It contains a sill that raises to within 80 meters of the surface. The semidiurnal tidal amplitudes at the northern and southern boundaries of the strait are only 17 and 10 cm respectively. There is, however, a large phase difference, of 174 degrees. The large phase difference and the geometrical constraints result in tidal velocities that can reach 3 m/sec. The motion of the semidiurnal tide over the sill depresses the thermocline and generates a bore. As the tide reverses a hydrologic jump of the bore occurs to the other side of the sill. The bore propagates away from the sill and its leading edge disintegrates into solitons, through amplitude and frequency dispersion.

Resonance occurrence and mechanisms

Zhou, *et al.*[1] have measured the frequency response of sound propagation in an area of the Yellow Sea that is located south of the Shan-Tung peninsula. The data was collected at various times over a period of four years. The source and receiver were located below the strong summer thermocline. Their measured power spectra at a range of 28 km have been published[1] and is reproduced here as Fig. 1. Their data shows an anomalous drop in acoustical intensity at around 630 Hz.

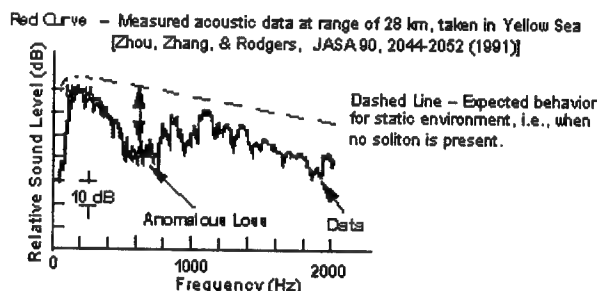


Figure 1. Reproduction of results published by Zhou, Zhang, and Rogers[1]

Corresponding transmission loss calculations, with no representation of solitons, using the acoustic parabolic equation (PE) model do not show an anomalous drop in acoustical intensity at 630 Hz. When, however, a hypothetical gated sine function representation of a soliton train is postulated in the thermocline, the PE model calculation shows a drop of acoustical intensity at around 630 Hz in agreement with the data. This good agreement between data and model prediction was first published by Zhou, *et al* [1] and is reproduced in Fig. 2.

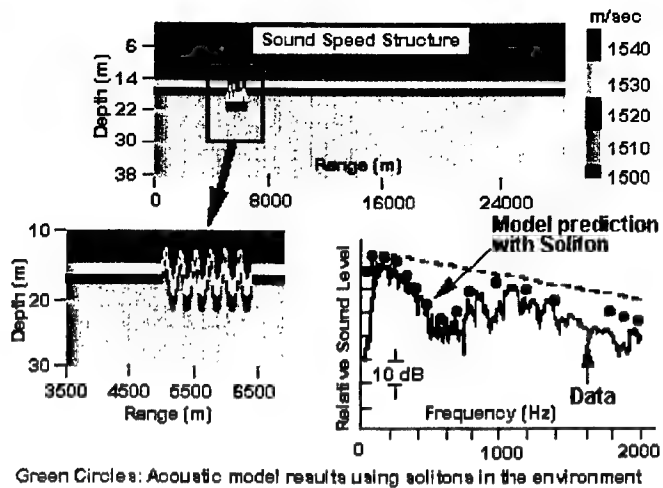


Figure 2. Results from the paper by Zhou, *et al.* when a soliton packet is used in the model predictions.

The physical mechanism for the resonant loss of acoustical intensity at a particular frequency can be understood in terms of mode coupling and energy redistribution among the normal (propagating) modes. Acoustical intensity calculations for the normal modes show that for frequencies outside of the narrow bandwidth containing the resonant frequency, a redistribution of energy does *not* occur when the solitons are present. This is shown in Fig. 3 (upper right) where the simulated acoustic pressure field has been decomposed into its spectral (wavenumber) components. The mode intensities are virtually unchanged when the soliton is placed between the source and receiver. However, near and at the resonant frequency, the redistribution of energy among the modes is quite different when the soliton is present between source and receiver (Fig. 3, lower right). The presence of the soliton results in acoustic mode coupling, redistributing energy from the lowest-order mode (mode 1) into higher-order modes (modes 2, 3, 4, 5, 6, and 7). The simulation modeling results shown in Fig. 3 are our duplication of the acoustic modeling analysis done by Zhou, *et al.*[1]. We have used high-fidelity PE models, FEPE and RAM[6,7] in the simulations shown in Fig. 3. The new FEPE and RAM PE models use improved energy conservation techniques[8]; their predictions represent both an improvement on, and verification of the results published by Zhou, *et al.*[1].

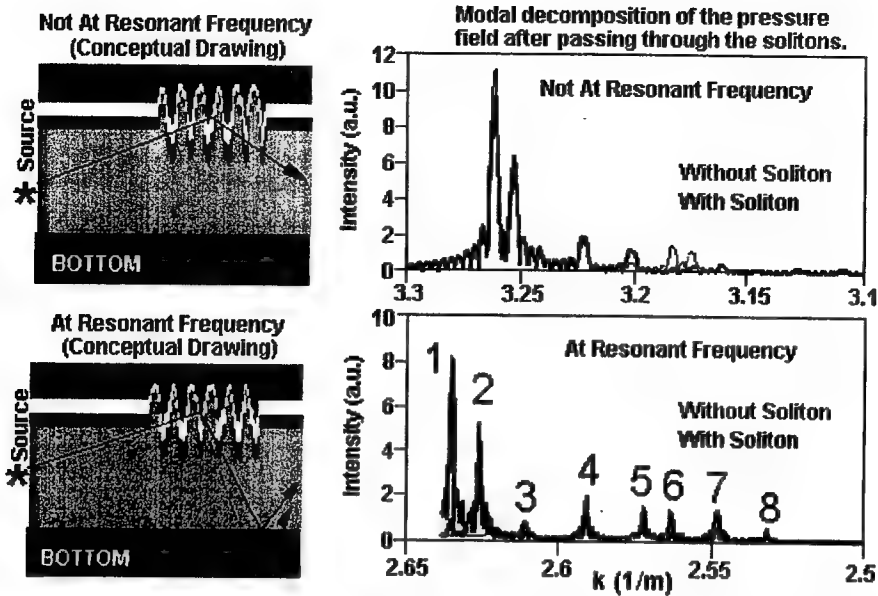


Figure 3. At the resonance frequency mode coupling transfers energy from mode 1 into higher modes.

Mode coupling and the associated redistribution of energy among the modes will not result in the large loss in transmitted signal seen in Fig. 1 unless the higher-order modes have a significantly greater bottom attenuation than do the lower order mode(s). This was the situation shown in Fig. 1 where the higher-order modes (2 through 8) had a bottom attenuation that was an order of magnitude larger than the lower-order mode (mode 1). This cumulative loss over the 28 km track resulted in the large loss shown in Fig 1 for frequencies around 630 kHz.

The important role that the ocean bottom has in the soliton resonance effect is shown in Fig 4 where Yellow Sea acoustic simulations were made[3] for the following three cases: (1) soliton present but bottom attenuation was set to zero; (2) no soliton was present but bottom attenuation was present; and, (3) both soliton and bottom attenuation were present. The soliton redistributes the sound speed of the media; at the resonance frequency this produces mode coupling and a redistribution of energy among the propagating modes. However, when no bottom attenuation is present (or if each mode has identical attenuation), the total pressure due to the redistributed modes is the same as it was before the redistribution. In fact, Fig. 4 shows that the affect of bottom attenuation is more significant on signal loss than is the presence of solitons. The greatest loss occurs when both solitons and higher bottom attenuation (in the higher-order modes) are present.

In summary, at the resonant frequency the acoustic field interacts with the soliton packet and acoustic mode coupling occurs; this results in mode conversions (acoustic energy is redistributed from lower-order to higher-order modes). When the converted modes have higher bottom attenuation than the original modes, high signal loss can occur at the resonance frequency. If the bottom attenuation is not significantly higher for the converted modes, then only a modest signal loss will occur. If the acoustic frequency is not at or near the resonance frequency, no appreciable loss will occur due to the acoustic field passing through the soliton. It should be noted that the mode coupling and mode conversions can go from lower-order modes to higher-order modes and vice-versa. Furthermore, these mode conversions occur continually as the acoustic field passes through the environmental inhomogeneity (i.e., soliton)

and that the environmental inhomogeneity is in a media where random fluctuations are continuously occurring. Thus, the problem is a very complex and difficult one.

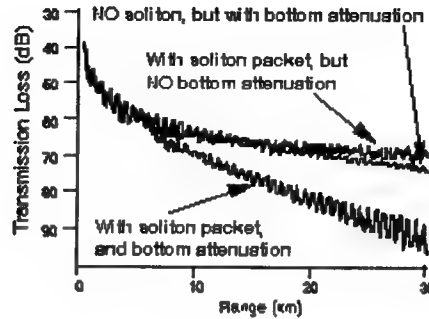


Figure 4. Mode conversion (lower to higher order modes) + higher bottom attenuation of the converted modes = high loss at the resonance frequency

It has been asserted that the simple relationship between the soliton's spatial wavenumber ($K_{Soliton}$) and the adjacent wavenumbers ($k_{Acoustic\ modes}$) of the propagating acoustic modes can predict the frequency (or wavelength) where mode coupling is likely to occur[1].

$$K_{Soliton} = \Delta k_{Acoustic\ modes} = \left(\frac{2\pi}{\lambda_m} - \frac{2\pi}{\lambda_s} \right)_{Acoustic\ modes} \quad (1)$$

We have used computer simulations to show that it is the "effective" horizontal (or vertical) component of $K_{Soliton}$ in Eq. (1) that is important. This is shown in Fig. 5(a) where the track between source and receiver is parallel ($O=0$) to the propagation direction of the soliton, and at angles, O , to the propagation direction of the soliton. Note that the "effective" horizontal (or vertical) component of $K_{Soliton}$ in Fig. 5(a) will change as O changes, i.e., as the source-receiver track changes relative to the soliton's direction of propagation.

Figure 5(b) shows a computer simulation for a soliton environment similar to that used in the Yellow Sea simulations. Note that significant signal loss occurs at two resonant frequencies for transverse angles $O=0$ and $O=50^\circ$, and does not occur at all for $O=30^\circ$. Note also that while large signal loss is observed for both $O=0$ and $O=50^\circ$, the magnitude of the losses and the resonant frequencies are different in the two cases. These results are consistent with Eq. (1) and the concept of "effective" horizontal (or vertical) component of $K_{Soliton}$.

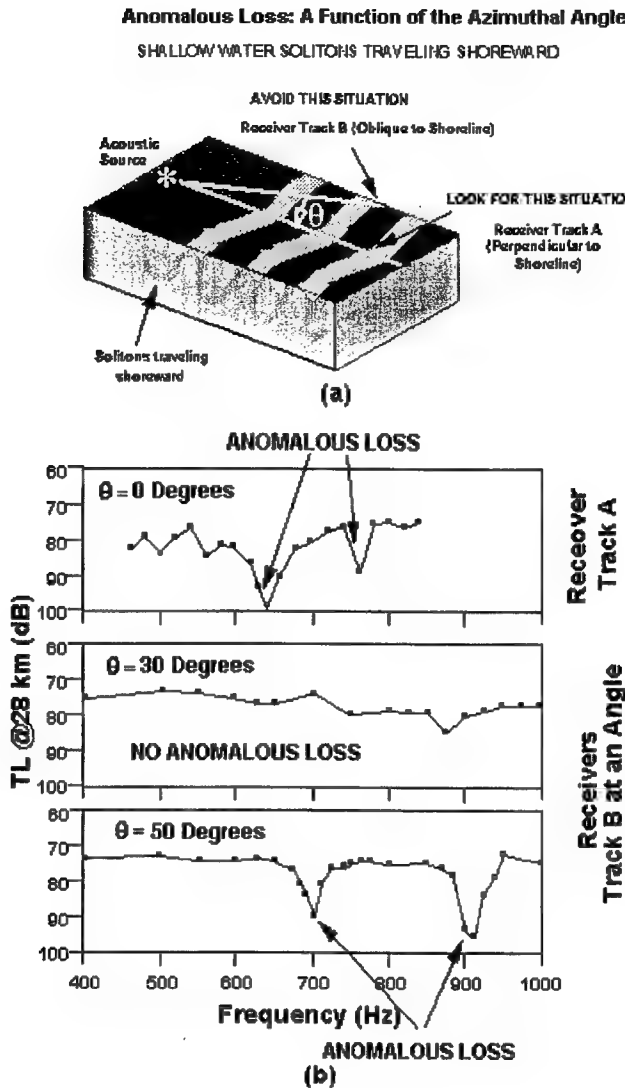


Figure 5. Acoustic computer simulations showing the effects on anomalous loss as a function of angle between the soliton's direction of propagation and the acoustic source/receiver track.

Soliton Modeling in the Strait of Messina and the Yellow Sea.

In the Strait of Messina, we are performing simulations of solitons with a two-layer reduced gravity model. The model was developed at the University of Hamburg by Brand, *et al.*[9]. It is formulated in terms of equations for the transport and variation of layer thickness. The channel width enters into the transport formalism besides the layer thickness and velocity. The topography is in the lower layer and the interface deviation is able to intersect it. Density is prescribed in each layer. The model is essentially two dimensional with grid points in the horizontal and layers in the vertical. Its formalism is weakly non-hydrostatic.

Solitons are generated in the sill region by the semidiurnal tide. The varying tide depresses the

thermocline and generates bores that propagate away from the sill. Under favorable conditions the nonlinear terms cause the leading edge of the bore to steepen. Then through amplitude and frequency dispersion the bore disintegrates into solitons. The parameters of the model are the prescribed densities, the depth of the thermocline (top layer thickness), depth of ocean, topographic variations, and semidiurnal tidal amplitudes and phase.

We have performed a parameter space study of conditions representing summer, fall, and winter. We have conducted simulations of physical states encountered during the October 1995 cruise in the Strait of Messina that was conducted by NATO's SACLANT Undersea Research Center in La Spezia, Italy. Sensitivity studies of parameter ranges were also undertaken.

Table 1. PARAMETER VARIATIONS

Case #	h_l	α_1	α_2	Tides	Topo	Width
8	30m	1026.5	1028.0	<i>M</i>	<i>M</i>	<i>M</i>
8a	15m	1026.5	1028.0	<i>M</i>	<i>M</i>	<i>M</i>
8b	60m	1026.5	1028.0	<i>M</i>	<i>M</i>	<i>M</i>
8t	30m	1026.5	1028.0	<i>M</i>	Tyr-150m	<i>M</i>
9	30m	1026.5	1028.5	<i>M</i>	<i>M</i>	<i>M</i>
10	30m	1026.5	1029.0	<i>M</i>	<i>M</i>	<i>M</i>
10a	30m	1027.0	1028.0	<i>M</i>	<i>M</i>	<i>M</i>
10b	30m	1027.5	1028.0	<i>M</i>	<i>M</i>	<i>M</i>
11	50m	1028.2	1029.0	<i>M</i>	<i>M</i>	<i>M</i>
11a	50m	1028.5	1029.0	<i>M</i>	<i>M</i>	<i>M</i>
11b	150m	1028.5	1029.0	<i>M</i>	<i>M</i>	<i>M</i>
11q	50m	1028.5	1029.0	<i>M</i>	Tyr-150m	<i>M</i>
11v	50m	1028.5	1029.0	<i>M</i>	Ion-200m	<i>M</i>
11t	30m	1026.5	1028.0	$A_i=30\text{cm/s}$	<i>M</i>	<i>M</i>

Legend: *M* is Strait of Messina Values. For tides: $A_i=10\text{cm/sec}$, $A_t=17\text{cm/sec}$, phase=174 degrees.

The most relevant case studies and corresponding parameter values are listed in Table 1. The point of departure for the simulations was a range of parameter values encompassing summer values and

conditions encountered during the October 1995 cruise in the Strait of Messina. Case 8 reflects a summer situation.

We have plotted a progression diagram of the interface deviation for case 8 in Fig. 6. The semidiurnal tide moves over the sill, depresses the thermocline, and generates a bore. As the tide reverses the bore retreats and does a hydrologic jump over the sill. Its leading edge propagates away from the sill and steepens through the action of the nonlinear terms. As it propagates amplitude and frequency dispersion set it and it disintegrates into solitons. The wavelengths of the solitons increase in time through the action of the nonlinear terms. The amplitudes decrease in the process and are damped by the viscous terms.

Cases 9 and 10 represent larger stratifications with increasing density values in the lower layer.

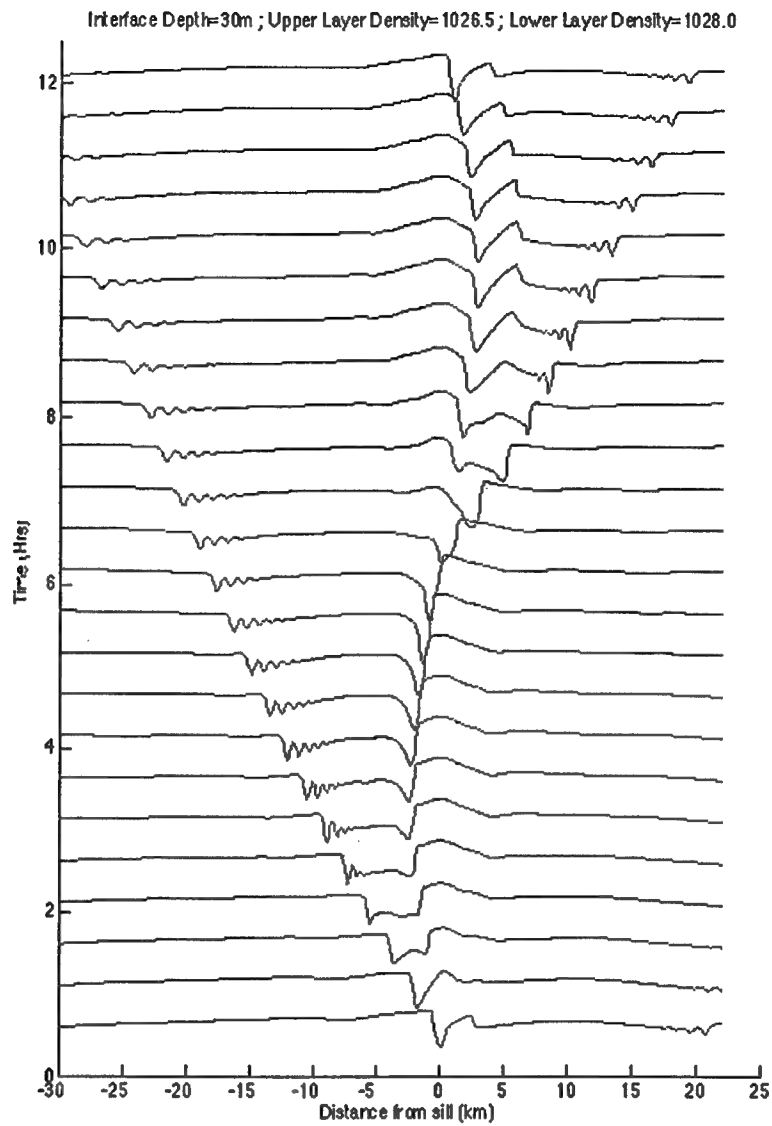


Figure 6. Progression diagram of the interface deviation for case 8.

We analyzed the phase speed, C , of the solitons. For a two-layer model, it can be expressed as,

$$C^2 = \Delta \rho g \frac{h_1}{1 + h_1/h_2} \quad (2)$$

where $\Delta\sigma$ is the change in density, h_1 is the distance from the sea surface to the thermocline, h_2 is the distance from the thermocline to the sea floor, and g is the acceleration due to gravity.

As the stratification is increased, cases 8, 9, and 10 in Table 1, the phase speed of the solitons increases as expected. The amplitude of the solitons does not change among the three cases. The number of solitons on the south side of the strait remains the same. On the north side cases 9 and 10 have two more solitons than case 8. The topography on the north side is shallower than on the south side. The channel width on the north side is larger. The nonlinear dynamics must be influenced by the geometrical constraints.

In the set of cases 8, 10a, and 10b the stratification is decreased. From 8 to 10a and 10b, the phase speed of the solitons decreases. The solitons of case 10b have a larger amplitude than those of case 8. Case 10b, however, has fewer solitons on the north and south side of the sill in relation to case 8. This is counter to expectations since as the amplitude increases more solitons tend to appear.

A winter type of situation is represented in case 11b. The phase speed in this case is influenced by the decreased stratification and the increased upper layer depth. The solitons have a larger amplitude than in case 8. They appear, however, only on the south side of the sill. No solitons are generated on the north side. The topography on the north side of the sill is shallow and ranges from 400 to 600 m. The upper layer depth of 150 m is becoming comparable in magnitude to the lower layer depth. As a result the nonlinear effects in the upper layer tend to be compensated by the nonlinear terms of the lower layer, resulting in less steepening of the bore's edge and no disintegration into solitons.

In case 8t we have restricted the topography on the north side of the sill, Tyrrhennian Sea, to 150 m. This results in no solitons on the north side but more of them appear on the south side relative to case 8. The phase speed on the south side is somewhat smaller than in case 8.

In the Yellow Sea we are using a 2.5-D level nonhydrostatic model. The model is based on the Navier Stokes approach with prognostic equations for the velocities (u, v, w) and temperature and salinity. It is 2.5-D because the derivatives along the y -axis are neglected, Martin[10]. The Coriolis force is included. The boundaries are rigid at the top and bottom with prescribed inflow and outflow. Viscosity is included.

The physical parameters of the model are the stratification (temperature and salinity), depth of thermocline and halocline, topographic variations, depth of the ocean, Coriolis effects, and tidal amplitude/phase.

South of the Shan-Tung peninsula the semidiurnal tide can have velocities from 40 to 80 cm/sec along the coast, Guo-hong[11]. We used the value of 1 m/sec for forcing the model at the left boundary. The topography in the area of concern is in the 40 to 50 m range. The prescribed topographic variation was a step type idealized drop over 8 km down to 50 m from a 20 m coastal shelf.

For our initial simulations we have prescribed summer conditions. Generic temperature and salinity profiles were constructed on the basis of monthly climatology and measurements by Lie[12] in August of 1983. Some of the results for a thermocline/halocline location of 10 and 20 meters are shown in Fig. 7. At 20 hours the second train of solitons is propagating away from the shelf. The remains of the first soliton train are still visible as a depression of the thermocline near the right hand side boundary. The depression of the thermocline eventually recovers to the original position in time and space. This space

behavior can be seen proceeding left from the remains of the first soliton train. The spatial recovery is characteristic of the semidiurnal tidal influence on the thermocline. The damping of the first soliton train is brought about by model viscosity. The initial over the step depression leads, also, to a bore like disturbance that propagates on to the shelf.

The first soliton train has advanced closer to the right hand boundary for the 20 m thermocline as compared to the 10 m one. The 20 m thermocline has a larger effective upper layer depth and therefore a higher soliton phase velocity, as discussed before for the Strait of Messina.

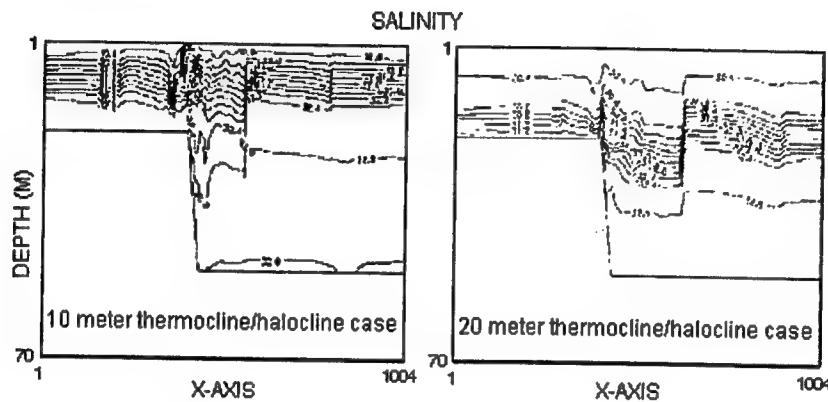


Figure 7. Results for a thermocline/halocline location of 10 and 20 meters at 20 hours.

A zoom of the third soliton train at 32 hours is shown in Fig. 8. The 10m thermocline case has about 4 solitons in the train. The initial thermocline depression is around 8 m. The wavelength of the first soliton in the train is around 200 m. The horizontal resolution of the model is 100 m and therefore coarse for resolving the solitons in the train. Vertical resolution is 1 m.

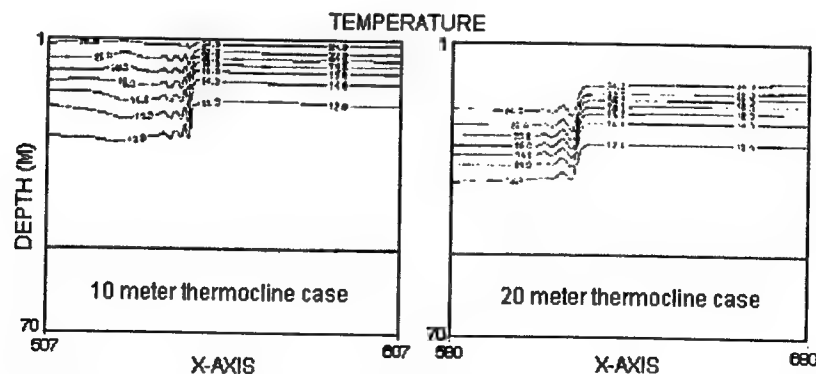


Figure 8. A "zoom" view of the soliton train at 32 hours.

The 20 m thermocline solitons train is shown on the right hand side of Fig. 8. The initial depression is the same as before, 8 m. The wavelength of the first soliton is around 400 m. This solitons train has moved faster, traveled further and undergone more spreading through the nonlinear effects.

Concluding remarks.

We are studying a drop in acoustical intensity that can occur in shallow water around the resonant frequency. The phenomena has been shown to occur when solitons are present. The mechanism for the anomalous intensity drop in presence of solitons consists of energy transfer to higher acoustical modes. The intensity of the modal energy is attenuated by bottom effects.

Our studies are conducted in the Strait of Messina and the Yellow Sea. We are approaching the problem from the experimental, modeling, and theoretical side. In the Yellow Sea we have measurements that show an anomalous drop in acoustical intensity at around 630 Hz. We have shown that the resonant drop is due to solitons by performing transmission loss calculations with a parabolic equation (PE) model and a postulated soliton train. Model results show a drop around 630 Hz, in agreement with data.

We are presently modeling the solitons in the Yellow Sea with a nonhydrostatic level model. Our preliminary results indicate generation and propagation of solitons in an area south of the Shan-Tung peninsula. The simulated solitons will be coupled with acoustical PE models in the future.

In the Strait of Messina we have performed a parameter space study of soliton generation and propagation. The parameters span the summer to winter seasons and the conditions of the October 1995 cruise that tracked the solitons with a CTD chain. The phase speed trends are sensitive to upper layer thickness and density differences between the layers. This reflects the pycnocline shape or its strength and location in depth. On the seasonal scale the model's upper layer convergence behavior agrees with the trends of SAR data.

A 2-D sound speed was extracted from the two-layer model simulations. The approach is based on a perturbation expansion of the transport equation for the sound in conjunction with the two-layer model. It is analogous to the expansion for the density in conjunction with two-layer modeling that was used in Essen's Ph.D. thesis[13], at the University of Hamburg. The result gives the sound speed as a mean state versus depth plus a perturbation consisting of the vertical derivative of the sound speed times the interface deviation from the two layer model. The mean state of the sound speed can come from climatology or measurements. We are performing transmission loss calculations (with the PE model) with sound speeds constructed from the two-layer model simulations. Our understanding of the mode conversions at resonant frequencies has resulted in a model that uses Eq. (1) to predict the resonant frequency without running an acoustic model. This Search Algorithm for Resonance Anomalies (SARA) has been successfully applied to oceanographic soliton data taken in the Strait of Messina[8].

During the October 1995 cruise in the strait of Messina a southward propagating trains of solitons was chased 5 times and measured with a CTD chain. A northward propagating train was measured 4 times in a corresponding manner. We have extracted the temperature and salinity profiles from the data and have calculated the density and sound speed distributions. Some preliminary transmission loss calculations have been performed with the measured sound speeds using a PE model. There are indications of resonance at some of the frequencies.

References.

1. J. X. Zhou, X. Z. Zhang, and P. H. Rogers, "Resonant interaction of sound wave with internal solitons in coastal zone," *J. Acoust. Soc. Am.* **90**(4), 2042-2054 (1991).
2. S. A. Chin-Bing, D. B. King, and J. E. Murphy, "Numerical simulations of lower-frequency acoustic propagation and backscatter from solitary internal waves in a shallow water environment," in *Ocean Reverberation*, edited by D. D. Ellis, J. R. Preston, and H. G. Urban, (Kluwer Academic Press, Dordrecht, The Netherlands, 1993).
3. D. B. King, S. A. Chin-Bing, and R. W. McGirr, "Effect of shallow water internal waves on broadband acoustic wave propagation," in *Environmental Acoustics: International Conference on Theoretical & Computational Acoustics Vol. II*, edited by D. Lee and M. Shultz (World Scientific Press, Singapore, 1994) p. 793-808.
4. The SWARM Group, "An overview of the 1995 SWARM shallow water internal wave acoustic scattering experiment," *IEEE J. Oceanic ENG.*, **22**(3), 465-500 (1997).
5. The Shelfbreak PRIMER Group, "Shelfbreak PRIMER - An integrated acoustic and oceanographic field study in the middle Atlantic bight," in *Shallow-Water Acoustics*, edited by R. Zhan and J. X. Zhou.
6. M. D. Collins, "FEPE user's guide," NORDA TN-365, Naval Research Laboratory, Stennis Space Center, Mississippi, 1988.
7. M. D. Collins, R. J. Cederberg, D. B. King, and S. A. Chin-Bing, "Comparison of algorithms for solving parabolic wave equations," *J. Acoust. Soc. Am.* **100**, 178-182 (1996).
8. S. A. Chin-Bing, D. B. King, R. A. Zingarelli, and A. Warn-Varnas, "A Search Algorithm for Resonance Anomalies (SARA)," *1999 NRL Review*, Naval Research Laboratory, Washington, DC, 1999.
9. P. Brand, A. Rubino, W. Alpers and J. Backhaus, "Internal waves in the Strait of Messina studied by a numerical model and synthetic aperture radar images from the ERS-1 Satellites," *J. Phys. Oceanogr.*, **27**(5), 648-663 (1997).
10. P. Martin, Private communication (1999).
11. F. Guo-hong, "Tides and tidal currents in East China Sea, Huanghai Sea and Bohai Sea," *Oceanology of China Seas*, **1**, 101-112 (1994). Kluwer Academic Publishers.
12. H. Lie, "Summertime hydrographic features in the southeastern Hwanghae," *Prog. Oceanogr.*, **17**, 229-242 (1986).
13. H. Essen, "Interpretation of Observed Fluctuations of the Acoustic Field in the SOFAR-Channel as Result of Internal-Wave Disturbances," PhD thesis. University of Hamburg (1976).

Preliminary observations of optical variability associated with internal solitary waves during the Coastal Mixing and Optics experiment

G. C. Chang and T. D. Dickey

Ocean Physics Laboratory, University of California at Santa Barbara,
6487 Calle Real Unit A, Goleta, CA 93117; e-mail: grace@icess.ucsb.edu

Abstract. Observations of internal solitary waves (ISWs) were obtained on a continental shelf during the Coastal Mixing and Optics (CMO) experiment. High-frequency, high-energy bursts were seen in north-component current data and temperature data, as well as in chlorophyll *a* concentration and beam c data. ISWs resulted in vertical pumping of biogenic and non-biogenic material, as observed in the optical data. Tidal phase and direction, and strength of stratification have a direct influence on the formation and characteristics of ISWs.

Introduction

Observations of high-energy, large-amplitude solitary waves on continental shelves are common (e.g., Sandstrom et al. [1989]). The interaction of tides with the continental shelf edge during periods of stratification leads to the formation of internal tides. These internal tides are modified over time into non-linear, high-energy bursts, called internal solitary waves (ISWs), or solitons. ISWs are important to vertical transport and mixing of biogenic and non-biogenic components in the water column [Weidemann et al., 1996]. These high-energy bursts bring nutrients and phytoplankton into or out of the euphotic layer, resulting in blooms or death. ISWs also resuspend sediment from the ocean bottom [Bogucki et al., 1997].

Methods

The site of the Coastal Mixing and Optics (CMO) experiment was the "Mud Patch" of the Mid-Atlantic Bight (MAB) continental shelf. We collected high temporal resolution time-series of physical and optical data at four depths (14, 37, 52, and 68 m) using instruments on bio-optical systems (BIOPS) [Chang et al., 1997] on a mooring and a tripod. BIOPS instruments used in this study include: 1) PAR sensors, 2) stimulated fluorometers, 3) temperature sensors, and 4) beam transmissometers (660 nm). The sampling rate was eight times per hour. This paper focuses on observations obtained during our fall 1996 CMO mooring deployment between Julian Day (JD) 224 and 244 (August 11 and 31).

Oregon State University (OSU) scientists deployed several physical instruments on a subsurface mooring [Boyd et al., 1997]. An uplooking RD Instruments Acoustic Doppler Current Profiler (ADCP) at 65 m, and temperature and salinity sensors at several depths were used in this study. ADCP current data were obtained every two minutes between 3 and 55 m with 4 m bins. Brunt Vaisala frequency ($N^2(z)$, expressed in s^{-2}) was calculated between depths where subsurface mooring temperature data were available. All data used in this study were band-pass filtered between 10 minutes and one hour to highlight high-frequency ISWs.

Observations

Solitary waves were not uncommon on the MAB continental shelf during the CMO experiment. ISWs were observed in band-passed filtered north-component current data (Figures 1 and 2) and temperature data (data not shown) as high-frequency bursts. The waves passed through the mooring site at a frequency similar to the semi-diurnal tides. The highest amplitude solitons occurred at depths of 20 and 50 m, which were the depths of highest stratification (seen in the N^2 data; not shown). Stratification increased between JD 241 and 244; the frequency and amplitude of ISWs also increased over the same time period (Figures 1 and 2).

Oscillations in band-pass filtered chlorophyll *a* concentration ([Chl *a*], expressed in mg l^{-1}) at 14 m were at times correlated with ISWs seen in the 15 m velocity data with a 2.5 to 5 hour time lag (Figure 1). It appears that the ISWs passing at 20 m may have pumped nutrients up from below the euphotic layer (~ 25 m) to depths where phytoplankton were able to utilize them, as well as moved phytoplankton to depths below the euphotic layer.

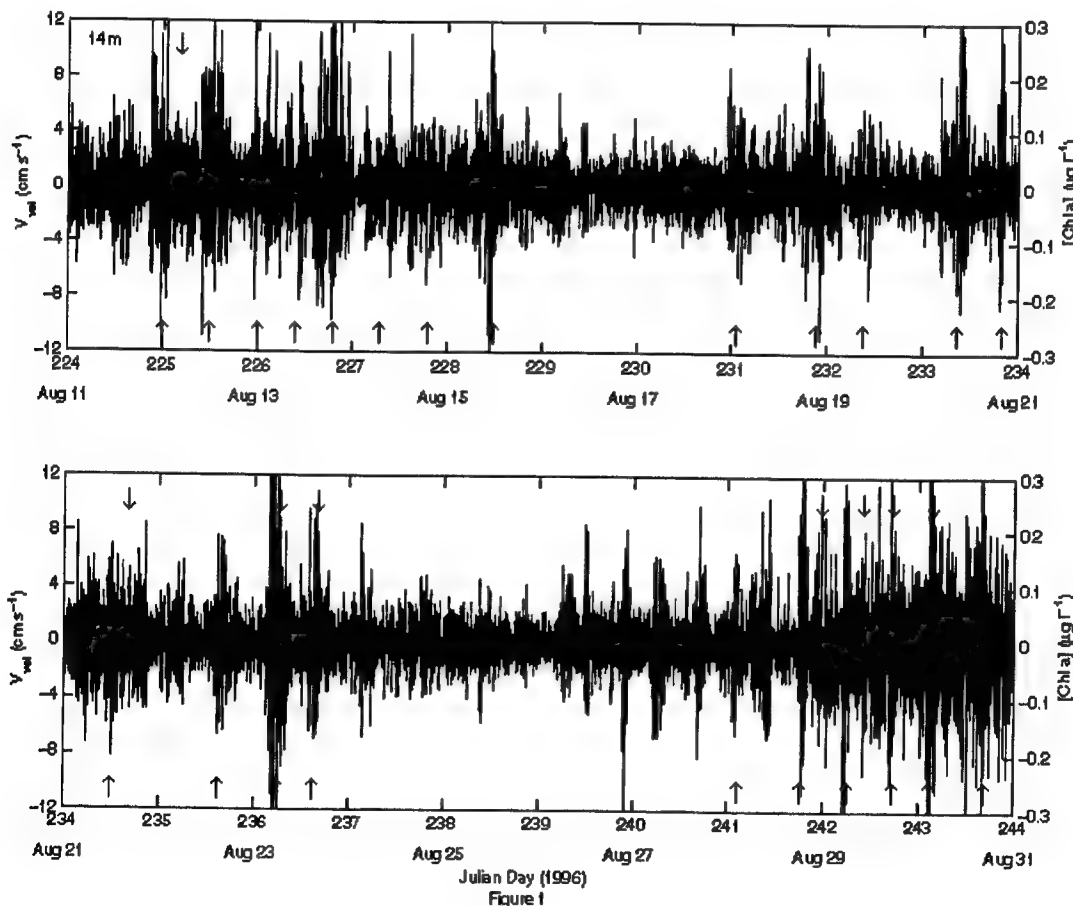


Figure 1. Time-series of band-passed filtered north-component velocity (blue) measured at 15 m and chlorophyll *a* concentration (red) measured at 14 m. The arrows represent times where internal solitary waves were observed.

In addition, bursts in the beam c data at 52 m were at times correlated with ISWs seen in the 51 m velocity data (Figure 2). No time lag was found between beam c and current bursts. Increases in beam c at deep depths in the water column are generally attributed to sediment resuspension. Interestingly, during periods of beam c bursts at 52 m, the 68 m beam c values did not increase from mean conditions. One hypothesis for this is that the ISW amplitudes were not high enough to resuspend sediment from the ocean bottom, but rather, the solitons pumped sediment from the upper part of the nephloid layer. Another hypothesis is that the sediment resuspension caused by the ISWs was not significant to the background beam c values at 68 m. Also, it is possible that the increases in beam c were the result of sinking biogenic particles from above.

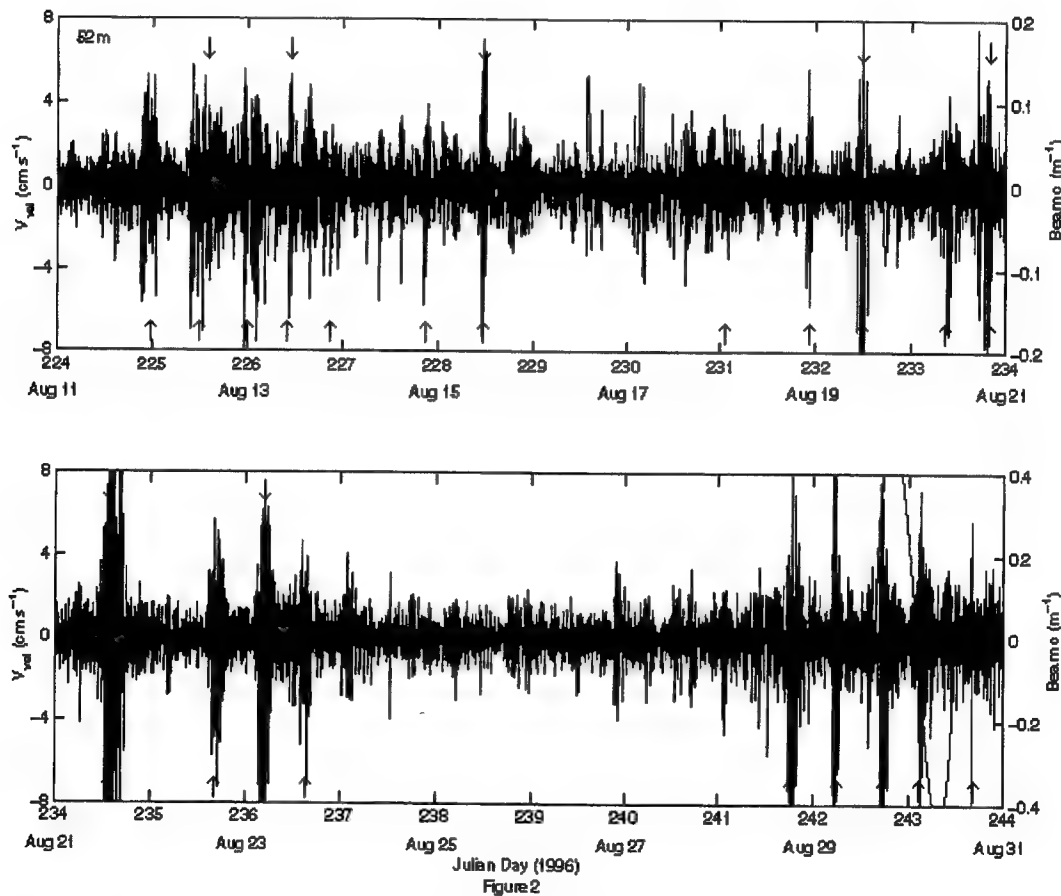


Figure 2. Time-series of band-passed filtered north-component velocity (blue) measured at 51 m and beam c (red) measured at 52 m. The arrows represent times where internal solitary waves were observed.

Conclusions

Internal solitary waves were observed in high temporal resolution physical and optical data collected on a continental shelf during the CMO experiment. Optical data were not always correlated with high-frequency ISW packets seen in current data. The phase and direction of the semi-diurnal tides onto the continental shelf edge have a direct influence on the characteristics of ISWs. In addition, soliton formation depends on the strength of stratification in the water column. Biological processes associated with ISWs (blooms, death, etc.) are dependent on the euphotic layer depth, nutrient availability, mixing rate, etc.

Acknowledgements. This work was supported by the Office of Naval Research as part of the Coastal Mixing and Optics program. We would also like to thank Murray Levine and Tim Boyd (OSU); Derek Manov and David Sigurdson for their engineering and technical support; and Joe McNeil for his help in statistical analyses.

References

Boyd, T., M.D. Levine, and S.R. Grad, Mooring observations from the Mid-Atlantic Bight, *OSU 97-2-164*, 226 pp., Oregon State Univ., Corvallis, OR, 1997.

Bogucki, D., T. Dickey, and L. G. Redekopp, Sediment resuspension and mixing by resonantly generated internal solitary waves, *J. Phys. Oceanogr.*, 27, 1181-1196, 1997.

Chang, G.C., T.D. Dickey, D.V. Manov, D.E. Sigurdson, and J.D. McNeil, Data report: Coastal Mixing and Optics Deployment I, *OPL-4-97*, 44 pp., Ocean Physics Laboratory, Univ. of Calif., Santa Barbara, CA, 1997.

Sandstrom, H., J. A. Elliott, and N. A. Cochrane, Observing groups of solitary internal waves and turbulence with BATFISH and echo-sounder, *J. Phys. Oceanogr.*, 19, 987-997, 1989.

Weidemann, A. D., W. S. Pegau, L. A. Jugan, and T. E. Bowers, Tidal influences on optical variability in shallow water, *Ocean Optics*, 2963, 320-325, 1996.

Phytoplankton patchiness and high-frequency internal waves

Cleridy E. Lennert-Cody and Peter J. S. Franks

Marine Life Research Group
Scripps Institution of Oceanography
La Jolla, California, 92038-0218, USA
clennert@iattc.ucsd.edu
pfranks@ucsd.edu

Long, narrow sea surface slicks associated with internal waves are common features of exposed coastal environments. Such slicks, which may be accompanied by foam or debris, also have been shown to be associated with high concentrations of many types of planktonic organisms. Shanks (e.g., 1983, Mar. Ecol. Prog. Ser., Vol. 13) proposed that organisms in these sea-surface slicks are concentrated by currents associated with the internal waves. Although most observations have been made near the sea surface, recently published data suggest that the effects of internal waves on the distribution of the plankton and small fishes may extend throughout the water column. Still, the magnitude of internal wave-induced changes in the concentration of planktonic organisms and its relationship to the physical forcing remain largely unexplored. Using a low order analytical model we predict the effects of high-frequency internal waves on the patchiness of planktonic organisms within the water column, and test those predictions using field data.

Simple model predictions for high-frequency interfacial waves suggest that organisms that swim vertically, in opposition to the physical flow, will experience ephemeral changes in concentration throughout the water column as a wave passes. Previous modeling studies of surface-trapped particles have shown that the maximum concentration should occur over the trough of the wave. Using two interfacial wave profiles, a small-amplitude wave and a weakly nonlinear wave, we also find that increases in the concentration of planktonic organisms within the upper layer are predicted to occur over the wave trough. That is, changes in concentration of planktonic organisms within the upper layer are predicted to be out of phase with displacements of the interface. Within the lower layer, the perturbations are predicted to be in phase. The maximum wave-induced increase in concentration is predicted to increase linearly with either the wave amplitude or the wave period, depending on the swimming behavior. Maximum increases in concentration are predicted to be less than twice the background concentration.

To compare field data to these model predictions, we have computed estimates of along-isotherm fluorescence, along-isotherm beam attenuation coefficient and isotherm depth. If organisms behave completely passively, then on short time scales we would expect the organisms to be advected with the water, similar to temperature. That is, we would expect no coherent relationship between along-isotherm concentration anomalies and isotherm displacements. Data were collected using a profiling CTD\fluorometer\transmissometer instrument package during the spring and summer of 1997 in depths of 30 m or less off Mission Beach California. Spring sampling occurred during a bloom of dinoflagellates, including *Lingulodinium polyedrum*, *Ceratium* spp. and *Prorocentrum* spp. Profiling data were collected at a fixed station for up to 6 hours at a time. During the summer, profiling data were also collected by sampling at a near-surface drifter, drogued at 0.5-1.5 m. High-frequency internal waves with periods less than 30 minutes were often observed, sometimes accompanied by high-frequency changes in the level of fluorescence (Fig. 1).

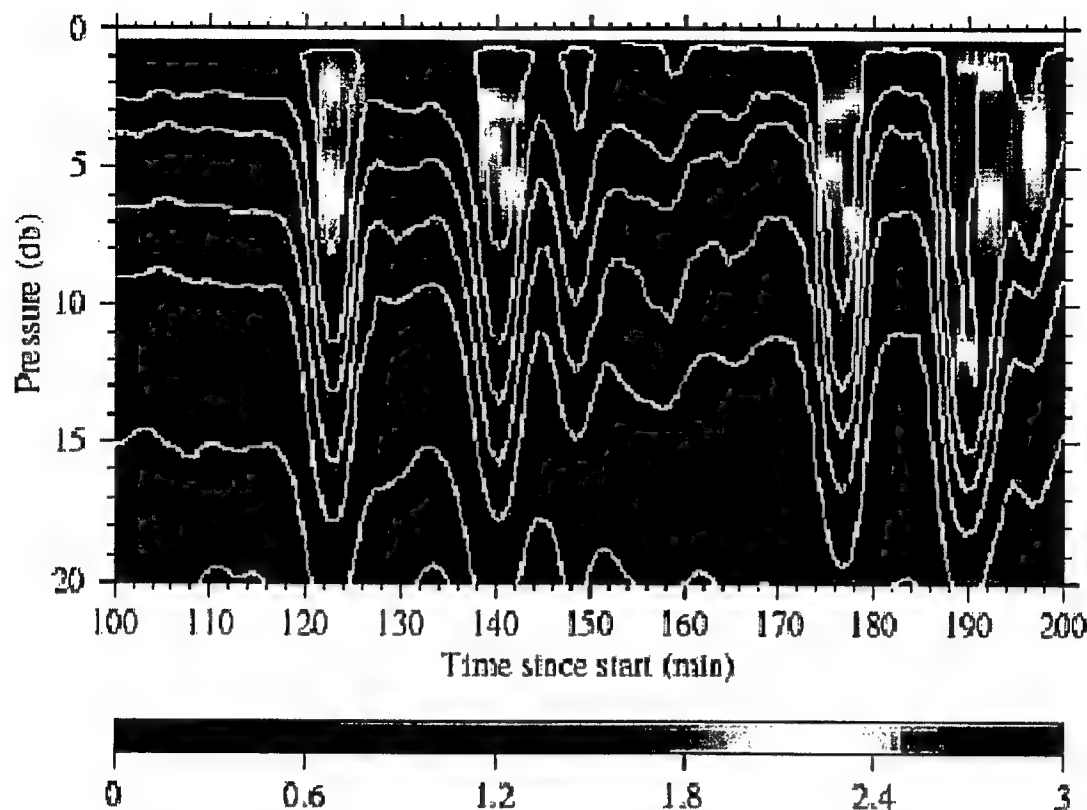


Figure 1. Fluorescence (color image; in $\mu\text{g/l}$) and temperature (1°C contours; $11-17^\circ\text{C}$) for profiling data collected on April 17, 1997 in 30 m water depth. Vertical sampling resolution is approximately 0.5 m; horizontal sampling resolution is approximately 1 min. The horizontal axis shows time in minutes from the start of sampling. The vertical axis shows pressure (db). Fluorescence and temperature have been smoothed slightly using linear interpolation.

Our analyses so far show that temporal variability in the relationships between along-isotherm fluorescence, along-isotherm beam attenuation coefficient and isotherm depth are often consistent with model predictions of high-frequency internal wave-induced changes in the concentration of planktonic organisms. Estimates of the phase relationship between along-isotherm fluorescence and isotherm depth at periods between 5-30 minutes suggest that these quantities are often out of phase in the upper part of the water column, with a possible phase shift deeper down (Fig. 2). This general pattern holds for both spring and summer; however, there is a considerable amount of day-to-day variability, particularly in spring. Although the phase relationship between along-isotherm beam attenuation coefficient and isotherm depth was more variable, at periods between 5-30 min, along-isotherm fluorescence and along-isotherm beam attenuation coefficient were approximately in phase throughout the water column. For data collected in a quasi-Lagrangian sampling mode, depressions of isotherms often corresponded to localized maxima in along-isotherm fluorescence indicating that increases in fluorescence were occurring over the trough of the waves (Fig. 3). Also associated with some isotherm depressions were localized increases in the along-isotherm beam attenuation coefficient. Cell counts computed for water samples collected during the spring suggest that high-frequency variability in fluorescence at a fixed depth can be due to changes in the concentration of swimming dinoflagellates. More extensive testing of the model predictions is currently being done using data from individual internal wave events.

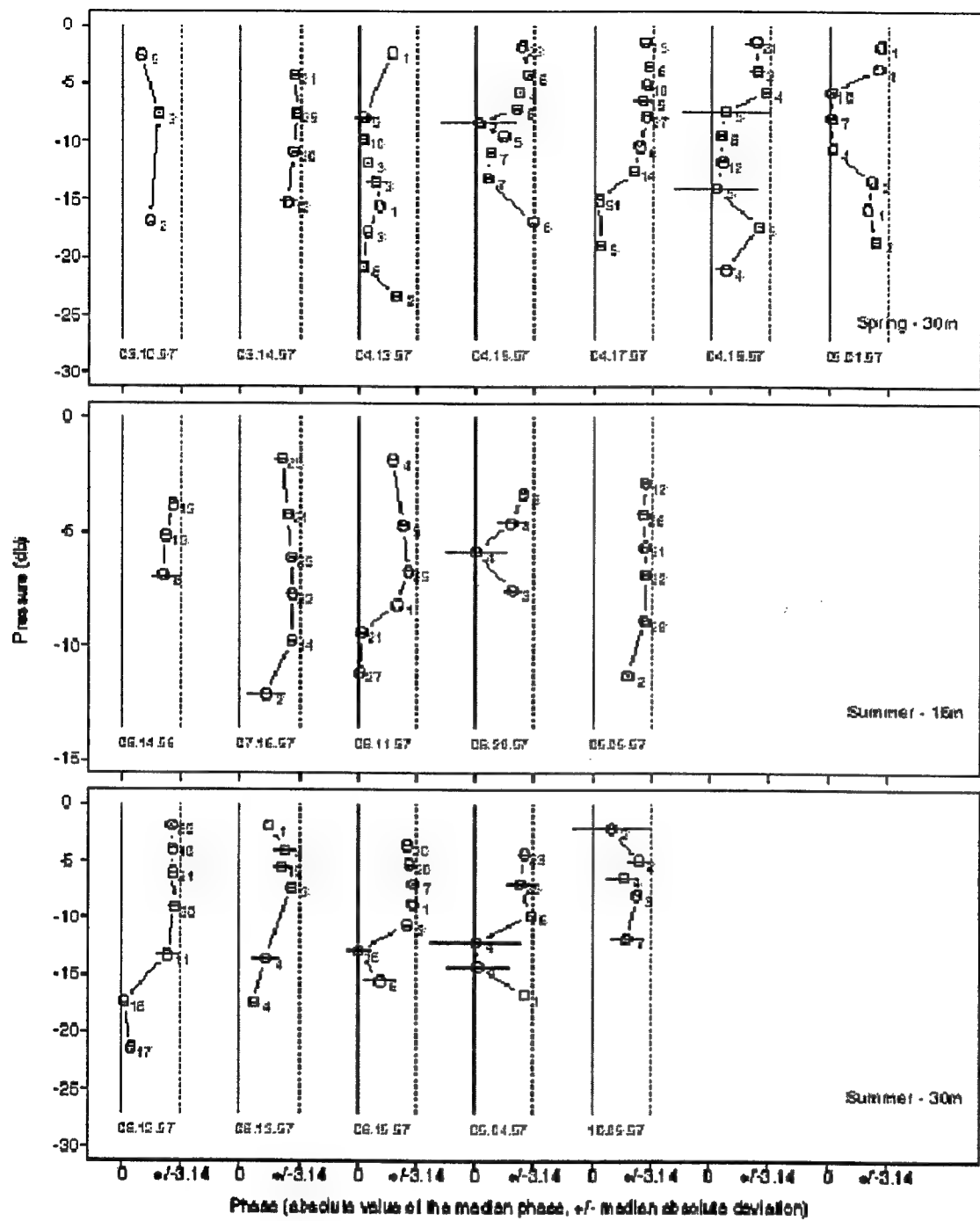


Figure 2. Waterfall plots showing the phase relationship between along-isotherm fluorescence and isotherm depth versus the median isotherm depth on 17 days during spring and summer of 1997. Open circles correspond to the absolute value of the median of phase estimates at periods between 5-30 min. The horizontal bars indicate plus/minus the median absolute deviation. Panels represent data collected in 30 m water in spring (top panel), 15 m of water in summer (middle panel) and 30 m of water in summer (bottom panel). Only phases at frequencies for which the squared coherency was significantly greater than zero (5% level) were used to estimate the phase in this frequency band. The number of frequencies associated with each phase estimate is shown to the right of the point estimate. The horizontal axis shows the phase in radians from $-\pi$ to π . Note that π radians for a previous profile corresponds to $-\pi$ radians for the next profile. The solid gray vertical lines correspond to 0 radians and the dashed gray lines correspond to $\pm\pi$ radians. Dates of sampling are shown at the bottom-right of each zero line. Our simple model would predict along-isotherm fluorescence and isotherm depth to be out of phase (*i.e.*, phase = π) above the pycnocline and in phase (*i.e.*, phase = 0) below the pycnocline.

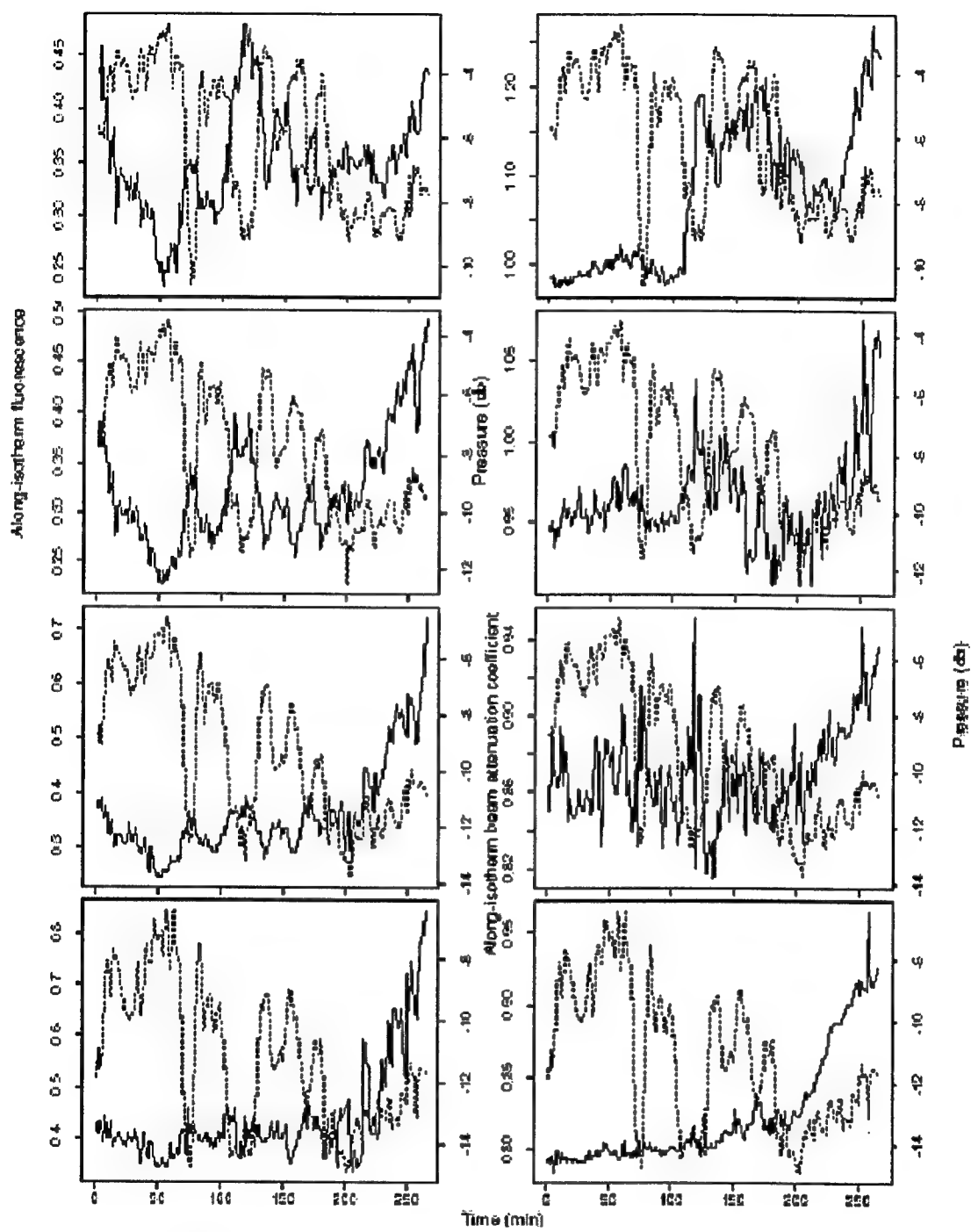


Figure 3. Median along-isotherm fluorescence (solid line, left panel) and isotherm depth (dashed line, left panel), and along-isotherm beam attenuation coefficient (solid line, right panel) and isotherm depth (dashed line, right panel) for profiling data collected at a near-surface drifter on September 10, 1997. Isotherms for both sets of plots were defined (from bottom to top) using the following temperature ranges: 18.0-18.5 °C, 18.5-19.0 °C, 19.0-20.0 °C, and 20.0-21.0 °C. The horizontal axis shows time in minutes from the start of sampling. Vertical axes on the left show fluorescence ($\mu\text{g/l}$) or beam attenuation coefficient (m^{-1}); vertical axes on the right show the depth of the isotherm in units of pressure (db). Note that the scale of the vertical axes changes from panel to panel.

Issues in larval transport by internal tidal bores

Jesús Pineda

Biology Department MS 34
Woods Hole Oceanographic Institution
Woods Hole, MA 02543
jpineda@whoi.edu
(508) 289-2274

The problem of larval return for nearshore species.

The majority of species associated to the seafloor inhabiting the nearshore, ~0 to 30 m water depth, have two-phase life cycle, where adults are conspicuous and live associated to the seafloor, while larvae are minuscule, and drift at the mercy of the currents. After a period of time ranging from minutes to years, with a ~1 month mode for temperate species, larvae drift, diffuse, and accumulate in an offshore larval pool, far from their adult habitats. These larvae must return shoreward in order to complete their life cycle. Transport of larvae from offshore to nearshore waters is critical for understanding issues from population dynamics to species geographical ranges, from fisheries-management to design of marine reserves.

This problem involves larval behavior and physical transport mechanisms. Invertebrate larvae are generally small (~< 1 mm), with limited swimming capabilities, and it is generally agreed that because larval swimming speeds are so small, these larvae must transport shoreward by some sort of advection. On the other hand, by controlling its vertical position within the water column, larvae may exploit different transporting or concentrating mechanisms. Understanding physical transport for nearshore species involves characterizing the mechanism and its temporal and spatial variability. One must understand how transport occurs, and also the secondary flows responsible for the accumulation of larvae in hydrographic features, if any, and how the mechanism responds to large-scale disturbances and the mechanism's alongshore variability. There is evidence that internal tidal bores can transport larvae (Pineda, 1991; Pineda, 1995; Leichter, et al., 1996; Leichter, et al., 1998).

Internal tidal bores in Southern California

Sharp surges of cold water (Winant, 1974) that often surface the thermocline at diurnal or semidiurnal periodicities have been identified as internal tidal bores; (Cairns, 1967; Pineda, 1991; Pineda, 1994) (Fig.1)

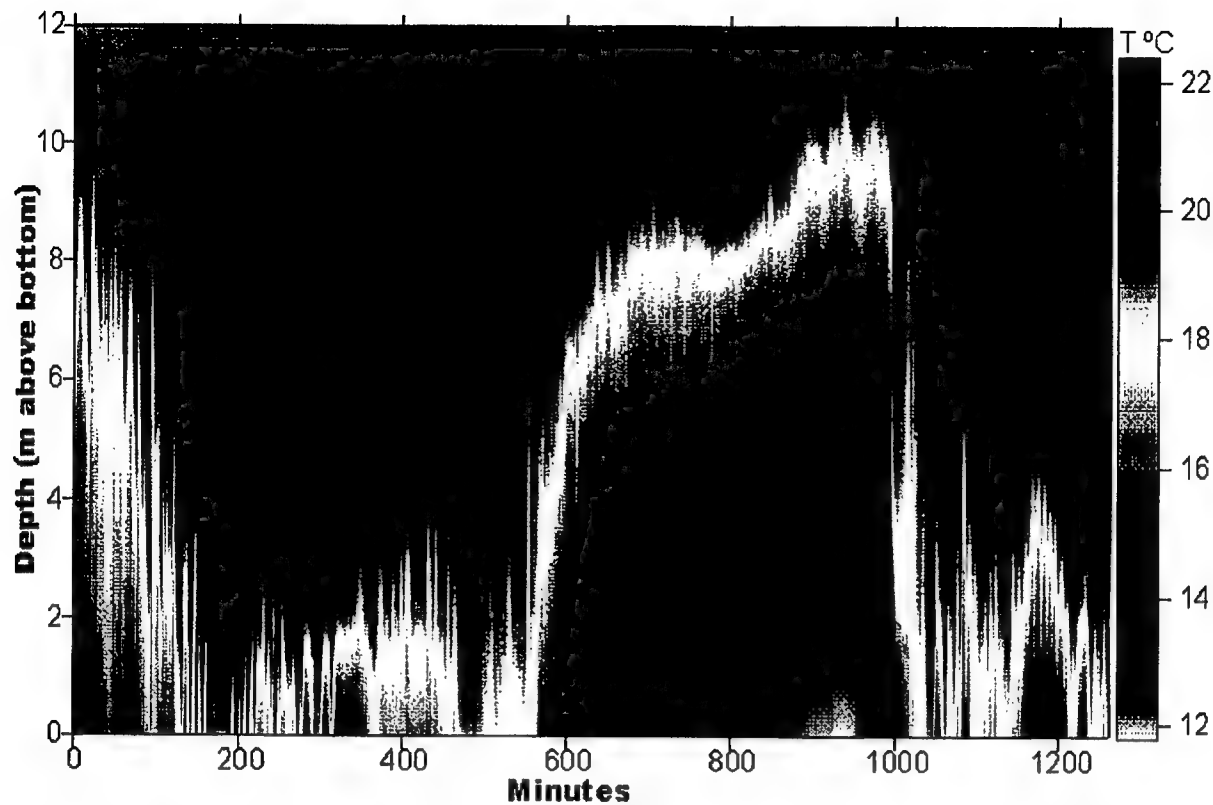


Fig. 1. Temperature on June 4-5 1996 off La Jolla, California at ca. 12 m water depth. Temperature loggers at 1, 3, 5, 7, 9 m above the seafloor, and floating. 5 s record low passed filtered with a 12 point running mean filter and subsampled every 1 minute. (J. Pineda, unpub.)

Internal tidal bores occur in groups of events lasting 2-10 days in Spring and Summer, when the water column is strongly thermally stratified. Groups of events are unpredictable in the short term. Periodicity in surface water temperature suggests that, on average, internal tidal bores tend to occur around neap tide (Pineda, 1991; Pineda, 1995). During these events, temperature records imply that the nearshore water body is replaced at diurnal or semidiurnal periods for several days. (Figure 2 and 3).

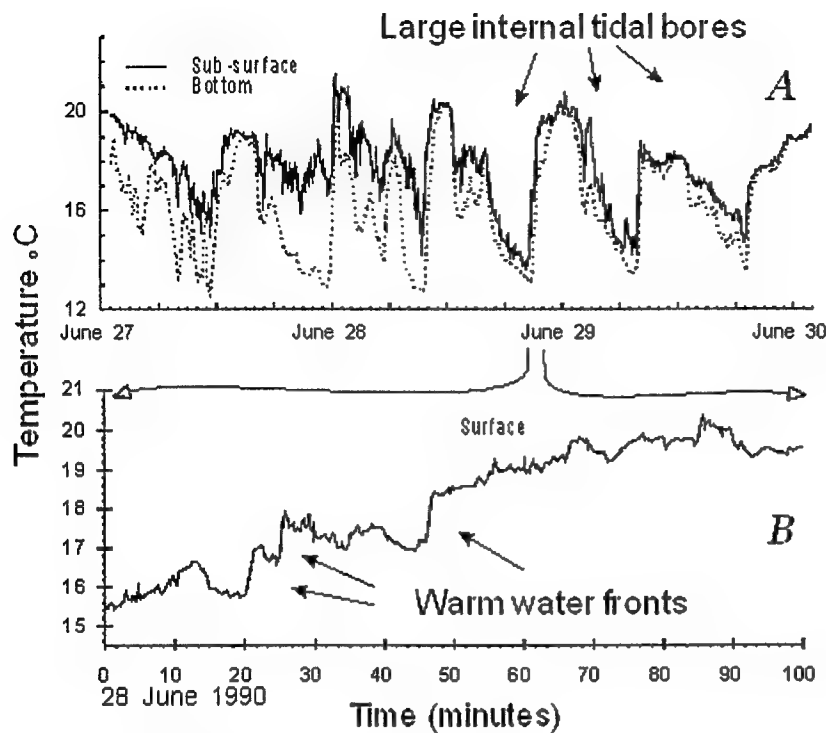


Figure 2. Temperature records at the Scripps Inst. Ocean. Pier in ~7 m of water. (From Pineda, 1994.)

The sequence of events during an internal tidal bore event has been interpreted as follows. At first, a cold water bore is advected shoreward (Cairns, 1967), displacing warm water offshore. This creates an imbalance in hydrostatic pressure between heavier inshore water and lighter offshore water. A front forms between the inshore cold water and the displaced offshore warm water. Then, as cold water recedes offshore because of its density, currents reverse, and a "warm" internal bore returns, pushing the front all the way back to the shore (Figure 3)(Pineda, 1994).

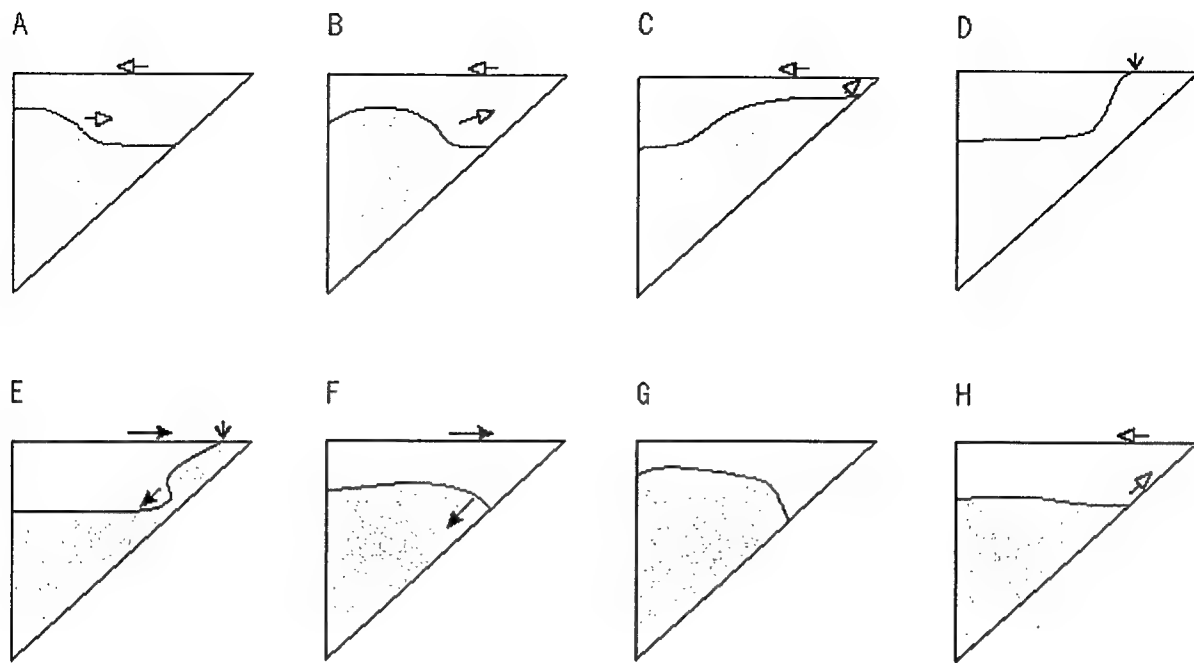


Figure 3.- Schematic representation of the onshore advection of a dense water body (large internal tidal bore; panels A-C), followed by its subsequent down slope progression and the corresponding onshore advection of a warm-water body (panels E-G). Triangular sections represent cross-shore profiles. Dotted regions within the triangles represent denser water and clear regions lighter water. The vertical arrow represents position of warm-water front and the other arrows represent currents. Horizontal scale greatly reduced relative to vertical scale. (From Pineda, 1994.)

Recent observations on the onshore migration of internal-bore warm-fronts in shallow water revealed that fronts are followed by large-amplitude high-frequency internal waves. Warm bore fronts had concentrating currents resulting from high-frequency internal motions and a larger two-way flow, with surface onshore currents, and bottom offshore. Onshore currents were faster closer to the seasurface, while faster offshore currents occurred at a distance from the bottom. In some cases, averaged onshore currents $u > c$, propagation speed. Faster currents than the rate of advance of the front implies that the origin of surface material accumulated in the front is behind the fronts, not in front of the front. Three nearshore invertebrate larval taxa showed contrasting horizontal and vertical distributional patterns. All were found in all sites across fronts, but only larvae of two shore barnacles, *Chthamalus spp.* and *Pollicipes polymerus*, were concentrated at the front's surface, while the subtidal bryozoan *Membranipora spp.* was not. *Pollicipes* was more abundant in the fronts' surface, and appeared to be more concentrated than *Chthamalus*. Observed frontal downwelling currents suggest that larvae would have to swim upward to withstand currents and accumulate. Larval distribution around the front suggests that in some cases frontal *Pollicipes* originates offshore if the front, while *Chthamalus* may originate at either side of the front.

Literature cited

Cairns, J.L. 1967. Asymmetry of internal tidal waves in shallow coastal waters. *J. Geophys. Res.* **72**, 3563-3565.

Leichter, J.J., G. Shellenbarger, S.J. Genovese et al. 1998. Breaking internal waves on a Florida coral reef: a plankton pump at work? *Mar. Ecol. Prog. Ser.* **166**, 83-97.

Leichter, J.J., S.L. Wing, S.L. Miller et al. 1996. Pulsed delivery of sub-thermocline water to Conch Reef, Florida keys by internal tidal bores. *Limnol. Oceanogr.* **41**, 1490-1501.

Pineda, J. 1991. Predictable upwelling and the shoreward transport of planktonic larvae by internal tidal bores. *Science (Washington D.C.)* **253**, 548-551.

Pineda, J. 1994. Internal tidal bores in the nearshore: warm-water fronts, seaward gravity currents and the onshore transport of neustonic larvae. *J. Mar. Res.* **52**, 427-458.

Pineda, J. 1995. An internal tidal bore regime at nearshore stations along western USA: predictable upwelling within the lunar cycle. *Continental Shelf Research.* **15**, 1023-1041.

Winant, C.D. 1974. Internal surges in coastal waters. *Journal of Geophysical Research.* **79**, 4523-4526.

OBSERVATIONS OF ISOLATED WAVES IN TWO-LAYER DOWNSLOPE FLOWS

Peter G. Baines, David Murray and Thierry Ruchon*

CSIRO Atmospheric Research
Aspendale 3195
Australia

1. Introduction

In this paper we describe the results of an experimental study of wavy disturbances on otherwise steady downslope flows of dense fluid into a homogeneous environment. The waves were generated by causing periodic variations in the supply of dense fluid at the top of the slope. The results are compared with a theoretical model of the Korteweg - de Vries type for non-linear disturbances on such flows.

2. Theoretical Preliminaries

As described below, the onset of a supply of dense fluid at the top of the slope sets up a downslope gravity current, which has an approximately uniform thickness down the slope. The dynamics of this steady flow is governed by a balance between the buoyancy force, and the drag of both the bottom surface and the fluid above, giving a mean state governed by

$$g' \sin \theta = (k + C_D) U^2 / d \quad , \quad (2.1)$$

where U is the mean speed of the dense current, d is its thickness, $g' = gD r / r$ is the buoyancy, r is the ambient fluid density and $D r$ is the additional density of the dense fluid, C_D is the drag coefficient of the bottom and k is an effective drag coefficient for the overlying fluid.

If we consider disturbances propagating on this flow and write

$$d = \bar{d} + \eta \quad , \quad (2.2)$$

one may obtain an equation for η of the form

$$\eta_t + c_0 \eta_x + \mu \eta \eta_x + \lambda \eta_{xxx} + \gamma \eta = 0 \quad , \quad (2.3)$$

where

$$c_0 = u_0 (1 - d_{10} / D) + (g' d_{10} \cos \theta)^{1/2} [(1 - F_0^2 d_{10} / D)(1 - d_{10} / D)]^{1/2} \quad , \quad (2.4)$$

$$\mu = \frac{3}{2} \cdot \frac{c_0 (1 - 2d_{10} / D) - u_0 (1 - d_{10} / D)}{d_{10} (1 - d_{10} / D)}, \quad (2.5)$$

$$\lambda = \frac{d_{10} (D - d_{10})}{6} \cdot \frac{c_0^2 + (u_0^2 - 2c_0 u_0) d_{10} / D}{c_0 - u_0 (1 - d_{10} / D)}, \quad (2.6)$$

$$\gamma = \frac{g' \sin \theta}{u_0} \cdot \left[1 - \frac{F_0}{2} \left(\frac{1 - d_{10} / D}{1 - F_0^2 d_{10} / D} \right)^{1/2} \right], \quad F_0 = \frac{u_0}{(g' d_{10} \cos \theta)^{1/2}}. \quad (2.7)$$

Here D is a mean total depth, u_0 is the speed of the lower layer, d_{10} is the depth of the lower layer and F_0 is a Froude number based on the lower layer alone. The expressions for l and m are obtained from Grimshaw (1996). The parameter g may be positive or negative depending on whether F_0 is greater or less than 2. Some solutions to (2.3) with external forcing have been given by Smyth (1988). Equation (2.3) itself does not appear to possess solitary wave solutions, but it presents us with a basis for comparisons between these dynamics and the experiments.

3. The Experiments

The experiments were carried out in a rectangular glass-sided tank that was approximately 80 cm high, with internal dimensions of 299 cm in length and 38 cm in width, open at the top with a horizontal bottom. The configuration was similar to that described in Baines (1998a,b) for stratified experiments. Only part of the width (23 cm) of the tank was used for the downslope experiments; this was partitioned from the remainder of the tank by a vertical perspex wall that ran along its length, with a gap of 35 cm at one end. At the other end, in this working part, a horizontal shelf 40 cm in length was fitted against the end wall, and this was extended further by a downward slope at 3° to the horizontal, two metres in length. A barrier (or gate) was fitted on the horizontal shelf with a gap of 1 cm at the bottom, at a distance of 40 cm from the end of the tank (i.e. at the top of the slope). In a typical experiment, the tank was filled with fresh water to a depth above the gap at the bottom of this barrier, and a steady flow of dense salty water was supplied by a hose at the end of the tank, to provide a dense downslope-flowing bottom current. Porous mesh barriers were placed 10 cm from the end of the tank to reduce the turbulence generated by the inflow from the hose. The arrangement of these barriers ensured that the flow emerging from them was effectively uniform across the width of the working region. Before each run, a solid temporary barrier was inserted on the shelf. It was then removed at the start of the experiment to ensure a sudden onset to the downslope flow, which was sustained for a typical period of several minutes. At the bottom of the two-metre slope, the dense fluid overflowed the end in a stratified waterfall, accumulating in a pool on the floor of the tank.

The above procedure produced steady currents of dense fluid flowing down the slope. The object of the experiment was to study waves on this current, and to do this a wave generator was inserted on the shelf between the two barriers. Several types of generator were tried, and the design adopted consisted of a mechanically driven movable perspex paddle, spanning the width of the tank and oriented vertically

across it. This paddle moved in an elliptical path, forward towards the slope, then upwards, back, down and then forwards again. This had the effect of producing a succession of surges in the current, that took the form of waves of elevation when they emerged onto the top of the slope from under the gate. The amplitude of the stroke of the paddle was 2.7 cm with a period of 3.6 sec for a full circuit of its motion, and this was unchanged for all the experiments described here. The properties of the waves produced were studied for a variety of densities of the inflow and initial flow rates. For virtually all experiments, $F_0 < 2$.

4. Observations and Results

In all experiments, the downslope flow reached a steady state before the motion of the wave-generating paddle was commenced. This downflow was observed to have effectively uniform thickness down the slope, and its dynamical balance is therefore largely governed by (2.1). For the smaller flow rates Q these flows are nearly laminar, but as Q increases they progressively develop features of Kelvin-Helmholtz waves, implying mixing with the fluid above. This tends to cause some degree of downslope flow in this fluid also (Ellison and Turner 1959), which becomes more pronounced as one moves further down the slope, but these effects are relatively small here and will be neglected for the purposes of describing the waves.

The waves generated on these currents had a characteristic life cycle of growth and decay, which is illustrated in Figure 1. Typically, at the top of the slope, the newly generated wave had a smooth, laminar and nearly symmetric appearance. As it moved down the slope with (and faster than) the mean current, it grew in amplitude and steepened on its forward face. This continued until some roughness appeared on the lee side, which then became more pronounced and developed into a full turbulent wake of the wave. This lee-side turbulence had the effect of removing fluid from the rear of the wave and mixing it with the environment, so that shortly after reaching its maximum amplitude and steepness, the wave collapsed as a result of this lee-side turbulent erosion. This left a residual lower, flatter wave structure of decaying turbulent dense fluid. This final process of collapse was often quite sudden and dramatic.

This cycle was not always repeated in exactly the same fashion in all experiments, partly because the variations in the current meant that the initial wave was different and began at different parts of this cycle, with breaking occurring earlier in a more turbulent current than in a laminar one.

For solitary waves with $g = 0$, from (2.3) their speed is given by

$$c = c_0 + \frac{1}{3} \alpha, \quad (4.1)$$

where α is the amplitude of the wave. For most of their life cycle, the observed speeds of the waves were consistent with this. However, the g -term is generally not negligible, being often

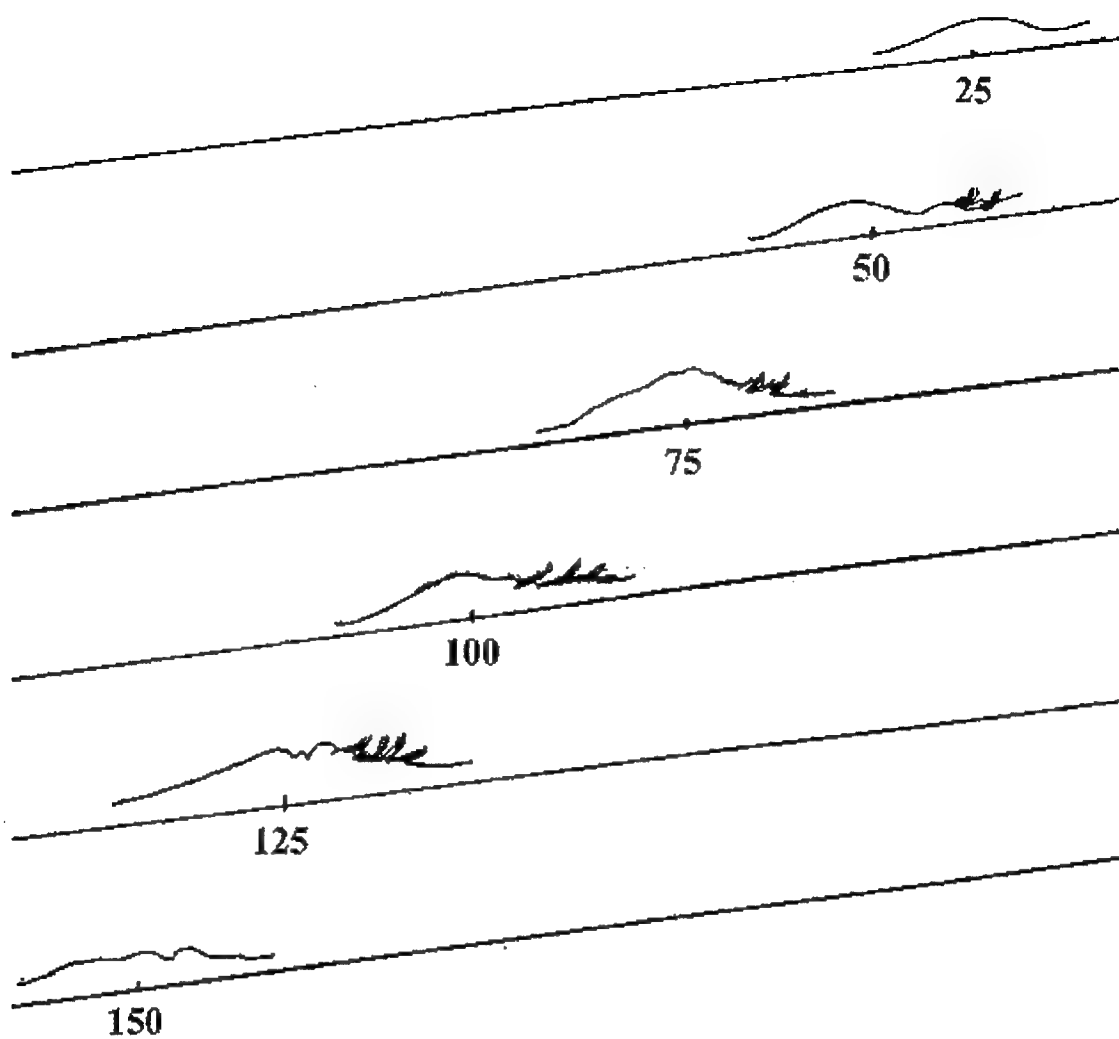


Figure 1. Sketch of the growth and decay of an isolated wave disturbance as it propagates down the slope, for $F_0 = 0.51$. The numbers denote distance from the top of the slope in cm.

larger than the dispersion term (with factor 1). The observed values of other properties relating to (3.2) showed considerable scatter, and this model does not seem to be the most suitable for these waves. This question is being pursued further.

5. Conclusions

The most prominent observed property of the waves was a cycle of growth and decay, which was not satisfactorily described by the model of Section 2. Specifically, the waves grow in amplitude as they move down the slope, and during this phase their speed is generally consistent with (2.3), as non-linear

advection and the dispersive term are small. However, as the wave amplitude grows, dissipation and mixing on the lee side increase in magnitude and rapidly erode the wave. The result is a significant mixing event in which the fluid in the wave is mixed with the environmental fluid above, leaving a residual much lower, flatter wave structure on the lower layer. This process seems to be more related to the steepness of the wave and lee-side wake effects rather than shear flow instability, and theoretical models need to take this process into account in order to describe these waves satisfactorily.

References

Baines, P.G. 1998a: Downslope flows into a stratified environment - structure and detrainment. In *Mixing and Dispersion in Stably Stratified Flows*. Proc. 5th IMA Conference on Stratified Flows, Dundee. P.A. Davies, editor, to appear.

Baines, P.G. 1998b: Downslope flows into stratified environments. To be submitted to *J. Fluid Mech.*.

Ellison, T. and Turner, J.S. 1959: Turbulent entrainment in stratified flows. *J. Fluid Mech.* **6**, 423-448.

Grimshaw, R.H.J. 1996: Internal solitary waves. *Monash University Mathematics Department Preprint 96/7*.

Smyth, N. 1988: Dissipative effects on the resonant flow of a stratified fluid over topography. *J. Fluid Mech.* **192**, 287-312.

INTRUSIVE SOLIBORES IN KNIGHT INLET

Eric A. D'Asaro
Applied Physics Laboratory
University of Washington
dasaro@apl.washington.edu

[For Knight Inlet Turbulence, Click Here](#)

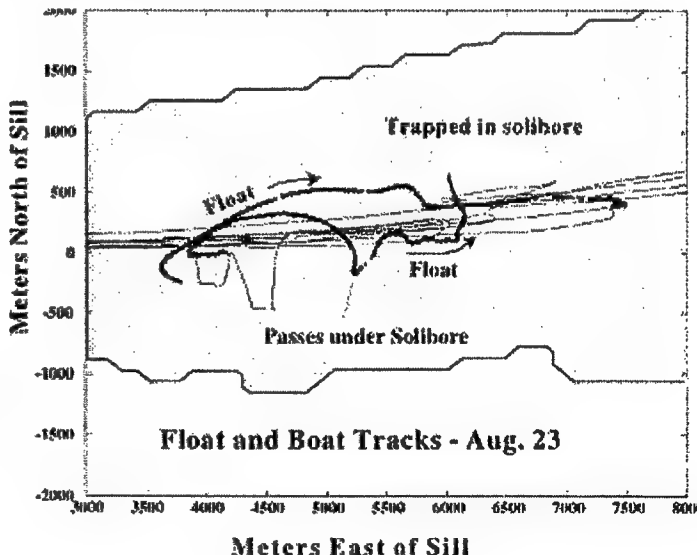
Introduction

The overall goal of the [Knight Inlet experiment](#) was to study the generation, propagation and decay of energetic, propagating features, commonly seen in coastal regions. These are neither completely wave-like, as the common term 'soliton' would imply, nor entirely bore-like, hence the term '[Solibore](#)'.

The solibores described here were of a new type with **little surface expression**. Several varieties exist; we describe the most energetic here. They are generated near the Sill, but the mechanism is not clear since they appear a few kilometers downstream of the Sill on Flood tide with no obvious link to structures observed at the sill. They are clearly **Intrusive Solibore** propagating up the inlet and carrying water from near the sill up-inlet. This page describes observations of intrusive solibores

Methods

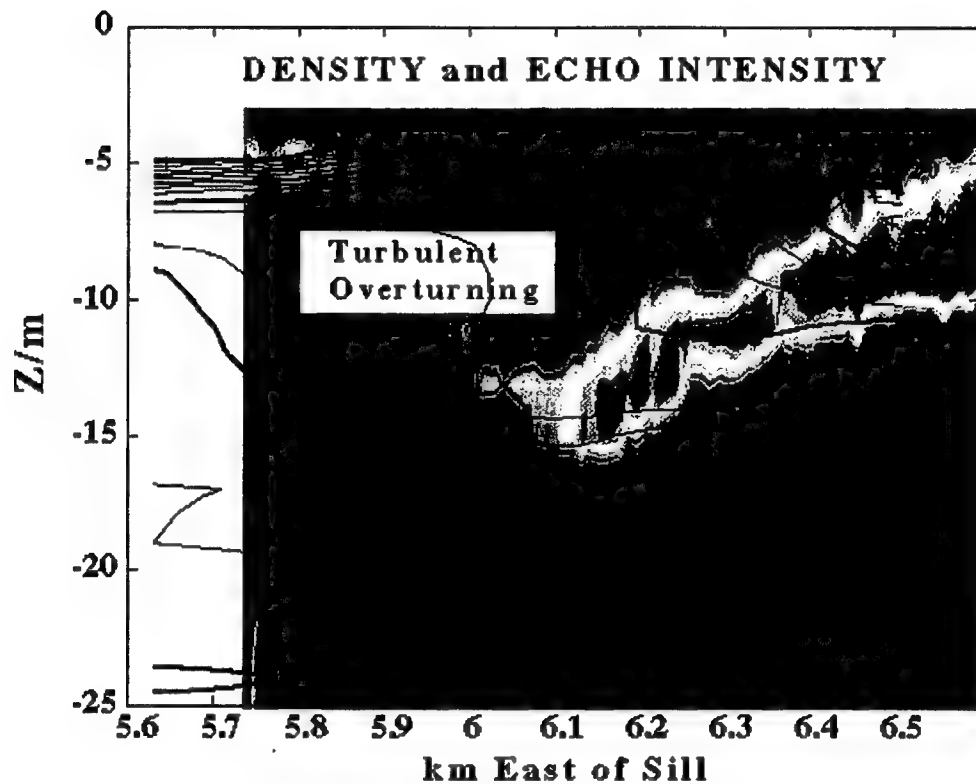
Observations were made from the *C.R.V. Bazan Bay*, which was equipped with a 300 kHz ADCP, a narrow beam echosounder and a CTD. Solibores were tracked by repeatedly running a line up inlet from the Sill at maximum speed and thus obtaining repeated sections of velocity (ADCP) and echo intensity. Neutrally buoyant [Lagrangian floats](#) were deployed from the boat and acoustically tracked as they passed through the solibores. The chart shows the track of the boat (thin black lines) and the floats (red and black lines) on August 23. The solibore is propagating to the East (left to right) on a flooding (eastward) tide.

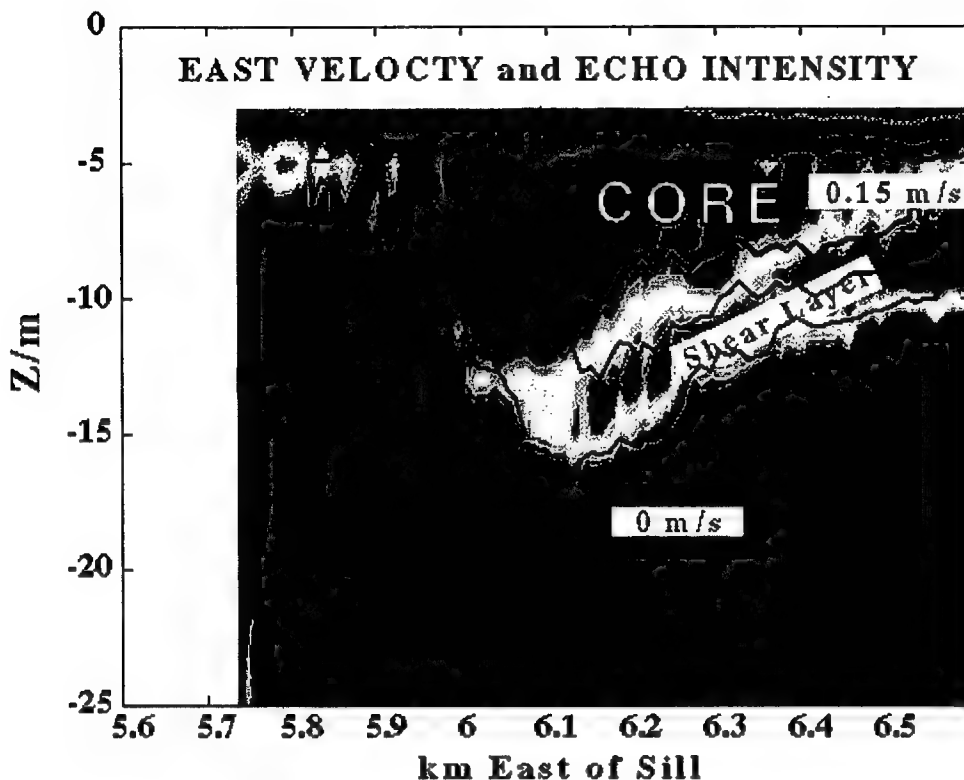


Structure of the Solibore

A detailed CTD/ADCP section across an intrusive solibore shows its structure. This data is superimposed on the backscatter echo intensity from the ADCP. The leading edge of the solibore is marked by a region of high backscatter (red/orange) in the figures below. This corresponds to a strong **shear layer**, which separates the

eastward-moving **Core** of the solibore, above, from the nearly stationary water, below. The high backscatter is probably due to high levels of temperature and/or salinity microstructure in Kelvin-Helmholz instabilities in the shear layer. ([click here for more details on similar K-H instabilities in Knight Inlet](#)). Ahead of the shear layer, the stratification is strong; behind it the stratification is weak with density **overturnings** indicative of active **turbulence**. The solibore propagates at approximately the speed of the core. The core water is therefore carried along with the solibore, slowly being modified by mixing at its lower edge and leakage from its back.





A Lagrangian View

The trajectories of two Lagrangian floats deployed ahead of the solibore are shown in the chart. Their motion relative to the solibore is shown below.

These frames are taken from a movie which shows the full sequence of acoustic backscatter and float trajectories. The movie is made by interpolating the echo intensity data between successive surveys in a bore coordinate system and superimposing the float trajectories. The solid lines show velocity streamfunction in the bore coordinate system computed from the ADCP data.

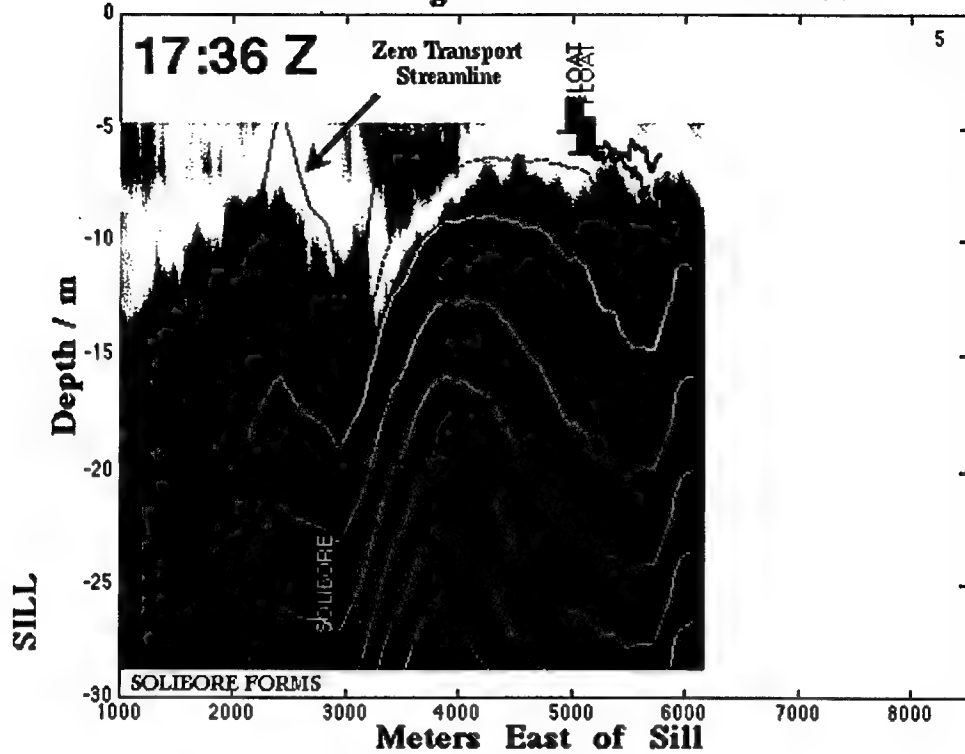
[CLICK HERE TO DOWNLOAD QUICKTIME MOVIE \(2.2 MB\)](#)

(better colors on most screens)

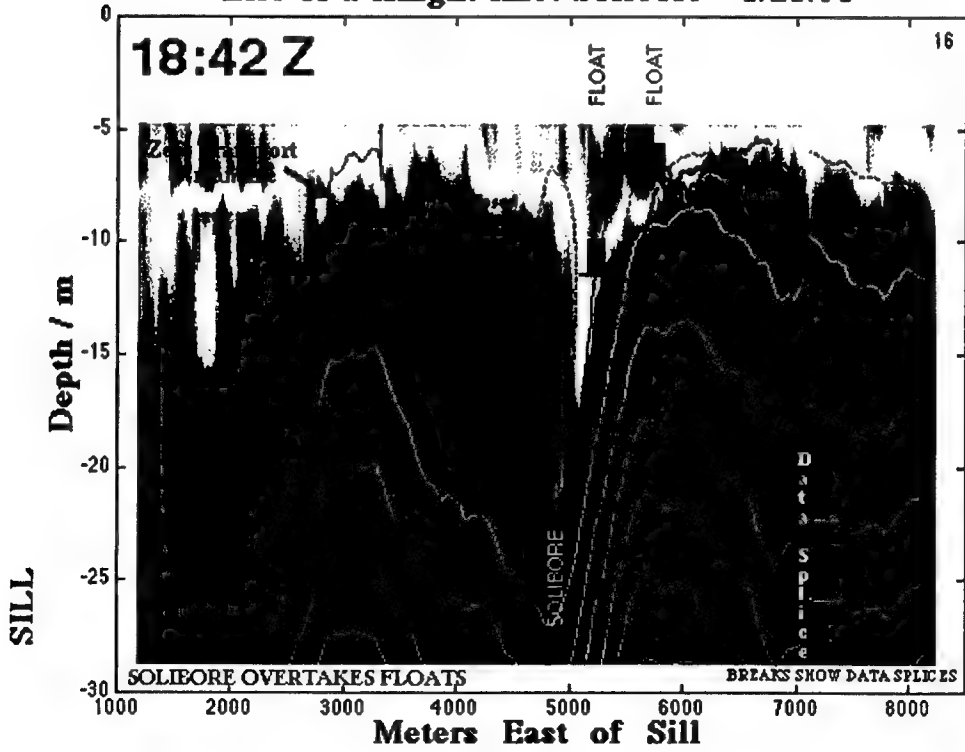
[CLICK HERE TO DOWNLOAD MPEG MOVIE \(1.8MB\)](#)

(needs displays with more than 256 colors)

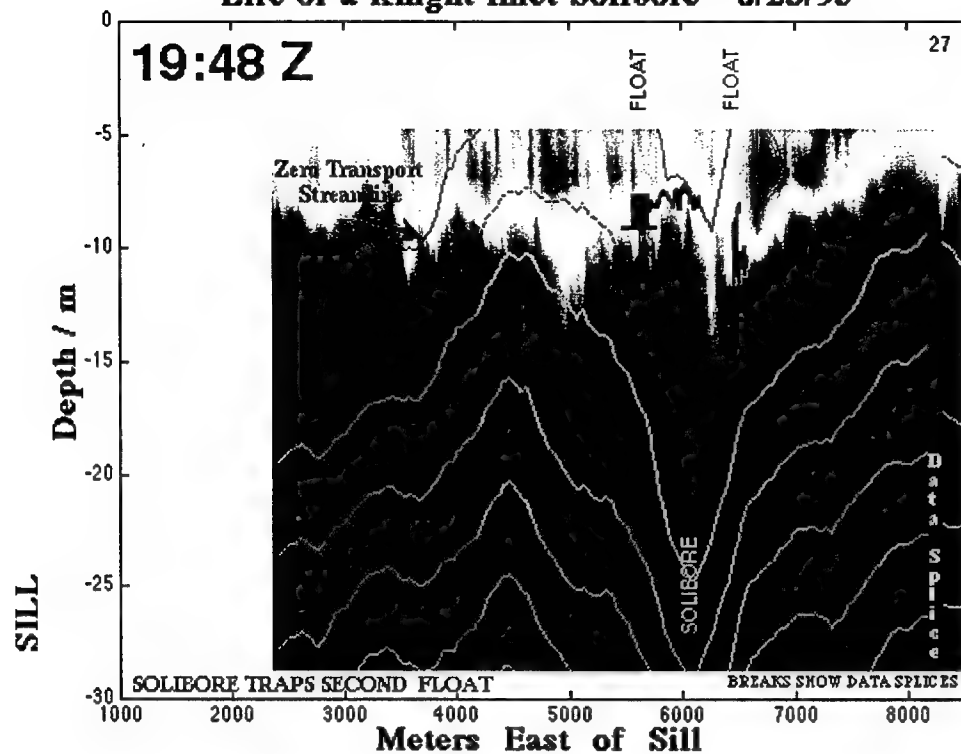
Life of a Knight Inlet Solibore - 8/23/95



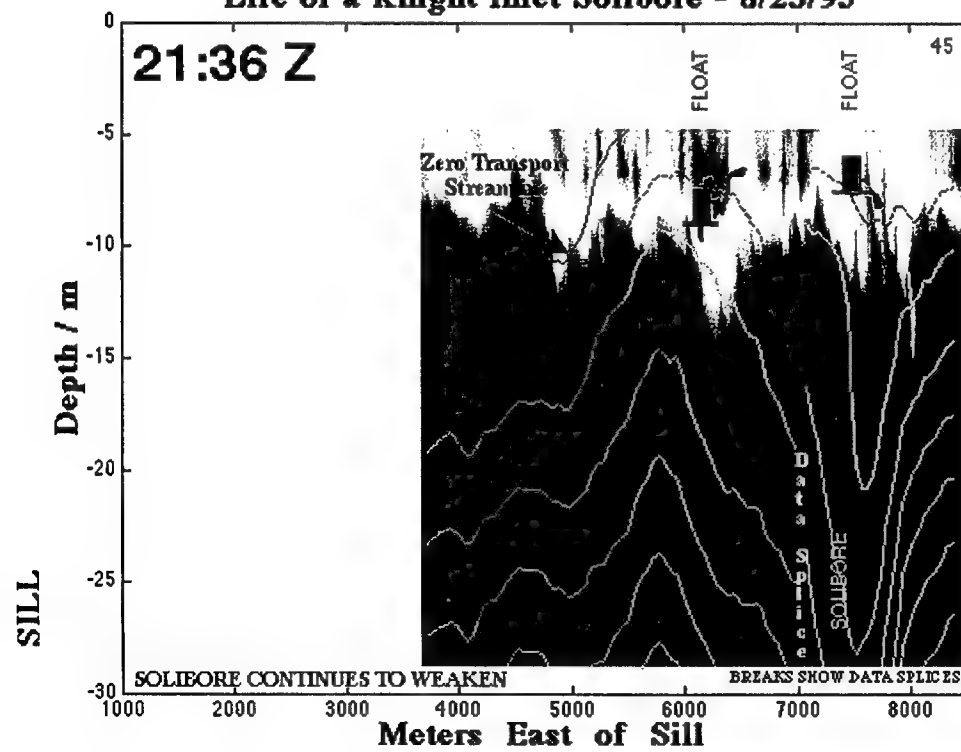
Life of a Knight Inlet Solibore - 8/23/95



Life of a Knight Inlet Solibore - 8/23/95



Life of a Knight Inlet Solibore - 8/23/95



The solibore starts out as a nearly sinusoidal wave, then steepens into a nonlinear shape with a strong **recirculation**. The solibore then overtakes the two floats, showing that it **propagates** relative to the surrounding water. The first float (black) passes under the core of the solibore and is quickly left behind. Note that **acoustic tracking** is briefly lost as the float is rises behind the solibore. The second float (magenta) is entrained into the core of the solibore and travels with it for about 2 hours, clearly showing that the solibore is not merely a wave, but **transports water**. Measurements on the trapped float show **density inversions** and rapid vertical motions indicating strong **turbulence** in the solibore. The temperature records indicates a vertical **heat flux** from below of about 200 W/m^2 . The solibore slowly weakens with time probably due to mixing; the recirculation disappearing and the core becomes deeper and presumably denser. The trapped float is released. At all times, the highly nonlinear structure in the top 10 m is tied to a depression of the streamlines in deeper layers.

SUMMARY

These data clearly illustrate several key features of these solibores. They:

- Are a major feature of Knight Inlet
- Propagate through the surrounding water
- Carry water from their generation site near the sill
- Are sites of strong turbulence and mixing
- Are tied to deeper internal waves



[return to Solibores and Sill Flows](#)

Fully nonlinear simulations of upstream waves at a topography

John Grue

Mechanics Division, Department of Mathematics, University of Oslo, Norway

Introduction

The aim of this paper is to describe recent research at the University of Oslo on internal waves generated upstream of a topography. Our investigations have both practical and general motivations. The practical needs relate to offshore activity in deep water and to certain proposed installations in coastal water like submerged floating tunnels. In both cases the effects due to internal waves may be important. It is of interest in this connection, among others, to investigate how internal waves in an actual ocean basin or fjord may be generated.

Two-layer model

Here we focus on waves in a two-layer fluid generated by flow over topography. We have developed a two-dimensional, transient, fully nonlinear model for this purpose. The two-fluid system has a lower layer with thickness h_1 and constant density ρ_1 , and an upper layer with thickness h_2 and constant density $\rho_2 < \rho_1$. A coordinate system $O-xy$ is introduced with the x -axis along the interface at rest and the y -axis pointing upwards. We model the flow in each of the layers by potential theory. A Lagrangian method is adopted, where pseudo Lagrangian particles are introduced on the interface, each with a weighted velocity defined by $\mathbf{v}_x = (1 - \alpha)\mathbf{v}_1 + \alpha\mathbf{v}_2$, where \mathbf{v}_1 and \mathbf{v}_2 denote the fluid velocities in the respective layers, and $0 \leq \alpha \leq 1$. The prognostic equations are obtained from the kinematic and dynamic boundary conditions at the interface, i.e.

$$D_x(x, y)/dt = \mathbf{v}_x, \quad D_x(\phi_1 - \mu\phi_2)/dt = \mathbf{v}_x \cdot (\mathbf{v}_1 - \mu\mathbf{v}_2) - (1/2)(\mathbf{v}_1^2 - \mu\mathbf{v}_2^2) - (1 - \mu)gy$$

where $\mu = \rho_2/\rho_1$, $D_x/dt = \partial/\partial t + \mathbf{v}_x \cdot \nabla$ and the gravity g acts downwards. The prognostic equations are expanded in Taylor series, keeping several terms, in order to obtain an efficient scheme. Accurate solution of the Laplace equation is crucial to an algorithm for computing interfacial flows, and we here apply complex theory and Cauchy's integral theorem for this purpose.

For interfacial waves with finite amplitude the physical Kelvin-Helmholtz instability is inevitably included in the theoretical model. This represents a difficulty since the space discretization cannot be too fine. Instability is removed by a regridding procedure and smoothing. We are, however, able to document convergence of the method and accuracy in all cases considered. The mathematical model is documented in reference 1.

Undulating bore

In the first example we apply the model to fluid layers with thicknesses h_2 and $h_1=4h_2$, and densities $\rho_2 = 0.8 \text{ g cm}^{-3}$ and $\rho_1 = 0.986 \text{ g cm}^{-3}$. A body, starting from rest, is moving horizontally with speed U in the upper layer, and we shall compute the resulting motion of the interface. The shape of the body is determined by $y=h_2-H_0\operatorname{sech}^2(Kx)$, where $H_0=0.4h_2$ and $KH_0=0.1989$. This configuration corresponds to a set of experiments described by Melville & Helfrich (1987). (We have been able to simulate their experiments with good agreement using the present fully nonlinear method, where weakly nonlinear KdV-theory exhibits severe shortcomings). First we consider two examples where the speed of the body is either $U=0.81c_0$ or $U=0.94c_0$, where c_0 is the linear shallow water speed of the two-fluid system. The resulting profiles of the interface exhibit an undular depression that is developing ahead of the body, with a number of oscillations which is increasing with time, see figure 1. Behind the body an almost horizontal elevation develops, with length which also is increasing with time. We find that the results in figure 1 are typical for speed of the body in the interval $0.38 < U/c_0 < 1.02$, approximately, for this configuration. The lower limit corresponds to the lower limit of the transcritical regime.

Solitary waves

In the next example we consider the same problem as above, but let the body have speed $U/c_0=1.09$. Now we also want to vary the thickness of the body, to investigate the effect of various forcing. In the first case (figure 3a) the thickness of the body is $H_0=0.4h_2$. Now the moving body generates a train of solitary waves propagating upstream, with an amplitude $a=1.171h_2$. We have compared the saturated leading waves with fully nonlinear solitary wave solutions of the corresponding steady problem, with a very high agreement (see also figure 4d for another example).

We then halve the thickness of the body ($H_0=0.2h_2$) and display results in figure 3b. The generated solitary waves have now somewhat reduced amplitude and generation rate as compared to the previous example. The reduction of the body thickness is once more repeated (figure 3c), i.e. $H_0=0.1h_2$, but still upstream solitary waves are generated, now with a quite reduced generation rate, however. When the height of the body is reduced still more, to $H_0=0.05h_2$, solitary waves are not generated. The flow becomes supercritical, with a minor depression moving with the same speed as the body (figure 3d).

In another example the two-fluid system at rest has thicknesses h_1 and $h_2=4h_1$ (a thin layer below a thick) and ratio between the densities $\rho_2/\rho_1 = 0.7873$. A half-elliptical body with horizontal and vertical half-axes $10h_1$ and $0.1h_1$, respectively, is moving horizontally with speed $U=1.1c_0$ along the bottom of the lower (thinner) layer. This geometry has approximately the same volume as the former one but is more slender, and therefore imposes weaker nonlinearity on the problem. Still upstream solitary waves with height of the order of the thinner layer are generated, see figure 4.

For both geometries we have found that solitary waves are generated for a rather narrow interval of the

speed, i.e. $1.05 < U/c_0 < 1.15$, approximately. The generated solitary waves have always an amplitude comparable to the depth of the thinner layer.

Topography in the thicker layer

We have also performed some simulations for a body moving horizontally with constant speed in the thicker of the two layers (results not shown). If the lower layer is the thicker one, a depression of the interface develops behind the body. This depression may be rather significant, depending on the size of the body. Correspondingly, the interface is lifted upstream of the body. We have not observed that waves are generated upstream for this configuration.

Another interesting problem, which we have not yet investigated, is that with an oscillatory flow at stationary body, which is relevant to tidal driven flow at a bottom topography. We aim to perform simulations for this problem and present the results at the workshop.

Comparison with experiments

In the ocean (or in the atmosphere) the density profile is seldom very sharp, and one may question the relevance of a two-layer model where two homogeneous fluids are separated by a sharp interface. On the otherhand, if an infinitely sharp pycnocline could be created in nature, one would expect any wave motion to break up due to the Kelvin-Helmholtz instability. In order to investigate these issues we have performed several experiments in a wave tank on internal solitary waves. The solitary waves may propagate along a pycnocline separating a thinner layer of fresh water above a thicker layer of brine. The thickness of the pycnocline is in the interval 0.13 - 0.26 times the depth of the thinner layer, approximately. The induced fluid velocities are measured quite accurately using Particle Tracking Velocimetry. In figure 2 we show an example of the velocity profile at the crest of a solitary wave. Data from several experiments are included. Also is shown a comparison with the fully nonlinear theory, with good agreement. We have performed several other experiments, also with good agreement with theory (results may be found in reference 2). We have observed that Kelvin-Helmholtz instability only occurs for the largest waves (close to the maximal amplitude). Instability appears to occur according to the theorem of Miles and Howard.

This research was supported by The Research Council of Norway.

References

GRUE, J., FRIIS, H. A., PALM, E. AND RUSÅS, P. O. A method for computing unsteady fully nonlinear interfacial waves. *J. Fluid Mech.*, 351, 1997.

GRUE, J., JENSEN, A., RUSÅS, P. O. AND SVEEN, J. K. Properties of large amplitude internal waves. *J. Fluid Mech.* (to appear). 1998.

Figure 1: Elevation of interface. (a) $U/c_0=0.81$. (b) $U/c_0=0.94$. $t(g/h_2)^{1/2}=480$ (solid line), $t(g/h_2)^{1/2}=870$ (dashed line). $\rho_2/\rho_1 = 0.8114$, $h_1/h_2=4$. (t =time.)

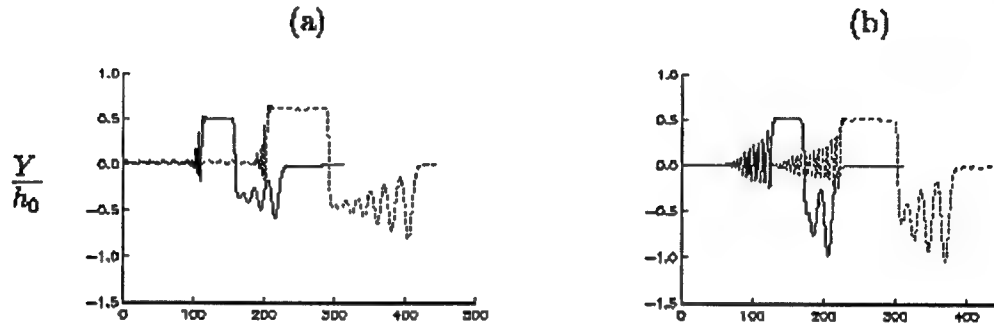


Figure 2: Velocity profile $u(y)/c_0$ at the crest of solitary wave. c_0 the linear shallow water speed.

Depth of upper layer: h_2 . Depth of lower layer: $h_1=4.13h_2$. Amplitude $a=0.78h_2$. $\rho_2/\rho_1 = 0.975$. Dots: Experiments. Solid line: Fully nonlinear theory.

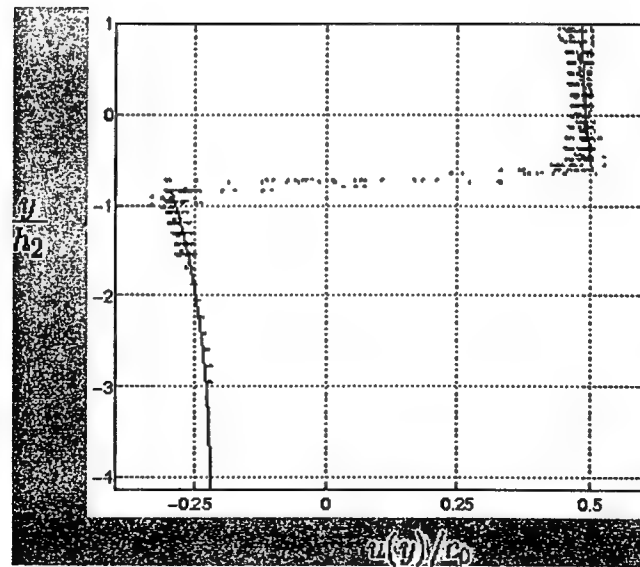


Figure 3: Elevation of interface. $Fr=1.09$. Decreasing height H_0 of moving geometry, i.e. $H_0 \operatorname{sech}^2 Kx$. $t(g/h_2)^{1/2}=1020$ (dashed line) $t(g/h_2)^{1/2}=1500$ (solid line). Height of the body: a) $H_0=0.4h_2$. b) $H_0=0.2h_2$. c) $H_0=0.1h_2$. d) $H_0=0.05h_2$. $\rho_2/\rho_1 = 0.8114$, $h_1/h_2=4$. (Note the differences in vertical scale.)

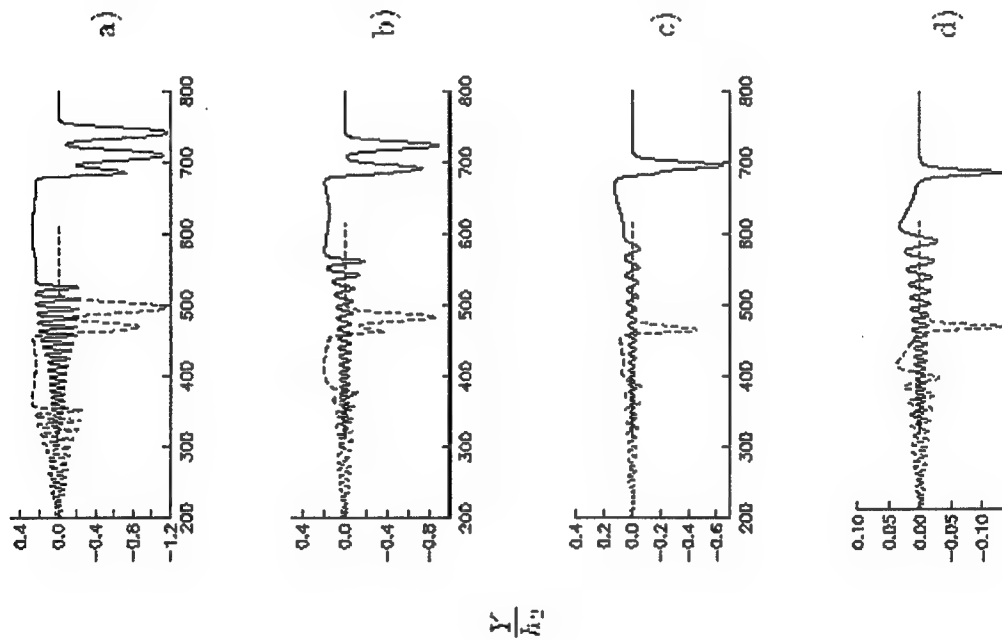
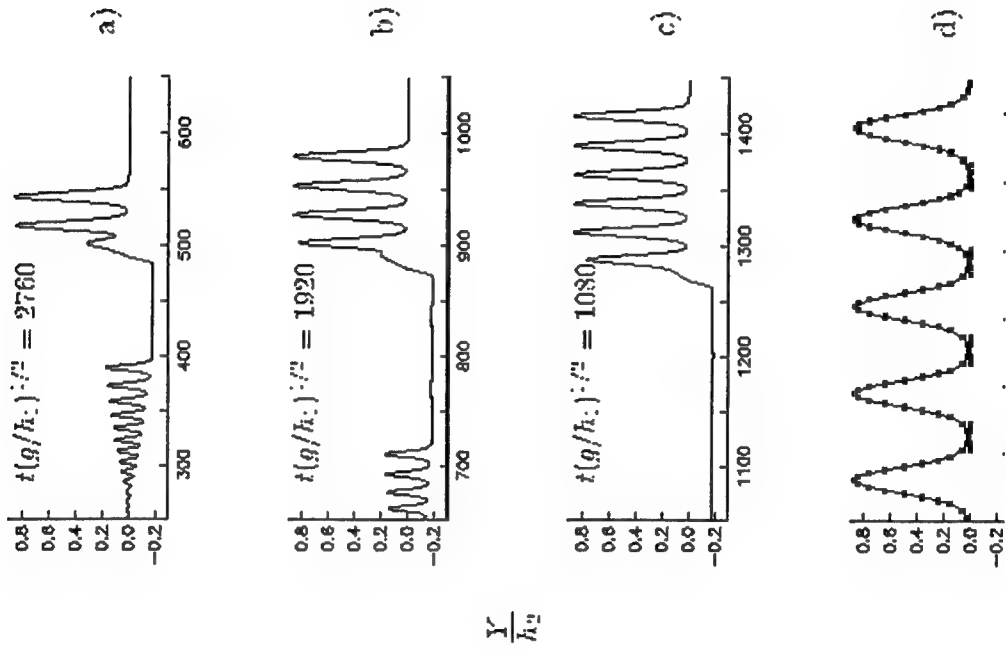


Figure 4: Generation of upstream solitary waves. Moving bottom topography being a half ellipse, horizontal half-axis $10h_1$, vertical half-axis $0.1h_1$. $U/c_0=1.1$, $\rho_2/\rho_1 = 0.7873$, $h_2/h_1=4$. a) $t(g/h_1)^{1/2}=1080$. b) $t(g/h_1)^{1/2}=1920$. c) $t(g/h_1)^{1/2}=2760$. d) Close up of figure c), black squares mark steady solitary wave solution with $|Y|_{max}/h_1=0.869$.



- About this document ...

[Next](#) [Up](#) [Previous](#)

Next:About this document ...

1998-09-10

Flows in Rotating Channels: Hydraulic Adjustment, Jumps and Shocks

K. R. Helfrich and L. J. Pratt

*Department of Physical Oceanography
Woods Hole Oceanographic Institution
Woods Hole, MA 02543*

1. Introduction

Nonlinear internal waves are common features of straits and are a consequence of the complicated interaction of time-dependent stratified flow with topographic features. These underlying flows are themselves highly nonlinear (typically hydraulically controlled) and exhibit significant spatial and temporal variation. Thus a full understanding of internal solitary wave propagation must include an understanding of the underlying flow which both generates and affects the evolution of the waves. In this short contribution we describe some results of two related problems which address the nonlinear dynamics of flow in rotating channels. The first is an extension of the dam break problem to the case of a rotating channel (Rossby adjustment in a channel). The second is the extension of Long's classic study of upstream influence and hydraulic adjustment over topography to flows in a rotating channel. In both examples we rely on solutions of the single layer shallow water equations and therefore do not model the nonhydrostatic effects which lead to solitary waves. However, the fully nonlinear shocks and hydraulic jumps which do arise are resolved and described.

2. Rossby Adjustment in a Channel

The setting for the dam break problem is a rectangular channel of width w . A cross-channel (y -direction) barrier separates two semi-infinite regions of homogeneous fluid of different depths. At time $t = 0$ the barrier is destroyed causing the upper fluid to intrude into the shallower fluid and the formation of a leading shock, or bore. The hydrostatic solution for no rotation is given by Stoker (1957). Gill (1976) examined the linear limit when rotation is included. A steady current is set up by Kelvin waves moving away from the barrier position. The Kelvin wave moving into the shallower layer is trapped to the right-hand wall (looking in the direction of the shallow layer) while the Kelvin wave moving into the deeper layer is trapped to the left wall. The steady flow approaches the section of the initial barrier along the left wall, crosses the channel at that section, and continues along the right wall.

When the initial depth difference is finite and rotation is included, the Kelvin wave moving into the shallow layer is replaced by a Kelvin bore. Because of the uncertainty of the proper shock-joining conditions and non-conservation of potential vorticity across the shock, an analytical solution to this

problem has not been found. Thus we employ numerical methods to study the flow. Figure 1 shows a the depth field for a channel of nondimensional width $w = 4$ and an initial nondimensional depth in the shallow section $d_0 = 0.1$, which is scaled by the initial depth in the deep region D . The horizontal dimensions are normalized by the deformation radius based on D . The flow is shown at $t = 20$. In this example the leading shock curves back upstream and its amplitude decays away from the right wall. Trailing the bore is a geostrophic boundary current. Near $x = 0$ there is a cross-channel geostrophic current due to the along channel gradient in depth.

Figure 1. Depth field for $w = 4$ and $d_0 = 0.1$ at $t = 20$.

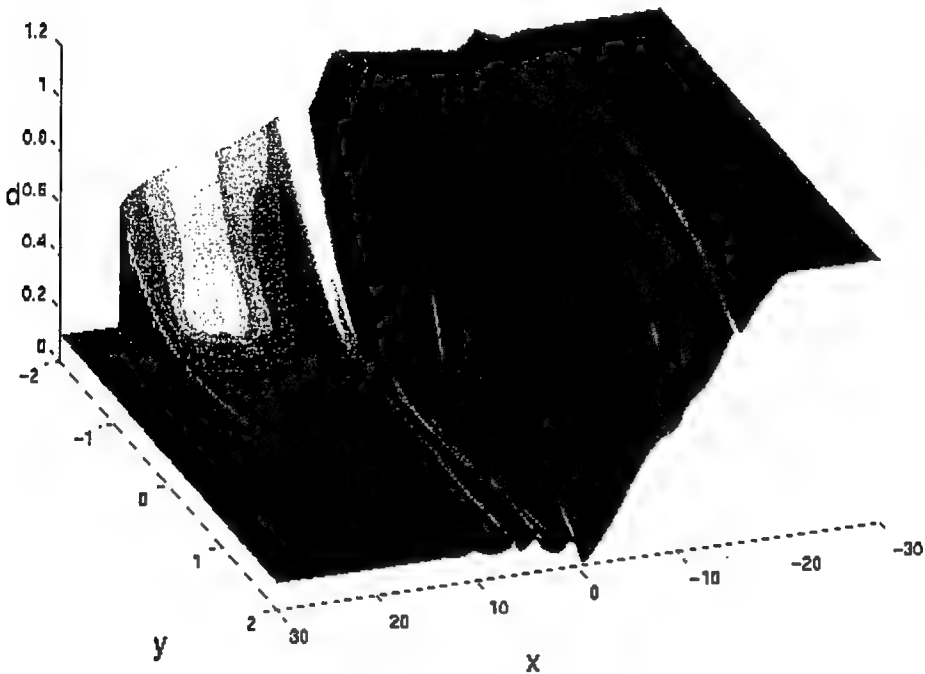


Figure 1

In a narrower channel the shock structure is rather different. Figure 2 shows a case with $w = 1$ and $d_0 = 0.25$. The leading bore is now nearly straight across the channel. The amplitude decays away from the right wall ($y = -0.5$), but increases near the left wall. Trailing the bore near the left wall is a packet of Poincaré waves. These waves appear to be generated by the resonant mechanism described by Tomasson and Melville (1992).

We find that the leading bore extends across the channel to attach at the left wall (within one deformation radius of its position on the right wall) when the channel width scaled by the deformation radius in the upstream region, $w d_0^{-1/2}$, is less than about 3. In all cases the shock is connected to the following geostrophic current by an ageostrophic boundary layer characterized by a strong transverse jet. Shock amplitudes, measured on the right wall, and shock speeds increase above the nonrotating solutions as w is increased for a given d_0 . However, the relation between bore speed and amplitude branches below the nonrotating relation as w (rotation) is increased. Finally, the potential vorticity jump across the shock is shown to depart significantly from the pseudo-inviscid estimates due to the viscous flux of vorticity, an effect that is at best crudely parameterized and poorly understood.

Figure 2. Depth field for $w = 1$ and $d_0 = 0.25$ at $t = 20$.

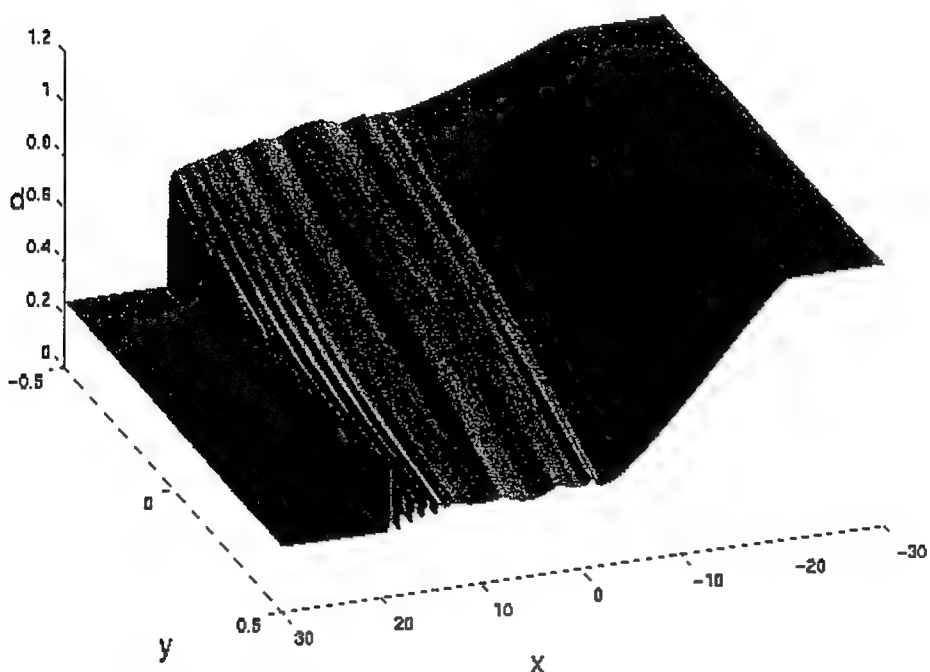


Figure 2

3. Long's Problem in a Rotating Channel

In Long's (1954, 1970) classic problem on upstream influence a topographic feature is rapidly grown

into a nonrotating, hydrostatic, single layer flow. The response of the fluid, and in particular the development of upstream influence, can be determined by the location of the flow in the $F - h_m$ plane, where F is the Froude number of the initial flow and h_m is the final height of the topography. Upstream influence occurs through the propagation of a shock, or bore, which causes a permanent change in the flow approaching the obstacle. At the crest of the obstacle the flow is critical and downstream a hydraulic jump back to subcritical flow may exist. In the weakly nonlinear and dispersive limit the upstream influence is achieved by the radiation of a train of solitary waves (e.g., Grimshaw and Smyth, 1986).

Using the semigeostrophic approximation and the assumption of uniform potential vorticity a theory is developed which gives the critical obstacle height above which upstream influence and hydraulic control at the topographic crest is achieved for rotating flow in a uniform channel. The critical height is a function of the initial flow Froude number (defined using the appropriate characteristic speeds in the rotating system) and the channel width relative to the deformation radius based on the upstream potential depth. The structure of the critical height curve is similar to the nonrotating version with increasing critical height as F increases above, or decreases below, one.

Figure 3. Adjustment to topography for $F = 1$, $w = 2$ and $h_0 = 0.5$

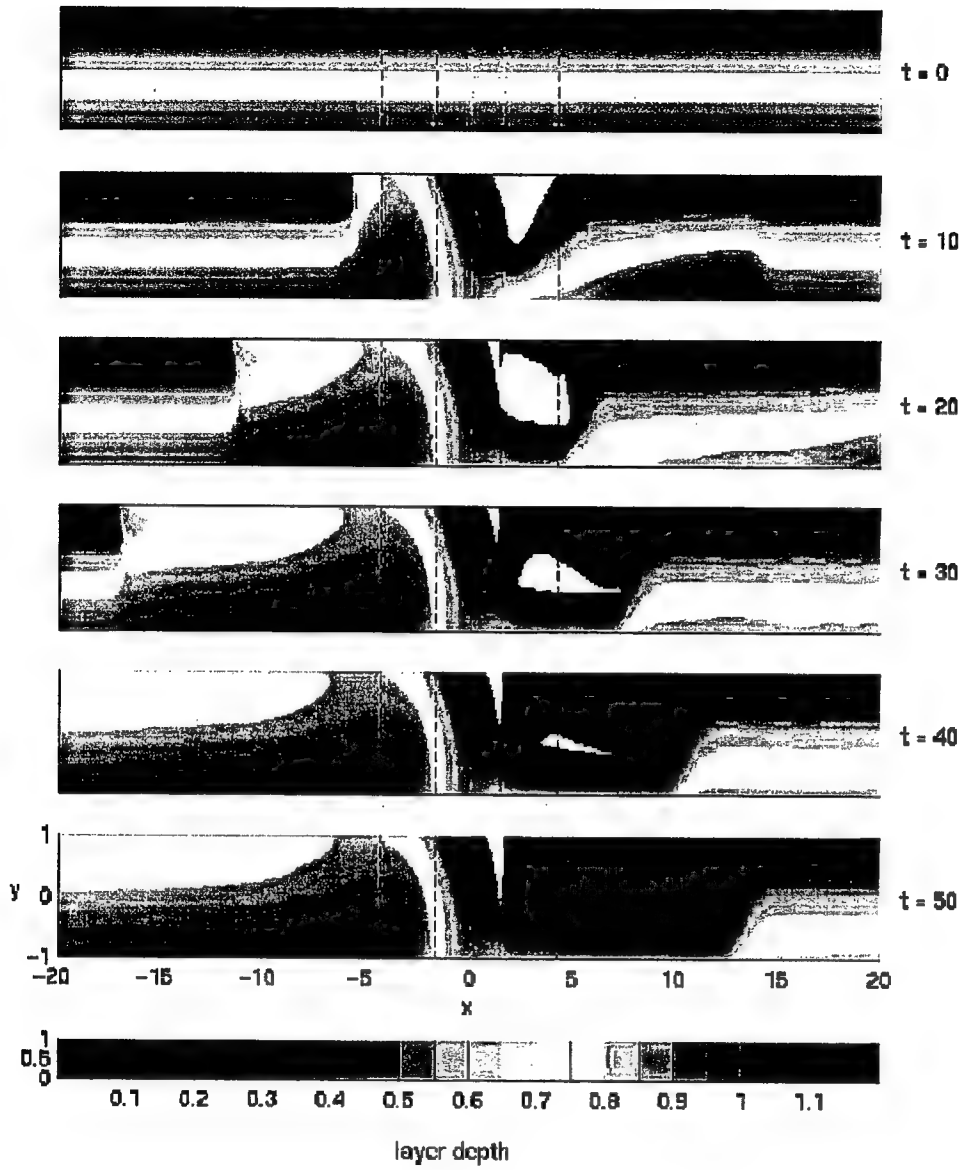


Figure 3

The theory is supplemented by numerical solutions of the full shallow water equations to explore the temporal development of the flow. The numerical solutions reveal numerous interesting features including upstream propagating shocks and separated rarefying intrusions, downstream hydraulic jumps (in both flow depth and width), flow separation and recirculation. Figure 3 shows one typical example for a channel of $w = 2$ and initial flow with $F = 1$. A symmetric topographic feature of height $h_m = 0.5$ is grown into the flow between $t = 0$ and 2. A bore propagates upstream leaving behind a new subcritical

upstream state which becomes supercritical as it flows over the topographic crest ($x = 0$). Just downstream of the topographic crest the flow separates from the left wall to form an expanding recirculation gyre. A small wedge of separated flow (zone of zero depth) remains over the topography. The numerical solutions show the semigeostrophic theory to give a generally good prediction of the critical obstacle height for upstream influence.

4. Summary

One goal of our work is to better understand the adjustment to hydraulically controlled flows in rotating channels. A consequence of the adjustment process, either in the Rossby adjustment problem or in the rotating version of Long's problem, is the generation of shocks, bores and jumps. In the context of internal solitary waves, the topic of this workshop, we repeat that wave generation often occurs due to flow interaction with topography and so any information on the dynamics of that interaction is useful in the question of solitary wave generation and propagation. Secondly, the shocks, bores and jumps we calculate are the fully nonlinear, hydrostatic limits of the (typically) weakly nonlinear solitary wave and undular bore solutions. As such, they may provide information on the initial, or boundary, conditions which result in solitary waves in the far field after enough time has passed for dispersive effects to become important.

References

Gill, A. E. 1976. Adjustment under gravity in a rotating channel. *J. Fluid Mech.* **77**, 603-621.

Grimshaw, R. H. J. & N. Smyth 1986. Resonant flow of a stratified fluid over topography. *J. Fluid Mech.* **169**, 429-464.

Long, R. R. 1954. Some aspects of the flow of stratified fluids. II. Experiments with a two-fluid system. *Tellus* **6**, 97-115.

Long, R. R. 1970. Blocking effects in flow over obstacles. *Tellus* **22**, 471-480.

Stoker, J. J. 1957. *Water Waves*. Interscience Publishers, 567 pp.

Tomasson, G. & W. K. Melville 1992. Geostrophic adjustment in a channel: nonlinear and dispersive effects. *J. Fluid Mech.* **241**, 23-58.

[Next](#) | [Up](#) | [Previous](#)

[Next](#): About this document ...

Nonlinear Internal Wave Observations on the Continental Shelf

Murray Levine and Timothy Boyd

*Oregon State University
Corvallis, OR*

INTRODUCTION

Packets of nonlinear internal waves (NIW) have been observed throughout the world, primarily on continental shelves. These waves are sometimes referred to casually as solitary waves, solitons, or solibores. We choose to use a more inclusive, generic name because of the uncertainty between our observations and the dynamics implied by the other terms.

These waves are generated by the interaction of the tide with topography, such as sills and continental slopes. In recent years NIW have commanded the attention of a diverse group of researchers studying: geophysical fluid dynamics, acoustics, ocean optics, sediment transport, plankton advection and vertical mixing. This conference provides an opportunity to ask a fundamental question of all disciplines: *Why study nonlinear internal waves?* Two answers come to mind: they are interesting, and they may be important.

Demonstrating that they are interesting is easy. They often make a striking appearance in observations, commanding attention. They invite explanation of fluid dynamicists and are probably worth studying in name of knowledge for its own sake.

As to whether they are important, the reason may depend upon the discipline answering the question, and we are eager to learn the viewpoints of others. As for physical oceanography, one of the measures for importance is: Do nonlinear internal waves contribute significantly to mixing on continental shelves?

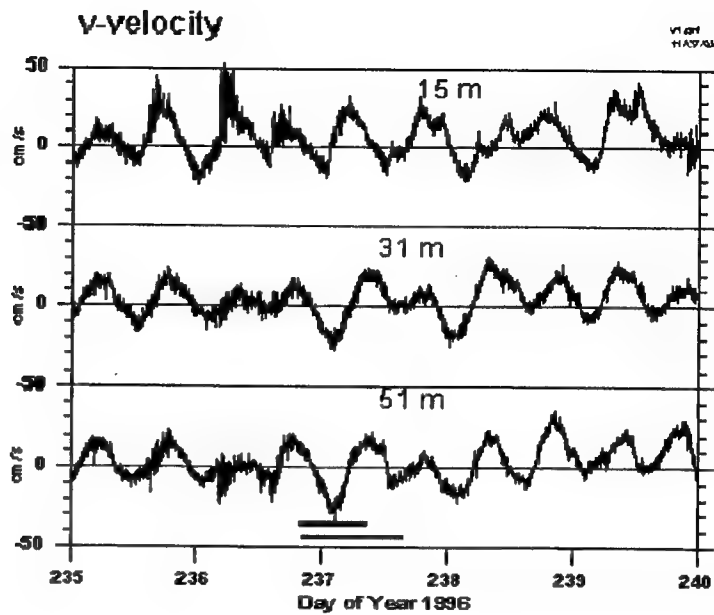
We will discuss our observations of NIW highlighting how they relate to the issues of *interest* and *importance*.

OBSERVATIONS: *Interesting?*

The observations presented here were obtained from a mooring in the Mid-Atlantic Bight (40.5 deg N, 70.5 deg W) during the Coastal Mixing & Optics / SAS Primer experiment. Temperature and velocity time series were recorded from July through September 1996 spanning the 70 m water depth. It is instructive to look at the NIWs in the context of the oscillations at other scales that are due to other processes. For example, the 5-day time series of northward velocity shown in Figure 1 is dominated by the semidiurnal tide, which is primarily barotropic.

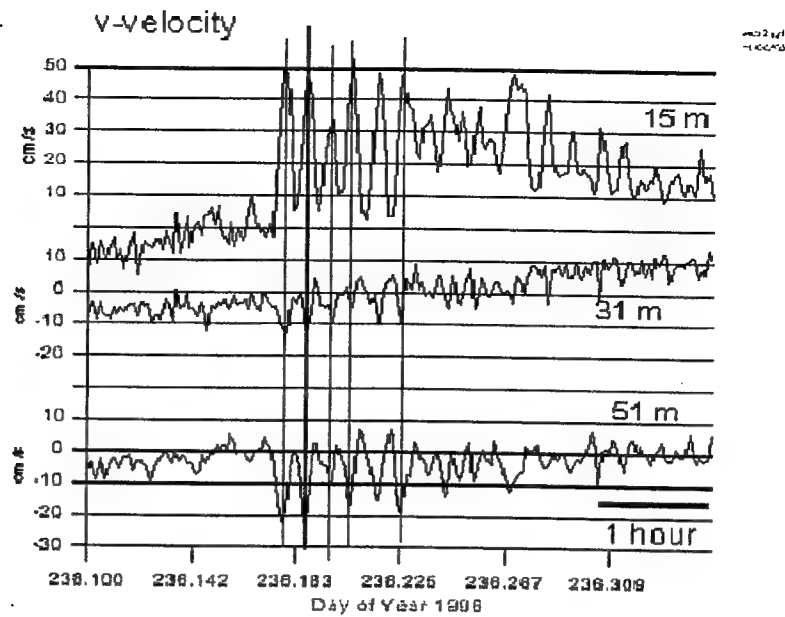
NIWs appear as high-frequency packets separated by about 12 hours during the first 2 days; the NIWs are nearly absent in the last 3 days. The background oceanic conditions do not change much during this time, but the NIW signal does.

Figure 1



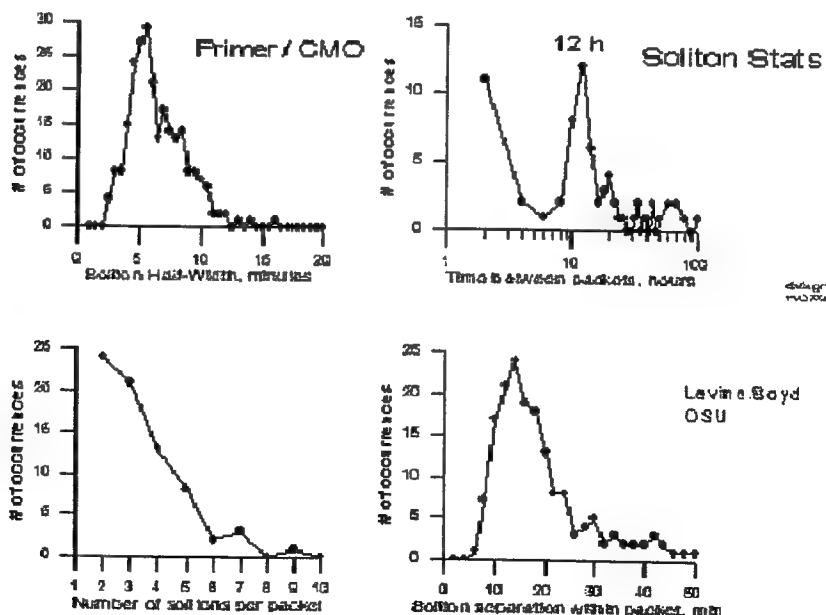
Expanding the time axis for one packet (Figure 2), we can see the packet is composed of 6 large "solitons". (Note: we use the term soliton here for convenience rather than to imply that these satisfy the precise fluid mechanical definition of soliton.) The velocity pulses are indeed significant, reaching 40 cm/s in the upper layer. The vertical structure is consistent with mode 1 behavior with a zero-crossing near 30 m depth. Each soliton has a temporal width of about 10 minutes. The corresponding temperature signal of this packet shows that the solitons are waves of depression with vertical displacements of up to 15 m.

Figure 2



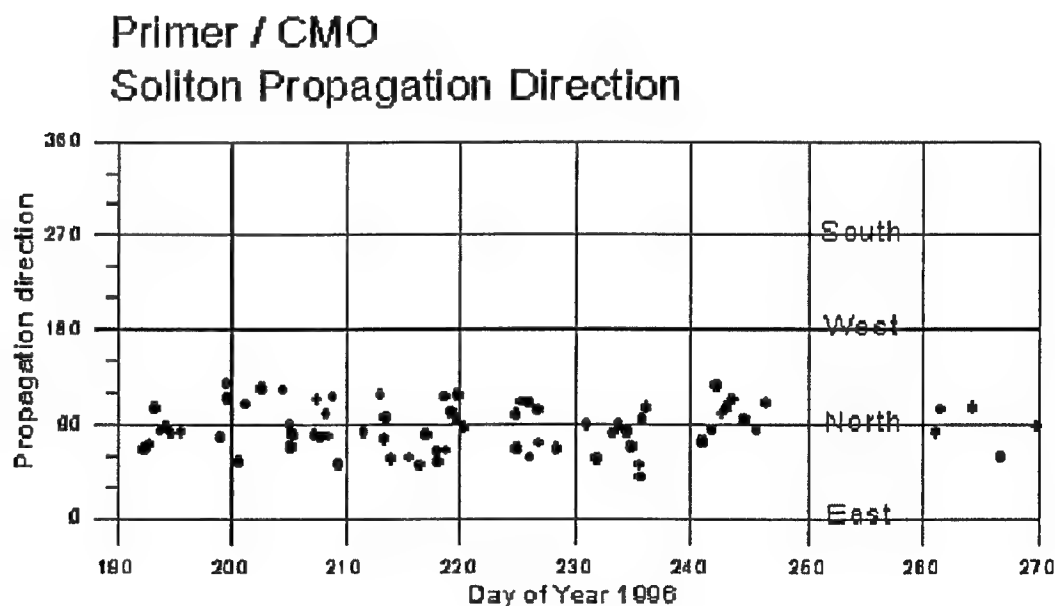
Despite the regularity of the barotropic tide, the characteristics of the NIWs vary in time. To summarize this variability, statistics were compiled of all packets that were observed during a 60 day period (Figure 3). These statistics are based on certain subjective criteria in defining a signal as a soliton. There are undoubtedly many less energetic NIWs that

Figure 3



escaped our census. Packets are most often separated by about 12 hours as expected for semidiurnal generation. However, there are often gaps in this regular generation, as seen in Figure 1, and the separation between packets is often longer than 12 hours. The number of solitons in a packet also varies-most packets contain only 2 or 3, and they are not always rank ordered. The temporal width of the individual solitons was peaked around 10 minutes, with a significant number that were "wider". No attempt has yet been made to account for the effect of the low frequency tidal flow on this estimate of width. The propagation direction (Figure 4) of the packets was determined by looking at the velocity in the upper layer. On average the waves were definitely propagating onshore (northward) perpendicular to the topography. However, there was a significant variability in the direction of +/- 45 degrees. Part of the explanation for the observed variability can be found by looking at SAR images taken during the observations. Rather than long-crested waves following the mean topography, the images indicate the wave packets are generated from many localized sources. The observed waves are then composed of a sum of interacting wave packets. This spatial complexity does not, however, explain the temporal variability. We suggest that the generation or propagation properties must be sensitive to subtle variations in the stratification, tidal amplitude, etc.

Figure 4



We have begun a study to determine the appropriate dynamics that are needed to describe these NIWs.

One approach is to estimate the magnitude of individual terms in equations that describe NIWs. For example, we can estimate the linear, nonlinear, and dispersive terms in the KdV equation and determine whether using such a description is meaningful. Our results on this study are not yet completed.

MIXING: *Important?*

To assess whether the NIWs are important to mixing, the cumulative horizontal kinetic energy (HKE) flux from these packets was estimated (Figure 5). Each dot represents the contribution to the flux from a packet of solitons. This estimate was based on estimating the HKE in the packet assuming a propagation speed of about 0.5 m/s. The average flux is about 11 W per meter of crest—the total energy flux (including potential energy) would be at least a factor of 2 higher.

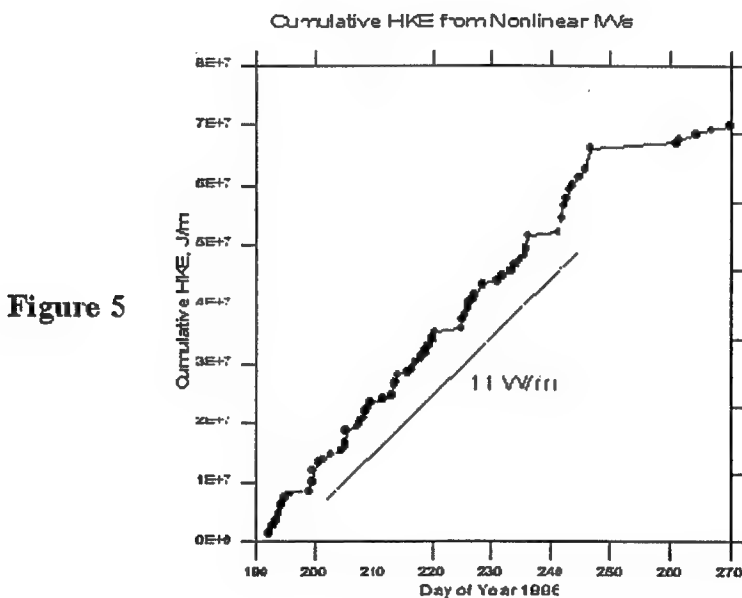


Figure 5

To determine if this flux is important to mixing, an estimate needs to be made of the distance over which these waves are dissipated. If they are gone after traveling 10 km, then the average dissipation would be $1 \times 10^{-3} \text{ W/m}^2$. This value is discounted if they travel farther. Most likely they do not propagate more than 50 km beyond the mooring. Is this a significant dissipation? As an internal wave enthusiast, it is tempting to compare with the internal wave energy in the deep ocean, as described by the Garrett-Munk spectrum. The value of $1 \times 10^{-3} \text{ W/m}^2$ is believed to be about the right order of magnitude of the energy flux through the internal wave field, dissipating the internal wave energy in 30 days. On the shelf the internal wave energy is about 10 times less, making $1 \times 10^{-3} \text{ W/m}^2$ dissipation relatively more important.

The importance to mixing depends upon just where and how the energy in the NIWs is lost. This is perhaps a topic for future study. Comparison with other shelf processes may provide some perspective. Hurricane Edouard passed the mooring site in September and mixed the water dramatically in about 6 hours. If the observed NIWs were to do this mixing, it would take 15 to 30 days!

A caveat on this energy flux estimate: only the "soliton" pulses were included. The lower frequency nonlinear internal tide may provide significant flux and should be counted as part of the NIW field.

CONCLUSIONS

Nonlinear Internal Waves are common enough to appear in observations around the world and have caught the attention of many varied disciplines. The answer to the question, *Why study these waves?*, will depend on the discipline responding, but two general answers are that they are *interesting* and *important*. Obviously they must be interesting, stimulating a great body of literature and generating conferences such as this one. As to importance, for physical oceanography mixing is one of the measures. They undoubtedly play an important role in specific regions at certain times, but the verdict is still out on their general importance to mixing on the shelf.

Internal Solitary Waves in the Western Tropical Pacific

Robert Pinkel

Marine Physical Laboratory
La Jolla, CA 92093-0213

From November 1992 through February 1993 a major air-sea interaction study was conducted in the western tropical pacific. Termed the Intensive Observation Period of the TOGA COARE experiment, the effort involved 15 ships, several aircraft and numerous land stations. The experiment was centered at 2°S, 156°E, in 2 km deep waters above the Ontong-Java Plateau.

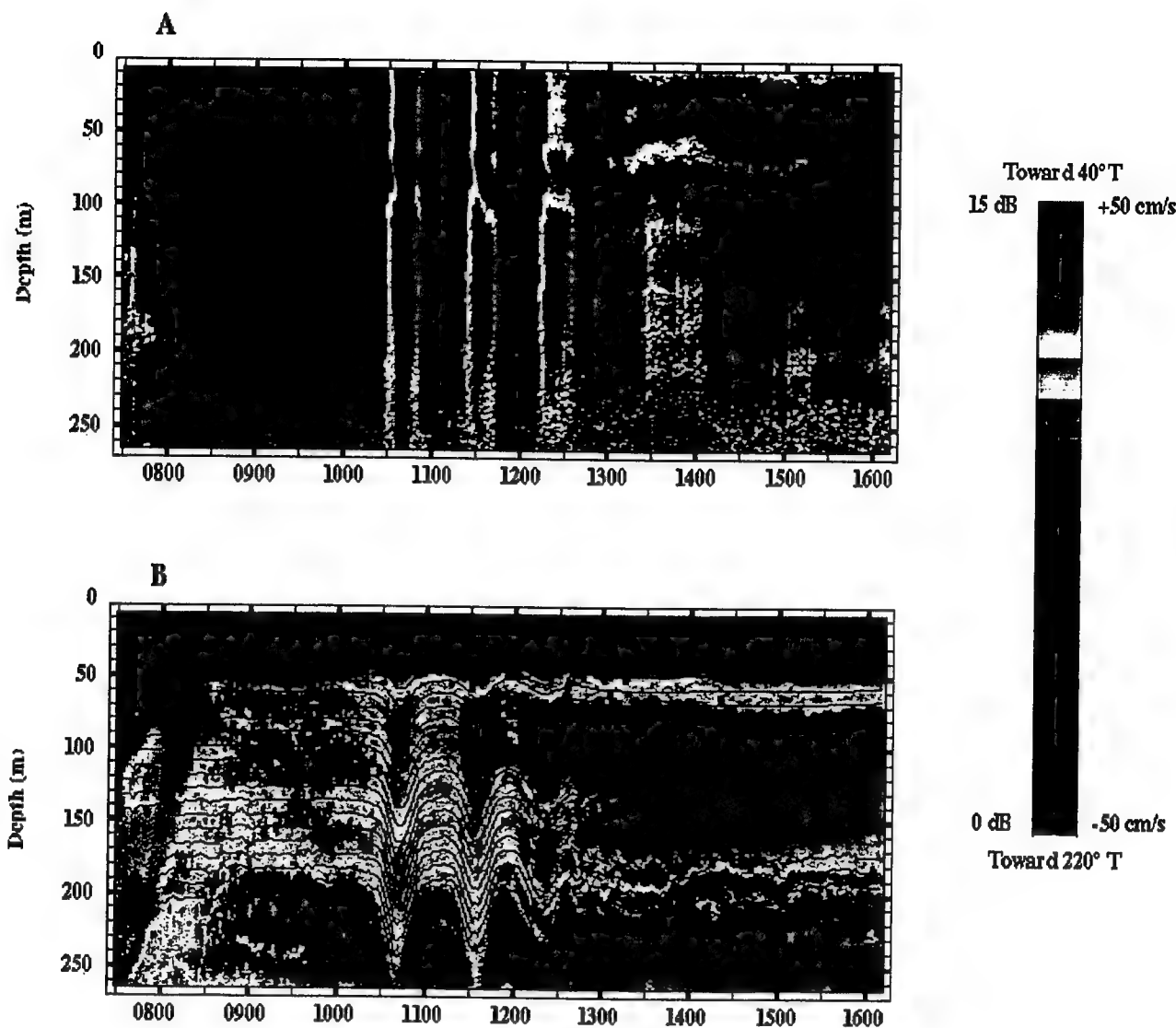
During the spring tides of late November, and early January, and early February, groups of internal solitary waves propagated through the COARE domain. They traveled north-eastward at 2.5 ms^{-1} , closely coupled with the semi-diurnal baroclinic tide. Peak amplitudes exceeded 60 m. Velocities in excess of 80 cm s^{-1} were seen (Figure A).

We report on observations made from the R.V. John Vickers (2°15'S, 156°E) using a vertically profiling coded pulse Doppler Sonar. 8 to 200-300 m, with 2.5 m depth resolution at 2 minute intervals.

The solitons are associated with the 5-7 largest crests of the Spring tides. They do not evolve from the spread of a tidally induced random disturbance, as in Massachusetts Bay (Haury, et al, 1988) or the Sulu Sea (Liu, et al., 1986). Rather, they appear phase-locked to the underlying tide. Aspects of classical solitary wave behavior, soli-bore behavior and parasitic instability are seen in the observations.

A surprising aspect of the observations is that there appears to be a critical threshold for the development of instability. The variation in astronomic forcing between the spring tides associated with soliton formation and those which did not develop solitons is only 10-20% (Feng et al., 1998). It might be that solitary wave behavior often develops but only after the tidal crests pass the COARE site.) In the absence of soliton-like instability, the underlying tide often has a highly skewed waveform. In one instance, a six-hour period cnoidal wave was observed.

The picture one gets of these instabilities is highly dependent on the sensor that is used. Vertical displacement measurements, fixed depth temperature measurements, etc., display the classical soliton signal. Horizontal velocity records, particularly in the mixed layer, emphasize the bore-like nature of the events. While the solitons are clearly mode-one disturbances, propagating at the phase speed of the mode-one tide, it is not clear that the vertical structure of the entire disturbance is well described by a mode-one wave function. Specifically, horizontal currents in the mixed layer seem to be exaggerated relative to deeper observations. This surface enhancement is associated with the bore-like aspect of the events.



UTC, Jan 11 1993

The two dimensional nature of motions, when coupled with the ability to measure absolute velocity (GPS), present a unique opportunity. The stream function of the flow can be inferred directly from the observations. Inferred streamlines are given in B. Jitter in the vertical displacement of the deep streamlines results from GPS error. The streamlines are plotted against a background of acoustic scattering intensity which has been corrected for inverse square spreading and attenuation. Observed vertical displacements of scattering layers are in agreement with the calculated streamline. Acoustic scattering strength increases in the core of the first soliton, decreases following its passage, and then increases with the passage of each subsequent crest. Evidence of increased scattering is present in all soliton observations, both day and night. Bragg scattering from micro-scale (.46 cm) fluctuations in the

sound speed (salinity) field is responsible for the increase.

The Richardson number perturbation associated with event passage can be inferred directly from the stream lines. It is, in fact, quite small. In the absence of pre-existing flows the solitons are capable of inducing instability in the weakly stratified region of the lower mixed layer, but not in the thermocline. However, the strong ambient shears associated with the equatorial current system are always near instability. The solitons are effective triggers of instability for these marginally critical flows.

INTERNAL WAVE INDUCED VARIABILITY IN THE VICINITY OF STEEP ISLAND FLANKS

Dr. Dayananda Vithanage, P.E.

Dr. Patrick K. Sullivan, P.E.

Oceanit Laboratories, Inc.

Honolulu, HI

BACKGROUND

Municipal wastewater has density characteristics similar to fresh water. Therefore, in a homogeneous ocean the waste field will always rise to the surface. However, under adequately stratified conditions, effluent surfacing is suppressed. Variability of water density and velocity profiles in relatively shallow depths strongly influence wastewater discharge outfall design. Degree of density stratification and ambient currents are major factors that determine the extent of wastewater dilution during the buoyancy phase (initial or near-field dilution) as well as the equilibrium depth of the waste field.

In order to investigate variability of parameters due to internal wave effects in the vicinity of steep slopes and their influence on mixing and dispersion, an experiment funded by the Office of Naval Research was conducted adjacent to an ocean wastewater outfall in Mamala Bay, Oahu, Hawaii. The site is located on the south shore of Oahu approximately 2 miles offshore at a water depth of 230 feet. Wastewater is released at an average rate of 75 million gallons per day (mgd) through a diffuser approximately 1400 feet long. The dispersion characteristics and the fate of the wastewater after discharge is of great importance because of extensive coral reefs in the nearshore area and relative proximity of the outfall to popular recreational beaches. The study location is shown in Figure 1.

MEASUREMENTS

A thermistor string with 14 thermistors at 10-foot intervals and a downward-looking Acoustic Doppler Current Profiler (ADCP) were moored at a site close to the outfall diffuser at a depth of 200 feet. The measurement profile was designed to sample both temperature and velocity from 50 feet below the surface to the bottom to avoid navigational hazards. Velocity and temperature profiles were measured at one-minute intervals. Data were downloaded monthly from loggers; conductivity and temperature profiles were measured monthly at the site using a Seabird CTD profiler to supplement data and to check for possible drift in thermistor measurements.

DATA ANALYSIS

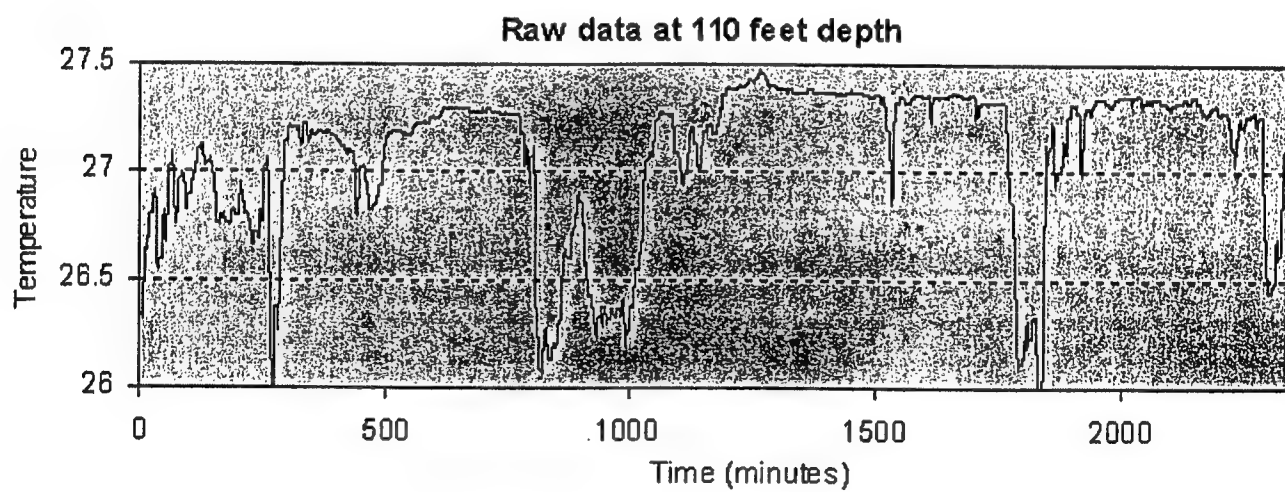
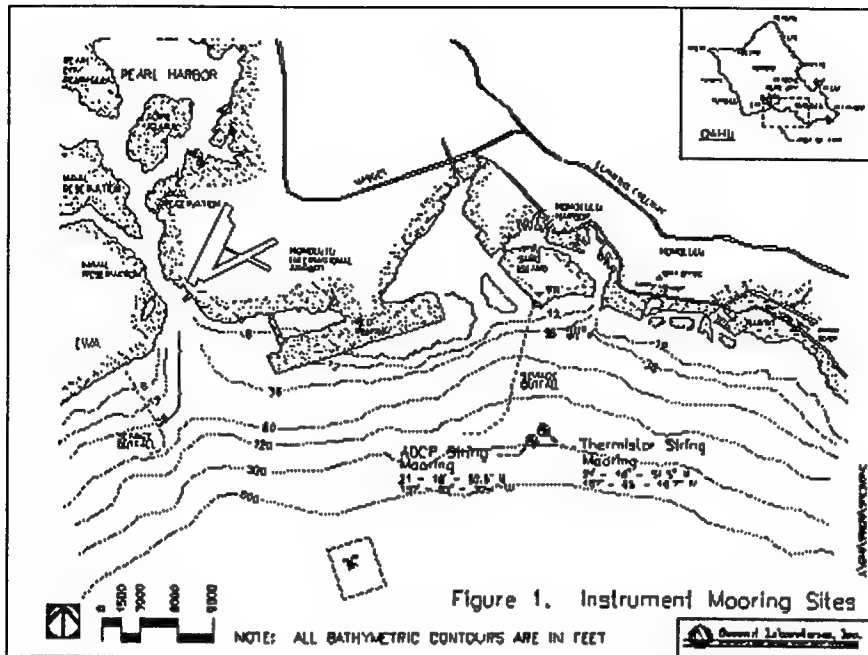
Temperature and velocity data were used to investigate wastewater dilution and plume equilibrium depths. In

addition, statistics for all data sets were calculated. In order to investigate high frequency variability, one-hour segments of data were analyzed for variance. Hourly calculated variances at all depths were averaged. Average temperature variance distribution for September 1997 are shown in Figure 3.

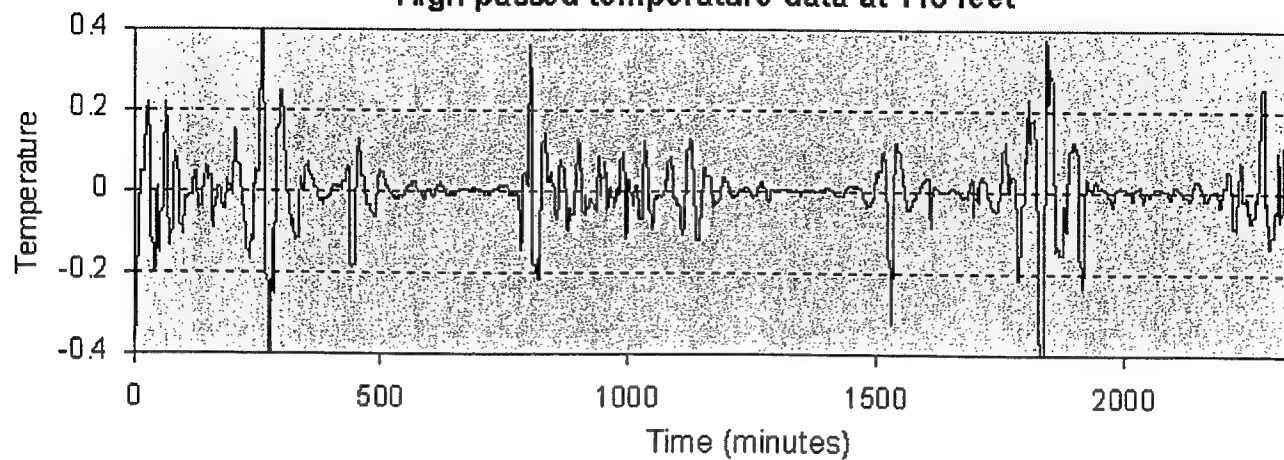
The data was high passed to filter out low frequency phenomena that dominated the raw data. A Fourier filter with a cut off at 60 minutes was used for this purpose. A cosine taper was used at the cut off to reduce data contamination. The high passed temperature data had a weak periodicity at about 40 minutes. High passed data was demodulated at a period of 40 minutes to remove noise. The original data, high passed data and demodulated high passed data are shown in Figure 2. Spectral density of high passed data at different depths was calculated using a data length of 256. The spectral density distribution of high frequency temperature data over the depth for the month of September 1997 is shown in Figure 4.

OUTSTANDING QUESTIONS

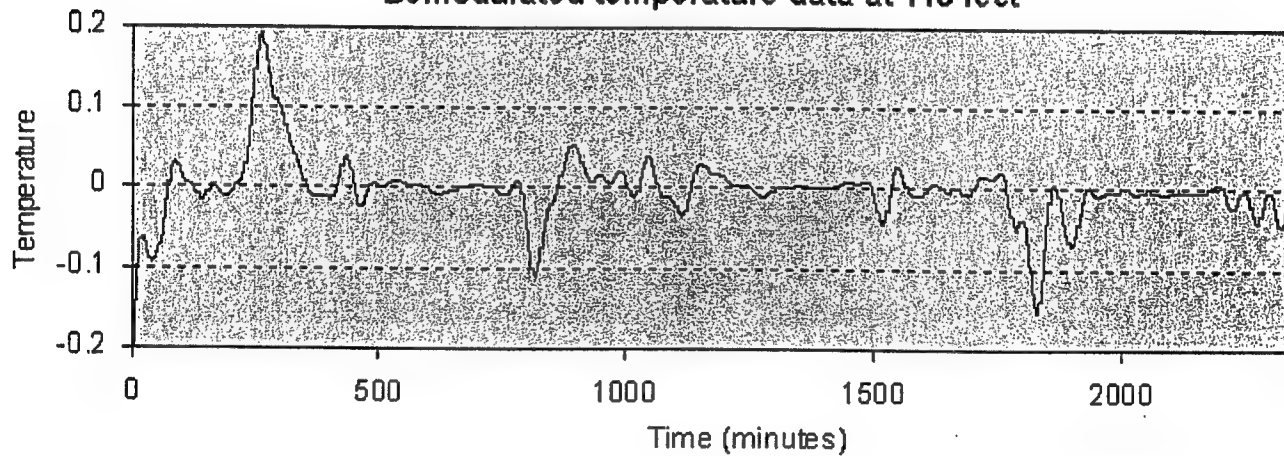
1. Raw temperature data shows sudden changes at approximately tidal periods. High passed data shows high perturbations when this occurs. These perturbations show a periodicity of about 40 minutes and die off gradually, until excited again by a sudden temperature change. Could the perturbations be due to solitons associated with tides? If these are solitons, are they produced by the interaction of the tide with the island flank?
2. High passed data show high energy at about 0.0234 cycles per minute (43 minutes). The phenomena are intermittent and there are periods of no activity in between. Is this related to the amplitude of the surface tide?
3. Similar high energy density is seen at the same frequency for all components of velocity. Could this be due to resonance of an internal wave with the bottom slope?



High passed temperature data at 110 feet



Demodulated temperature data at 110 feet



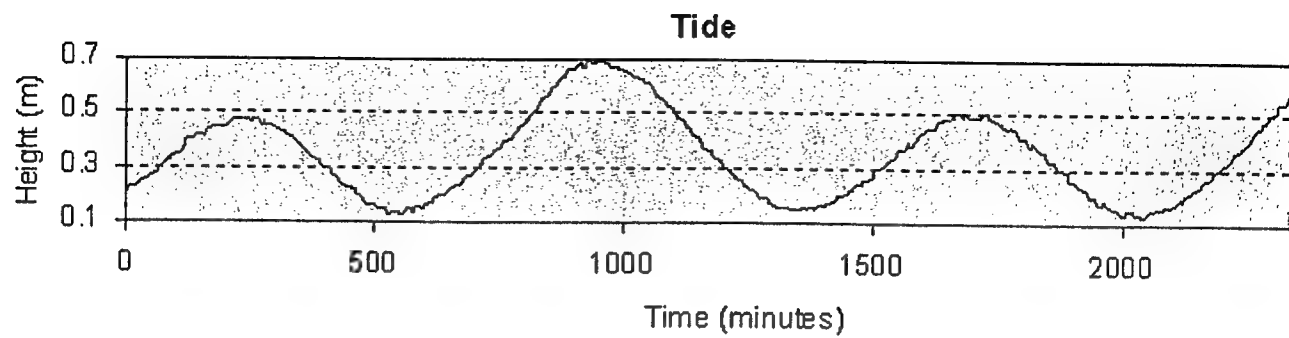


Figure 2. Time series of raw data, high passed data, demodulated high pass data (0.0234cpm) for temperature at 110 feet depth, and surface tide.

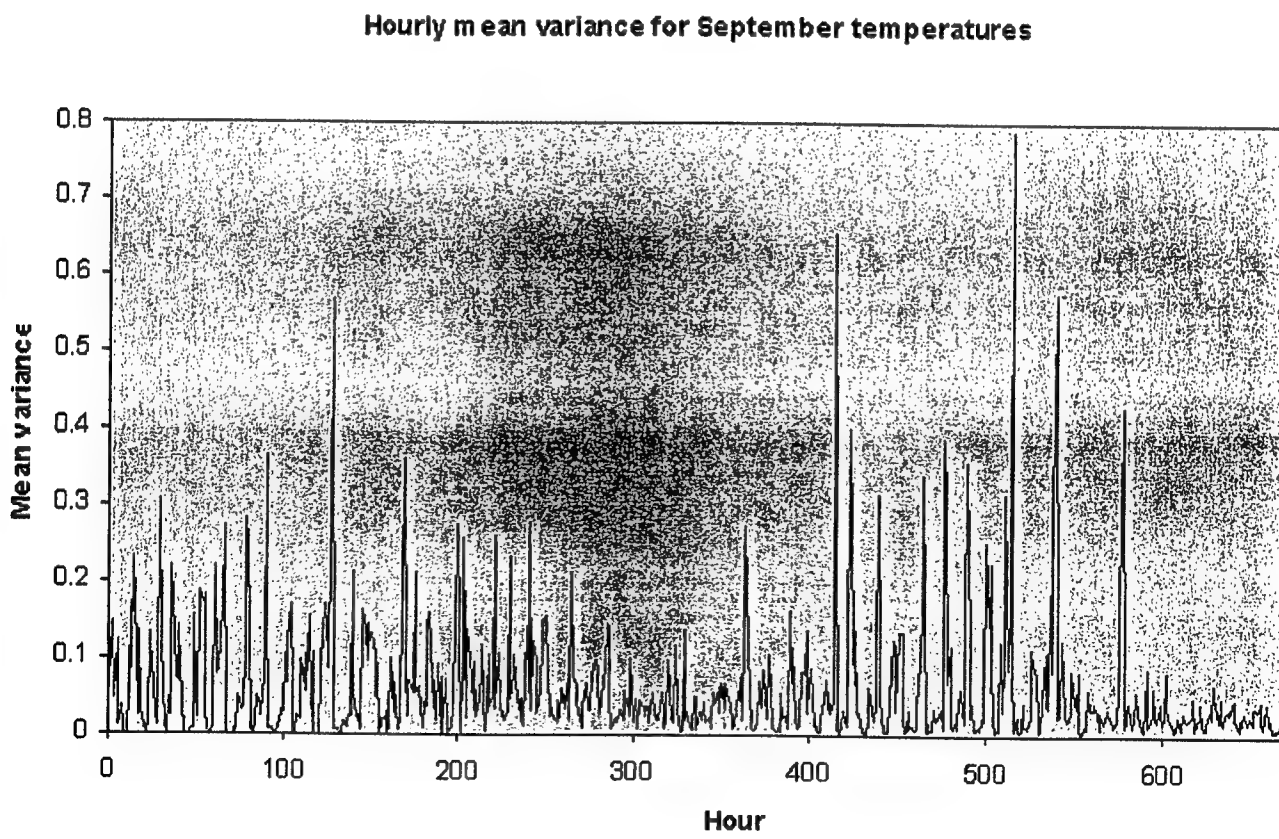


Figure 3. Average hourly variance of Temperature for September 1997.

September temperature high-pass spectra

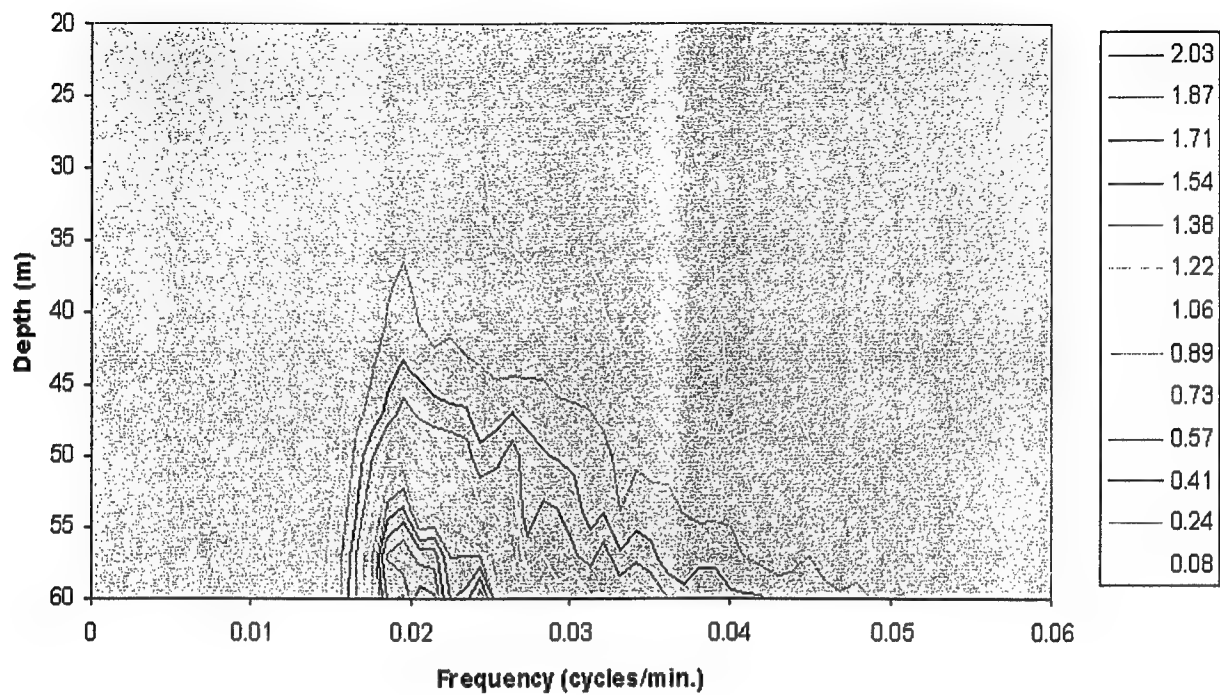


Figure 4. High frequency spectral density distribution over depth.

A study of dissipative, shoaling high-frequency internal waves in shallow water

James Lerczak, Clinton Winant and Myrl Hendershott

Scripps Institution of Oceanography, CCS 0209

University of California at San Diego

La Jolla, California 92093-0209

<http://www-ccs.ucsd.edu/iwaves/>

The evolution of shoreward propagating, high-frequency, mode one internal waves was studied in a nearshore region where water depths ranged from 30 to 15 m. The data for this study were obtained from upward-looking acoustic doppler current profilers (ADCPs) deployed off of Mission Beach, California in 1996 and 1997 (Table 1). The ADCPs were rigidly mounted on the bottom, allowing vertical velocities to be unambiguously distinguished from the more energetic horizontal velocities. The bathymetry was approximately planar, with an onshore bottom slope, α , of approximately 0.01. Data were analyzed over the period 26 September to 23 October (26.2 days) in 1996 and 4 September to 18 October (44.0 days) in 1997.

Ten frequency bands, having equal widths on a logarithmic scale, between 0.0167 and 0.3 cycles per minute ($T = 60$ to 3.33 min) were studied. Within this range, coherences between vertical velocity, w , and horizontal velocities, \vec{u} , were high. This range contained approximately 80% of the mid-depth w signal variance. The

ADCP signal to noise variance ratio was approximately 20, where the noise level was estimated to be the high-frequency noise floor of w . Vertical velocities were studied because, when measured from a stable platform, they are a very sensitive index of high-frequency internal wave variability (Marsden *et al.*, 1994), and are less likely to be contaminated by other dynamics, such as barotropic eddies, than horizontal velocities. While w of long-wavelength waves is much weaker than \vec{u} , the maxima of \vec{u} of mode one waves occur near the surface and near the bottom. These regions of the water column were not well-covered by the ADCPs, which sampled the center 67 to 75% of the water column. In contrast, the single maximum of w of mode one waves occurs near the thermocline. This maximum was always detected by the ADCPs.

To isolate the mode one internal wave variability, the vertical velocities at each mooring were decomposed into complex empirical orthogonal functions (cEOFs) (Wallace and Dickinson, 1972) within each of the ten frequency bands for consecutive blocks of data 2^{12} minutes (2.84 days) in duration. Some of the results of the cEOF analysis are briefly summarized here. From 70 to 90% of the variance in each band was explained by the first cEOF mode, \hat{w}_1 , indicating the high frequency wavefield was dominated by mode one waves.

The vertical structure of \hat{w}_1 was consistent with mode one waves, having a single, mid-column maximum.

The average depth of this maximum varied approximately linearly from 7 to 12.5 m as water depth changed from 15 to 30 m. The relative phases between \hat{w}_1 and horizontal velocities in the upper and lower water

column were consistent with onshore propagation (\vec{u} leading w by 90° near the surface, and lagging w by 90° near the bottom). The square of the ratio of major to minor axis horizontal velocities coherent with \hat{w}_1

(ellipticity) was as high as 16, and major axis angles were nearly cross-isobath, consistent with uni-directional, cross-isobath propagating waves.

The variance of the amplitude of \hat{w}_1 as a function of frequency and water depth was calculated. For linear waves, this variance is an estimate of $\frac{1}{2} \langle w_0(\sigma)^2 \rangle$, where $w_0(\sigma)$ is the vertical velocity amplitude of the mode one internal wave at the depth of maximum variance within the frequency band σ . Since cEOFs were estimated for consecutive ensembles of length 2.84 days, a smoothed time series of the internal wave variance, summed over the frequency range, was obtained (Fig. 1). The time series were quite coherent from mooring to mooring, and the variance clearly decreased with decreasing water depth. The frequency spectra of cEOF amplitude at each mooring had a peak at approximately 0.11 cpm ($T = 9$ min) (Fig. 2). The amplitude of this peak decreased with decreasing water depth, however, there was no obvious frequency shift in the peak or change in the spectral shape. The variance, summed over the frequency range, and averaged over ensembles, decreased nearly monotonically with decreasing water depth (Fig. 3).

This decrease is well described by a simple shoaling model with linear dissipation in which, for time independent propagation of waves up a beach with constant slope, α , the divergence of the energy flux is balanced by dissipation. Thus

$$\frac{D_g}{Dt} E = -rE \quad (1)$$

in which E is the depth-integrated, time-averaged energy density, and the substantial derivative is taken in a frame moving at the waves group velocity, c_g , so that

$$\frac{d}{dx} c_g E = -rE \quad (2)$$

For a fluid with constant stratification, the amplitude, $w_0(\sigma, D)$, of the wave consequently varies with water depth according to

$$\frac{w_0(\sigma, D)}{w_0(\sigma, D_0)} = \left[\frac{D}{D_0} \right]^\gamma, \quad \gamma = \frac{r\pi N^2}{2\alpha(N^2 - \sigma^2)^{3/2}} - 1 \quad (3)$$

where N is the buoyancy frequency of the fluid. For inviscid propagation ($r = 0$), the amplitude is inversely proportional to water depth. The variance would then increase by a factor of 4, as a wave propagates from a water depth of 30 m to 15 m. This was clearly not observed in our data. When linear dissipation is included in the model, the amplitude may increase or decrease as the wave shoals, depending on the size of r . We estimate r by minimizing the mean square error between the observed variance at each depth, and the estimated variance using the above shoaling model, the spectrum at 30 m (Fig. 2), and an assumed buoyancy frequency of 0.263 cpm obtained from the estimated long-wave phase speed at different water depths (

$c_p \approx \frac{\pi N}{D}$). The resulting estimates for r were 2.0×10^{-4} and $1.6 \times 10^{-4} \text{ s}^{-1}$ for 1996 and 1997, respectively.

These values correspond to decay time scales of 1.4 and 1.8 hours, respectively, which are comparable to the typical time (~ 3 hours) it takes a wave packet to pass from the 30 m to the 15 m moorings (cross-shore distance = 1.5 km). Such time scales are consonant with those use by Pringle and Brink, in prep., in somewhat deeper water depths.

- [Bibliography, Table and Figures](#)
- [About this document ...](#)

[Next](#) | [Up](#) | [Previous](#)

[Next: Bibliography, Table and Figures](#)

1998-09-08

Bibliography

- 1 Marsden, R. F., R. Paquet, and R. G. Ingram. 1994. Currents under land-fast ice in the Canadian Arctic Archipelago Part 1: Vertical velocities. *J. Mar. Res.* 52:1017-1036.
- 2 Pringle, J. M., and K. H. Brink. In prep. High frequency internal waves on a sloping shelf.
- 3 Wallace, J. M., and R. E. Dickinson. 1972. Empirical orthogonal representation of time series in the frequency domain. Part I: Theoretical considerations. *J. App. Met.* 11:887-900.

Table 1: Cross-shore array configuration and ADCP parameters for the 1996 and 1997 data analyzed in this study.

D (m)	1996					1997				
	vert. res. (m)	x-shore dist. (m)	sample time (min)	pings per sample	freq. (kHz)	vert. res. (m)	x-shore dist. (m)	sample time (min)	pings per sample	freq. (kHz)
30	2	0	1	30	300	2	0	1	107	300
27.5	2	250	1	30	300					
25	2	500	1	30	300	2	500	1	111	300
22.5	2	750	1	30	300					
20	2	1000	1	30	300	1	1000	2	260	300
17.5	2	1250	1	30	300					
15	1	1500	1	30	1200					

Figure 1: Variance of the mode one vertical velocity cEOF amplitude, effectively the variance of mode one internal wave vertical velocity at the depth of maximum variance, at the ADCP stations of Table 1. In 1996, the variance was summed over all ten frequency bands within the range 0.0167 to 0.3 cpm. In 1997, the tenth band (0.225 to 0.3 cpm) was left out, because the Nyquist frequency for the 20 m ADCP (0.25 cpm) was within this band. At each station, the vertical velocity time series were broken into blocks of length 2^{12} min (2.84 days), and cEOFs are calculated separately for each block. The plots show the variance estimated for each time block.

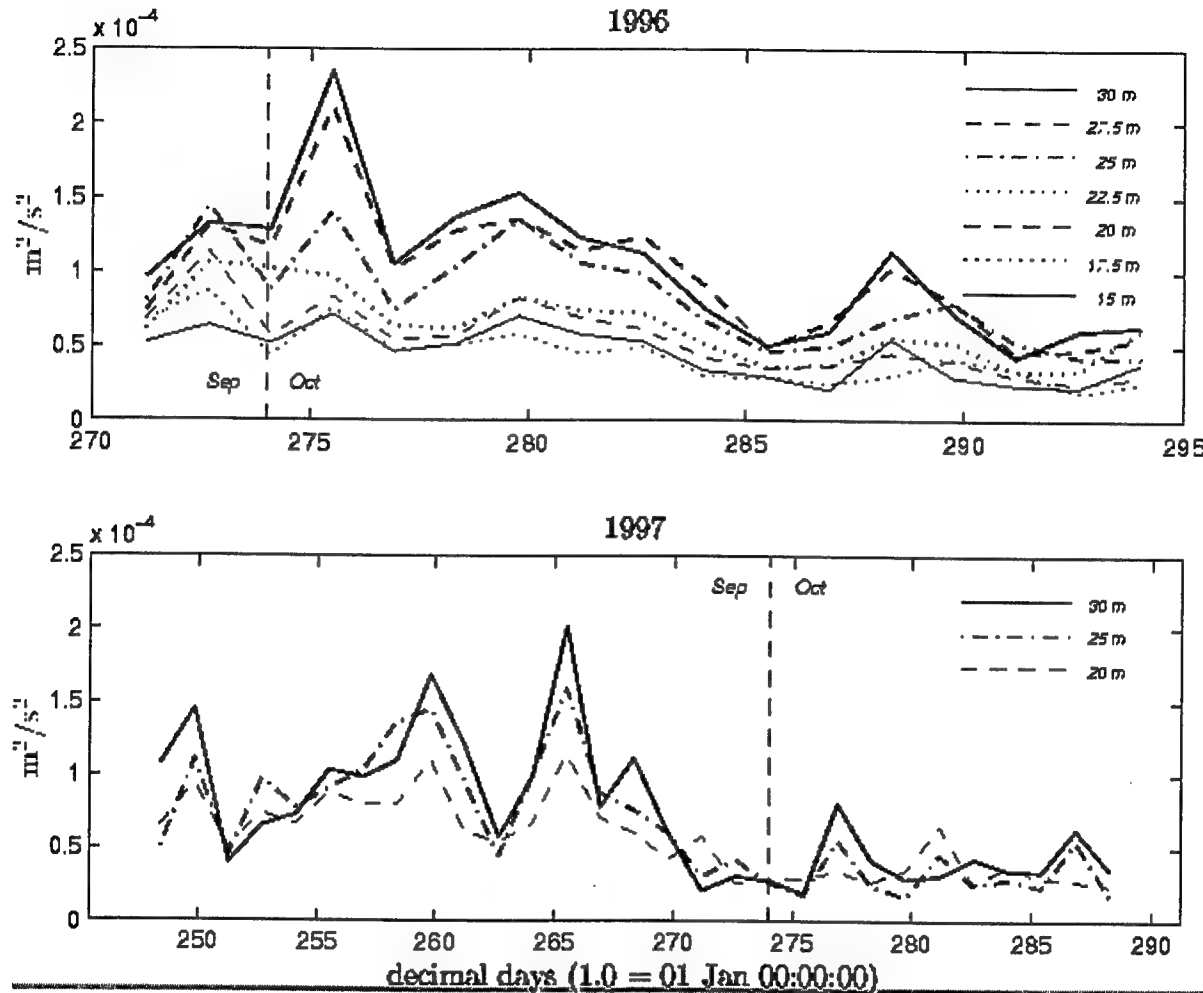


Figure 2: Variance preserving power spectra of the mode one vertical velocity cEOF amplitude for the stations of Table 1. The vertical dashed lines mark the range of frequencies analyzed in this study (0.0167 to 0.3 cpm). For the 1996 data, all ten frequency bands were analyzed. For the 1997 data, the highest frequency band (0.225 to 0.3 cpm) was not analyzed, because the Nyquist frequency for the 20 m ADCP (0.25 cpm) was within this band.

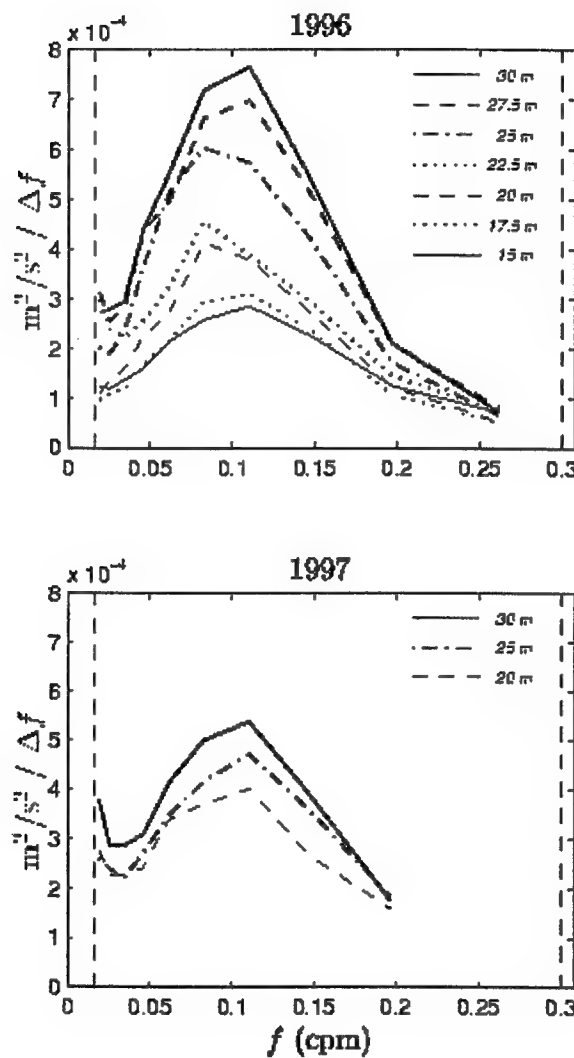
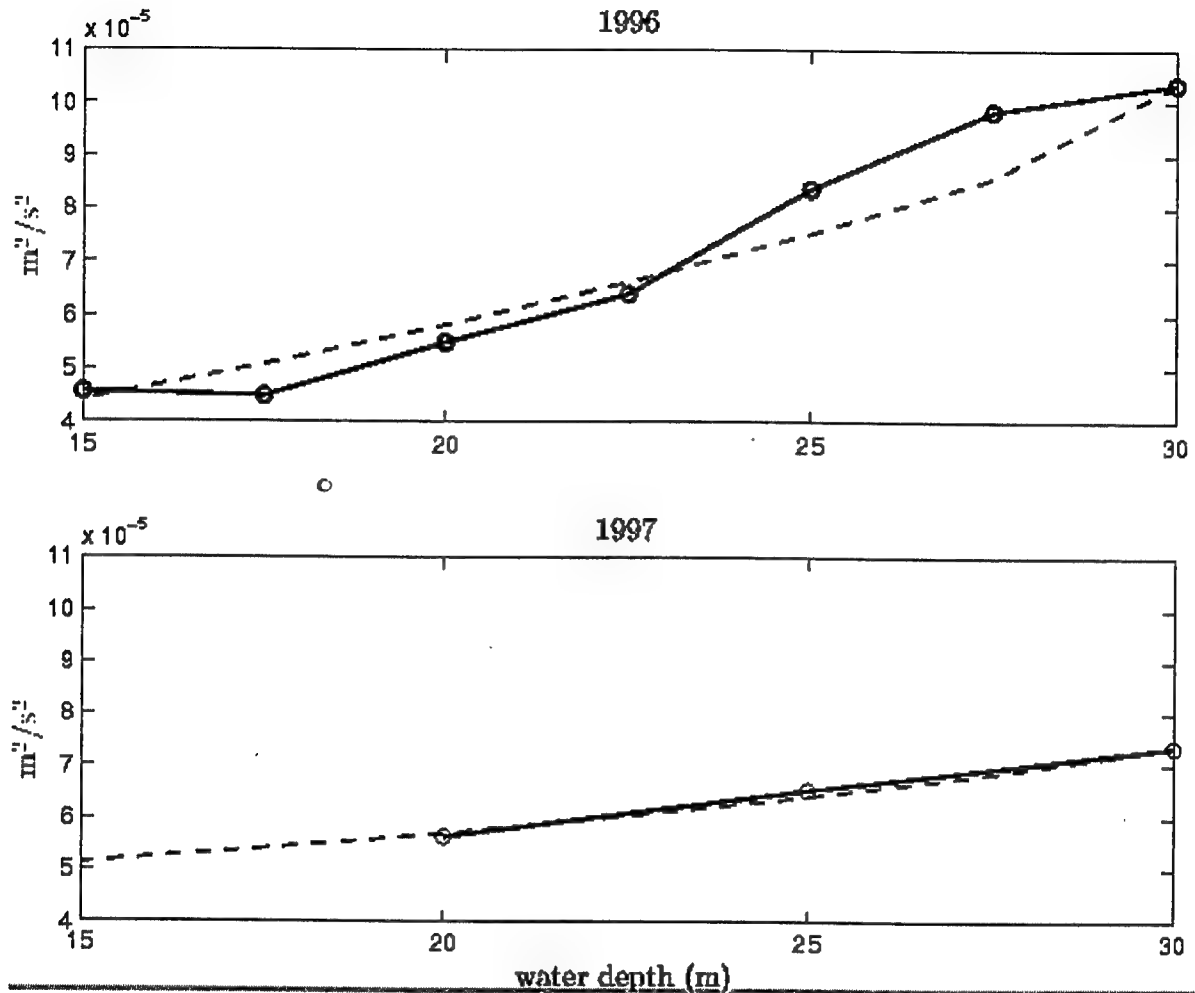


Figure 3: Variance of the mode one vertical velocity cEOF at the depth of maximum variance. In 1996, the variance was summed over all ten frequency bands within the range 0.0167 to 0.3 cpm. In 1997, the tenth band (0.225 to 0.3 cpm) was left out, because the Nyquist frequency for the 20 m ADCP (0.25 cpm) was within this band. The variance was averaged over the duration of the analysis period in both years. The dashed lines are estimated variances using the shoaling model described in the text, an assumed buoyancy frequency of 0.263 cpm, and a dissipation constant, r of $2.0 \times 10^{-4} \text{ s}^{-1}$ in 1996 and $1.6 \times 10^{-4} \text{ s}^{-1}$ in 1997.



[\[Next\]](#) [\[Up\]](#) [\[Previous\]](#)

Next: [About this document ...](#) Up: [No Title](#) Previous: [No Title](#)

1998-09-08

Turbulent Mixing in Solitons

Neil S. Oakey and Norman A. Cochrane

Ocean Sciences Division
Bedford Institute of Oceanography
Department of Fisheries and Oceans
Dartmouth, Nova Scotia, Canada B2Y4H2

Abstract

Simultaneous measurements of microstructure and acoustic backscatter in a packet of mixing solitary waves indicate that the intensity of acoustic backscatter is related to the level of turbulent mixing. We have tested our data with the simple model of Thorpe and Brubaker and found that it is consistent with this formulation.

Introduction

Solitons or packets of solitary waves are generated in many places but in particular on the Scotian shelf in a region called "The Gulley" near Sable Island it has been easy to predict their generation time and to find them. Essentially at each tidal cycle when the tides are high enough, solitons are generated at the shelf break. Since in very simple terms the development of the internal tide in a modal sense is primarily first mode the development of an appropriate density structure is also necessary. Enhanced mixing associated with these packets has been postulated as a mechanism (Sandstrom, Elliott and Cochrane, 1989) for enhanced nutrient supply and coincident higher biological productivity.

In 1987 we did a short study of Solitons using BATFISH, CTDs, a microstructure profiler (EPSONDE) (Oakey, 1988) and acoustic backscatter instruments. The area was surveyed with BATFISH at the correct time and place to observe solitons until we had fine-tuned our ability to predict exactly where and when to find them. We set up our sampling instruments on the ship to sample the solitary wave packet, as it arrived and passed under us, with a multi-frequency acoustic array and with EPSONDE.

In the paper we will ask the following questions:

- Are turbulence and acoustic backscatter well correlated in the solitons?
- Are simple models such as the ones described by Thorpe and Brubaker able to describe the acoustic backscatter in terms of the turbulent properties?

Turbulence and Acoustic Backscatter Models

One sees acoustic echoes from a variety of scatterers in the ocean including biological, bubbles and temperature and salinity microstructure. There is a problem in calibration acoustic backscatter intensity in terms of the processes causing it. In the absence of competing processes a particular process such as turbulence may give the largest signal. The soliton provides this special laboratory.

Thorpe and Brubaker (1983) devised a model to describe the acoustic backscatter in terms of the turbulent temperature and velocity field. They derived an equation to describe the backscatter as follows

$$\sigma(k) = -\frac{1}{8} \pi k^3 \frac{d}{dk} (k^{-2} S_g) \left(\frac{1}{C} \frac{dC}{d\theta} \right)^2 \quad (1)$$

evaluated at $k = 2\pi/\lambda$ (Munk and Garrett, 1973) where λ is the sonar wavelength and C is the speed of sound. At 120 kHz, λ is 1.3 cm. For isotropic turbulence the Batchelor spectrum is

$$S_g = \left(\frac{q}{2} \right) \frac{\chi}{k_s D} f(\alpha) \quad (2)$$

where the Batchelor universal form is given by

$$f(\alpha) = \alpha \left\{ \exp \left(-\frac{\alpha^2}{2} \right) - \alpha \left(\frac{\pi}{2} \right)^{1/2} \operatorname{erfc} \left(\frac{\alpha}{\sqrt{2}} \right) \right\} \quad (3)$$

The Batchelor wavenumber is $k_s = (\epsilon/vD^2)^{1/4}$ and $\alpha = \frac{k}{k_s} (2q)^{1/4}$ where $q = 3.9$. Evaluating this at $k = 2\pi/\lambda$ gives

$$\sigma(k) = \frac{\chi \lambda}{64 D} \alpha^2 \exp \left(-\frac{\alpha^2}{2} \right) \left(\frac{1}{C} \frac{dC}{d\theta} \right)^2 \quad (4)$$

where

$$\alpha^2 = \frac{32}{\lambda^2} \pi^2 q \left(\frac{vD^2}{\epsilon} \right)^{1/4} \quad (5)$$

This is typically presented as

$$S_\nu = 10 \log(\sigma(k)/4\pi) \quad (6)$$

expressed ad dB. Typical values are $D = 1.4 \times 10^{-7}$ m²/s and $\nu = 1.4 \times 10^{-4}$ m²/s with $\frac{1}{C} \frac{dC}{d\theta} = 1.6 \times 10^{-3}$ K-1. To put the scales into context, λ at 50 kHz is 3cm and at 120 kHz is 1.3cm. By comparison to the Batchelor cut-off scale $\lambda_s = 2\pi(vD^2/\epsilon)^{1/4}$ is about 0.81 cm and the turbulence viscous cut-off scale $\lambda_\nu = 2\pi(\nu^3/\epsilon)^{1/4}$ is about 2.7 cm for dissipation $\epsilon = 1.0 \times 10^{-8}$ W/kg, remembering that the peak in the dissipation spectrum is at a length scale about a factor of three larger. This means that the overlap in scales of the turbulence and acoustic backscatter overlap well at these scales.

Experimental Setup

The experimental site was on the Scotian Shelf Northeast of Sable Island in a region called "The Gulley" (44°10' N, 58°50' W). The area was surveyed using the BATFISH and CTD Tow YO's to determine accurately when and where the solitons were being generated in respect to a tidal reference (high tide at

Halifax). The measurement strategy, which worked reasonably well, was to position the ship where we expected to see the soliton packet and shortly before its predicted arrival and set up our EPSONDE and the Multi-Frequency Acoustic Array. Using such things as the ship radar backscatter to see the surface expression of the Solitons (the surface roughness using long band radar) we were able to confirm the arrival of a soliton packet and initialize sampling. Both acoustic data and microstructure data were recorded on board simultaneously but not on the same computers. The clocks were synchronized to about 1 second. One second represents about 0.7 meters vertically for EPSONDE and about 0.5 meters horizontally for the internal wave. Patches of turbulence may be only a few meters thick. The simultaneity in space and time was a critically important sampling problem. Because EPSONDE is a tethered free-fall vehicle it may be some 10's of meters separated from the region sampled by the acoustic system which also complicates the notion of simultaneity. After the soliton packet had passed we moved the ship and set up further onshore to wait for another look at the same soliton packet. This was done to try and determine the change in the soliton structure as well as the change in turbulence and acoustic backscatter as the packet moved on the shelf.

Microstructure Measurements

EPSONDE was used in a total of 12 stations including over 200 profiles to depths of about 50 m to obtain velocity and temperature microstructure simultaneously with the acoustic backscatter data. Data were logged on a PC computer. Fifty meter profiles were obtained at intervals as short as 2 minutes. In one instance the ship drifted at a similar speed and direction as the soliton so sampling continued over a period of two hours before the solitary wave packet had passed below the ship. Temperature, temperature microstructure and dissipation profiles were obtained using standard analysis techniques (Oakey, 1982). The depth of an isotherm clearly showed the movement of the base of the mixed layer by the soliton (Sandstrom and Oakey, 1995). The measure of temperature variance, χ_0 , and the dissipation, ε , were both seen to be stronger at the interface where mixing was being caused by the shear in the soliton.

Acoustic Backscatter Measurements

Acoustic backscatter signals were logged simultaneously at frequencies of 12, 50.5, 121 and 250 kHz concurrent with repetitive EPSONDE casts. Demodulated signal envelopes furnished by two DATASONICS DFT-210 dual-channel acoustic transceivers were individually digitized at 5kHz every 2 seconds and logged to tape on a computer. The 12 kHz transducer was the ship's keel transducer and the three higher frequency channels utilized transducers lowered over the side in a weighted "Bucket" to about 6 meters depth in order to minimize near surface bubble attenuation. A selected signal was displayed in real-time on a gray scale recorder at one transmission per second. A failed preamplifier in the 200 kHz channel limited useful data in this channel to a few high signal amplitude events. Intermittent operation of the 120 kHz channel was also experienced but most of the collected data was unaffected. The three high frequency channels were calibrated pre-cruise at BIO. The 12 kHz channel was calibrated at sea by suspending an air filled spherical target (ping-pong ball) beneath the keel axis on a 2-point monofilament suspension.

Data Analysis

The EPSONDE data were analyzed to obtain σ and χ_s estimates using standard spectral analysis techniques (Oakey, 1982). Data were analyzed to give microstructure profiles in 2 second (about 1.4 meter) segments. To merge the data with the acoustic data, profile start times were carefully checked. Acoustic data from the different transducers was analyzed to give profiles of backscatter strength averaged over 20 seconds and 1 meter vertical bins. It was later smoothed to 1 minute when merged with the microstructure data.

Using the Thorpe-Brubaker model the microstructure data were used to calculate a "Microstructure Backscatter", σ_{ws} , and these data were merged in space and time with the measured "Acoustic Backscatter", σ_a .

Each data point represents about 3 meters in the vertical and 3 seconds? acoustic average. For each box a point could be plotted on a regression curve. This produced a scatter of points to which regression statistics could be done. Data from all runs combined to give composite pictures are summarized using box and whisker plots in Figure 1 for 50.5 kHz and in Figure 2 for 121 kHz.

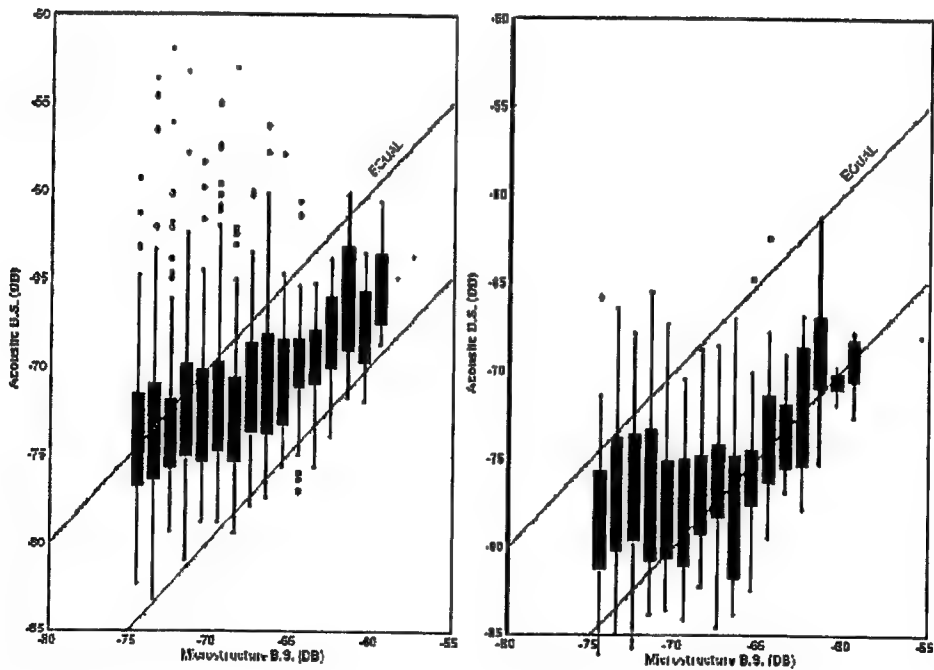


Figure 1: Measured acoustic backscatter intensity is plotted versus the inferred microstructure backscatter intensity for 50.5 kHz on the left and 121 kHz on the right.

Discussion of Results

From Figure 1 and Figure 2 there is a clear relationship between σ_{bs} and the corresponding σ_A . For the 50 kHz data all of the runs were combined and they result in a regression plot with a large scatter. There appears to be a reasonable correlation. The acoustic backscatter data are less than that predicted from the Thorpe-Brubaker theory; about 7dB less at 50 kHz and about 10 dB less at 120 kHz. There is less scatter at 120 kHz than at 50 kHz. There is a large excess of high acoustic scatterers that are probably biological in origin.

References:

Sandstrom, H, and N.S. Oakey, 1995: Dissipation in Internal Tides and Solitary Waves. *J. Phys. Oceanogr.*, 25, 604-614.

Munk, W. and C.J. Garrett, 1973: Internal Wave Breaking and Microstructure (the chicken and the egg), *Boundary Layer Meteorology*, 4, 37-45.

Oakey, N.S., 1982: Determination of the Rate of Dissipation of Turbulent Energy from Simultaneous Temperature and Velocity Shear Microstructure Measurements. *J. Phys. Oceanogr.* 12, 256-271.

Oakey, N.S., 1988: EPSONDE: An Instrument to Measure Turbulence in the Deep Ocean, *IEEE Journal of Oceanic Engineering*, 13, 124-128.

Sandstrom, H., J.A. Elliott and N.A. Cochrane, 1989: Observing Groups of Solitary Internal Waves and Turbulence with BATFISH and Echo-Sounder, *J. Phys. Oceanogr.*, 19, 987-997.

Thorpe, S.A. and J.M. Brubaker, 1983: Observations of Sound Reflection by Temperature Microstructure, *Limnology and Oceanography*, 28, 601-613.

Observations of Turbulence Associated with Highly Nonlinear, Near-Surface Solitons Over the Continental Shelf

T. P. Stanton

Department of Oceanography, Naval Postgraduate School, Monterey, CA 93943
stanton@oc.nps.navy.mil

Abstract

A three week observation of upper ocean current, temperature, density and dissipation profiles near the shelf break off Northern Oregon has allowed the form and effects of solitons generated at the nearby shelf break to be studied. Strongly nonlinear Solitary Internal Waves (SIW) were continually observed on the leading edge of a semi-diurnal internal tide which propagated past our measurement site throughout a neap to spring tidal period. SIW timeseries of displacement, currents, dissipation rates and turbulent diffusivities from neap and spring tide forcing conditions are being used to characterize the effects of these energetic SIW/internal bore structures on the upper ocean.

The COPE Experiment

The Coastal Ocean Probe Experiment (COPE) was an interdisciplinary experiment designed to study the surface signatures and hydrodynamics of coastal internal waves over the continental shelf. The observation site, offshore from Tillamook Oregon, was chosen for the shallow pycnocline and strong surface signatures of internal waves which had previously been observed in satellite SAR imagery and visual observations from aircraft overflights prior to the experiment. High powered Ka and X band Doppler radars overlooked the ocean from a 750m high coastal mountain top, to measure radar surface backscatter properties (see Kropfli et al, 1998). The radars also made timeseries maps of 150m horizontal resolution surface backscatter levels and scatterer velocity spanning an 50 Km radius offshore from the radars. These map sequences provided a high resolution view of the two dimensional structure of the propagating internal wave surface signatures. FLIP was tri-moored in 140m of water near the edge of the shelf, providing a stable platform for atmospheric, surface interface and oceanographic measurements during a three week period in October 1994.

Observations of the upper ocean structure were made with an automated Loose-tethered Microstructure Profiler (LMP) which measured 0.1m resolution temperature, conductivity (and hence density) from the ocean surface to a depth of 35m while simultaneously measuring temperature and velocity microgradients, allowing thermal and turbulent energy dissipation rates to be estimated. LMP profile cycles were completed every 80 s resulting in 24000 temperature and density profiles during the observation period. An 8m length instrumented frame suspended from a boom extending southward from FLIP supported 5 acoustic travel time 3 component velocity sensors, and an inertial tilt and heave sensor package, while a BADCP extended the velocity profiles to 40m below the frame.

SIW Observations

The amplitude and nonlinearity of the SIW packets observed on the leading edge of the semidiurnal internal

tidal bore generated offshore from the observation site were impressive. An example of a 24 hour temperature profile timeseries in Figure 1 shows two cycles of a semidiurnal internal tidal displacement of the pycnocline. The leading edge of the internal tide consists of a series of strong negative SIW displacements up to 20m downward from the initial 5m deep pycnocline depth at just prior to the arrival of the bore / SIW structure (barely resolved on the 24 hour timescale in Figure 1). Near the spring tide forcing, these SIW displacements had surface signatures with longshore coherent scales beyond the 40-60 Km range of the radars on Onion Peak. The leading edge of the SIW groups during periods of strong offshore forcing had largely parallel wave fronts propagating onshore, which can be seen in Figure 2, which is a snapshot of cross polarized radar backscatter intensity measured at yearday 269.54, near the middle of the timeseries in Figure 1. Onshore current pulses at the peak of the displacements reached 0.8 ms^{-1} , approaching the phase velocity of the SIW. Stanton and Ostrovsky, 1998, showed that the highly nonlinear SIW displacements were well modeled by a second order CombKdV equation, a form which also matches the observed weak dependence between soliton width and amplitude. The shallow initial depth and very large amplitudes suggest that these SIW observations have record breaking nonlinearity in geophysics.

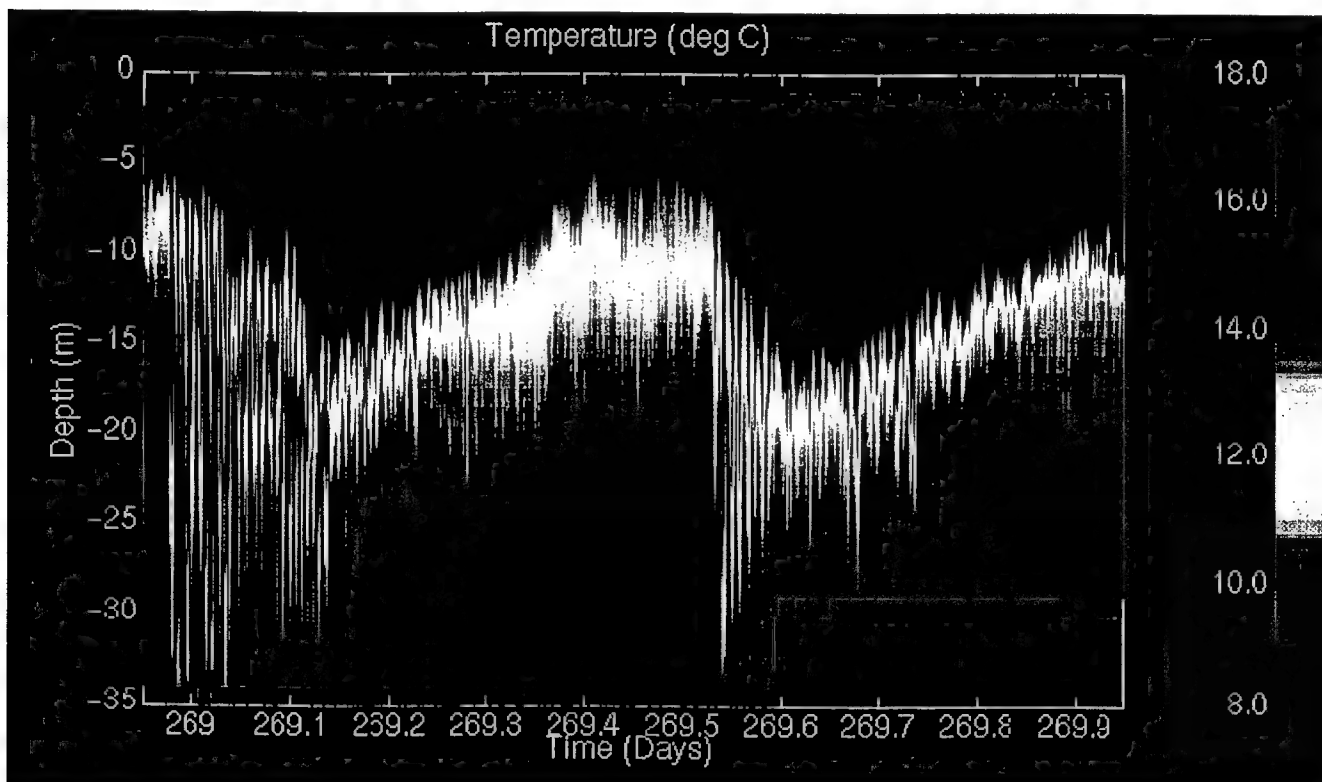


Figure 1. A 24 hour profile timeseries of temperature at the COPE site showing two cycles of a semidiurnal internal tidal bore with solitons on the leading edge. This structure was characteristic of spring tide forcing at the measurement site near the shelf break off Northern Oregon.

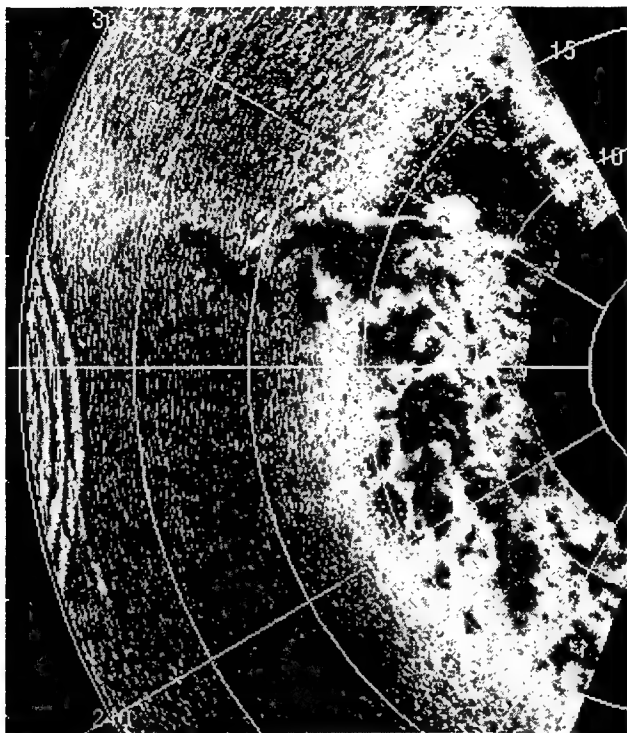


Figure 2. A radar map of VVHH cross polarized radar backscatter measured from a coastal mountain top as the leading edge of the SIW set moved past FLIP at Yearday 269.54. FLIP can be seen as a small line at 28Km range at approximately 255 T bearing. (Courtesy of Bob Kropfli, NOAA ETL, Boulder Colorado).

Concurrent observations of turbulent thermal and velocity dissipation rates, c and e , made by microstructure sensors on the LMP have allowed changes in turbulence levels caused by the propagation of the SIW/internal bores to be estimated. Changes in turbulent diffusivity of the water column arise from a combination of modulation of the local buoyancy frequency and thermal gradients by the internal bore / SIW packets, a decrease in dynamic stability as vertical shear associated with the strong SIW current pulses acts against the modified density profile, and a range of interactions which occur between the strongly nonlinear SIW field, surface gravity waves, and background internal wave field. Figure 3 illustrates the net effects of these processes in changing the thermal turbulent diffusivity, $K_T = c / T_z^2 / 2$, where the vertical thermal gradient T_z and thermal variance dissipation rate, c , are estimated over 5 min and 1m vertical averaging intervals in order to resolve changes within SIW displacement times, but with resulting marginal robustness of the turbulence estimates. The two hour timeseries was taken at the start of the 24 hour temperature profile timeseries in Figure 1, and has high resolution isotherms superimposed to show the position of the SIW displacements. This timeseries, which is representative of conditions during strong forcing, suggests a sequence of events where the first SIW simply displaces high diffusivity (low stratification) near-surface fluid downward, then even after a single displacement, the diffusivity of the water column between downward displacements increases significantly (keeping in mind the logarithmic scale used in Figure 3). Successive displacements further increase the turbulence (and therefore diffusivity) levels until the displacement amplitudes decrease.

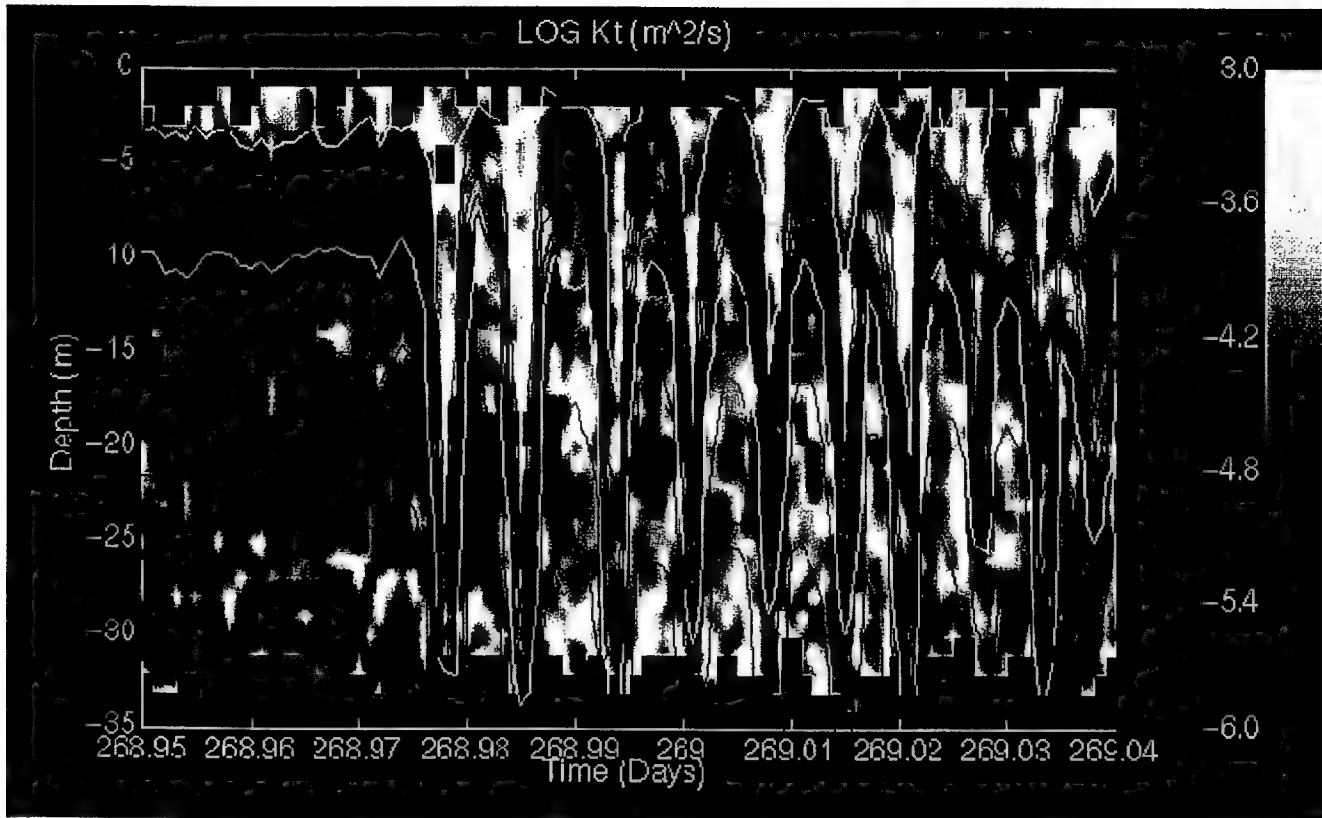


Figure 3 A two hour timeseries of turbulent thermal diffusivity, with the logarithmic gray scale ($\log_{10} \text{m}^2 \text{s}^{-1}$) shown on the right panel. 1°C interval isotherms have been superimposed to show the position of the SIW displacements.

Conclusions

Cope provided an opportunity to measure long timeseries of the detailed structure of strongly nonlinear SIW associated with an internal tidal bore near their source region at the outer edge of the continental shelf. It is clear that these energetic SIW pulses have a significant effect on vertical diffusive processes, net displacements of the surface layer, and large effects on near-surface acoustic propagation on the shelf. Contrasts in structure, directionality, net displacement, turbulent dissipation rates and modulation of turbulent diffusivity for both strongly and weakly forced SIW packets are further discussed in Stanton, 1998, and will be summarized at the SIW workshop. Limitations of the existing data set and suggestions for future SIW observations to better quantify and model SIW generation, propagation, shoaling, and breaking will also be discussed.

References

Kropfli, R. A., L. A. Ostrovsky, T. P. Stanton, E.A. Skirta, A. N. Keane and V. Irisov, 1998. Relationships Between Strong Internal Waves in the Coastal Zone and their Radar Signatures. *JGR*, accepted.

Stanton, T. P. and L. A. Ostrovsky, 1998. Observations of Highly Nonlinear Internal Solitons Over the

Continental Shelf. *Geophys. Res. Lett.*, 25, 14, 2695-2698.

Stanton, T. P., 1998. Upper Ocean Mixing by Highly Nonlinear Internal Solitons Over the Continental Shelf. Submitted to *JGR*.

Relationships Between Strong Internal Waves and Their Surface Signatures

R. A. Kropfli*, L. A. Ostrovsky**, T. P. Stanton***, E. A. Skirta****,
A. N. Keane**, and V. G. Irisov**

*) NOAA/Environmental Technology Lab., Boulder, CO;
**) Univ. of Colorado, CIRES/ NOAA Environmental Technology
Lab., Boulder, CO;
***) Naval Postgraduate School, Monterey, CA;
****) Dept. of Mathematics, Univ. of Toledo, Toledo, OH

Abstract.

Strong internal waves (IW) in the form of soliton groups were observed off the Oregon coast with in-situ and remote sensors, including shore-based Doppler radars and an airborne microwave radiometer. Here, we analyze the relationships between isotherm vertical displacements, internal currents, radar backscatter cross-sections, along with Doppler velocity signals at horizontal (HH) and vertical (VV) polarizations. Analysis of these observations shows that the phase of radar-signal modulation with respect to the IW is such that the minimum radar signal intensity and lowest microwave brightness temperature lies close to the maximum of the IW thermocline depression or, equivalently, the maximum horizontal current excursion near the surface.

I. Introduction

Theoretical and observational studies of nonlinear internal waves (IW) in a shallow sea have a long history. The observational data show that tidally-generated internal solitons are a ubiquitous phenomenon in coastal zones with stratification, generally during the summer months, and suggest that they may consume a non-negligible part of tidal energy. Remote observations of surface signatures are now a common way to study IWs. Satellite images of IWs have been obtained routinely since the 1970s by photography and by synthetic aperture radar (SAR). Systematic physical studies of this phenomenon started with the works of Hughes and Grant [1978].

However, in spite of a relatively large body of prior work, a thorough understanding of relationships between IW characteristics and those of centimeter-range SWs is still lacking. It is especially true for internal solitons and bores in shelf zones where the IWs may have pulse-like shapes and very large amplitudes so that even a description of subsurface IW currents is a complicated problem.

We describe here the results of observations of extremely large amplitude internal solitons on the East Pacific Shelf during the Coastal Ocean Probing Experiment (COPE) in which strong correlations were observed between IW hydrophysical parameters and radar signals.

2. Experiment

COPE was performed off the coast of northern Oregon from September 12 through October 7, 1995. This area was selected because of the frequency and intensity of internal waves caused by diurnal tidal

flow over a well-defined shelf break about 70 km offshore. The Columbia River, just 50 km to the north, was the source of warm, fresh water which generated a sharp and shallow pycnocline on which the IW packets could propagate.

Numerous sensors were mounted on the Scripps Institute Floating Instrument Platform, FLIP, moored about 25 km offshore in 150 m of water. These sensors enabled us to measure wind near the surface, air and sea surface temperatures, wave characteristics, and profiles of current, small-scale turbulence, temperature, salinity, and density. In addition, three arrays of thermistor chains and an inverted echo sounder operated by the Canadian Institute for Ocean Science were moored 6 km offshore in 75 m of water.

The K-band and X-band Doppler radars, 34.6 GHz and 9.3 GHz respectively, developed by the NOAA Environmental Technology Laboratory (ETL) were operated from a nearby hillside about 4 km from the shore and 744 m above sea level. Other ETL remote sensors, e.g., microwave radiometers, were operated at moderate incidence angles.

At the first stage, we concentrated on three cases in which the ETL radars operated in a fixed-beam mode and were directed at the ocean surface near FLIP, where current and temperature profiles were measured continuously along with near-surface wind. The in situ measurements were made from FLIP with a Loose-tethered Micro-structure Profiler (LMP), which provided temperature and salinity measurements at 0.1 m resolution. Current measurements were made with five ultrasonic travel time current sensors.

The measurements of temperature, salinity and density profiles prior to the passage of the IW front has indicated a very shallow (5-7 m) position of the pycnocline that is apparently due to the proximity of Columbia River. At the same time, during the strong spring tides, the 14EC isotherm, which is near the depth of the maximum density gradient, indicated up to 26 m displacements from the undisturbed depth. These extreme displacements suggest a very strongly non-linear wave which was the greatest thermocline displacement observed during COPE. Displacements were routinely observed in the range of 15 to 20 m. The initial displacement was usually followed by a train of pulses; we refer to these pulses as solitons when they are well-separated. Peak current magnitudes in the strongest solitons were also unusually large, up to 0.8 m/s, just slightly less than the IW speed of 0.9 m/s (see below).

The radars used in this study were originally designed and operated by ETL for meteorological research but were recently modified for detailed studies of the ocean. Here we used primarily fixed-beam data obtained when the antenna was directed near FLIP for several hours at a time while IW packets propagated through FLIP's position and, subsequently, the nearby radar sample gates.

The images collected in a 26-days period suggest that the structure and amplitude of IWs vary markedly with the strength of tidal forcing. Relatively strong spring tides generated rather regular and horizontally extended IW fronts. Weaker tidal forcing from neap tides seemed to generate IWs with greater curvature, distinctly separated from each other, as though they had been forced by sources associated with smaller-scale, localized features on the shelf break. In all cases, the IWs are presumably generated by tidal currents interacting with bottom topography near the shelf break located approximately 70 km off shore. These observations of IW structure suggest that the generating mechanisms during spring and neap tides might be different (such as lee waves in the former case and scattering on local bottom features in the latter).

The IW propagation velocity can be accurately determined from the slope of the wave fronts in range-time plots. Based on the slopes of the modulations in the range-time plot, the IW near FLIP was propagating onshore at .90 m/s.

Internal waves are observable to radars because of their strong modulations of the surface wave spectrum. Radar images, as described above, show bands of relatively high signal strength, where the SWs are enhanced by the IW, separated by low intensity bands where the surface waves are suppressed. Note that the direction of the near-surface current measured from FLIP is opposite to that of the Doppler velocity excursions in the weakly reflecting region of the IW, giving credence to the interpretation that observed modulations in Doppler velocity excursions are not caused directly by IW current.

3. Comparison of in-situ and radar data

Even cursory examinations of the radar data and the data obtained from FLIP show that they have highly correlated and unmistakably strong modulations during the IW passages (Fig.1).

FLIP parameters such as isotherm depth and current were plotted along with temporally-lagged radar measurements such as VV, HH, and Doppler velocity. In all analyzed cases the propagation direction of the IWs was such that our radar measurements near FLIP can be considered to be directly across the IW phase fronts.

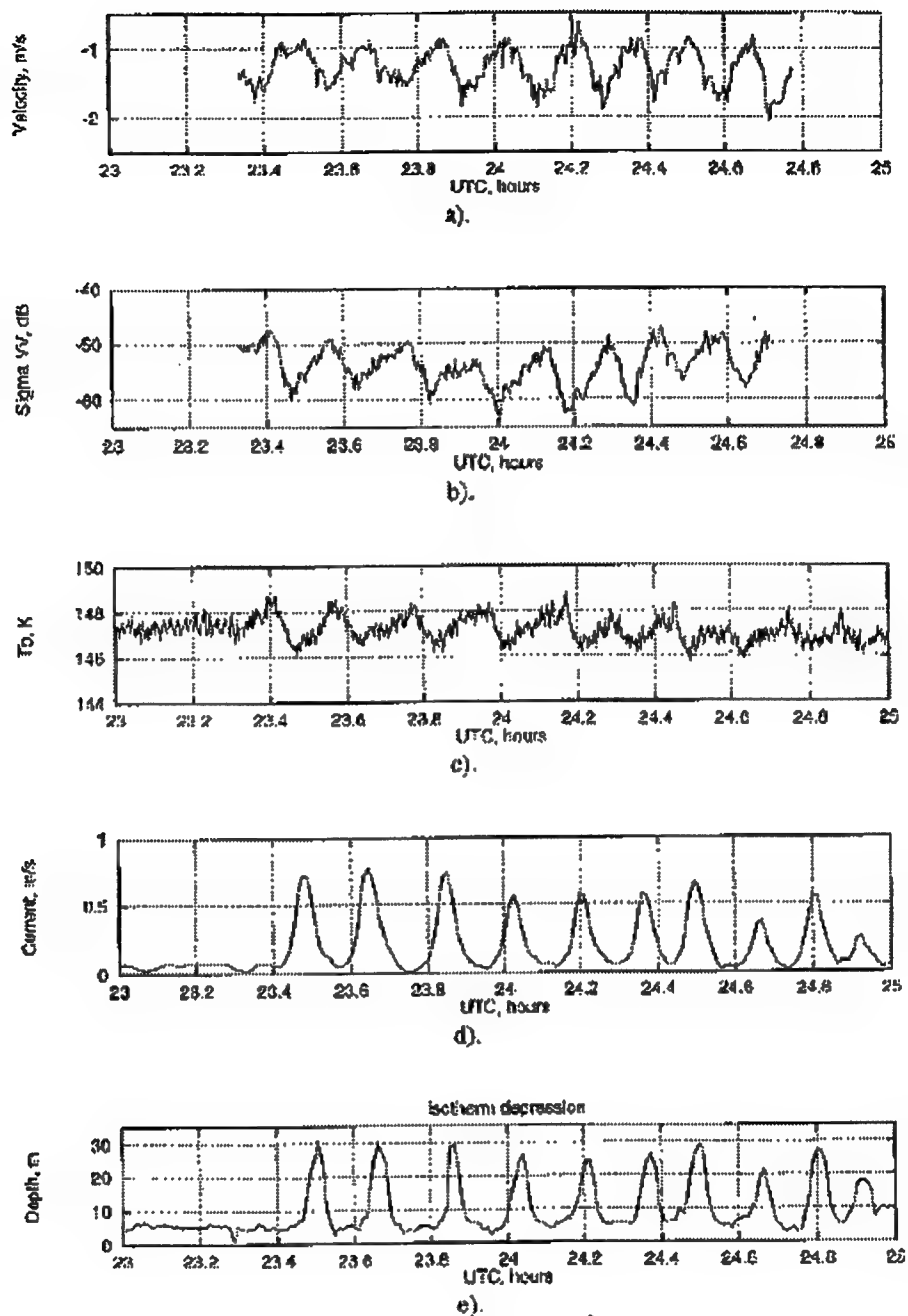


Figure 1. Temporal records of Doppler velocity (a); VV-signal intensity (b) (both from the ETL Ka-band radar); 37 GHz brightness temperature (c); horizontal current at 4.4 m depth (d); and depth of 14 C isotherm (e) for September 25/26, 1995

Generally, minima in radar signals are nearly coincident with maxima in the seaward component of Doppler velocity, with maxima in isotherm depths and maxima in IW-generated near-surface currents toward the shore. In particular, the near-surface current excursions are inferred to be toward the east in zones of minimum radar backscatter which we observe to have Doppler velocity excursions toward the west.

The brightness temperature as a function of time based on data taken from the radiometer during two passes by an airship over the IW were interpolated to FLIP's position from the observed positions of the smooth areas. The result shows that the 37 GHz brightness temperatures exactly in phase with the radar signal modulations. The radar and radiometric signals are well-correlated as expected because the small scale roughness is known to cause increases in both the radiometric brightness temperature and radar back scattering intensity. A remarkable feature is that the growth of the scattered radar signal level begins prior to the arrival of the IW train. This suggests that a 'precursor' to the IW is present in the spectrum of short surface waves. A similar phenomenon was reported before [Basovich et al., 1987; Gotwols & Sterner, 1988]. Finally, we note that the amplitude of modulations for both HH and VV polarizations increases monotonously with the isotherm displacement.

4. On mechanisms of SW-IW interaction

To choose between different candidate hydrodynamic processes which can explain the observed results, one should consider the main qualitative features of the signal modulation, in particular its depth and phasing between radar modulation and isotherm or current variations. A detailed theoretical consideration of the problem is beyond the scope of this work. Here we briefly discuss most relevant models which seem to fit the observations.

1. Effect of surface-active films

A possible candidate mechanism to explain the influence of IW-induced currents on short surface waves is the effect of surface-active films. This problem was considered in a number of works [e.g., Ermakov et al., 1980]. Horizontal currents induced by IWs could redistribute the surfactant which then damps the surface waves causing SW modulations. It is easy to show that in a steady-state regime, the film is concentrated over the solitons (where the IW current is minimal in the reference frame moving with the IW phase speed, where the current is stationary). In our case, the film concentration modulation can be strong. Because the short-wave damping rate is the greatest where film concentration is the greatest, the slick should be observed as a minimum in the radar signal directly over the solitons, which agrees with our observations. Unfortunately, surfactants are difficult to measure in open ocean environments and were not measured during COPE. The action of surfactants readily explains the phasing of maxima and minima of radar scattering with respect to IW described above. However, this mechanism fails to explain the observed Doppler-signal anomalies and the presence of precursors due to its local character.

2. Cascade mechanism

It has been suggested by a number of observers [e.g., Hughes & Grant, 1978; Basovich et al, 1987] that IWs act primarily on surface gravity waves of few decimeters to few meters in wavelength, which, in

turn, modulate the gravity-capillary waves that contribute to scattering at microwave frequencies. In these theories, surface gravity wavelengths affected the most by IWs are determined by the "group synchronism" criterion, i.e., the group velocity of surface waves c_{gr} plus IW-induced surface current being nearly the same as the phase velocity of the IWs. Under this condition, "blocking" is possible: the wave reaches a turning point and reflected (or refracted), which, in turn, may radically change the surface wave configuration and produce a strong modulation even for moderate-amplitude IWs. IWs were observed in COPE to propagate with typical velocities of 0.7 to 0.9 m/s; surface waves with such group velocities have wavelengths in the range of 0.8 to 2.0 meters between solitons, where the IW current is weak, and should be much shorter, from few centimeters to few dozens of centimeters, over strong solitons, where the IW current is 0.5-0.8 m/s. Because more intense surface gravity waves tend to break and form the capillary ripples or enhance the scattering anyway, the radar signal minima will coincide with those of the suppressed surface gravity waves. Such a cascade mechanism can explain the observation of minimum scattering directly over the solitons for weak winds; if the wind increases, the SW maximum will move toward the forward edge of the IW. This tendency is also seen in some of our COPE observations.

3. Direct modulation of SW by IW

As mentioned, the synchronous SW over the solitons, where the IW current is strong, are rather short and for strong currents can move into the centimeter wavelength range. It can be shown [Bakhakov, 1998], that while moderate current would amplify these waves, the current close to the IW phase velocity makes the opposite effect, and the wave intensity decreases over the solitons. This may explain the observed phasing without considering a cascade, although not the "opposite" Doppler shifts mentioned above.

There are not enough observational data analyzed so far to choose with any certainty between these mechanisms. Moreover, they all might contribute to some degree to the short wave modulation and formation of radar images.

5. Conclusions

Extremely strong, tidally-generated, internal-wave soliton trains were observed during COPE by means of contact sensors and microwave radars during a three and a half week experiment off the coast of northern Oregon. Very distinct radar signatures of IWs were the result of strong influences of the IWs on the surface wave spectrum. Correlations as high as .9 were found between the radar signals and current/isotherm records made at FLIP. Stronger signal modulations were always observed at HH compared to VV and detectable modulations were easily observed at HH even at wind speeds as high as 15 m/s when VV modulations were not observable. Radar observations showed that the IW spatial structure was determined by the tidal strength, i.e., whether the forcing was from strong spring tides or weak neap tides. The opposition of the Doppler velocity excursions (from the mean) to the direction of near-surface current measurements on FLIP indicates that the Doppler velocity excursions were not representative of IW currents; more consistent with the measurements was the interpretation that the Doppler excursions were caused either by orbital motions of SWs or by parasitic capillary waves.

A careful positioning of data from a single radar range gate onto time records of current and thermocline depression showed that the maximum radar returns were not coincident with the regions of highest strain rate (that is rather typical of the observations of weak IW) but were found to lead the current pulse/thermocline depression as it progressed shoreward with average speeds of about .8 m/s. Particle

velocities of nearly that magnitude attest to the strong non-linearity of these waves as does the extreme ratio of thermocline depression to ambient thermocline depth which was as great as 5:1. The portions of IWs weakly-reflecting to radars were roughly coincident with the solitons themselves, i.e., the current pulses/thermocline depressions.

A more detailed description of the results given above can be found in [1,2]

Acknowledgments

Support for this work was provided by the NOAA-DOD Advanced Sensor Applications Program and the Office of Naval Research Physical Oceanography Program.

References

1. T. P. Stanton and L. A. Ostrovsky, Observations of highly nonlinear internal solitons over the continental shelf. *Geophys. Rev. Lett.*, 25, 14, 2695-2698, 1998.
2. R. A. Kropfli, L. A. Ostrovsky, T. P. Stanton, E. A. Skirta, A. Keane, and V. E. Irisov, Relationships between strong internal waves and their surface signatures. Accepted for *J. Geophys. Res.*, 1998.

NONLINEAR INTERNAL WAVE INTERACTION IN THE CHINA SEAS

Antony K. Liu
Oceans and Ice Branch
NASA/Goddard Space Flight Center
Greenbelt, Maryland 20771 USA

Ming-K. Hsu
Department of Oceanography
National Taiwan Ocean University
Keelung, Taiwan

EAST CHINA SEA

Synthetic Aperture Radar (SAR) images have been used to study the characteristics of internal waves in the East and South China Seas (Liang et al., 1995; Liu et al., 1998). Rank-ordered packets of nonlinear internal waves in the East and South China Seas are often observed in the SAR images. Recently, the internal wave distribution maps have been compiled from hundreds of ERS-1/2, RADARSAT and Space Shuttle SAR images in the East and South China Seas from 1993 to 1998. In the northeast of Taiwan, the internal wave field is very complicate, and waves are propagating in all directions. Its generation mechanisms include the influence of the tide and the upwelling, which is induced by the intrusion of Kuroshio across the continental shelf (Hsueh et al., 1993). The Kortweg-deVries (KdV) type equation has been used to study the evolution of internal wave packets generated in the upwelling area. Depending on the mixed layer depth, both elevation and depression waves can be generated based on numerical simulations as observed in the SAR images. The merge of two wave packets from nonlinear wave-wave interaction in the East China Sea has been observed in the SAR image and demonstrated by numerical results.

SOUTH CHINA SEA

While most of internal waves in the north part of South China Sea are propagating westward. Some of these internal waves are generated from the shallow topography or sills in the Luzon Strait. The suggested mechanism is similar to the lee wave formation (Liu et al., 1985) due to strong current from the Kuroshio branching out into the South China Sea. The wave crest can be as long as 200 km with amplitude of 100 m. Some small internal waves observed on the continental shelf may be generated from the shelf break in the South China Sea. At the shelf break, a depression area may be induced by mixing or shear flow instability in the pycnocline. The disturbance of mixed area is then driven by the semi-diurnal tide onto the shelf and evolves into a rank-ordered wave packet (Liu 1988). In the summer, where the mixed layer is thinner than the bottom layer, depression wave train can be generated. During the spring/winter, as observed in the SAR image, elevation solitons can be evolved, because the mixed layer deepens caused by strong winds and its thickness is thicker than the bottom layer.

Based on the RADARSAT ScanSAR images collected on April, 26 and May 4, 1998, huge internal solitons were observed near Dong-Sar Island with crest more than 200 km long and wave speed of 1.9 m/s. Most interesting process is the detection of elevation internal waves in shallow water (220 m) and depression waves on the shelf break (500 m depth) in the same SAR image (5/4/98). The effects of water depth on the evolution of solitons and wave packets have been modeled by KdV-type equation and linked to satellite image observations. For a case of depression waves in deep water, the solitons

first disintegrate into dispersive wave trains and then evolve to a packet of elevation waves in the shallow water area after they pass through a "critical depth" of approximately equal layer thickness as demonstrated by numerical model (Liu et al., 1998). Based on the numerical simulations, the evolution time for conversion is about 20 hours, and the wave propagation distance can be as far as 200 km. Also, in the ScanSAR image near Dong-Sar Island, the westward propagating huge internal solitons are often encountered and broken by the coral reefs on the shelf. In some cases, the broken waves will merge after passing the island and interact with each other.

WAVE-WAVE INTERACTION

The wave-wave interaction has been observed in many SAR images of the East China Sea. The internal solitons are nonlinear, thus their interaction are much more complicated than the regular linear waves. One of the well-known phenomena is the phase shift when two solitons are collided. In the northeast of Taiwan, the interaction patterns are very complicated. In the southeast of Yellow Sea near South Korea coast, the internal waves are generated from several islands, so the wave interaction pattern is much more organized. Especially, during the summer time, a shallow mixed layer of 15 m persists in the water of 100 m depth. The internal wave packets with more than 15 solitons of equal amplitudes were observed and measured by the thermistor chain from a research ship in the Yellow Sea during the field test in August 1996. These many solitons in a wave packet may be caused by the internal wave-wave interaction in the Yellow Sea, which results in the merge of solitons to a single large internal wave.

From the SAR images obtained on July 23, 1997, several internal wave packets were generated from the islands near the southwest tip of Korea Peninsula by the collision of Korea coastal current and semi-diurnal tide. There are at least two generation sources (islands), one from the east and the other from northeast. The phase/front of internal wave packets are shifted and distorted in the interaction areas due to the nonlinear wave-wave interaction. The direction of shifted wave train is in between two incident wave packets without interaction. Not only the direction shifted after the wave-wave interaction, but the number of waves in the wave packet, wavelength, and amplitude of the waves are also changed. In order to demonstrate the wave-wave interaction, a numerical calculation with two wave packets moving in the same direction is performed. Although the wave-wave interaction in the Yellow Sea is definitely a two-dimensional process, however, the one-dimensional results may shed some lights on the merge of wave packets.

ACKNOWLEDGMENT

This research was supported by the National Science Council of Taiwan, National Aeronautics and Space Administration and Office of Naval Research.

REFERENCES

- Hsueh, Y., C.-S. Chern, and J. Wang (1993), Blocking of the Kuroshio by the continental shelf northeast of Taiwan. *J. Geophys. Res.* 98, 12351-12360.
- Liang, N. K., A. K. Liu, and C. Y. Peng (1995), A preliminary study of SAR imagery on Taiwan coastal water. *Acta Oceanogr. Taiwanica* 34, 17-28.
- Liu, A. K (1988), Analysis of nonlinear internal waves in the New York Bight. *J. Geophys. Res.* 93, 12317-12329.

Liu, A. K., J. R. Apel, and J. R. Holbrook (1985), Nonlinear internal wave Evolution in the Sulu Sea. *J. Phys. Oceanogr.* 15, 1613-1624.

Liu, A. K., Y. S. Chang, M. K. Hsu and N. K. Liang (1998), Evolution of nonlinear internal waves in the East and South China Seas. *J. Geophys. Res.* 103, 7995-8008.

This is a portion of a paper by Porter, D. L. and D. R. Thompson, 1998, Continental shelf parameters inferred from SAR internal wave observations. *J. Atmos. Oceanic Tech.* In press, used with permission.

Continental Shelf Parameters Inferred from SAR Internal Wave Observations

D. L. Porter and D. R. Thompson (The Johns Hopkins University, Applied Physics Laboratory, Laurel, MD 20723; 240-228-4230; e-mail: David.Porter@jhuapl.edu 240-228-4559; email: Donald.Thompson@jhuapl.edu)

Abstract

This paper shows a preliminary results on the use of Synthetic Aperture Radar (SAR) imagery to extract oceanographic information about the continental shelf. The surface manifestation of internal waves is observed using the Synthetic Aperture Radar (SAR) onboard the European Research Satellite 1 (ERS-1). The depth of the pycnocline and the density of the surface layer can be estimated from the dispersion relation obtained from a two-layer fluid model. The other parameters that are required to make this estimate are obtained by assuming climatological bottom density, estimating the speed of propagation from the tidal-generated wave packets, and calculating the depth of the pycnocline based on the isobath where the internal waves are dissipated. This robust method for obtaining quantitative information about the structure of the shelf's water column shows good agreement with the *in situ* observations from that area.

Results

Figure 1 is a SAR image from ERS-1 of the waters just south of central Long Island. The image is 100km on the side. The internal wave crests in this image are one tidal cycle apart, (i.e., 12.42 h) and by measuring the distance between the wave packets we can estimate their speed of propagation. Figure 1 shows nine lines equally spaced along the wave crests of two internal-wave trains whose generation time is assumed to be separated by 12.42 h. We have averaged the length of the nine lines and divided that by the tidal cycle period to obtain a speed of 0.62 ± 0.06 m/s, which is within the range of speeds observed in the New York Bight by Liu [1988].

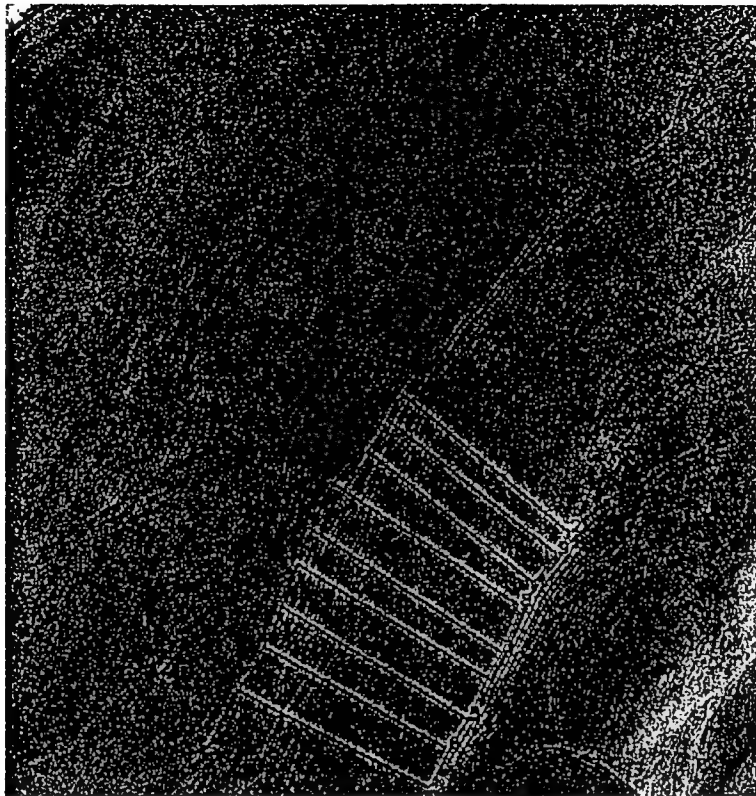


Figure 1. Image of July 18, 1992, the upper left hand corner shows a small section of the south shore of Long Island, NY.

What does this information tell us about the density structure of the water column? From CTD measurements, conducted concurrently during JUSREX, we observe the depth of the pycnocline in the region between the two internal-wave packets was in the 20 m range with a bottom-layer density of 1.0253 gm/cm³ and an upper-layer density of 1.0224 gm/cm³. Thus the density difference between the two layers was 0.0029 gm/cm³.

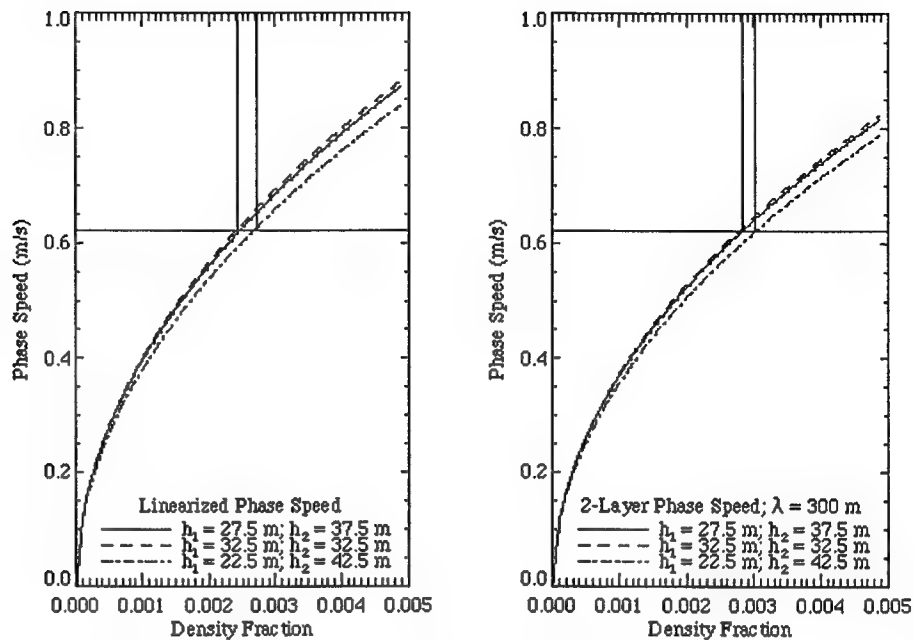


Figure 2. Phase speed vs. density fraction computed from linearized relationship (left panel), and full 2-layer dispersion relation (right panel) for several combinations of layer depths. The horizontal line shows where a phase speed of 0.62 m/s intersects the various curves, and the vertical lines indicate the error bounds on the density fraction corresponding to the depth variations.

We have developed a procedure that uses linear wave theory to infer oceanographic parameters. The assumptions and steps in this procedure are: 1.) The total depth at the position where the internal waves no longer appear in the SAR image was determined from bathymetry to be about 55 m. With the assumption that in a two-layer regime, the waves dissipate when the layer depths are equal, we deduce layer depths of 27.5 m at this position. 2.) A further assumption is that the upper-layer depth remains roughly constant over the entire region from shelf break to the dissipation location. 3.) The bathymetry at the position where the internal-wave phase speed is measured from the imagery (as discussed above in conjunction with Figure 1), then implies the lower-layer depth at this location. For the present case, the depth at the phase-speed measurement location is 65 m, which implies a bottom-layer depth of 37.5 m. 4.) We may now use the linearized phase-speed equation to determine the fractional density change, $(\text{density}_2 - \text{density}_1)/\text{density}_1$, between the two layers, or, if the lower-layer density is known (from climatology for example), the absolute upper-layer density. If we take the value of $\text{density}_2 = 1.0253 \text{ gm/cm}^3$ measured during JUSREX, the density difference from the linearized phase-speed estimate in Figure 2 yields an upper-layer density $\text{density}_1 = 1.0228 \text{ gm/cm}^3$ in good agreement with the estimated value of 1.0224 gm/cm^3 .

There are, of course, several caveats that need to be stressed in connection with discussion presented above. First of all, one must keep in mind that SAR observations are time limited. This means that an estimate of the location of the dissipation region may be in error simply because the waves haven't yet propagated further onto the shelf at the time of the image. This usually results in an over-estimate of the critical depth (and the pycnocline depth). Also, there will certainly be cases when the water column is not well characterized as a simple two-layer system. Especially near the shelf break for example, a thin but well-defined bottom layer is sometimes observed below the usual two-layers typical of the region further in shore [Lynch, et al., 1997].

CONCLUSIONS

We have shown in this paper how it may be possible to remotely estimate various properties of the water column on the continental shelf using SAR imagery in conjunction with knowledge of the local bathymetry, climatological density data, and simple models for internal-wave evolution. Theoretical studies of two-layer fluids indicate that dissipation of internal waves impinging on shoaling water occurs when the depth of the bottom layer, which is decreased by the shoaling, becomes equal to that of the upper layer. Using this idea, we have determined this critical depth for a particular case study by noting the location in the SAR image where the internal-wave surface signatures disappear. The depth of each layer at this position is then half the total depth. By assuming that the internal waves are generated at the shelf break on each diurnal tidal cycle, we have also estimated their phase speed by measuring the distance between successive packets in the image. With this information along with the 2-layer dispersion relation, we have been able to estimate the fractional density change between the two layers. Furthermore, an estimate of the surface density is possible by using the climatological bottom density. We have compared the parameters extracted using these methods with *in situ* measurements collected concurrently with the SAR imagery. This comparison showed good agreement, and gives us confidence that our techniques are robust.

REFERENCES

Liu, A. K., 1988: Analysis of Nonlinear Internal Waves in the New York Bight. *J. Geophys. Res.*, **93**, 10, 12 317-12 329.

Lynch, J. F., G. G. Gawarkiewicz, C. S. Chiu, R. Pickart, J.H. Miller, K. B. Smith, A. Robinson, K. Brink, R. Beardsley, B. Sperry, G. Potty, 1997: Shelfbreak PRIMER - An Integrated Acoustic and Oceanographic Field Study in the Middle Atlantic Bight. *Proceedings: Shallow Water Acoustics Conference*, Beijing, China, (in press).

Internal solitons in the ocean: prediction from SAR ©

Justin Small, Dr Bob Hornby, Dr Mark Prior and Dr John Scott

Oceanography, Defence Evaluation and Research Agency (DERA)
Winfrith Technology Centre, Dorchester DT2 8XJ, UK
e-mail: jsmall@taz.dera.gov.uk

1. Introduction

Internal solitary waves have been frequently observed in the ocean, and are often generated by the non-linear deformation of internal tides [1]. The waves are often termed solitons, in analogy with the waves discussed by Zabusky and Kruskal [2]. Oceanic internal solitons vertically displace the thermocline and cause internal currents, with near-surface flow convergence and divergence [3]. The latter effects can modulate the sea-surface roughness on small length-scales ($O(1\text{cm}-10\text{ cm})$), which can be imaged by radar such as satellite-borne Synthetic Aperture Radar (SAR) [4]. SAR consequently appears to be an attractive method for predicting solitons, due to its ability to show the complete 2D surface distribution of wave-packets. Its disadvantages include the present infrequent repeat-cycle of satellite SAR (typically 20-30 days), and the masking of internal wave signatures at high wind speeds (e.g. 10m/s or above).

This paper summarises the results from an international collaborative experiment involving DERA which investigated the effects of internal solitons at the shelf-edge, and tests the possibility of making accurate predictions of phase speeds and amplitudes from SAR.

2. KdV Solitons

The observed internal waves in SAR will be modelled in terms of the first order Korteweg de Vries equations. Although this theory clearly has limitations, in its assumptions that the waves are small amplitude, long wavelength and in shallow water, its simplicity allows for the rapid interpretation of SAR signatures, and the results will be assessed below.

The steady soliton solutions predicted by KdV are given by [1]

$$\eta(x, t) = \eta_0 \operatorname{sech}^2(((x - x_c) - c_1 t) / L) \quad \text{Eq. 1}$$

Here η_0 is the maximum displacement, x and t are range and time respectively, x_c is the soliton central position, and L (the soliton half width) and c_1 (the soliton phase speed) are given by

$$a) \quad L^2 = \frac{12\gamma}{\eta_0 \alpha} \quad b) \quad c_1 = c_0 \left(1 + \frac{\eta_0 \alpha}{3c_0}\right) \quad \text{Eq. 2.}$$

where c_0 , α and γ are the linear phase speed, and parameters of non-linearity and dispersion respectively, (defined in [1], also in Pelinovsky et

al, this workshop) strongly dependent on the stratification and water depth respectively. These equations demonstrate the well known dependence of amplitude on width L, and phase speed on amplitude

The internal currents can also be obtained by the approximation to the continuity equation

$$u = -c_1 \frac{\partial \eta}{\partial x} \quad Eq. 3$$

The surface currents induced by the soliton give rise to the areas of convergence and divergence which can modulate the surface roughness in the capillary-gravity range which is imaged by SAR. (see section 4 below). Of particular note is the range D between convergence and divergence, which in suitable circumstances can be measured from SAR. A fixed relationship between D and L is given simply by [5]

$$D = 1.32 L \quad Eq. 4$$

Together with equation 2 this gives a means of estimating amplitude and phase speed from the distance D on SAR signatures.

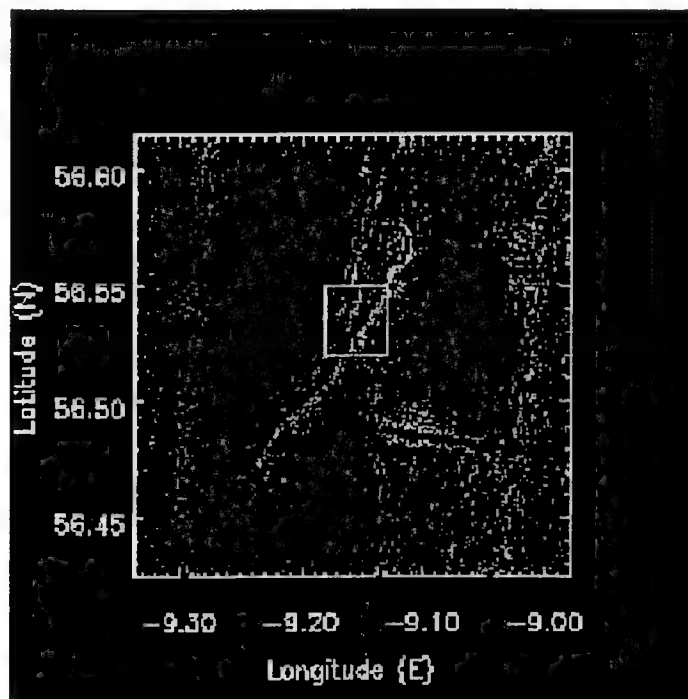


Figure 1. Close up of an ERS-1 SAR image of 20th August 1995, 1136 UTC, indicating the 160m, 600m and 1000m bathymetry contours (dashed lines, from right to left respectively, from swath surveys), together with the ship survey track on 19th August (solid black line), two mooring positions S and D, and the box used to derive a SAR profile across the leading wave (section 4).

3. SESAME- Internal solitons at the Continental slope/shelf-edge.

In August-September 1995 and August 1996 the Shelf Edge Study Acoustic Measurement experiment (SESAME) took place on the Malin shelf-edge, on the North-West UK shelf margin [5]. The experiment coincided with the NERC SES experiment, and a large complementary dataset of remotely sensed and in-situ measurements was gathered.

Figure 1 shows a close-up from an ERS-1 SAR image (20th August 1995, 1136 UTC) of the SESAME region. A prominent internal wave can be seen approaching the shelf edge, with the characteristic signature of an internal soliton of depression, with weaker undulations trailing it. Overplotted on Figure 1 is the tow-track of the survey vessel RV Colonel Templer from 0100 to 0200 UTC on the 19th August. The data gathered by towed thermistor chain is shown in Figure 2, and indicates the presence of a packet of four internal waves of depression, rank ordered in amplitude, the leading wave being a solitary wave with an amplitude of displacement of -49 m. On the survey track in Figure 1, the positions where the waves were measured are marked 1-4, from the leading wave to the back of the packet respectively. It seems likely that the waves in Figure 2 are of the same type as the internal bore and undulations seen in Figure 1.

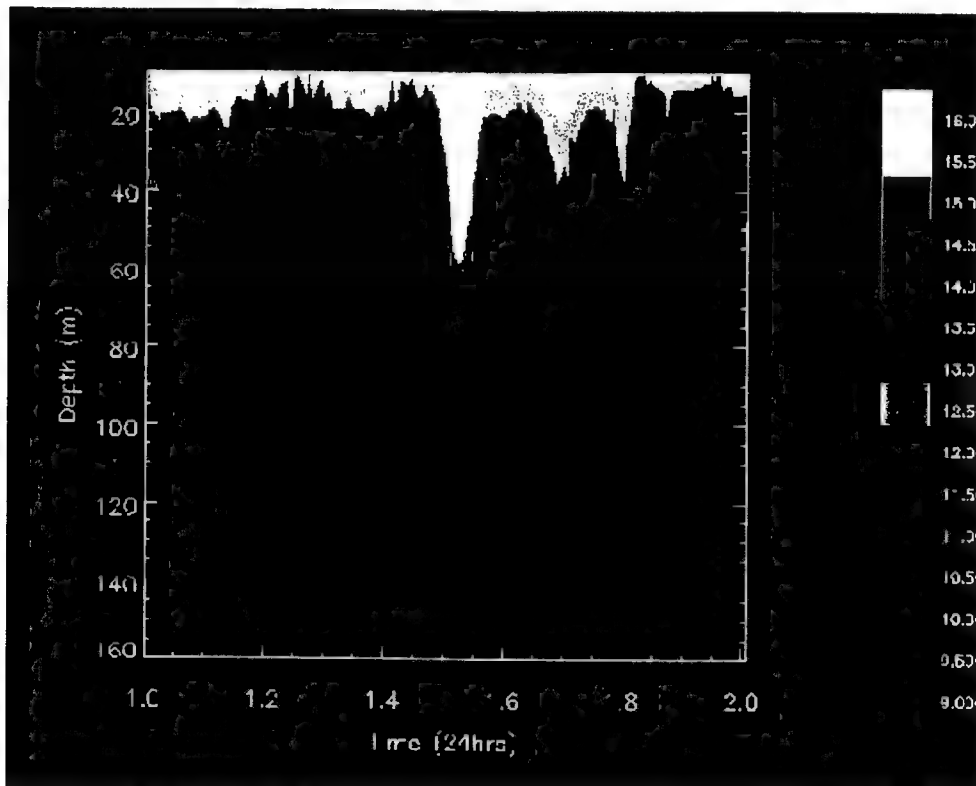


Figure 2. Thermistor chain cross-section of temperature ($^{\circ}$ C) through internal wave packet over Continental slope. Total water depth 400 m.

The phase speed of the waves has been derived independently by two methods

1. Comparing the SAR image in Figure 1, and an ERS-2 image 24 hours later showing a similar feature
2. Comparing the positions of the wave signatures in Figure 1 with the positions of the waves when measured by thermistor chain.

Here the assumption is made that the bore is regenerated every 12.4 hour M2 tidal cycle. The phase speed is then deduced by noting the distance between the wave positions, and the difference in tidal phase. These methods gave consistent values of phase speed between 55 and 65 cms^{-1} , confirming that the signatures are of the same feature, which propagates from deep on the slope towards the shelf edge, evolving into a set of large amplitude internal waves.

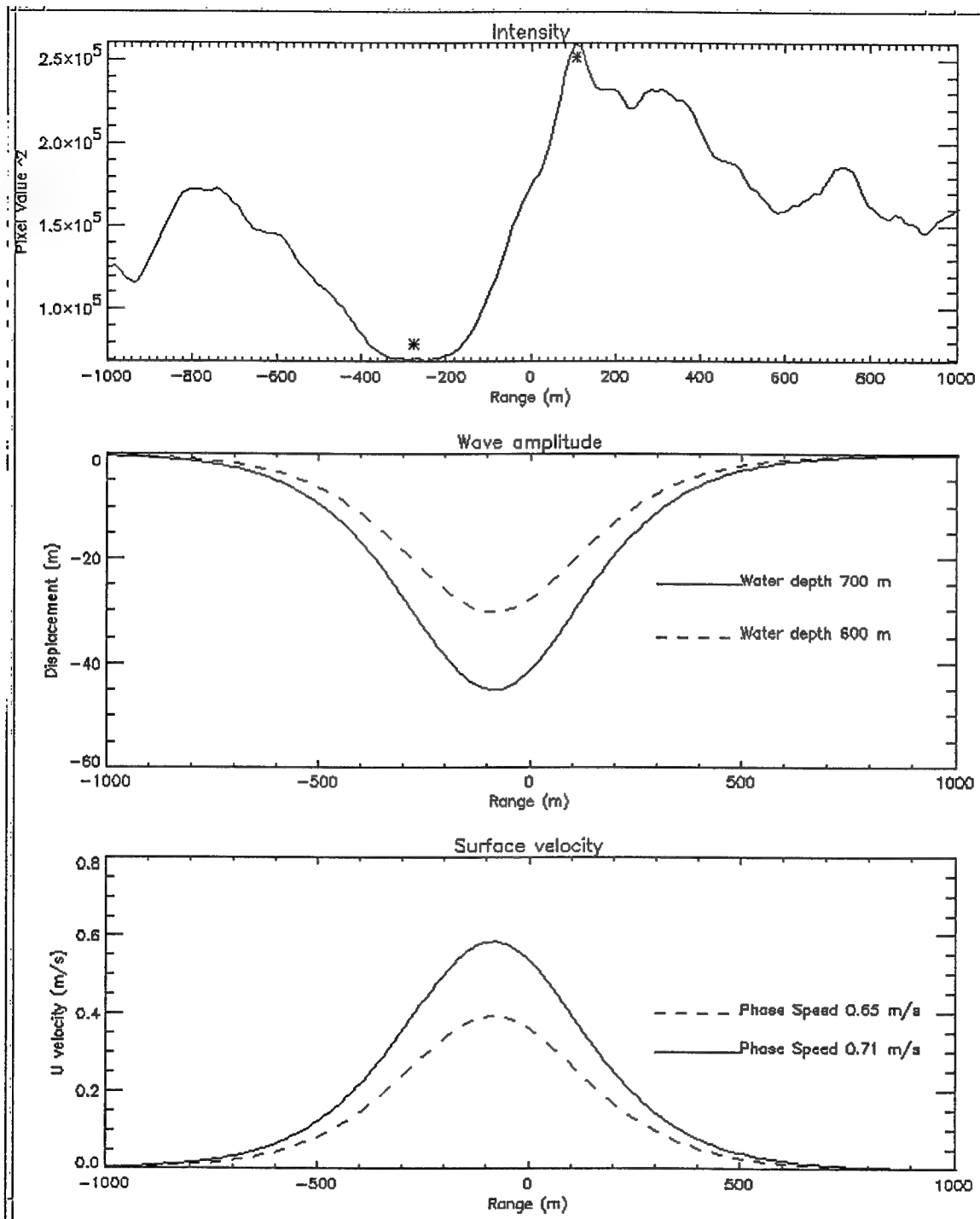


Figure 3. Profile of ERS image intensity across the internal wave (top), and the equivalent KdV soliton amplitude (middle) and surface current (bottom). Solid line: wave at 700 m water depth, dashed: in 600 m water depth.

4. Prediction from SAR

Figure 3 (top) illustrates a profile of image intensity perpendicular to the leading wavefront in Figure 1. The profile has been produced by averaging in the along-front direction over the box shown in Figure 1, to remove image speckle, without removing important length-scale information in the cross-front direction.

From the image intensity profile the peak and trough associated with the leading internal wave was identified (range positions marked with asterisks), and used to give the distance D defined above. From this the half width L of the equivalent KdV soliton was derived.

As discussed above, knowledge of the soliton half width and of the background environmental conditions allows an estimate of wave amplitude to be made. For this case, the basic 1 km geolocation accuracy of ERS-SAR enabled the water depth of the measurements to be calculated as between 600 and 700 m (see Figure 1). The environmental parameters of linear phase speed, and coefficients a and g were determined from coincident survey data and are listed in Table 1. Using this information, and equations 1-4, the wave amplitude was estimated for the two possible water depths, and the result is plotted in Figure 3(middle). Assuming the deeper water depth, an estimate of 45 m for the wave amplitude was derived, close to the observed value. For the shallower depth of 600 m, an amplitude of 30 m was calculated.

The soliton theory also allows estimation of surface velocity and phase speed. these are illustrated in Figure 3 (bottom). An important point here is that the surface velocity approaches the phase speed, implying that these are large finite amplitude waves which may be subject to turbulent processes and breaking. The large surface currents of $O(0.5 \text{ m/s} \sim 1 \text{ knot})$ explain why the wave has a striking signature on the SAR image. Further, the estimates of phase speed are close to the observations, indicating that this method may be used to predict the soliton position forward in time.

Table 1. Environmental parameters (coefficients of the KdV equation) for period 19-21 August, for three water depths, from SESAME survey data. c_0 is the linear phase speed, a is the non-linear coefficient, and g is the dispersive coefficient. The values were derived for the first mode solution to realistic density stratification.

Water Depth	c_0	a	g
400	0.48	-0.016	1535
600	0.5	-0.015	3202
700	0.51	-0.014	4449

Conclusions and Discussion

The SAR prediction method gives a good estimate of wave amplitude and phase speed from the

across-wavefront lengthscales. However, in practice the estimate is sensitive to the following two factors:

- The knowledge of water depth, as one of the environmental parameters (g) is critically dependent on depth. This is particularly important in shelf-edge regions.
- The measurement of the peak-trough distance D , and the related half width L . As the soliton amplitude is inversely proportional to the square of the half width, small changes in half width measurement lead to large changes in amplitude prediction.

In the example shown here, the phase speed estimate was less critically dependent on these two factors (as the coefficient a , which is related to the nature of the stratification, changes little). Consequently it seems that the method may be used to forecast the likely position of the wave, and give an order of magnitude (within a factor of two, say) estimate of the amplitude.

It should be noted, of course, that the type of signature of internal waves illustrated in Figure 1 (namely the bright and dark banding) does not always occur, especially in the presence of natural surface slicks [6]. The single sign signatures [7] produced in these other circumstances will need to be treated differently, and this is an area of future work.

A final point of interest is that the KdV soliton solution appears to well describe a wave of amplitude -49 m on a background thermocline which only extends to 60-80 m. Clearly the wave is finite (i.e. large) amplitude, and so the KdV solution (to first order in wave amplitude) should not be valid. However, detailed analysis of the thermistor chain data (see Annex and [5]) confirms that the wave shape is that of a KdV soliton. The question of why this solution is suitable for waves of such large amplitude remains open.

Related Work at DERA

The non-linear interactions of internal solitons, as observed in SAR imagery, is being studied using a three-dimensional CFD code and being compared to previous analytical results. Preliminary results indicate that the observations confirm the analytical predictions of Mach-stem formation due to phase shifts, and that the CFD code can be used to model complex three-dimensional interactions.

The effects of internal solitons on acoustic propagation has been studied using a simple surface duct propagation model. Results show that the typical internal solitons observed near shelf-edges in summer thermocline environments, which are solitons of depression, act to reduce diffraction leakage out of the duct due to deepening of the surface mixed-layer. Consequently this increases the range of acoustic frequencies which can be trapped in the duct. These results have been incorporated into a software demonstrator that takes a SAR image as input, and outputs estimates of internal wave amplitude and of the duct leakage.

References

[1] Ostrovsky, L A and YU A Stepanyants. Do internal solitons exist in the ocean, *Rev of Geophysics*, 27, pp293-310, 1989

[2] Zabusky N J and M D Kruskal (1965) ?Interaction of solitons in a collisionless plasma and the recurrence of initial states?, *Phys Rev Letters*, 15, 250-243, 1965

[3] Alpers, W. Theory of radar imaging of internal waves, *Nature*, 314, pp 245-247, 1985

[4] Gargett, A. E. and Hughes, B. A. (1972) ?On the interaction of surface and internal waves?, *Journal of Fluid Mechanics*, 52(1), 179-191.

[5] Small J, Hallock Z, Pavey G and J Scott. ?Observations of large amplitude internal waves at the Malin shelf-edge during SESAME 1995?, submitted to *Continental Shelf Research*, 1998.

[6] Ermakov SA, Salashin S G, and A R Panchenko. ?Film slicks on the sea surface and some mechanisms of their formation?, *Dyn. Atm Oceans*, 16 (1992), 279-304

[7] DaSilva et al.? Role of surface films in ERS SAR signatures of internal waves on the shelf 1. Short period internal waves?, *J Geo Res*, 103, C4, 8009-8031, 1998

Annex. Is the wave a soliton ?

Finally, the following question may be asked: was the solitary wave really a KdV soliton, or did the method give good predictions by chance, for a non-soliton wave ? This has been checked, by detailed analysis of the thermistor chain data. Using information on the wave speed and direction from the observations, it is possible to remove the Doppler shift due to ship towing through the internal wave. This has been done in Small et al 1998. Figure 4 shows an illustration of the results: here the displacement curves for a selection of isotherms have been normalised to unity and overplotted as a function of true range. Overplotted as asterisks is the KdV solution for a wave of -49 m in a water depth of 400 m, again using coincident survey data to provide the environmental parameters. The close fit of the KdV solution and the observations for the majority of the displacement curves indicate that the wave has soliton characteristics.

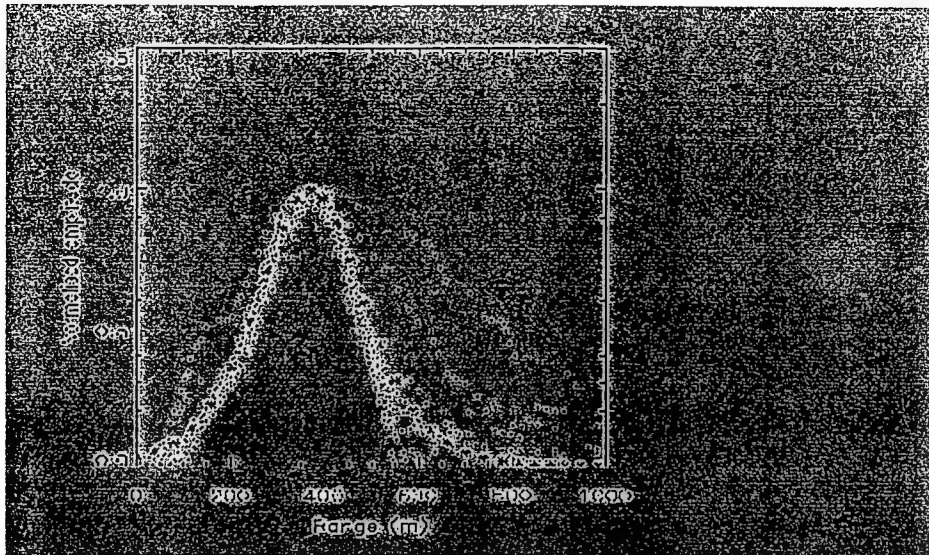


Figure 4. Profiles of normalised amplitude as a function of range for the lead wave in Figure 2, corrected for Doppler-shifting. Dotted lines are the normalised amplitudes of displacement for selected isotherms, and the asterisks are the KdV solution for a wave of -49 m amplitude.

Unresolved question

Observed mooring records sometimes have the appearance of classic internal tide bores (or ?solibores?), and at other times in the same location appear random (e.g. at the moorings S and D shown in Figure 1). The latter effect may be due to the influence of more than one internal wave source, together with the complex interaction phenomenon this implies. The question is: is it worthwhile to model the waves deterministically ? this is linked to the question: for how many tidal cycles can predictions based on one SAR image be valid ? (In the SESAME results above, the internal wave pattern repeated itself for at least 5 cycles).

British Crown Copyright 1998/DERA
 Published with the permission of the Controller of Her Britannic
 Majesty's Stationery Office.

A Mechanism for Sediment Resuspension by Internal Solitary Waves.

D. J. Bogucki and L. G. Redekopp

Department of Aerospace and Mechanical Engineering
University of Southern California
Los Angeles, CA 90089-1191

Convincing evidence is emerging that internal solitary waves and other longwave packets propagating in shallow seas can frequently stimulate remarkably elevated rates of resuspension of sedimentary material. The accumulating evidence suggests that, at least under some wave conditions, an interesting and effective coupling exists between the wave-induced velocity field and the associated boundary layer forming adjacent to the bottom surface. This note is directed toward revealing the peculiar dynamics associated with this coupling under a particular class of waves and to argue that the consequent dynamics underlies the observed bursts of resuspension under the footprint of many long wave features.

Long internal waves propagating within a waveguide in shallow seas can appear either as waves of elevation (crests containing elevated isopycnal lines) or waves of depression (crests containing depressed isopycnal lines). The particular wave polarity realized in any application is determined by the vertical structure of the density stratification and the background velocity shear of the water column. Now, the induced velocity field associated with a solitary wave or other longwave feature, and its coupling with the bottom boundary layer, will differ depending on the wave polarity. Under the crest of a wave of elevation, the induced velocity along the bottom surface (relative to a frame fixed to the wave) will experience a spatially-varying acceleration. Fluid parcels near the front of the wave will undergo a deceleration (adverse pressure gradient) followed by an acceleration downstream of the wave crest. Fluid parcels will experience a similar deceleration-acceleration sequence under troughs of a packet of waves of depression. In either case, the strength of the deceleration-acceleration will increase with wave amplitude (actually, in proportion to the $3/2$ power of the wave amplitude based on KdV theory). Hence, one anticipates that boundary layer separation, the creation of a boundary-trapped vortex or recirculation region, will appear in the footprint of larger amplitude waves. Furthermore, since the wave-boundary layer interaction is dependent of the vertical proximity to the peak wave-induced velocity to the bottom surface (i.e., on the eigenfunction), the strength of the interaction is probably quite dependent on environmental conditions.

The presentation here focuses primarily on the specific wave-boundary layer interaction associated with a solitary wave of elevation propagating against a large-scale shear flow. This configuration closely mimics the observed features on the Palos Verdes Shelf described by Bogucki et al [1997]. The flow state arises as the transient longshore current experiences a resonant interaction with cross-shelf topographic features. The topographic resonance stimulates solitary wave packets which propagate

counter to the sheared, longshore current. Instrumental records from the mooring reveal multiple instances of episodically-elevated resuspension rates as the solitary wave packets move slowly upstream past mooring positions.

The results presented below are based on a direct numerical simulation of the primitive equations of motion for a model flow that approximates the field experiment. The numerical model presupposes a base state consisting of a uniform shear flow (Couette flow) between parallel, horizontal boundaries defining the bottom of the wave guide and the level of the density interface in a two-layer stratification. The mean flow velocity and pressure along the upper boundary vary in the streamwise direction in accordance with an isolated KdV solitary wave. No-slip boundary conditions are applied on the bottom, impermeable surface. The wave-induced motion satisfies stress-free boundary conditions on the upper, moving surface. The speed of the mean flow along the upper surface (alternatively, the interface of a two-layer model) is prescribed according to the relation

$$U(x) = 1 - \Delta \operatorname{sech}^2(x) \quad (1)$$

The parameter Δ controls the amplitude and wave number of the solitary wave (alternatively, the streamwise deceleration-acceleration of the flow and the associated pressure gradient felt by the bottom surface). The other parameter that enters the problem is the Reynolds number based on the ambient flow velocity along the upper surface and the depth of the (lower) layer. The unsteady simulations are time-accurate and permit interrogation of any ensuing spatio-temporal dynamics as the wave amplitude and Reynolds number are varied.

For purposes of brevity, and in order to expose the onset of a particular dynamics termed a global instability as the wave amplitude increases, we only present results for a fixed Reynolds number of 10^4 . The stationary flow (steady streamline pattern) in the boundary layer under a wave with amplitude $\Delta = 0.34$ is shown in Figure 1. The flow in the boundary layer is unstable based on a local instability analysis, but the spatially-developing nature of the flow inhibits any streamwise growth of unstable disturbances. This is not to say that if some disturbance field (noise) were convected through the flow domain that some spatial amplification would not occur within the separation bubble. However, no intrinsic dynamics is observed. As shown in Figure 2, however, a completely spontaneous dynamics appears quite abruptly when the wave amplitude is increased to $\Delta = 0.36$. Figure 2 shows the spatial structure of the streamline pattern at different phases of the synchronous motion that accompanies the onset of the global instability. That the supercritical dynamics is synchronous is clearly evident from Figure 3 where frequency spectra at several streamwise positions within the separated region are superimposed. Here red and blue colors correspond to time series of w velocity and their power spectra at two streamwise positions separated by one-half the solitary wave length. The bottommost panel shows the coherence between these two points. The oscillations are clearly coherent for the base frequency and its harmonics. The global instability appears suddenly, is entirely intrinsic to the separation bubble, is a stable spatio-temporal finite-amplitude state saturated by nonlinearity, and, based on other work, is robust in the presence of disturbances that are convected through the flow domain.

The appearance of separated flow and consequent global instability as the wave amplitude increases comprise the basic hydrodynamical features of the proposed mechanism for enhanced resuspension by internal waves in shallow seas. As is evident from Figures 2 and 3, the global instability endows the flow with a spatio-temporal coherence that extends over the entire extent of the separated flow under the solitary wave. The coherent stress fields acting on the bottom surface, together with the coherent dynamics in the field extending considerably beyond the boundary layer proper, creates the environment

to both resuspend particles and to transport significant fractions to elevated levels. The latter statement is, of course, conjectural at this stage. However, we are preparing additional simulations where particles are introduced at the lowest level in order to quantify any preference for enhanced vertical particle transport by the global instability and attempt to place the conjecture on firm footing. The corresponding separated flow under the trough of a wave packet of depression is also being examined for its susceptibility to global instability and its possible contribution to resuspension by the same fundamental mechanism.

This work was supported by ONR Code 322PO.

References:

Bogucki, D., T. D. Dickey and L. G. Redekopp. 1997. Sediment resuspension and mixing by resonantly generated internal solitary waves. *J. Phys. Ocean.*, 27: 1181-1196.

This is work in progress; more up-to-date version can be viewed at:

<http://earth.usc.edu/~dbogucki>

Contact information:

Redekopp@spock.usc.edu or DBogucki@spock.usc.edu

- Figures ...
- About this document ...

[Next](#) | [Up](#) | [Previous](#)

Next:Figures ...
1998-09-16

D. Bogucki and L. Redekopp: A mechanism for sediment resuspension ...
Figures

Figure1:

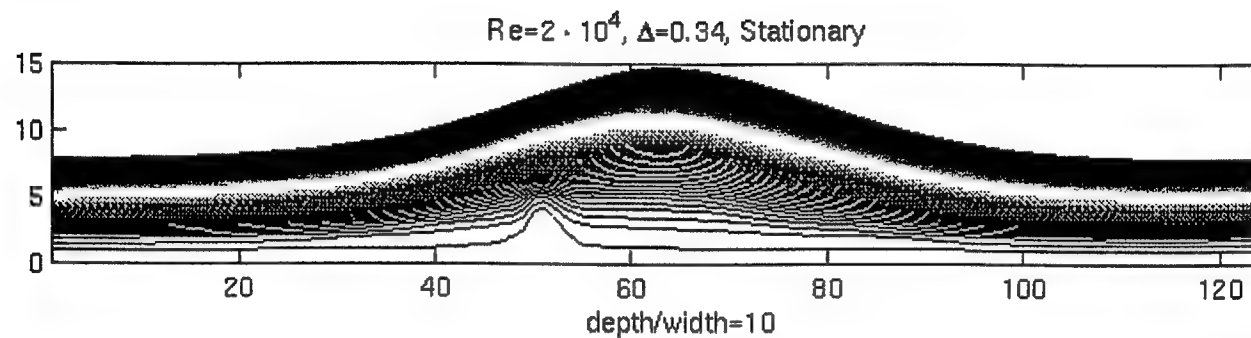


Figure 2:

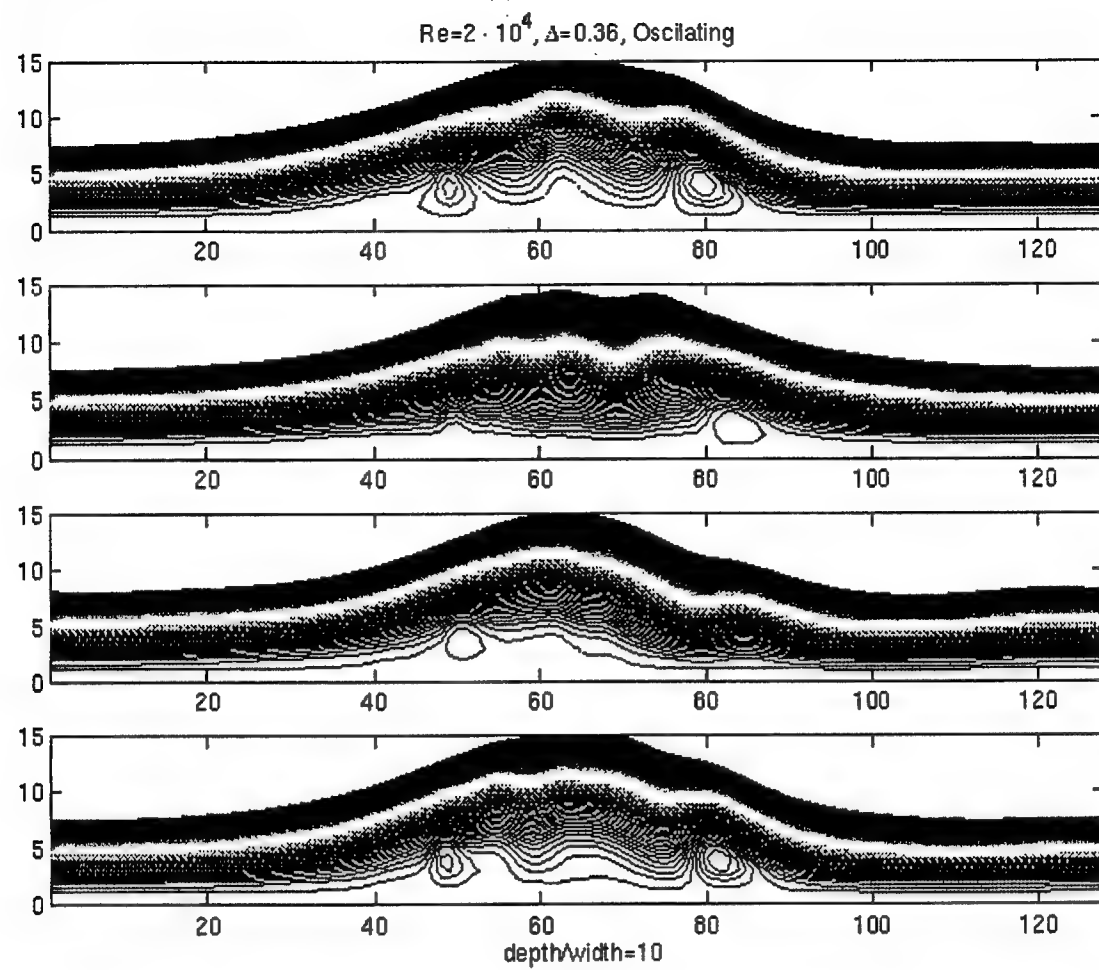
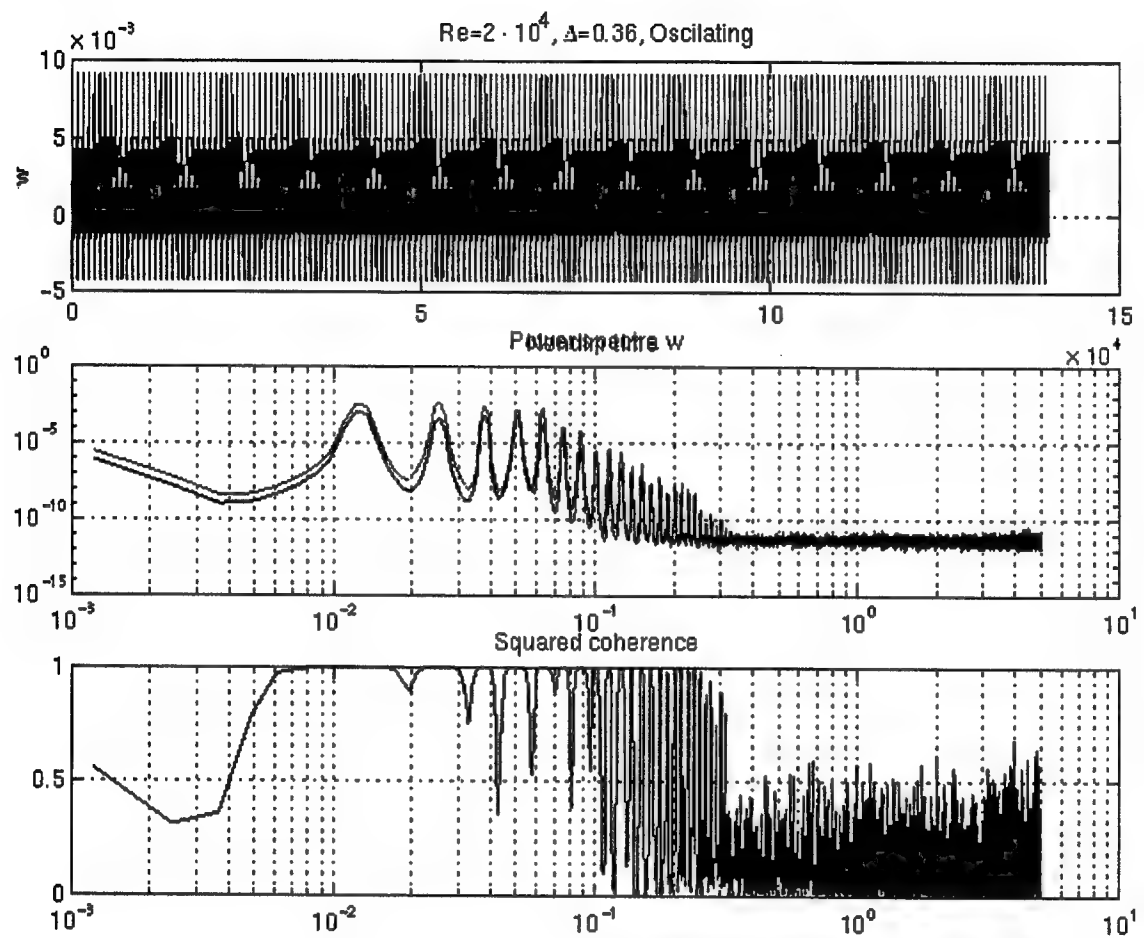


Figure3:



1998-09-09

The Massachusetts Bay Internal Wave Experiment - 1998: Do solitons resuspend the bottom sediments?

Bradford Butman¹, Steven P. Anderson², Alberto Scotti²,
Robert C. Beardsley², Richard P. Trask², and Robert A. Weller²

¹ U.S. Geological Survey, Woods Hole, Massachusetts

² Woods Hole Oceanographic Institution, Woods Hole, Massachusetts

Prepared for the Workshop on Internal Solitary Waves in the Ocean: Their Physics
and Implications for Acoustics, Biology, and Geology
27-29 October 1998, Victoria, BC, Canada

Abstract

A field experiment is being carried out in Massachusetts Bay to assess the role of internal solitons in resuspending the bottom sediments, to document how the waves change as they propagate inshore and dissipate, and to test whether the waves follow the KdV non-linear dispersion relation. The project consists of a field experiment consisting of a large moored array and hydrographic observations, and numerical modeling. This paper contains a description of the hypotheses to be tested in the project and the field program.

A. Introduction

The existence of large-amplitude internal solitons in Massachusetts Bay (Figure 1) has been known since 1971 (Halpern, 1971) and have been the subject of several investigations. In summer when the water is stratified, packets of waves propagate westward into the bay on the flood (westward flowing) tide at about 0.5 m/s. The internal waves are observed in packets, have periods of 5-10 minutes, and cause downward excursions of the thermocline of as much as 30 m. The waves are hypothesized to evolve from a lee wave that forms on the eastern side of Stellwagen Bank on the ebb tide (Haury et al, 1979). Surface expressions of the internal wave packets have not been observed in the set of SAR images obtained in 1975 in water shallower than about 50 m (Trask and Briscoe, 1983).

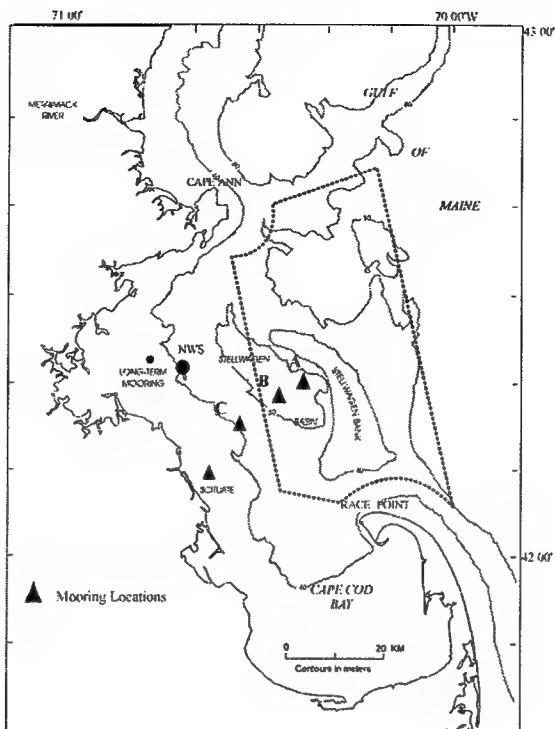


Figure 1: Instrumented moorings were deployed at four sites across Massachusetts Bay to investigate the internal waves that propagate westward from Stellwagen Bank each tidal cycle. A horizontal mooring, with instruments spaced about 30 m apart in the horizontal, was deployed at Site B.

The surficial sediment distribution (Figure 2) in Massachusetts Bay reflects the topography the processes which resuspend sediments, and the geologic history. Stellwagen Basin, the deepest part of Massachusetts Bay, is about 90 m deep and is floored with fine-grained mud. Along the western shore of Massachusetts Bay, the transition from mud to coarser sand, gravel and outcropping rock occurs at 40- 50 m water depth. Surface waves from winter storms, particularly waves generated from storms with winds from the northeast that enter Massachusetts Bay from the Gulf of Maine, are sufficiently to resuspend the bottom sediments in water depths shallower than 40 - 50 m. These waves winnow fine sediments that accumulate along the shallow western shore of Mass Bay, and the currents driven by the winds from the northeast carry the sediments southeastward toward Cape Cod Bay and offshore into Stellwagen Basin where they accumulate. Elevated levels of contaminants, introduced from the Boston Metropolitan region, are found in the sediments of Cape Cod Bay and Massachusetts Bay. The internal waves may cause resuspension and transport of these sediments and associated contaminants in summer. In addition, the dissipation of the internal waves may play a role in the transition of the sediment from fine to coarse along the western shore.

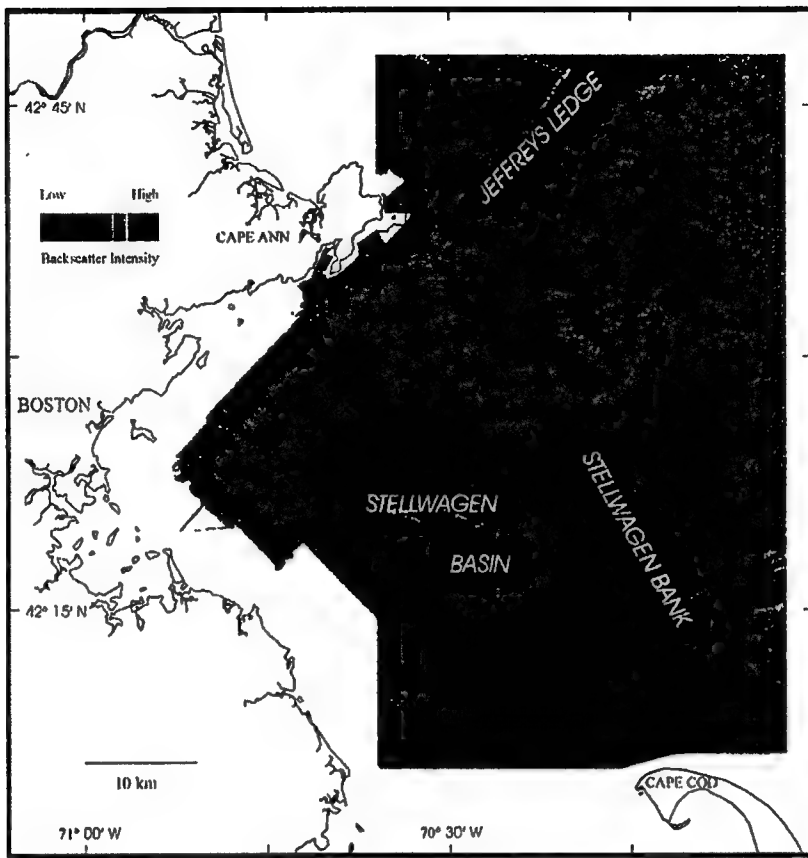


Figure 2: Sun-illuminated map of the coastal region to the east of Boston Massachusetts Bay, including the Stellwagen Bank National Marine Sanctuary. The backscatter intensity is draped over the topography. Red indicates high backscatter material (sand, gravel and rock); blue indicates low backscatter material (mud). Within each backscatter color, the intensity varies from dark to light depending on the sun illumination. The image illustrates shows a complex and wide variety of sedimentary environments. The transitions between sediment types is often very sharp. Topographic features observed here were formed for the most part by glacial processes. Ice containing rock debris moved across the region, sculpting its surface and depositing sediment to form basins, knoll, banks and other features. Stellwagen Bank and Jeffreys Ledge are shallow banks (20-40 m water depth) covered with sand and gravel. Stellwagen Basin (80-100 m) is floored with mud. In winter, the sea floor is modified by storm currents and waves from the northeast. These currents erode sand and mud from the shallow banks and transport them into the basins. Currents associated with internal waves generated by Stellwagen Bank may resuspend the fine sediments in Stellwagen Basin, and winnow sediments from the western shore of the bay.

B. Hypotheses to be tested in the Summer 1998 Field Experiment

The summer 1998 experiment was carried out to address the following questions:

- (1) Do the internal solitons cause resuspension of bottom sediments?

The maximum current speed reported by Trask and Briscoe (1983) during a 5-day experiment was about 60 cm/sec at 40 m depth. Near-bottom speeds of this amplitude would be expected to resuspend the muddy bottom sediments. Thus the solitons may be important in the transport of the contaminated sediments found in Stellwagen Basin. Transport and resuspension by the shoaling internal waves may also influence the

location of the transition from fine to coarse sediments that is observed at about 50 m water depth along the western shore of Massachusetts Bay. The internal solitons may undergo rapid changes and dissipate at some point along the western shore of Massachusetts Bay.

(2) How do the wave packets evolve as they propagate inshore?

Previous field observations were carried out at a single location in the center of Massachusetts Bay and did not investigate how the waves change as they propagate inshore. Of particular interest what how the waves dissipate along the western shore.

(3) Do the waves follow the KdV non-linear dispersion relation?

The Korteweg-de Vries equation (Gear and Grimshaw, 1983) describes to first order the propagation of solitons in shallow water. However, Holloway (1987) and others have found that they must employ second-order wave amplitude wave theory to account for the observed wavelength and phase speed of solitons. The horizontal mooring will allow for a direct measurement of phase speeds and horizontal wavelengths and the nearby surface-subsurface mooring pair will provide vertical mode structure and amplitudes of the waves. This data will allow for a direct test of the dispersion relation derived from the non-linear theory and determine if the second order theory is required to accurately describe the waves.

C. Summer 1998 Field Experiment

The MBIWE98 experiment has 3 components: moored array, hydrography, and numerical modeling.

Moored Array

The moored array consisted of instruments deployed at 4 stations spaced across Massachusetts Bay (Figure 1 and Figure 3). Station A, located about 5 km from the western edge of Stellwagen Bank at 95 m water depth, was placed to provide a description of the waves near the generation region. Station B was located approximately 12 km from the western edge of Stellwagen Bank in the center of Stellwagen Basin at 85 m water depth. Station B is near the location of previous observations of the internal solitons made by Halpern (1971) and Haury et al (1979). Site B was heavily instrumented from 10 m from the surface to 1 m above bottom with an array of temperature, conductivity, current, light transmission and pressure instruments deployed on 4 separate moorings. One of the moorings at the central site (B) was a horizontal mooring to provide closely spaced measurements in both the horizontal and vertical. Site C was located at 50 m water depth, just offshore of the transition from fine to coarse-grained sediments and included temperature, conductivity, current and light transmission. The inshore site was at 20 m water depth. In order to resolve the high-frequency motions caused by the internal waves, instruments in the array were set to sample every 15 s (for most temperature and conductivity observations), or every minute (for most current observations).

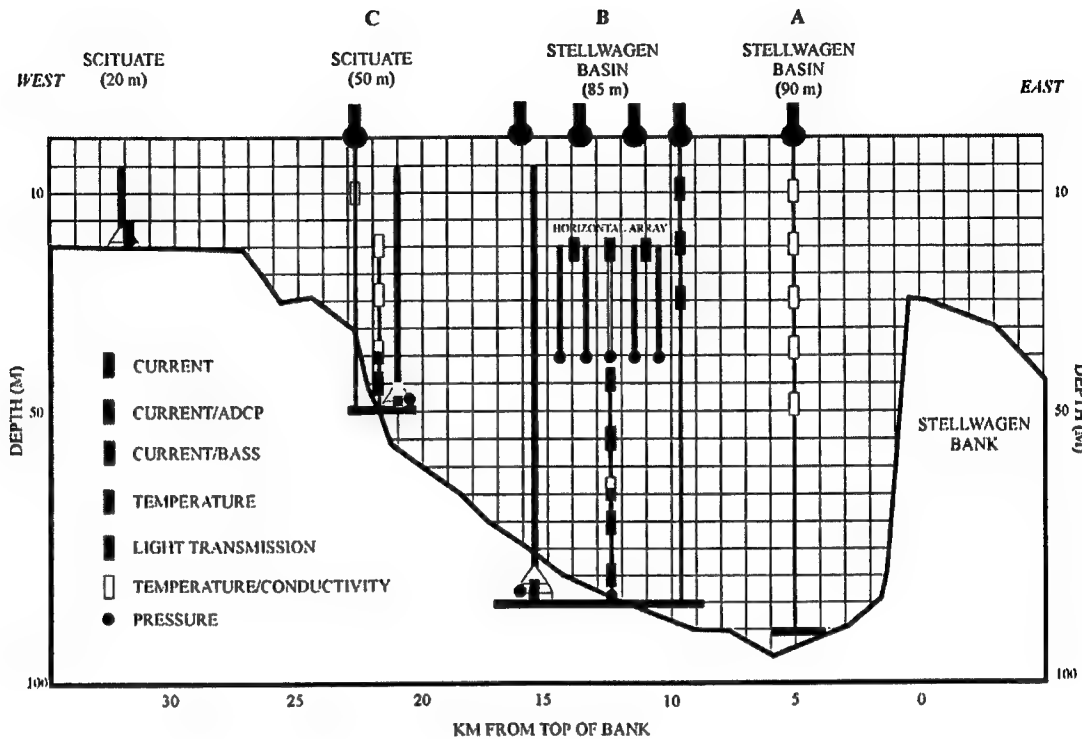


Figure 3: Instruments were deployed at four sites across Stellwagen Basin to observe the packets of internal solitons as they propagate westward across Massachusetts Bay from Stellwagen Bank. The horizontal array was deployed at site B.

The horizontal mooring deployed at Site B is a new technology, under development by WHOI in cooperation with ONR, designed to provide closely spaced (order 20 m) measurements in both the horizontal and vertical in the coastal ocean. The mooring consisted of a 160 m long horizontal wire tensioned between two 48" subsurface floats at 20 m below the surface. The floats are kept in position by anchors attached to each float and set at a 45° angle. Along the horizontal wire, 5 vertical wires spaced 30 m apart supported temperature and conductivity sensors 5 m apart in the vertical from 20 to 45 m water depth. In addition, three current meters were mounted on the horizontal wire, one at the center, and one at each end 55 m from the central meter.

Hydrography and water displacement observations

Single hydrographic sections (conductivity, temperature and light transmission) along the mooring line were obtained on August 6 and August 20 to provide a measurement of the water column structure along the mooring line. Fourteen stations were occupied along the mooring transect.

Scatterers on the thermocline and in the near-surface layer provide a marker of displacements in the water column that can be observed using a high frequency echo sounder. A 200 kHz echo sounder was used on the mooring deployment cruise to monitor the excursions of the thermocline at the central site. In addition, several sections were made between the 40 and 70 m at Site C to document the internal wave amplitude and structure as they propagate into shallow water.

Modeling

Numerical modeling is focused on both the generation mechanism (lee wave hypothesis) and the evolution of the wave packet as it moves onshore. In particular, we plan to focus on the following questions: Why do waves seem to develop only on the inshore site of the bank? Is the process influenced by the different bottom slope on either side of the bank? What are the factors influencing the splitting and ordering of the wave packet? What does the current field look like near the bottom (which is important for the resuspension problem)? To answer these questions we plan to solve the 2D Navier-Stokes equations for a stratified fluid in vorticity-streamfunction formulation, with a realistic bottom topography.

D. Results to date

The moored array was deployed August 4-6 1998 from the RV ARGO MAINE, and was recovered September 1-2. The horizontal array was deployed within 10 degrees of the desired alignment (60 - 240 degrees true) and within a few meters of the desired depth. The complex mooring required approximately 10 hours to deploy. All instruments were in good shape on recovery, and the mooring showed little signs of wear.

During the deployment cruise the weather was exceedingly calm, and bands of smooth and ruffled water, surface expressions of the internal wave packets, were clearly visible. Sometimes the slicks were observed in intersecting patterns, suggesting wave packets from different generation regions. Undulation of the thermocline caused by the high-frequency waves were clearly observed at Site B by the 200 KHz echo sounder. One of the observations of Halpern (1971) was that the waves were rank ordered, with the largest amplitude wave the first to arrive. On August 6 however, the 200 kHz record shows larger waves arriving later in the packet. The sections across the hypothesized dissipation region near Site C showed modification in amplitude and pattern as the waves moved into shallow water. Undulations of the thermocline were observed to water depths of 30 m with the 200 KHz echosounder. Time did not permit following the waves further inshore.

ACKNOWLEDGEMENTS

This work was supported by the Office of Naval Research and the U.S. Geological Survey.

REFERENCES CITED

Chereskin, T.K., 1983, Generation of internal waves in Massachusetts Bay. *J. Geophysical Res.*, 88(4), p. 2649-2661.

Gear, J. A., and R. Grimshaw, 1983, A second-order theory for solitary waves in shallow fluids. *Phys. Fluids*, 26, p. 14-29.

Halpern, D., 1971, Observations on short-period internal waves in Massachusetts Bay. *J. Marine Res.*, 29(2), p. 116-132.

Haury, L.R., Briscoe, M.G., and Orr, M.H., 1979, Tidally generated internal wave packets in Massachusetts Bay. *Nature*, 278(5702), p. 312-317.

Haury, L.R., Wiebe, P.H., Orr, M.H., and Briscoe, M.G., 1983, Tidally generated high-frequency internal wave packets and their effects on the plankton in Massachusetts Bay. *J. Marine Res.*, 41, p. 65-112.

Holloway, P. E., 1987, Internal hydraulic Jumps and Solitons at the Shelf Break Region on the Australian

North West Shelf. J. Geophysical Res., 92 (C5), p. 5405-5416.

Lee, C.Y., and R.C. Beardsley, 1974, The generation of long non-linear internal waves in a weakly stratified shear flow. J. Geophysical Res., 79, p. 453-462.

Trask, R.P. and M.G. Briscoe, 1983, Detection of Massachusetts Bay internal waves by the Synthetic Aperture Radar (SAR) on SEASAT. J. Geophysical Res., 88(3), p. 1789-1799.

Internal Tides and Sedimentation on Continental Slopes

David A. Cacchione

Woods Hole Group, 715 Colorado Avenue, Palo Alto, CA 94303

Introduction

Current and temperature measurements obtained on a long-term mooring in 450 m water depth on the upper continental slope off northern California during STRATAFORM in 1997 reveal energetic tidal and higher frequency internal waves whose intensity and structure have considerable temporal variability. We describe these data and discuss implications of internal tidal wave dynamics for continental slope sedimentation and the generation of bottom and intermediate nepheloid layers in this region. A global model for the interaction of internal semi-diurnal tides and sediment deposition on continental slopes is presented in the context of these new results.

Evidence for intensified internal tidal flows over sloping oceanic boundaries has been mounting over the past 30 years. Time-series measurements of currents, temperature and salinity have documented significant energy levels of these flows over sloping topography, and field experiments have shown the intensification of these motions near the seafloor (Erickson, 1982; Holloway and Barnes, 1998). The amplification of across-slope velocities associated with shoaling internal waves was originally proposed theoretically by Wunsch (1969), and more recently elucidated through numerical models that include non-linear and viscous effects (Slinn and Riley, 1996; Holloway and Barnes, 1998). Early laboratory studies of progressive internal waves over a linear bottom slope showed upslope amplification of the wave forms and near-bottom velocities for cases when the energy rays or characteristics were reflected upslope or were aligned parallel to the bottom slope (Cacchione and Wunsch, 1974). Later laboratory studies confirmed these results, and further elaborated on the nature of the turbulent boundary layer flows produced by the reflecting waves over the slope (Ivey and Nokes, 1989; Taylor, 1993).

Cacchione and Southard (1974) discussed the potential significance of shoaling internal waves for causing sediment movement on continental shelves and slopes. They proposed a simple model that predicted entrainment of natural sediment on shelves and slopes by internal waves. Laboratory experiments confirmed that shoaling interfacial waves could generate ripples and larger bedforms in artificial sediment (Southard and Cacchione, 1972). More recent studies also have found that internal waves of various types are potentially capable of resuspending and transporting sediment (Bogucki, et al., 1998).

Cacchione and Drake (1986) proposed a conceptual model for the generation and maintenance of bottom and intermediate nepheloid layers above continental shelves and slopes by turbulent shear caused by shoaling internal waves. This idea was also suggested by Dickson and McCave (1986) based on an analysis of transmissometer profiles on the continental margin west of Ireland. The latter study proposed that well-defined intermediate and bottom nepheloid layers which emanated from bottom slopes in 400 to 600 m depths were caused by bottom erosion under internal tides and higher frequency internal waves. They calculated that the bottom gradient was aligned with the slope of the energy ray for the semi-diurnal internal tide, leading to increased velocities and erosion of the bottom sediment. No corroborating data from direct observations or current measurements were available to support this conclusion.

Results

An instrumented mooring was deployed on the upper continental slope in 450 m water depth in the STRATAFORM field area off northern California. The mooring site is about 15 nm NW of Eureka, CA. Instrument clusters including temperature, salinity, current, and light transmission sensors were located on the mooring at 60, 180 and 435 m water depths. This mooring has been maintained at this site since September 1995. Locally the bottom slope has a gentle gradient of about 0.05 (2.8o), and the bottom is mantled with fine silt. The shelf break in this area is at 150-m depth. The analysis presented here uses data collected from January 18 (Day 18) until April 15 (Day 107), 1997.

Internal semi-diurnal currents measured at about 15 m above the seafloor during this period occasionally exceed 35 cm/s; these strong currents are correlated with considerable mixing above the seafloor as indicated by concurrent temperature records. During these periods of enhanced internal tidal flows, downslope-directed currents persist for longer durations than upslope currents, leading to net downslope transport over many tidal cycles. The most striking internal tidal event occurred during the latter ten days of the deployment period. Upslope flows were peaked and of shorter duration than downslope flows, leading to net downslope motion over this period. Hourly upslope speeds reach 35 cm/s; downslope maximum speeds are about 40 cm/s. Hourly temperature data from the three bottom temperature sensors indicate intense periods of mixing (periods of temperatures coalescing). Times when temperatures are falling are correlated with upslope flows, suggesting movement of deeper cold water associated with internal tidal motion. The general structure of the velocity and temperature records suggests bore-like propagation of the internal tide upslope. Holloway and Barnes (1998) have described these types of internal tidal motions above a sloping bottom recently from numerical simulations and other field data.

Discussion

We propose that the strong internal tidal currents and associated turbulent mixing retard the settling of fine-grained materials onto the seabed, thereby inhibiting deposition along this section of the slope as observed in surficial sediment samples. Net downslope flow provides a mechanism for transport of suspended materials into deeper water or into intermediate nepheloid layers. It is not known whether the episodic, strong internal tidal currents resuspend the local bottom sediment along this portion of the slope.

Based on CTD profiles taken in this region during the mooring deployments, the slope of the characteristics for the internal M2 tide are approximately critical for bottom slopes at the shelf break and in slightly deeper water (about 500 m). Power spectra of the cross slope component for the middle and lowest current meters indicate that the energy at M2 is largest near the bottom, and that substantially elevated energy levels are found throughout the frequency band from M2 to M4. The latter overtide is approximately critical at the 450 m site, and also is substantially more energetic in the across-slope flows at the bottom current sensor.

Conceptual Model

Semi-diurnal internal tidal currents are likely major factors in shaping continental slopes. Continental slopes are generally narrow physiographic seafloor features that mark the transition from shallow continental to deeper oceanic domains. Continental slopes span a depth range of about 2500 m, with the shallow edge averaging about 120-150 m. The regional gradients of continental slopes generally fall in

the range of 0.50 - 50, but locally these gradients can be much steeper.

As the sediment deposition through time progrades the surface of the continental slope, a gradual reduction in the steepness of the slope surfaces might result. The bottom shear and energy dissipation along the slope associated with the semi-diurnal internal tide will likely increase as the slope surface approaches "critical." The turbulent mixing and shear associated with this process will inhibit deposition of the fine-grained suspended materials, creating intermediate and bottom nepheloid layers, and will cause the regional slope to reach an equilibrium gradient.

References

Bogucki, D., Dickey, T., and Redekopp, L., 1997. Sediment resuspension and mixing by resonantly generated internal solitary waves, *J. Phys. Oceanography*, 27, 1181-1196.

Cacchione, D.A. and D.E. Drake, 1986. Nepheloid layers and internal waves over continental shelves and slopes, *Geo-Marine Letters*, 6, 147-152.

Cacchione D.A. and J.B. Southard, 1974. Incipient sediment movement by shoaling internal gravity waves, *J. Geophys. Res.*, 79, 2237-2242.

Cacchione, D.A. and C.I. Wunsch, 1974. Experimental study of internal waves over a slope, *J. Fluid Mechanics*, 66, 223-239.

Dickson, R.R. and McCave, I.N., 1986. Nepheloid layers on the continental slope west of Porcupine Bank, *Deep-Sea Res.*, 33, 791-818.

Eriksen, C.C., 1982. Observations of internal wave reflection off sloping bottoms, *J. Geophys. Res.*, 87, 525-538.

Holloway, P.E. and B. Barnes, 1998. A numerical investigation into the bottom boundary layer flow and vertical structure on internal waves on a continental slope, *Cont. Shelf Res.*, 18, 31-66.

Ivey, G.N. and R.I. Nokes, 1989, Vertical mixing due to the breaking of critical internal waves on sloping boundaries, *J. Fluid Mechanics*, 204, 479-500.

Southard, J.B. and D.A. Cacchione, 1972. Experiments on bottom sediment movement by breaking internal waves, in *Shelf Sediment Transport, Process and Pattern*, ed. by Swift, D.J.P., Duane, D.B. and Pilkey, O.H., Dowden, Hutchinson and Ross, Stroudsburg, PA, 83-98.

Taylor, J.R., 1993, Turbulence and mixing in the boundary layer generated by shoaling internal waves, *Dynamics of Atmospheres and Oceans*, 19, 233-258

Slinn, D.N. and J.J. Riley, 1996, Turbulent mixing in the oceanic boundary layer caused by internal wave reflection from sloping terrain, *Dynamics of Atmospheres and Oceans*, 51-62.

Wunsch, C.I., 1969. Progressive internal waves on slopes, *J. Fluid Mechanics*, 35, 131-144.

Are Strongly Sheared Baroclinic Currents Sources for Internal Solitons?

John R. Apel

P.O. Box 12131
Global Ocean Associates
Silver Spring, MD 20908

There are two pervasive, near-global source regions for the generation of internal solitons: (1) continental shelf breaks and (2) undersea sills or ridges protruding into the thermocline. A third, less ubiquitous source is found in the intrusion of fresher, lighter water (such as river outflow or glacial melt water) into the denser water of the sea. The mechanisms that are active in these regions usually involve current flows moving more or less normal to the bathymetry, either onshore or offshore, which have the effect of depressing or elevating the oceanic density distribution away from equilibrium. The excursion, if large enough, will propagate away as an internal solitary wave of some type or other.

One of the uncertainties in the understanding of solitons is found at the next level of detail, e.g.: What are the fluid/bathymetric conditions required for the generation process? For the continental shelf regimes, two hypotheses have been advanced. The first posits that an offshore current flow - typically tidal - forms a lee wave down-current, which may or may not undulate. When the tidal current goes slack, the lee wave, which had been propagating in the moving current at a speed equal and opposite to the current, now continues to hold that speed in the slackening water, and slips up and over the shoal. As it evolves in the radiation region beyond the source area, it oscillates with deepening modulation depth and soon becomes a solitary wave train. The second hypothesis holds that the barotropic ocean tide, when incident upon the continental shelf slope, may scatter into baroclinic modes at the shelf break, thereby setting up the needed density disturbance, which then proceeds as in the first case. For flow over sills, similar mechanisms are at work, but with the space into which it radiates, and thus its ultimate evolution, being different.

With the lee-wave mechanism occurring on the offshore phase of the tide and the baroclinic-scattering mechanism occurring during the onshore phase, they should be readily distinguishable. In fact, it has been difficult to sort them out observationally (R. Chapman, private communication). As Sabinin (K. Sabinin, private communication) has observed, these may be two faces of the same coin, with the different theoretical languages used to discuss them obscuring the possibility that both mechanisms are at work, the first during the offshore flow, followed by the second, during the onshore flow. I would consider the resolution of the generation mechanism questions to be a research priority of high order. These are fully testable hypotheses.

There appears to be yet another kind of region that generates internal solitons, likely very intense ones. Clear instances of this have been observed in two satellite images (both SAR). They are (1) the Yucatan Strait, where the headwaters of the Gulf Stream flow northward between Cuba and Mexico, and (2) the Luzon Strait between Taiwan and Luzon, where the Kuroshio is also north-flowing. Figures 1 and 2

show ERS-1 SAR images of these solitons. Figure 1, of the Yucatan Strait, was provided by D. Sheres, and Fig. 2, of the South China Sea, by A. K. Liu and M. K. Hsu. The geographical scales of the two figures are roughly comparable. Both regions are characterized by strong western boundary current flows that are in the process of turning from zonal to meridional flow, and by relatively steep topography on the cyclonic boundary of the current. Both are on the westward sides of the basins. While the barotropic tide (which is the usual causative agent) in the Caribbean is not as strong as that in the Western Pacific, and the geographical tidal exposure of the Yucatan Peninsula is not as great as the islands in the Luzon Strait, the intensities and dimensions of the surface signatures are similar.

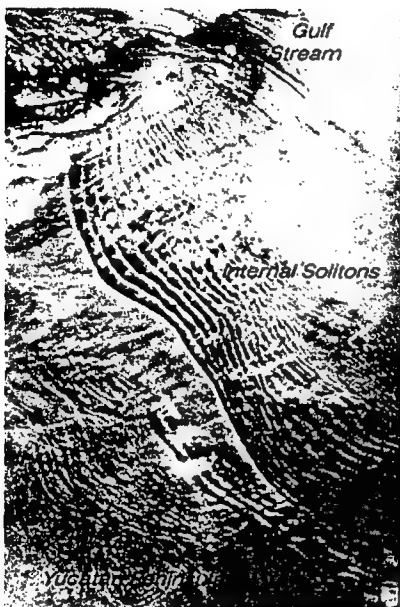


Figure 1 ...



Figure 2

Most interestingly, both soliton packets are propagating approximately normal to the mean direction of flow. Usually such waves propagate in roughly the same, or essentially opposite to, the direction of the current. Thus these observations raise the questions: Is there some new mechanism operating that produces waves at right angles to the mean flow; or are there simply the familiar processes at work here in unfamiliar geography? Perhaps the ever-present mesoscale meanders of the boundary current systems result in flows with some component normal to the isobaths, so that the old mechanisms can work. This is effective only as the sine of the angle, thereby reducing the component of flow to small values, probably below Froude Number one. Or perhaps the deep, 500-800-m thermocline of the boundary currents provides a buoyancy potential energy storage at the edge of the bathymetric gradient that somehow generates the soliton packet. The question then is where the wave momentum normal to the boundary current flow comes from.

Beyond these intense solitary waves apparently launched from boundary currents near their turning

points, there is some scattered evidence that there are analogous but smaller solitons to the north, moving toward the northwest, away from the cyclonic edge of the Gulf Stream. Such have been glimpsed in the Florida current off Cape Canaveral and the Gulf Stream north of Cape Hatteras.

This is a tantalizing problem for which the observational evidence is slim but provocative. It suggests that a modest field program should be undertaken to rough out the situation, perhaps at Yucatan, in order to understand more of what the remotely sensed imagery appears to be telling us.

The theoretical treatment we call the "dnoidal model". A paper outlining its properties is currently under review for publication. It asserts that the displacement, (r, z, t) of an isopycnal surface during the passage of an internal soliton can be written as the product of the little-known "dnoidal" solution to the Korteweg-deVries equation for the amplitude, and a numerical solution to the Taylor-Goldstein equation giving the vertical structure function, $W_k(z)$. The KDV solution is one involving the periodic Jacobian elliptic function, $dn_s(r)$ together with functions that modulate the oscillatory solution, to form three-dimensional wave packets of solitary waves. Under the guidance of field experiments and modeling efforts, it has been generalized to describe the internal tide on the continental shelf as an internal undulatory bore, with a jump discontinuity at the leading edge, soliton oscillations immediately following, and a long-term (tidal period) return to equilibrium at the trailing edge.

An expression for the dnoidal model amplitude is:

$$\eta(r, z, t) = \sum_{n=1}^N \eta_{o,n} W_{k,n}(z) \exp\{-\alpha_n r\} \left\{ 2 \operatorname{dn}_s^2 \left[\frac{1}{2} k_o (n x - V_n(s) t) \right] - (1 - s^2) \right\} I(r, t)$$

Beyond the simple oscillatory dnoidal wave having a vertical modal (n) structure to it, additional physics included in this relationship are (1) the modeling of a finite-length wave packet by allowing the nonlinear parameter s to vary throughout the wave group, (2) an exponential attenuation factor, and (3) the inclusion of a second, longer-term recovery function, as represented by the multiplicative quantity, $I(r, t)$, that converts the expression into one simulating the entire internal tidal cycle on the continental shelf. A graph of one cycle of this undulatory "solibore" is shown in Fig. 3.

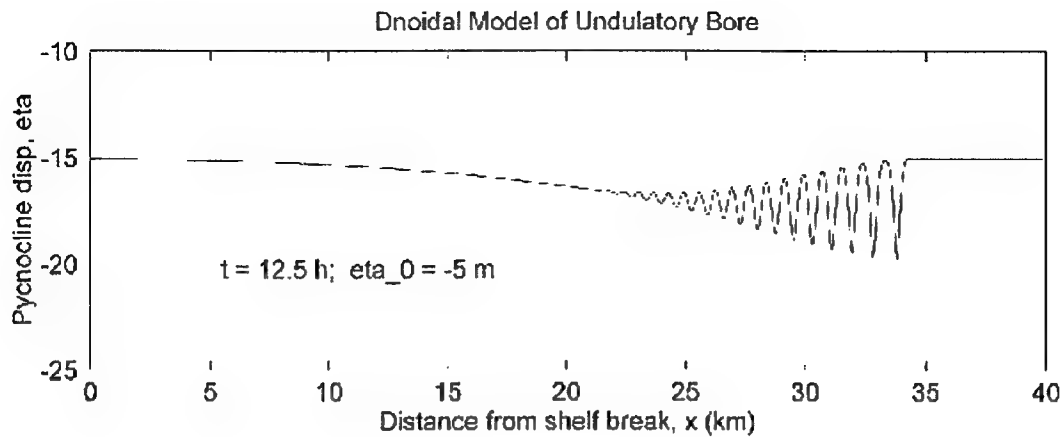


Figure 3

The two examples of large solitons presented here are to be included in an *Atlas of Internal Solitons* currently being produced under ONR sponsorship by myself and associates. The atlas will present some 50 to 60 instances of internal soliton observations at sites around the world, and will include ancillary data on bathymetry, temperature/density profiles, currents, tides, and the like. A theoretical treatment will be used to interpret the data and to provide estimates of wave amplitudes, currents, and phase velocities, which soliton dynamics allows. The atlas will be submitted for publication in about a year but as each example is completed, it will be posted on our web site. We solicit your input to the atlas, with full recognition of any contributions, of course.

On the maximal form of internal solitary waves

W. A. B. Evans,
Physics Laboratory, University of Kent,
Canterbury, Kent CT2 7NR, UK.

Abstract:

Recent integral equation computations (Evans and Ford 1996b; Turner and Vandenbroucke 1988) of large amplitude internal waves under *oceanic* conditions, $\rho_2/\rho_1 \lesssim 1$, have suggested a form with fixed maximal depth and of arbitrary, very large width in accord with Benjamin (1966)'s concept of 'conjugate flow'. Here we explore the 'conjugate flow' picture for both 'rigid-lid' and 'free top surface' boundary conditions. We discuss the limitations of this kind of extremal form - especially for cases where $\rho_2/\rho_1 \ll 1$.

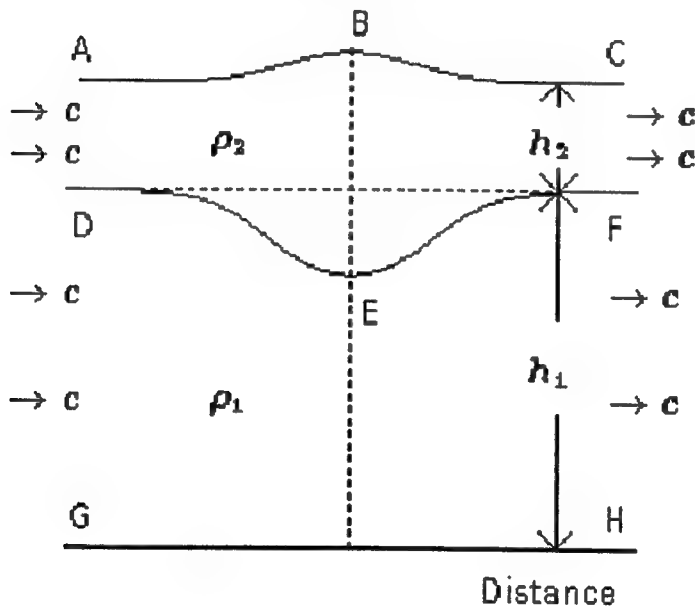
- [Introduction](#)
- [The Conjugate flow equations](#)
 - ['Rigid-Lid' case](#)
 - ['Free Top-Surface' case](#)
- [Bibliography](#)
- [About this document ...](#)

1998-09-18

Introduction

Figure: The figure depicts a typical internal wave with *oceanic* characteristics. The streamline interface DEF marks the boundary between the denser lower fluid region and the lighter upper fluid domain whilst the deformation of the free-surface, ABC, is very small as $\rho_2 \sim \rho_1$. The outskirts flow velocity, c , in the

co-ordinate system moving with the wave is also (minus) the wave velocity in the system where the outskirts fluid is at rest.



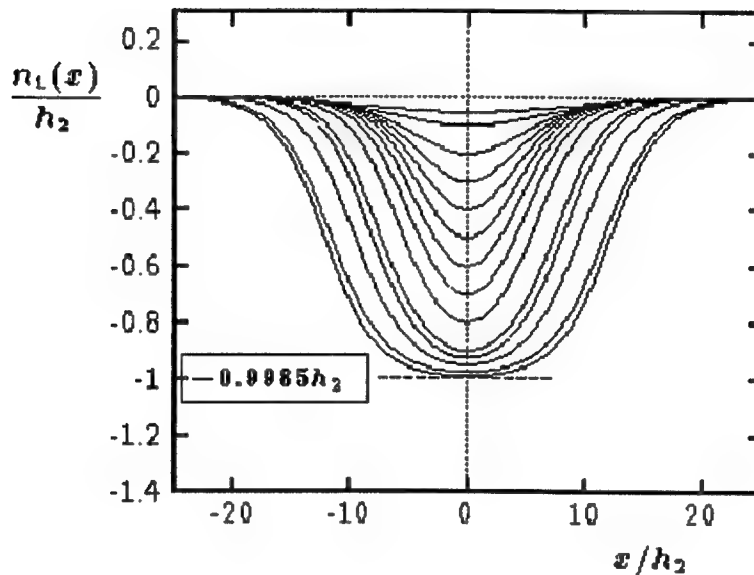
Oceanic internal waves arise principally because the density of the ocean water is not constant. To a fair approximation we may think of an upper, warmer layer of density, ρ_2 , and *undisturbed* depth h_2 , above a deeper, colder and more saline layer of density $\rho_1 \gtrsim \rho_2$ and depth, h_1 , as depicted in Fig. 1. These layers meet at the "thermocline" or "pycnocline" which is normally marked by a sharp change in water temperature with depth. Internal waves have amplitudes that distort the thermocline and the surface profile, though, in oceanic situations the latter deformation is much smaller and often ignored in theories that assume a "rigid-lid" (*i.e.* flat top surface) boundary condition. In the deeper marginal seas where internal waves are observed, h_1 is normally much larger than h_2 . This implies *negative* amplitude at the thermocline and, consequently, *negative* total mass (Evans and Ford 1996a).

Though not as destructive as "tsunamis", the larger oceanic internal waves carry a considerable amount of energy and the associated current flows can be strong enough to be an important factor in the design of coastal oil platforms and similar sea structures. Hence it is important to estimate the "*worst scenario*" i.e. the question of "how large . . . ?" can various properties be is of paramount importance. This puts the emphasis on estimating the size and associated currents, vorticity *etc.* of the maximal internal wave in any given oceanic locality. Of course, this presupposes the maximal internal wave form can be generated by the prevailing, natural formation forces. This is by no means clear and, hence, there is also the allied need to understand the mechanism(s) of formation of oceanic internal waves. Some time ago, Osborne and Burch 1980; Osborne 1990 observed very large internal waves in the tropical Andaman sea. These were prevailingly *easterly moving* and tended to recur after the semi-diurnal period of 12 hrs 26 mins which indicates convincingly that tidal forces play a key part in their formation mechanism. Unlike normal tides, there is no evidence of any correlation between internal wave size and the phases of the Moon. If, indeed, the formative forces are primarily tidal in origin, then the waves should be highly predictable with virtually no randomness. This would suggest that the *extremal* wave is limited by the magnitude of the prevailing tidal forces rather than by the maximal stable internal wave solution corresponding to the parameters at that location.

However, the latter is certainly an *upper bound* on the extremal form at any given location and is also, mathematically, a well-defined problem. Accordingly much attention has been devoted to this task. The nature of the solutions sought invalidate the small amplitude/long wavelength conditions required for an accurate description via the KdV theory. Consequently, integral equation techniques whose numerical solutions should be exact within potential flow have

Figure: The profiles of the range of internal wave solutions for $h_1/h_2=3$, $\rho_2/\rho_1 = 0.997$ (note the surface is at +1 and

the bottom at -3 on the vertical scale). The waves shown correspond to the amplitudes, $-n_1(0)/h_2 = 0.05, 0.1, 0.2, 0.3, 0.4, 0.5, 0.6, 0.7, 0.8, 0.9, 0.925, 0.95, 0.975$ and 0.99 . The horizontal line (---) marks the *conjugate flow* "maximum" amplitude of $-0.998498h_2$.



been utilised in order to gain insight on these extremal forms. Assuming rigid-lid boundary conditions, Turner and Vandenbroeck (1988) computed extremal forms of internal waves for parameters, $h_2/h_1=1$, $\rho_2/\rho_1 = 0.1$ (which are decidedly not typically *oceanic*) and concluded that the limiting form was one of finite amplitude and very large width - the middle part being essentially predictable as a uniform "2-layer-flow" domain that is "conjugate" to the outskirts flow where the fluid flow velocities in both layers is *c.* Evans and Ford (1996b) utilised a different integral equation form to investigate the limiting internal wave with *oceanic* parameters, $h_2/h_1=1/3$ and $\rho_2/\rho_1 = 0.997$. Their results are shown in Figure 2. Again it was seen that, at the largest amplitudes, the 'width' appears to diverge and, moreover, the largest solution amplitude, $\eta_1 \sim -0.99h_2$, agreed precisely with the predicted value from "conjugate flow" considerations *viz.* $-0.9985h_2$ (shown as a horizontal dotted line in the figure).

[Next](#) [Up](#) [Previous](#)

Next: [The Conjugate flow equations](#) **Up:** [On the maximal form](#) **Previous:** [On the maximal form](#)

1998-09-18

The Conjugate flow equations

Consider flow in a 2-layer system, where in one region we have uniform flow where the lower layer has velocity, c_1 , depth h_1 and density ρ_1 and the upper layer has c_2 , h_2 and ρ_2 . For our purposes here we have that $c_1 = c_2 = c$ i.e. both outskirts layer flow velocities are equal to (minus) the wave velocity. Suppose over some "surge-region", this uniform flow transformed into a distinct uniform flow where the corresponding velocities are now c'_1 and c'_2 and the depths h'_1 and h'_2 . For our purposes here [Benjamin \(1966\)](#) defined such regions of uniform 2-layer flows as being "conjugate" to each other if

1. the fluid flux in every layer is equal in both regions i.e.

$$c'_1 h'_1 = c_1 h_1 = c h_1 \quad \text{and} \quad c'_2 h'_2 = c_2 h_2 = c h_2$$

2. the momentum flux in both regions are equal i.e.

$$\begin{aligned} & \int_0^{h_2} dy (p_1 + \rho_2 gy + \rho_2 c^2) + \int_0^{h_1} dy (p_1 + \rho_2 gh_2 + \rho_1 gy + \rho_1 c^2) \\ &= \int_0^{h'_2} dy (p'_1 + \rho_2 gy + \rho_2 c'^2) + \int_0^{h'_1} dy (p'_1 + \rho_2 gh'_2 + \rho_1 gy + \rho_1 c'^2) \\ \text{i.e. } & p_1(h_1 + h_2) + \frac{1}{2} \rho_2 g h_2^2 + \rho_2 g h_1 h_2 + \frac{1}{2} \rho_1 g h_1^2 + c^2 (\rho_1 h_1 + \rho_2 h_2) \\ &= p'_1(h'_1 + h'_2) + \frac{1}{2} \rho_2 g h'^2_2 + \rho_2 c'^2 h'_2 + \rho_2 g h'_1 h'_2 + \frac{1}{2} \rho_1 g h'^2_1 + \rho_1 c'^2 h'_1 \end{aligned}$$

where p_1 and p'_1 are the pressures at the top surfaces of the upper layers in both uniform flow regions respectively.

3. the energy flux in both regions are equal or, equivalently, we can obtain a relation by summing all the pressure changes round a large loop bounded by the upper and lower streamlines and with vertical "arms" in the regions of uniform flow. This latter form is more convenient when we consider "free top-surface" boundary conditions. In the *rigid lid* flat-topped case we have, from Bernoulli's equation

$$p_t - p'_t = \frac{1}{2} \rho_2 (c'_2)^2 - c^2 \quad \text{and} \quad h_1 + h_2 = h'_1 + h'_2$$

or, alternatively, for the free surface case,

$$p_t - p'_t = 0 \quad \text{and} \quad \rho_2 g (h_1 + h_2 - h'_1 - h'_2) = \frac{1}{2} \rho_2 (c'_2)^2 - c^2$$

Applying Bernoulli's equation along the bottom streamline gives the difference between the bottom pressures, p_b and p'_b viz.

$$p_b - p'_b = \frac{1}{2} (\rho_1 c'_1)^2 - \rho_1 c^2$$

In either case, as the sum of the pressure changes round the closed path must add to zero,

$$\{p_t - p'_t\} + \{\rho_2 g h_2 + \rho_1 g h_1\} + \{p'_b - p_b\} - \{\rho_2 g h'_2 + \rho_1 g h'_1\} = 0$$

With h_1, h_2 given, the above effectively constitute seven equations in seven unknowns, $h'_1, h'_2, c, c'_1, c'_2, p_t - p'_t$ and $p_b - p'_b$. However they are easily reducible to virtually two equations in two unknowns, that can be taken as c^2/gh_2 and h'_1/h_2 , that can then be easily solved by the Newton method.

- 'Rigid-Lid' case
- 'Free Top-Surface' case

[Next](#) [Up](#) [Previous](#)

Next: 'Rigid-Lid' case Up: On the maximal form Previous: Introduction

1998-09-18

'Rigid-Lid' case

In this case, the conjugate flow equations, can be *algebraically* solved as was done by [Amick and Turner \(1986\)](#) who gave the *limiting* amplitude as

$$(n_1)_{\max} = h'_1 - h_1 = h_2 - h'_2 = \frac{h_2 \sqrt{\rho_1} - h_1 \sqrt{\rho_2}}{\sqrt{\rho_1} + \sqrt{\rho_2}} \quad (6)$$

and the limiting wave's velocity as

$$c = \left[g(h_1 + h_2) \left(1 - \frac{\rho_2}{\rho_1} \right) \right]^{\frac{1}{2}} \Big/ \left[1 + \sqrt{\frac{\rho_2}{\rho_1}} \right] \quad (7)$$

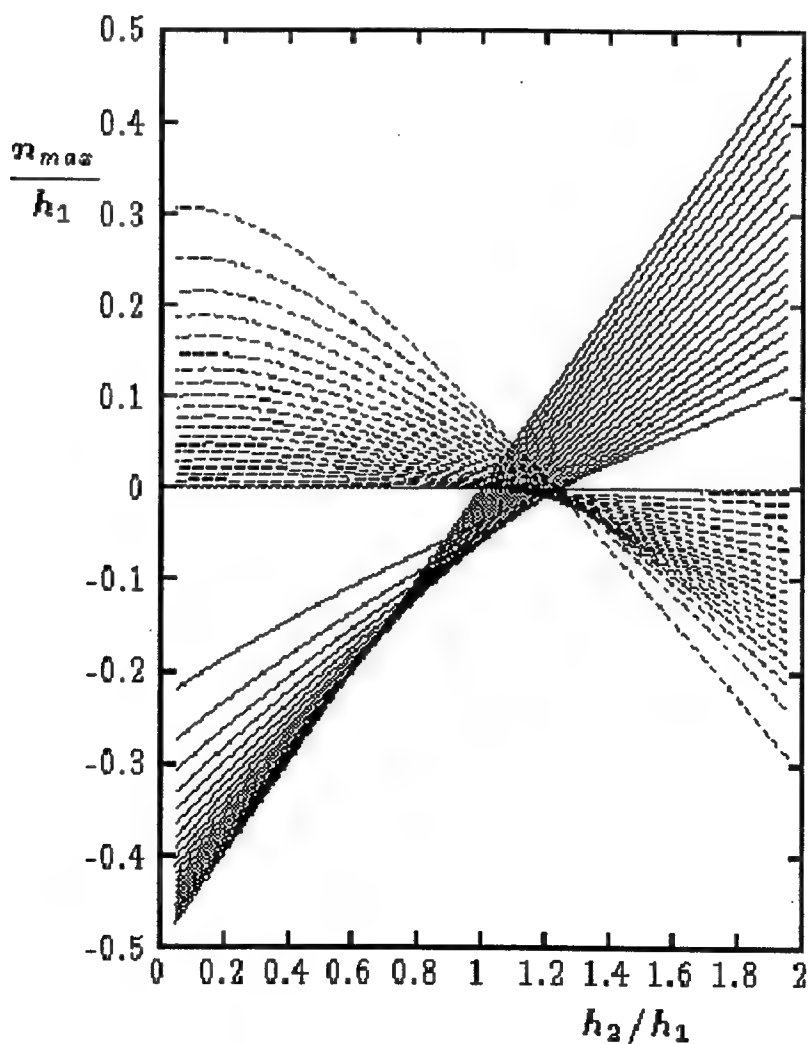
Note, in particular, that Amick and Turner's equation, (6), implies positive/negative waves if $(h_2/h_1)^2 \gtrless \rho_2/\rho_1$, as has also been subsequently concluded by several others *e.g.* [Craig and Sternberg \(1991\)](#).

For the case, $h_2/h_1=1/3$ and $\rho_2/\rho_1 = 0.997$, we see from Fig. 2 that the largest computed amplitude is $\sim -0.99 h_2$, and, indeed, the velocity of the largest computed wave is also $\sim 0.0548 \sqrt{gh_2}$. These values agree *precisely* with the predicted conjugate flow amplitude of $h'_1 - h_1 = -0.99849775 h_2$ and velocity of $c = 0.05481339 \sqrt{gh_2}$, as evaluated from (6) and (7). Further the trough becomes increasingly flatter in line with what would be expected if a uniform mid-section flow were to develop. *There can be no doubt* that the limit of the numerical solution branch investigated by [Evans and Ford \(1996b\)](#) is explicable in terms of conjugate flow in *precisely* the way [Turner and Vandenbroeck \(1988\)](#) advocated.

This conclusion is of some interest for large amplitude *overhanging* (or *underhanging*) profiles have been numerically found by [Meiron and Saffman \(1983\)](#) and [Grimshaw and Pullin \(1986\)](#). However, these calculations were of *periodic* internal waves, and it would appear that they became *overhanging* only because the imposed periodicity prevented their widths from expanding beyond the periodic length. At least along the solution branch investigated, solitary internal 2-layer waves never develop an infinitely steep gradient and, accordingly, never become *overhanging*.

'Free Top-Surface' case

Figure: Plots of the *limiting* interface amplitude, $(n_1)_{\max}$ (--) and the associated free surface amplitude, $(n_2)_{\max}$ (— — —), for $0.04 \leq \rho_2/\rho_1 \leq 0.99$ in steps of 0.05. Note the higher curves *on the left* (for both $(n_1)_{\max}$ and $(n_2)_{\max}$ pertain to the lower ρ_2/ρ_1 ratios.



The *conjugate flow* conditions given above can be solved *numerically* for free-surface boundary conditions as done by [Evans \(1996\)](#). In this case, there does not appear to be nice analytic forms¹, analogous to (6) and (7). It is imperative therefore to represent the numerical solutions for the amplitudes *graphically* as shown in Figure 3, where the *limiting* surface and pycnocline amplitudes, n_1 and n_2 , are plotted for $0.04 \leq \rho_2/\rho_1 \leq .99$ in steps of 0.05 over a range of h_2/h_1 values between 0 and 2.

Note that at the larger *oceanic* ratios of $\rho_2/\rho_1 \lesssim 1$ the pycnocline limiting amplitudes, $(n_1)_{\max}$, are

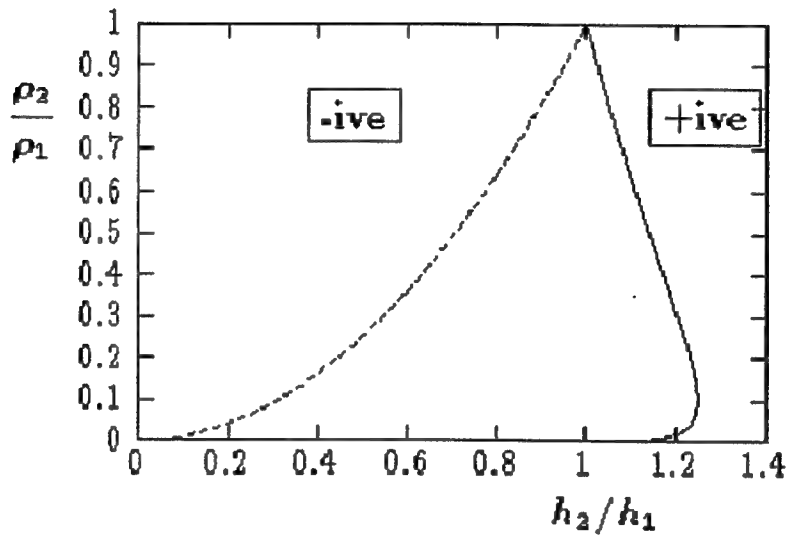
largest and the free-surface limiting amplitudes, $(n_2)_{\max}$, are smallest. In fact when $\rho_2 \sim \rho_1$,

$n_1 \rightarrow (h_2 - h_1)/2$, and then asymptotes to the 'rigid-lid' limiting amplitude. Note also that free-surface and pycnocline amplitudes are *always* of opposite sign and thereby become zero simultaneously at situations pertaining to *congruent* conjugate flows as described by the free-surface locus in Fig. 4. Hence, *negative* interfacial amplitude internal waves appear to have an associated free top surface 'bulge' whilst *positive* interfacial amplitudes are accompanied by a free top surface 'depression'.

Figure 4 shows the locus of the situations, characterised by values of ρ_2/ρ_1 and h_2/h_1 , at which the conjugate flows become 'congruent' (i.e. $h'_2 = h_2$, $h'_1 = h_1$ and $c'_1 = c'_2 = c$), implying the limiting amplitudes, n_1 and n_2 , are zero. Of course this marks the boundary between *positive* and *negative* internal waves.

Figure: The boundaries between negative (to the left) and positive (to the right) internal wave solutions, as determined by congruent conjugate flows. The solid (--) line (after [Evans \(1996\)](#)) pertains to the *free-surface* boundary condition whilst (— — —) represents the analytic boundary,

$\rho_2/\rho_1 = (h_2/h_1)^2$, that pertains to the "rigid-lid" boundary condition, as follows from (6).



Remarkably, it is observed that the locus of congruent conjugate flows for the "free-surface" case is confined *entirely* to the range $h_2/h_1 \geq 1$ and appears to end as well as start at values of $h_2/h_1 = 1$. Thus it appears that, *with free surface boundary conditions, no positive internal waves are possible at any density ratio if $h_2 \leq h_1$* . The maximum value of h_2/h_1 on the locus is 1.25 and occurs when $\rho_2/\rho_1 = 0.1$. These numbers are certainly valid to high numerical accuracy and, probably, can be shown to be *exact*.

At this point, it is apposite to sound a note of caution. In the limit when $\rho_2/\rho_1 \rightarrow 0$ and $h_2 \gg h_1$, it might be supposed that the motion of the bottom layer is unaffected by the presence of the tenuous upper layer and should behave like a normal "1-layer" solitary wave. The *conjugate flow* limiting amplitude in this situation would appear from (6) to be $(n_1)_{\max} \sim h_2$ i.e. as large as we care to make h_2 . Of course, this conclusion does not accord with what we know of the *maximum* solitary wave that has a 120° Stokes corner and a limiting amplitude of $0.83319918 h_1$ ([Evans and Ford 1996a; Williams 1981](#)). Both of these 'extremal scenarios', though different, are "exact" insofar as the relevant integral equations are exactly satisfied.

This heralds the question of stability. In our opinion it is most likely that the "conjugate flow" picture of an

extremal form of infinite width will prove unstable especially at the lower values of ρ_2/ρ_1 - indeed it is not clear that it is stable for *any* density ratio. Though a formidable task, this underlines the need for a stability analysis of all *large amplitude* internal wave solutions.

Acknowledgements:

The author is grateful for discussions on these topics with Prof. L. Vázquez, Dr. W.G. Easson, Dr. I-Fan Shen and Prof. G.L. Alfimov. This work was partially supported by a British Council "Acciones Integradas" award (ref: MDR/(1996/97)/1828) and the NATO grant (ref: OUTR.LG-960298).

[Next](#) | [Up](#) | [Previous](#)

Next: [Bibliography](#) **Up:** [The Conjugate flow equations](#) **Previous:** ['Rigid-Lid' case](#)

1998-09-18

Bibliography

Amick, C. and Turner, R. (1986).

A global theory of internal waves in two-fluid systems.
Trans. Am. Math. Soc., 298:431-481.

Benjamin, T. B. (1966).

Internal waves of finite amplitude and permanent form.
J. Fluid Mech., 25:241-270.

Craig, W. and Sternberg, P. (1991).

Comparison principles for free-surface flows with gravity.
Phys. Fluids, 230:231-243.

Evans, W. A. B. (1996).

Exact Numerical Solutions to Large Amplitude Internal Solitary Waves.
The Proceedings of the Sixth (1996) - International OFFSHORE AND POLAR ENGINEERING CONFERENCE (ISOPE-96), Los Angeles, USA, May. 26-31, 1996, III:124-130.

Evans, W. A. B. and Ford, M. J. (1996a).

An exact integral equation for solitary waves (with new numerical results for some 'internal' properties).
Proc. Roy. Soc. A, 452:373-390.

Evans, W. A. B. and Ford, M. J. (1996b).

An integral equation approach to internal (2-layer) solitary waves.
Physics of Fluids, 8(8):2032-2047.

Fordy, A. P., editor (1990).

Soliton theory: a survey of results.
Manchester University Press, Manchester and New York.
see article by A. R. Osborne, p152-173.

Grimshaw, R. and Pullin, D. (1986).

Extreme interfacial waves.
Phys. Fluids, 29:2802-2807.

Meiron, D. and Saffman, P. (1983).

Overhanging interfacial gravity waves of large amplitude.
J. Fl. Mech., 129:213-218.

Osborne, A. R. and Burch, T. L. (1980).

Internal solitons in the Andaman Sea.
Science, 208:451-460.

Turner, R. and Vandenbroeck, J. (1988).

Broadening of interfacial solitary waves.
Phys. Fluids, 31:286-290.

Williams, J. M. (1981).

Limiting Gravity Waves in Water of Finite Depth.
Phil. Trans. Roy. Soc. Lond., A302:139-188.

Abstract: Internal Solitary Wave Workshop, Dunsmuir Lodge, 27-29 October 1998

Solitary waves formed over topography

David Farmer¹ & Laurence Armi²

¹*Institute of Ocean Sciences, 9860 West Saanich Road, Sidney, BC, V8L 4B2*

²*Scripps Institution of Oceanography, La Jolla, San Diego, CA 92093*

Internal solitary waves are generated as a result of stratified flow over topography. There appear to be several ways in which this can happen, but detailed observations of the generation process are sparse. Here we discuss the generation of waves *upstream* of the topographic maximum during a strong tidal current and suggest the possible role of shear flow instability in this process. Observations and discussion relating to this presentation appear in Farmer and Armi (1999a).

Calculations of upstream solitary wave generation have been approached in two different ways. Weakly nonlinear models have been used, such as the fKdV or BBM methods. These are suitable for small amplitude features, but their accuracy remains unclear for large amplitude wave generation. Second, the fully nonlinear equations for layered flow have been integrated to simulate upstream solitary wave evolution, following the methods of Roberts and Dold (see abstract by J. Grue in this workshop). However the numerical technique is inherently unstable to small scale instability and filtering is required to remove Kelvin-Helmholtz and related shear flow instabilities. Even a steady flow over topography can generate upstream solitary wave propagation (i.e. Melville and Helfrich, 1987, Cummins, 1995). However, the numerical techniques to date have not been suitable for exploring the role of small scale shear flow instability in solitary wave generation. We present observations of upstream wave generation and suggest two possible routes through which they may be formed.

Our measurements were made by slow ship traverses back and forth across the sill, using a combination of Doppler profiler, acoustic echo-sounder imaging, continuous CTD profiling and a towed vertical string of salinity/temperature/current-meters. Aerial photography was used to map the surface modulations. All positions were referenced with DGPS. Successive traverses through an increasing tidal current show the internal hydraulic response as the flow gradually becomes established. As the current slackens, the interface continues to deepen so as to maintain control over the sill crest until relaxation takes place and the current reverses. The particular process with which we are concerned takes place near maximum tidal current.

Observations of tidal flow over a sill show trains of internal solitary waves upstream of the crest during periods of strong forcing. The process does not repeat with every tidal cycle and occurs in the subcritical portion of a controlled flow in which the upper layer is drawn down as the current moves over the sill. Solitary waves appear quite suddenly as the tidal flow develops and may be seen both in aerial photographs and in acoustic measurements (Figure 1). A characteristic of continuously stratified controlled flows of this kind is the formation of a bifurcation in the streamlines (Farmer and Armi, 1999b). A quasi-steady internal hydraulic analysis shows that if the bifurcation is forced downstream

over the sill crest, it will move very rapidly, even though the tidal current is changing slowly. Although the quasi-steady approximation can hardly be expected to apply in this case, rapid adjustment is observed. Moreover, the waves appear at approximately the same time as this adjustment takes place, suggesting that the rapid downstream movement of the bifurcation may itself be responsible for interfacial solitary wave generation. The waves subsequently advance slowly upstream.

Internal solitary waves also appear to be formed in the presence of shear flow instabilities when there is a more gently sloping interface (Figure 2a,b). As the ship travels above these instabilities, their instantaneous properties are mapped, analogous to the operation of a focal plane shutter in a camera. The ship moves faster than the unstable structures, producing in effect a rapid sample of the shear layer in position and time; however some Doppler distortion is unavoidable. The surface modulation produced by the waves is readily apparent as almost straight slicks formed by the combination of changing color due to thickening of the silt laden surface layer and to the effect of local divergence on the gravity-capillary wave-field.

In a sheared flow, instabilities grow to produce interfacial disturbances that may propagate either with or against the current. Those travelling downstream are quickly lost and are of little further interest in this context, but those travelling upstream may move faster than the oncoming flow and subsequently evolve into solitary waves. We distinguish between instabilities created downstream and those formed upstream of the control. Downstream of the control, all linear waves are swept away, but upstream of the control interfacial waves of sufficient length may escape.

Figure 2c shows the dispersion diagram for internal waves as a function of position, including effects of the variable shear, depth and density structure. From the perspective of upstream wave generation, instabilities must be of sufficient length to travel against the current. However, it appears that waves long enough to propagate upstream exceed the length of unstable modes. We hypothesize that subharmonic interaction could lead to the observed longer wavelengths which also have the required speed. Upstream propagation ducts the waves along a progressively shallower interface so that a wave of small amplitude may eventually become large enough, relative to its distance from the boundary, to acquire the characteristics of a solitary wave. The mechanism described here does not necessarily occur in isolation from wave generation caused by time dependent flow over the sill crest.

Since nonlinear waves have higher celerities than linear waves it is possible for them to propagate against the background flow even if they are slightly downstream of the control. Position B identified in Figure 2c indicates such a location on the dispersion diagram. Internal solitary waves were observed just downstream of the crest during a flood tide, where they remained trapped for two hours before escaping upstream as the tidal current slackened. In summary, detailed observations have been acquired of internal solitary waves formed in the vicinity of topography. In contrast to the nonlinear evolution of internal tides propagating across the continental shelf, the generation mechanism appears closely linked to the internal hydraulic response.

Acknowledgement: This work was supported by the US Office of Naval Research and the Institute of Ocean Sciences.

Additional figures may be viewed at: <http://pinger.ios.bc.ca/cruises/knight95/sill.html>

(A)



(B)

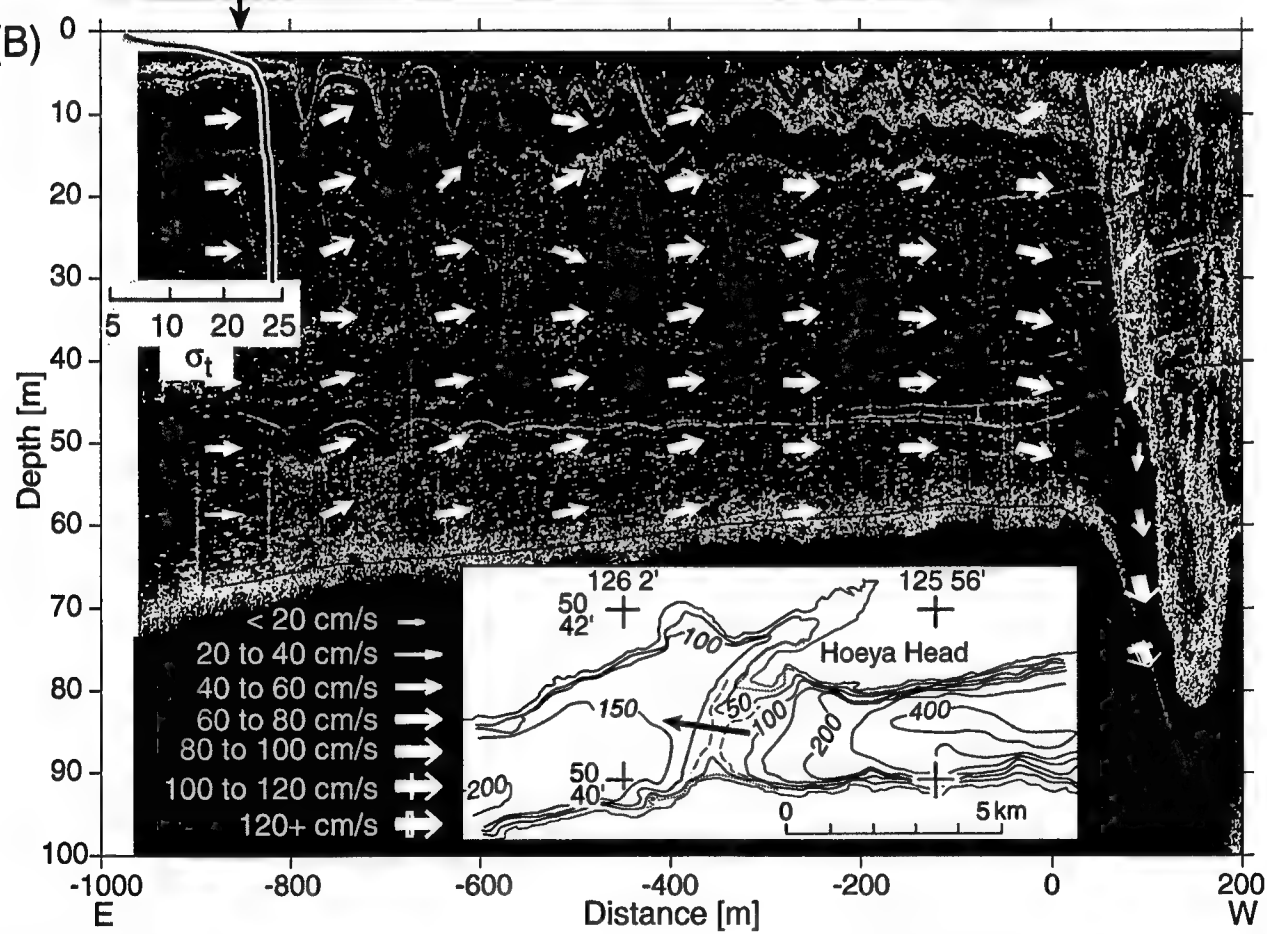


Fig. 1.(A) Aerial photograph showing the C.S.S. Vector about to traverse a group of solitary waves over the sill in Knight Inlet, British Columbia, 0212 UTC on 28 August 1995. **(B)** Corresponding echosounding image of solitary waves. Arrows indicate current vectors shown at the same aspect ratio as figure and coded as to magnitude. (Top left) Upstream density profile in σ_t . (Inset) Chart of sill area with arrow showing ship track. Reprinted with permission from *Science*, Farmer D. and L. Armi, The Generation and Trapping of Solitary Waves over Topography, 8 January 1999, volume 283, pp. 188-190. Copyright 1999 American Association for the Advancement of Science.

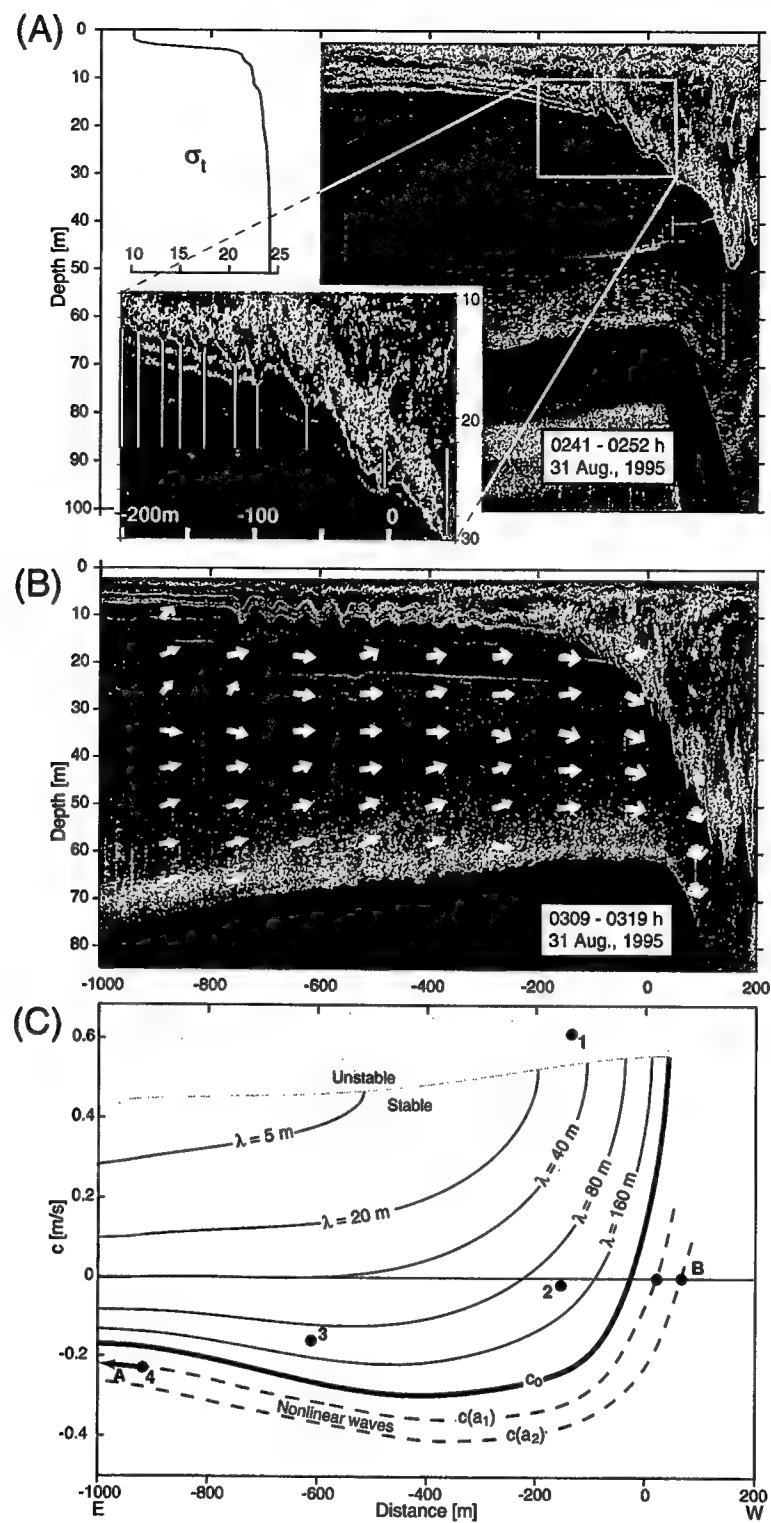


Fig. 2.(A) (Top left) Upstream density profile in σ_t . (Right) Echo-sounding image of downstream traverse showing unstable interface. (Inset) Vertical lines identify instability scale. (B) Repeat traverse traveling upstream approximately 30 min after (A). (C) Dispersion diagram for internal waves applicable to (A) propagating against the current. Dashed curves represent nonlinear waves (not modeled). Blue shading indicates unstable flow. "1" → "2" (red dots) represents subharmonic formation of longer waves from instabilities; "2" → "3" represents linear propagation; "3" → "4" represents transition to nonlinearity. Reprinted with permission from *Science*, Farmer D. and L. Armi, The Generation and Trapping of Solitary Waves over Topography, 8 January 1999, volume 283, pp. 188-190. Copyright 1999 American Association for the Advancement of Science.

References:

Farmer, D. and L. Armi, The generation and trapping of solitary waves over topography, *Science*, 283, 188-190, 8 January 1999.

Farmer D. M. and L. Armi, Stratified flow over topography: the role of small scale entrainment and mixing in flow establishment, in press,
Proc. Roy. Soc., Series A, 1999.

Cummins, P., Numerical simulations of upstream bores and solitons in a two-layer flow past an obstacle, *J. Phys. Oceanogr.*, 25, 1504-1515, 1995.

Melville, W. K. and K. R. Helfrich, Transcritical two-layer flow over topography, *J. Fluid. Mech.*, 178, 31-52, 1987.

MODELING INTERNAL SOLITARY WAVES IN THE OCEAN

Roger Grimshaw¹ and Efim Pelinovsky²

¹ Department of Mathematics and Statistics, Monash University, Clayton, Vic 3168, Australia

² Institute of Applied Physics, 46 Uljanov Street, 603600 Nizhny Novgorod, Russia

Presented by Roger Grimshaw

In their simplest representation internal solitary waves are nonlinear waves of permanent form which owe their existence to a balance between nonlinear wave-steepening effects and linear wave dispersion. They are now recognised as ubiquitous in nature, and are a commonly occurring feature of coastal seas, fjords and lakes, and also occur commonly in the atmospheric boundary layer (see, e.g., the reviews by Apel et al, 1995 and Grimshaw, 1997). On the theoretical side, it is well-established that nonlinear evolution equations of the Korteweg-de Vries (KdV) type form at least a first-order basis for qualitative modeling and prediction (Grimshaw, 1997).

In general, the study of oceanic internal waves can be separated into three linked components, generation, propagation and decay. Of these three the propagation aspect is perhaps the best understood and indeed will be the focus of this presentation. However, first it is pertinent to make some general comments about the generation and decay processes.

It is widely accepted that in shelf and slope regions the most common generation mechanism is the interaction of the barotropic tide with the continental shelf and slope, resulting in the formation of an internal tide, which in turn can evolve into a structure which allows for the generation of internal solitary waves. In essence, the internal tide can be conceived as a long wave which through a process of local steepening then evolves into a form which supports internal solitary waves of much shorter wavelength. However, this mechanism is certainly not unique, and internal solitary waves can be generated in partially-enclosed regions such as fjords or straits, by current flow over pronounced bottom features, or in fully-enclosed basins through the action of wind stress in tilting the thermocline, followed by relaxation into internal solitary waves.

Direct oceanic observations of decay mechanisms seem to be relatively sparse, but the likely candidates in shallow water regions are bottom friction, and, on the basis of numerical and laboratory experiments, internal wave breaking on a sloping boundary. However, there are certainly other candidates, such as pre-existing turbulence or shear-induced instability.

Next we turn to our main focus, a model for the propagation of internal solitary waves, but importantly we note that this model can also encompass some aspects of the generation and decay processes. The model we propose is an evolution equation of the KdV-type, which incorporates the effects of background shear, variable bottom topography, both quadratic and cubic nonlinearity, the earth's rotation and dissipative processes. To describe the model we shall at first suppose that the waves are propagating in the x -direction relative to a background state consisting of a density profile $\rho_0(x, z)$ and a horizontal current $u_0(x, z)$ in the x -direction, where z is a vertical coordinate. The depth of fluid is $h(x)$, and here we are assuming that the x -dependence in the basic state is slowly-varying with respect to the

horizontal scale of the waves.

In dimensional coordinates we suppose that the isopycnal displacement $\zeta(x, z, t)$, where t is the time, can be represented at leading order by

$$\zeta = A(x, t)\phi(x, z) + \dots, \quad (1)$$

where the modal function $\phi(x, z)$ is defined by

$$(\rho_0(c - u_0)^2\phi_z)_z - g\rho_0\phi = 0, \quad \text{for } -h < z < 0, \quad (2)$$

$$\phi = 0, \quad \text{at } z = -h, \quad (3)$$

$$(c - u_0)^2\phi_z = g\phi, \quad \text{at } z = 0. \quad (4)$$

Note that this is an equation in z only, and the slow x -dependence is parametric. This modal equation also defines the linear long wave speed $c(x)$. The system in general defines an infinite system of possible modes, including a barotropic mode, and of these just one is selected, usually the dominant first baroclinic mode. Although we choose to represent the internal solitary waves in terms of the amplitude of the isopycnal displacement, the other fluid variables such as the currents are readily obtained at leading order using local linear long wave theory in the conventional manner. Higher-order correction terms for all fields are also available in principle, and have been explicitly calculated in some special cases.

The amplitude A then evolves according to the generalised Korteweg-de Vries (gKdV) equation,

$$A_s + \frac{\sigma}{2\sigma}A + \frac{\mu}{c}AA_B + \frac{\nu}{c}A^2A_B + \frac{\lambda}{c^3}A_BAA_B + \gamma\Gamma(A) = \frac{1}{2}f^2 \int_{\infty}^{\theta} Ad\theta'. \quad (5)$$

The independent variables s and θ are given by

$$s = \int_0^x \frac{dx'}{c(x')} \quad , \quad \theta = s - t, \quad (6)$$

while the coefficients $c, \sigma, \mu, \nu, \lambda$ and γ are all functions of s . Thus, for instance,

$$\sigma = c^2 I, \quad (7)$$

$$I\mu = 3 \int_{-h}^0 \rho_0(c - u_0)^2\phi_z^3 dz, \quad (8)$$

$$I\lambda = \int_{-h}^0 \rho_0 (c - u_0)^2 \phi^2 dz, \quad (9)$$

$$\text{while } I = 2 \int_{-h}^0 \rho_0 (c - u_0) \phi_z^2 dz. \quad (10)$$

The coefficient ν is also available, but is given by a much more complicated expression. $\Gamma(A)$

represents dissipation, while f is the local Coriolis parameter. The derivation of equation (5) is sketched in Grimshaw (1997) (see also Holloway et al, 1997). Note that s is a time-like variable describing the evolution of the waves along the ray path determined by the linear long-wave speed, while θ is a phase variable for the solitary waves in a frame of reference moving with the linear long wave speed $c(x)$. More generally, if the spatial variability of the background occurs in both horizontal directions, then s is a coordinate along a ray path defined by c , θ is a phase variable on this path, while transverse effects can be included by adding KP-like terms.

The “initial” condition for equation (5) requires specification of $A(s, \theta)$ at some specific location, $s=s_0$ (i.e. $x=x_0$) say. In essence, this is a time series for the amplitude of the baroclinic mode being considered, and in principle can be obtained from a suitable data set. However, there is an assumption of “one-way” propagation underlying equation (5), and hence to determine an appropriate initial condition, it is first necessary to determine that component of the disturbance which is propagating in the positive x -direction.

Although the full equation (5) has not yet been used in an oceanic context (excepting some very recent work by Holloway et al, 1998), various reductions have been considered. For example, recently Holloway et al (1997) used (5) with the omission of the cubic term ($\nu = 0$) and the rotational term ($f=0$) to examine the propagation of internal solitary wave son the NW shelf of Australia. In general, it is well-known that a constant-coefficient KdV-model with no dissipation (i.e $\sigma = \nu = \gamma = f = 0$ with μ and c constant) will evolve into a finite set of amplitude-ordered solitary waves (i.e. solitons). Further, the effect of a variable background on an individual KdV-solitary wave is also relatively well understood. However, the interplay between quadratic and cubic nonlinearity, variable background state, dissipation and rotational effects, are issues which now need to be explored more fully.

This presentation will discuss recent work addressing some of these aspects. For instance, we will discuss the role of the cubic nonlinear term in generating kink-like structures, or in the formation of KdV-like solitary waves riding on a background pedestal (Grimshaw et al, 1998b). Also, we will discuss the role of the rotational term in providing an effective damping mechanism through the radiation of small-amplitude waves (Grimshaw et al, 1998a) If time permits we will also discuss recent work on large-amplitude internal solitary waves with vortex cores, which are capable of transporting mass over long distances (Derzho and Grimshaw, 1997).

References

J. R. Apel, L. A. Ostrovsky, and Yu. A. Stepanyants (1995). Internal solitons in the ocean. *Report MERCJRA0695, Applied Phys. Lab., The John Hopkins University*.

Oleg G. Derzho and R. Grimshaw (1997). Solitary waves with a vortex core in a shallow layer of stratified fluid. *Phys. Fluids*, **9**, 3378-3385.

R. Grimshaw (1997). Internal solitary waves. "Advances in Coastal and Ocean Engineering", ed. P.L.-F. Liu, World Scientific Publishing Company, Singapore, **3**, 1-30.

R.H.J. Grimshaw, J-M. He and L.A. Ostrovsky (1998). Terminal damping of a solitary wave due to radiation in rotational systems. *Stud. Appl. Math.*, (accepted).

R. Grimshaw, E. Pelinovsky, and T. Talipova (1998). The modified Korteweg-de Vries equation in the theory of the large-amplitude internal waves. *Nonlinear Processes in Geophysics*, (accepted).

P.E. Holloway, E. Pelinovsky, T. Talipova, and B.A. Barnes (1997). A nonlinear model of internal tide transformation on the Australian North West Shelf. *J. Phys. Ocean.*, **27**, 871 - 896.

P.E. Holloway, E. Pelinovsky and T. Talipova (1998). A generalised Korteweg-de Vries model of internal tide transformation in the coastal zone. *J. Geophys. Res.*, (submitted).

About this document ...

1998-08-19

Strongly Nonlinear Internal Waves on the Australian North West Shelf

Peter E. Holloway

School of Geography and Oceanography

University College, University of New South Wales

Australian Defence Force Academy, Canberra, Australia

E. Pelinovsky and T. Talipova

Department of Nonlinear Waves, Institute of Applied Physics

Russian Academy of Science, Nizhny Novgorod, Russia

Introduction

Soliton-like waves, often called internal solitary waves, are frequently observed to form in the stratified ocean as a result of oscillatory flow over topographic features or from the evolution of large amplitude long internal waves. On the Australian North West Shelf (NWS) a large amplitude semi-diurnal internal tide is generated over the continental slope and propagates shoreward with a wavelength of $\sim 20\text{ km}$ and amplitude of a few 10 s m at the shelf break. This long wave evolves into a variety of strongly nonlinear wave forms including internal solitary waves.

In this paper current meter and thermistor observations are presented of varying internal wave forms. Also, numerical solutions of a Korteweg de-Vries model are presented for the evolution of an initially long sinusoidal wave. The model includes varying topography and stratification, the Earth's rotation, cubic nonlinearity and frictional dissipation.

Observations

Examples of different internal wave forms are presented as shown by the velocity component flowing across the bathymetry (the dominant wave-propagation direction) and of vertical displacements of isotherms derived from temperature time series at different depths. Measurements are from a NWS location in water 78 m deep close to the shelf break at 19.71°S 116.14°E with instruments sampling at 2 min intervals. Additional examples showing soliton-like wave forms are presented by Holloway et al. (1997).

Figure 1a shows a large amplitude wave (peak-trough $\sim 40\text{ m}$ in water 78 m deep) with a downwards shock followed by a number of positive internal solitary waves. At the end of the wave profile when the waveform is again at a crest, negative internal solitary waves are seen. The change in polarity is associated with the dramatic change in the stratification associated with the very large amplitude internal tide. The properties are also revealed in the baroclinic currents (depth average has been removed) at 8 and 68 m depth.

Figure 1b shows a square wave form in displacement and currents where a downward shock of 40 m is followed by an equal upward shock about 2 hrs later. The downward shock produced no short period waves while the upward shock is followed by a large number of oscillatory waves. Figure 1c shows a small number of internal solitary waves following a weak downward jump. The first wave is "wide" or longer in period than other examples.

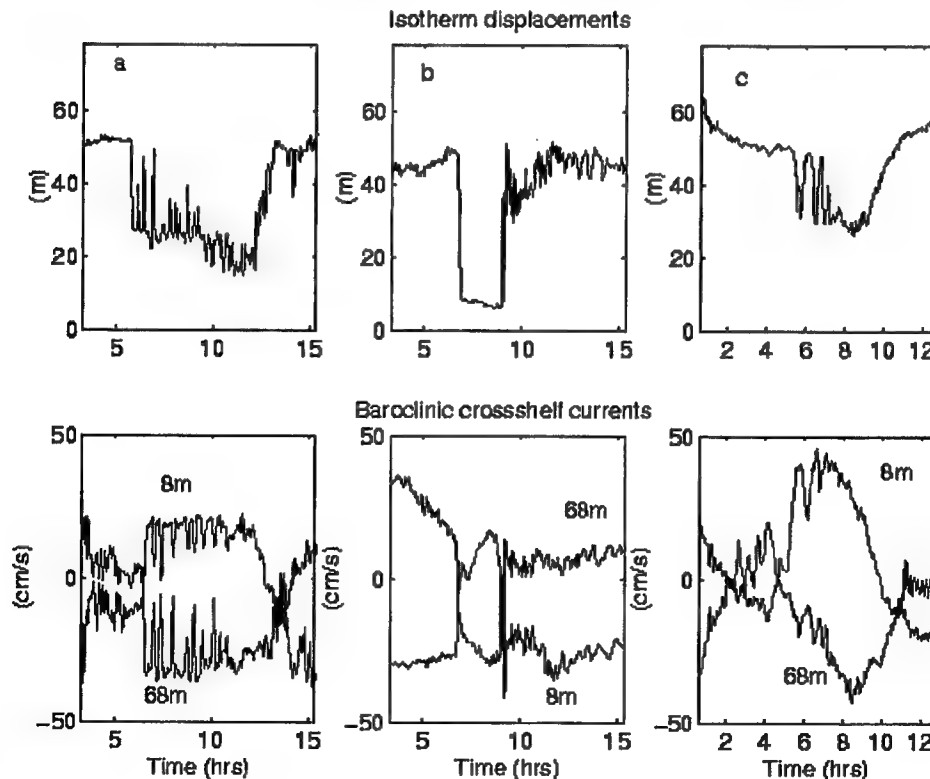
Korteweg de-Vries Model

The evolution of internal waves is studied using a Korteweg de-Vries (KdV) model. An initial waveform is defined as a sinusoidal long wave, representing an internal tide, and the wave is allowed to propagate over shoaling topography and through arbitrary density stratification. The model includes the effects of rotation, cubic nonlinearity and dissipation through turbulent bottom friction. Full details are given by Holloway et al. (1998).

The model is based on the rotated-modified extended KdV equation (reKdV) which is obtained from a perturbation method in second order in wave amplitude and first order in wavelength and is valid when nonlinearity, dispersion and rotation are small. The reKdV equation is,

$$\frac{\partial}{\partial x} \left(\frac{\partial \eta}{\partial t} + (c + \alpha \eta + \alpha_1 \eta^2) \frac{\partial \eta}{\partial x} + \beta \frac{\partial^3 \eta}{\partial x^3} \right) = \frac{f^2}{2c} \eta, \quad (1)$$

Figure 1: Observed time series of vertical displacements of isotherms and corresponding baroclinic cross-shelf currents on the NWS.



where η is the wave profile, x the horizontal coordinate, t time, and f the Coriolis parameter. The phase

where η is the wave profile, x the horizontal coordinate, t time, and f the Coriolis parameter. The phase speed of the linear long wave c is determined by the eigenvalue problem (where f is neglected)

$$\frac{d^2\Phi}{dz^2} + \frac{N^2(z)}{c^2}\Phi = 0 \quad (2)$$

with boundary conditions $\Phi(0) = \Phi(H) = 0$, normalisation $\Phi_{\max} = 1$ and where H is total water depth and $N(z)$ is the Brunt-Vaisala frequency. The coefficients of dispersion (β), quadratic nonlinearity (α) and cubic nonlinearity (α_1) are (Lamb & Yan, 1996),

$$\beta = \frac{c}{2} \frac{\int \Phi^2 dz}{\int (d\Phi/dz)^2 dz}, \quad (3)$$

$$\alpha = \frac{3c}{2} \frac{\int (d\Phi/dz)^3 dz}{\int (d\Phi/dz)^2 dz}, \quad (4)$$

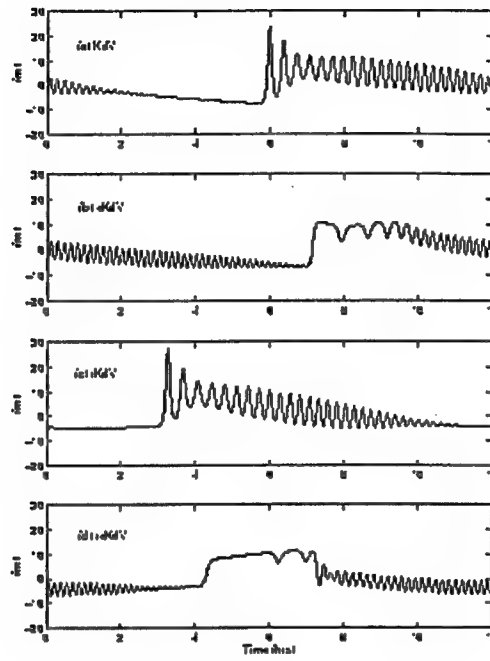
$$\begin{aligned} \alpha_1 = & -\frac{\alpha^2}{c} + 3c \frac{\int ((d\Phi/dz)^4 - (N\Phi/c)^4) dz}{\int (d\Phi/dz)^2 dz} + \\ & + 3c \frac{\int (c(d\Phi/dz)^2 + (N^2\Phi^2/c) - (2\alpha/3)(d\Phi/dz)) (dT/dz) dz}{\int (d\Phi/dz)^2 dz}, \end{aligned} \quad (5)$$

where integration is over the total water depth. $T(z)$ is the first correction to the nonlinear wave mode, given by the solution of

$$\frac{d^2T}{dz^2} + \frac{N^2}{c^2}T = \frac{\alpha N^2}{c^4}\Phi + \frac{dN^2/dz}{c^3}\Phi^2 \quad (6)$$

with $T(0) = T(H) = 0$ and the normalised condition $T(z_{\max}) = 0$, where $\Phi(z_{\max}) = 1$.

Figure 2: Calculated waveforms, at a depth of $\sim 70m$, using different model assumptions with $k = 0$. (a) kdV model, (b) eKdV model, (c) rKdV model, (d) reKdV model.



The effects of slowly varying depth can be included in (1) by introducing a weak source term, as described by Zhou & Grimshaw (1989), defined as,

$$Q = \sqrt{\frac{c_0^3}{c^3} \frac{\int (d\Phi_0/dz)^2 dz}{\int (d\Phi/dz)^2 dz}}, \quad (7)$$

where values with subscript ' 0 ' are the values at some origin x_0 . Quadratic bottom friction with a drag coefficient k can also be introduced. Finally, introducing a change in variable $\zeta(x, \kappa) = \frac{\eta(x, t)}{Q(x)}$ and coordinate $\kappa = \int \frac{dx}{c(x)} - t$, the model equation becomes.

$$\frac{\partial \zeta}{\partial x} + \left(\frac{\alpha Q}{c^2} \zeta + \frac{\alpha_1 Q^2}{c^2} \zeta^2 \right) \frac{\partial \zeta}{\partial \kappa} + \frac{\beta}{c^4} \frac{\partial^3 \zeta}{\partial \kappa^3} + \frac{kcQ}{\beta} \zeta |\zeta| = \frac{f^2}{2c} \int \zeta d\kappa. \quad (8)$$

Equation (8) is solved numerically with periodic boundary conditions and an initial condition of a sinusoidal internal tide.

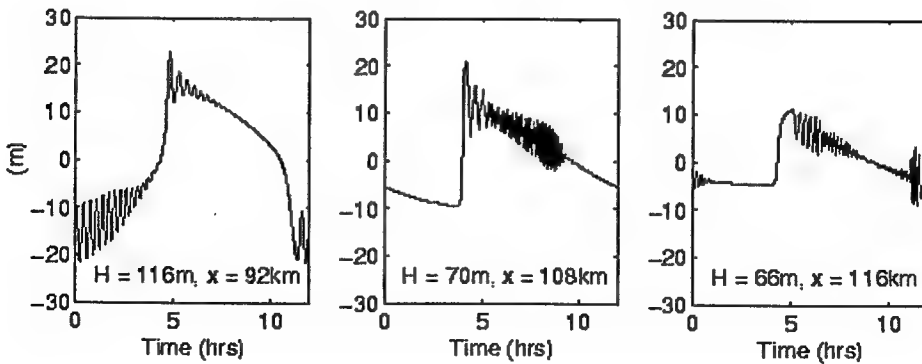
Model Results

Model results are presented for a bathymetric cross-section on the NWS, corresponding to the location of the observations presented in Section 2, using observed stratification from a summer period to define the coefficients in the reKdV model.

The first results presented consider an initial wave of 12 hr period and 2 m amplitude originating in water 500 m deep, although results are not sensitive to the initial water depth as little wave transformation occurs in deep water. Frictional dissipation is also neglected ($k = 0$). Figure 2 shows the wave forms predicted after the wave has propagated 110 km, to a water depth of ~ 70 m, under different model assumptions. Results are shown neglecting cubic nonlinearity and rotation (KdV model), neglecting only rotation (eKdV model), neglecting only cubic nonlinearity (rKdV model) and including all terms (reKdV model). Solutions without cubic nonlinearity show two solitons forming followed by a train of oscillatory waves. Rotation slows the phase speed of the long wave (latitude is 20° S). Cubic nonlinearity dramatically changes the form of the solitary waves to produce wide solitons. The full reKdV model produces a nearly square wave form with a train of oscillatory waves.

Larger amplitude initial waveforms become unrealistically large as they shoal if dissipation is not included in the model. Figure 3 shows the evolution of a 15 m amplitude wave originating in water 1000 m deep for the same bathymetry and stratification as above using the reKdV model and including dissipation with $k = 0.0013$. A variety of waveforms result as the wave evolves showing bores, solitons and wide solitons and oscillatory waves.

Figure 3: Calculated waveforms from the reKdV model at different depths for an initial wave in water 1000 m deep and amplitude 15 m, with $k = 0.0013$.



Discussion

The use of KdV-type models is one possible tool for developing an understanding of the way nonlinear internal waves can form from an internal tide and how they can evolve as they propagate. Solutions to the model are sensitive to background stratification and initial wave amplitude. Cubic nonlinear effects are dramatic for large amplitude waves and higher order terms could also be important. From theory, background shear flow, not considered here, can also be important in determining the model solutions by changing the values of the coefficients of the KdV model.

References

Holloway, P.E., Pelinovsky, E., Talipova, T., and Barnes, B. A nonlinear model of internal tide transformation on the Australian North West Shelf. *J. Phys. Oceanogr.*, 1997, **27**, 871-896.

Holloway, P.E., Pelinovsky, E., and Talipova, T. A generalised Korteweg-de Vries model of internal tide transformation in the coastal zone. Submitted to *J. Geophys. Res.*, 1998.

Lamb, K.G., and Yan, L. The evolution of internal wave undular bores: comparisons of a fully nonlinear numerical model with weakly nonlinear theory. *J. Phys. Oceanogr.*, 1996, **26**, 2712-2734.

Zhou, X., and Grimshaw, R. The effect of variable currents on internal solitary waves. *Dynamics Atm. Oceans*, 1989, **14**, 17-39.

About this document ...

1998-08-19

Preliminary Results from Observations on Internal Tides and Solitary Waves in the Bay of Biscay

Frans-Peter A. Lam*, Theo Gerkema and Leo R.M. Maas

Netherlands Institute for Sea Research (NIOZ)
PO Box 59, 1790 AB Texel, The Netherlands

*) Present affiliation:
TNO Physics and Electronics Laboratory
(TNO-FEL), Underwater Acoustics,
PO Box 96864, 2509 JG The Hague, The Netherlands
e-mail: Lam@fel.tno.nl

1. Introduction

The Bay of Biscay is well known for its energetic internal tides [1]. This is caused by the combination of (summer) stratification, steep (shelf-edge) topography and strong (cross-slope) tidal currents, especially at spring tides [2]. The disintegration of the internal (or: interfacial) tide in internal solitary waves (ISWs from now on), eg. [3], is of importance for biology and fishery [4], sedimentology [5] and has big consequences for acoustics [6] as well as for mooring design.

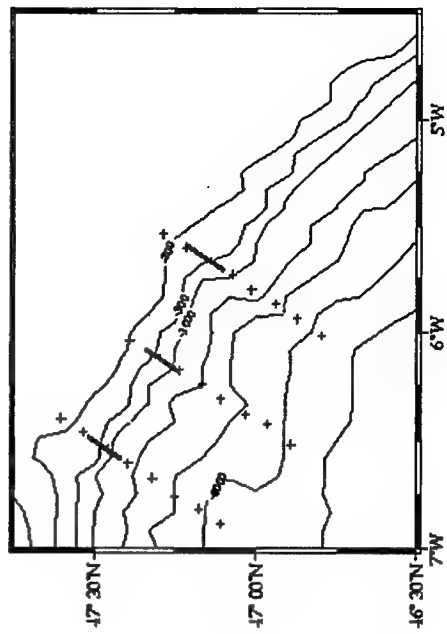
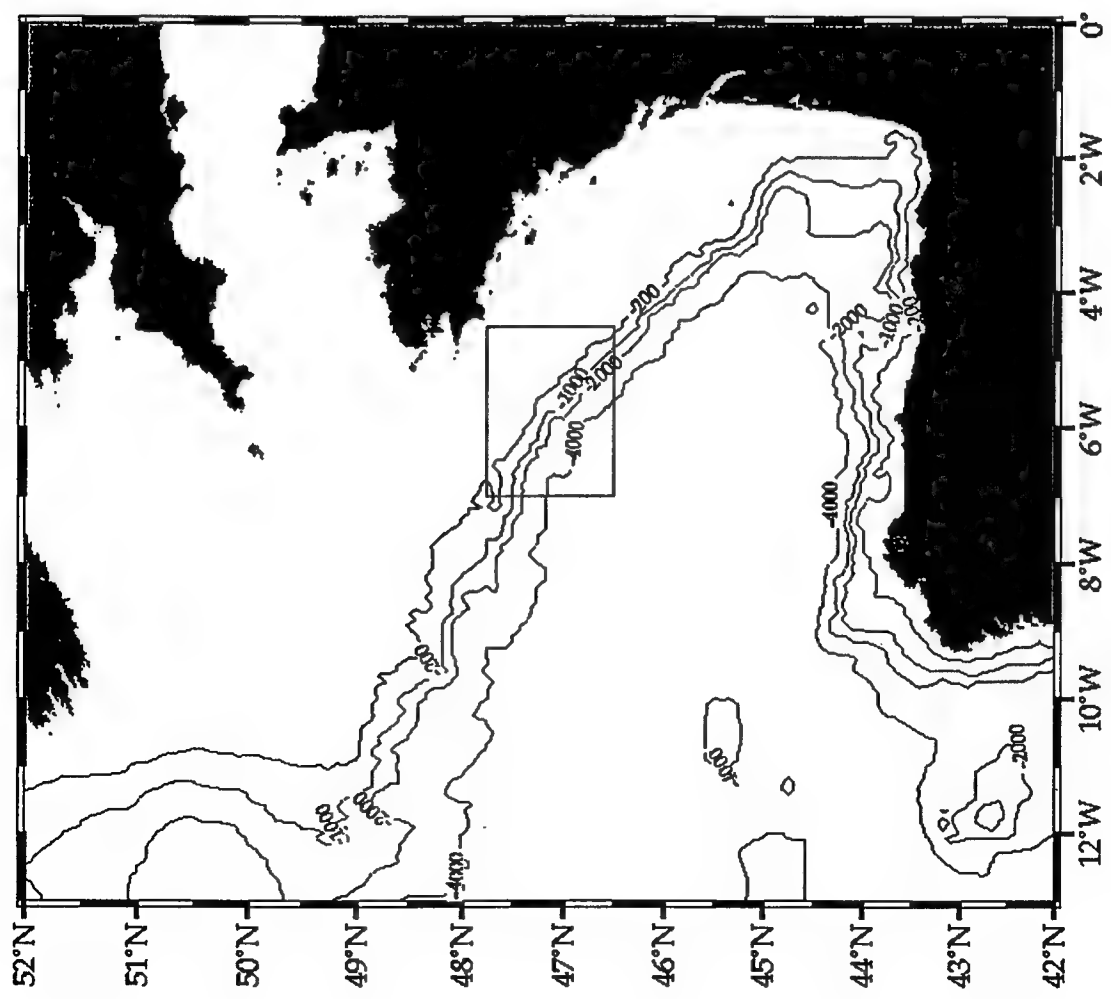
In a numerical study on the generation of ISWs in the Bay of Biscay, Gerkema showed [2,7] that at neap tides the additional dispersion supplied by the Earth's rotation does prevent the disintegration of the internal tide into ISWs. This was corroborated by earlier measurements [3] on the shelf over a whole spring-neap cycle.

2. Experimental setup

Encouraged by the success of Gerkema's model in verifying observations at different forcing magnitudes and in different geographical regions [2,7], additional measurements have been performed at the shelf-edge region in the Bay of Biscay (see figure 1) in August 1995 and in July 1996. Aim of these experiments was to check details of the generation process near the shelf-edge region (figure 2). In order to do so, we tried to observe the travelling internal tide and/or ISWs in both the oceanward and the coastward direction (leftward and rightward direction in figure 2 respectively). This was done by yo-yoing ship's CTD on the slope for 25 hours, and with two thermistor chain and current meter moorings on the shelf respectively.

The simultaneous observations of the travelling ISWs in both directions should provide insight into the precise generation location, and eg. give answer to the question whether the two "trains" are originating from the same depression, or from two separate depressions, as can be seen in figure 2. By measuring with the highest possible resolution --- twice every 5 minutes for the yo-yo station and every 10 seconds for the moored 2x11 thermistors on shelf --- additional and useful information about the fine-scale structure of the passing ISWs can be expected.

Figure 1. The Bay of Biscay (left) as part of the west European shelf-edge. In the inset (right) the shelfbreak region can be seen in more detail. The yo-yo stations has been performed at the middle indicated line at the crossing with the 1000 m isobath. The 2 thermistor chain moorings were located on the shelf, about 32 and 54 km shoreward along this line. Depths are taken from NOAA-ETOPO5; a 5-minute bathymetry database.



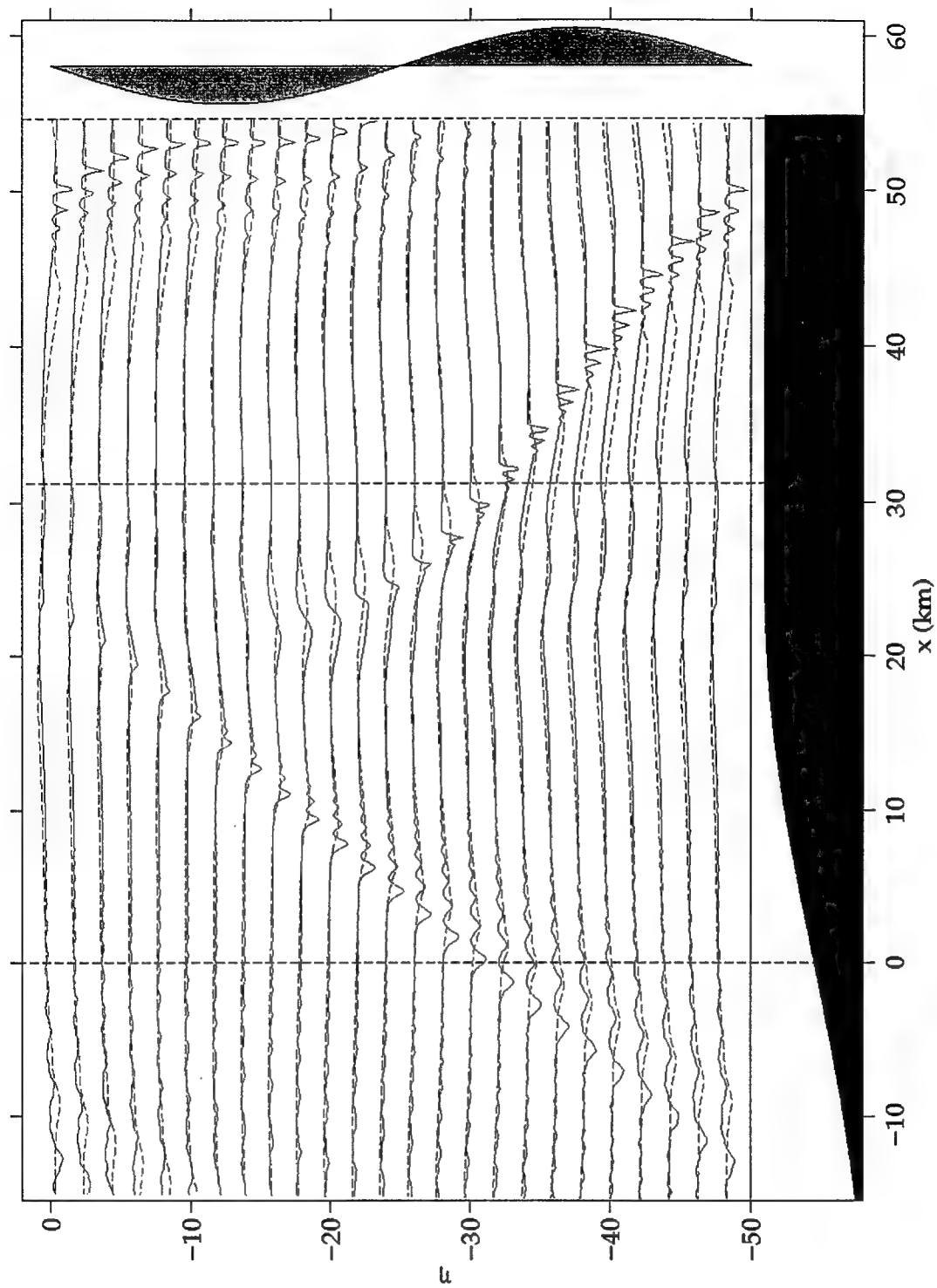


Figure 2. The generation of the internal tide at the transect indicated in figure 1 during spring tides (full lines) and neap tides (dashed) for 1 tidal period as calculated with Gerkema's model [2, 7]. Upper (lower) part of the figure shows the ebb (flow) phase, as is indicated schematically in the right margin. The time differences between successive interface shapes is 1/24 tidal period, corresponding with a dimensionless elevation offset of -2. Topography is sketched at the bottom. Measurements are performed at the positions of the 3 vertical dashed lines: yo-yo station at $x=0$, and the 2 on-shelf moorings at $x= 32$ and 56 km respectively.

3. Observations

In both years the yo-yo measurements have been successful, while some problems had to be faced with the on-shelf moorings. The mooring nearest to the shelf-edge (T1, at $x=32$ km in figure 2) suffered both years from a buoyancy defect, and the other mooring (T2, at $x=56$ km in figure 2) was lost in 1996.

Figure 3 shows an example of the observed temperature, corrected for the varying depths of the thermistors, at the near shelf-edge mooring T1 in 1996. Though there is no maximal stratification (early summer; 2-3 July) the forcing at this time is (nearly at spring tides), and the observed trains of high-frequency waves can probably be identified as ISWs.

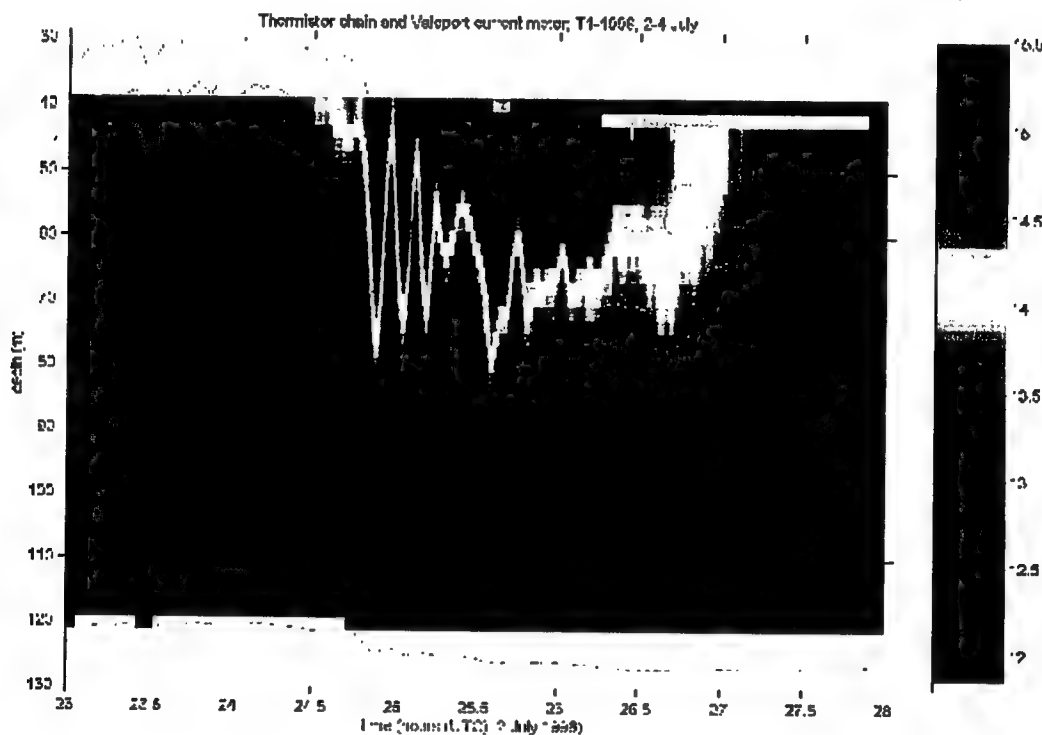


Figure 3. Part of the on-shelf mooring registration 1996. Temperature (in degrees Celsius) has been measured every 10 seconds at the indicated gray lines. The dashed lines are for the current meter positions, where temperature and pressure sensors were located as well. It can be seen that measurements are taken relatively deep, and at variable depth, due to buoyancy problems of the mooring. The red/orange colour in the upper right corner are an artefact of the gridding used.

An example of a part of the yo-yo cast ($x=0$ in figure 2) in 1995 is given in figure 4. Now, August 2, we have a fully developed seasonal thermocline. This measurement is almost 4 days after spring tides, but it can be seen that the vertical elevations of the interface are very large (order 50 m) and fast (20 minutes). High frequency temporal coherence is not easy (if at all) to recognize, and as a result ISWs cannot be positively identified.

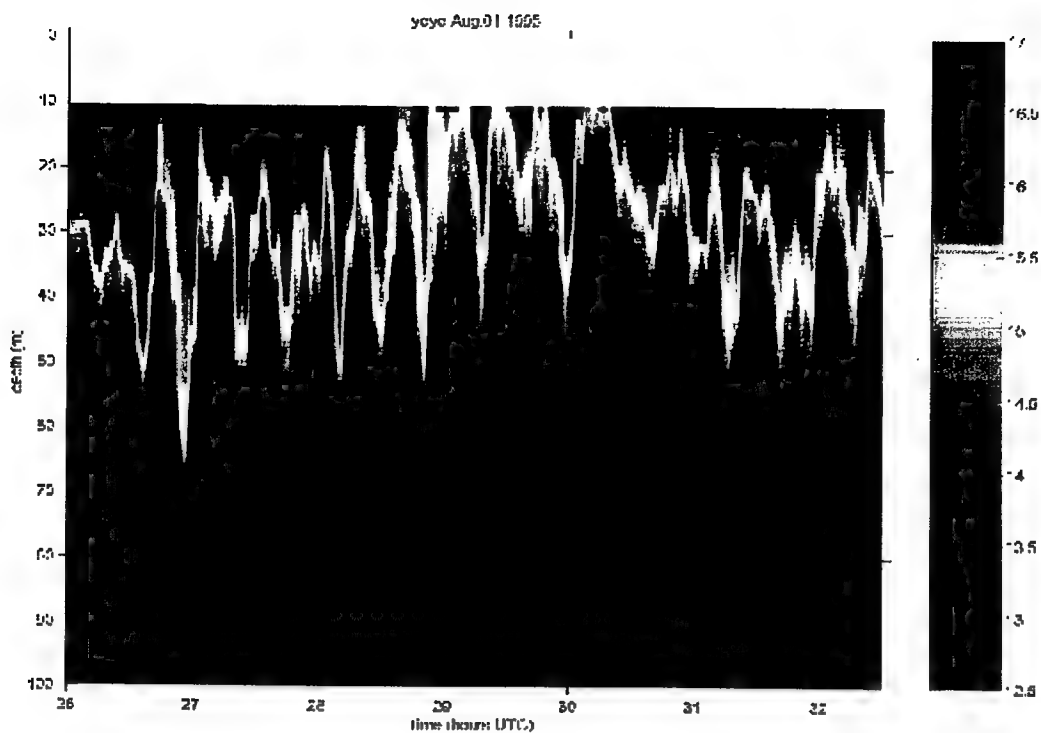


Figure 4. Part of the temperature measurements at the yo-yo cast in 1995. Note the different temperature scale as compared with figure 3. Furthermore, the vertical axis is 30 m shifted, and a somewhat larger time span is selected.

4. Conclusions and discussion

Further work on the data presented here is in progress. Arrival times of oceanward and shoreward travelling ISW fronts at measurement locations (yo-yo station and on-shelf moorings respectively) still have to be compared, but correlation is hard to recognize. This might be due to the fact that topography is far from two-dimensional, as is illustrated in ref. [8]; it can lead to the interference of internal tide and ISW patterns, originating from different generation areas. In figure 3b of ref. [9] this complex interference is visualized by analysing a SAR image.

Another topic concerns the propagation of the internal tide into the deep ocean, which owes its behaviour to the continuous stratification, and can therefore not be described in terms of a two-layer model. This part of the internal tide is of course generated in the same region, and most energetic wave rays are emanating from the shelf-edge into the deep ocean[1]. In ref. [10] it is suggested that another group of ISWs is generated by the oceanward travelling internal-tidal beam, when it crosses the thermocline after its first reflection at the bottom.

In 1995 we did an additional deeper CTD yo-yo: between 950 and 1250 meter, just above the bottom of the shelf slope on the same transect. The measured isotherm elevations were surprisingly high (order 100 m), and these will also be shown in Victoria BC.

References

1. Baines, P.G. (1982) On internal tide generation models. *Deep-Sea Res.* **29**, 307-388
2. Gerkema, T. (1994) *Nonlinear dispersive internal tides: generation models for a rotating ocean.* Ph.D. thesis, Utrecht Univ.
3. Pingree, R.D and G.T. Mardell (1985) Solitary internal waves in the Celtic Sea. *Prog.Oceanog.* **14**, 431-441
4. Holligan, P.M. et al. (1985) Oceanic solitons, nutrient pulses and phytoplankton growth. *Nature* **314**, 348-350
5. Heathershaw, A.D. et al. (1987) Internal tides and sediment transport at the shelf break in the Celtic Sea. *Cont.Shelf Res.* **7**, 485-517
6. Apel, J.R. et al. (1997) An overview of the 1995 SWARM shallow water internal wave acoustic scattering experiment. *IEEE J.Oceanic Eng.* **22**, 465-500
7. Gerkema, T. (1996) A unified model for the generation and fission of internal tides in a rotating ocean. *J.Marine Res.* **54**, 421-450
8. Holt, J.T. and S.A. Thorpe (1997) The propagation of high frequency internal waves in the Celtic Sea. *Deep-Sea Res.* **44**, 2087-2116
9. New, A.L. (1988) Internal tidal mixing in the Bay of Biscay. *Deep-Sea Res.* **35**, 691-709
10. New, A.L. and R.D. Pingree (1992) Local generation of internal soliton packets in the central Bay of Biscay. *Deep-Sea Res.* **39**, 1521-1534

THEORETICAL DESCRIPTIONS OF SHALLOW-WATER SOLITARY INTERNAL WAVES: COMPARISONS WITH FULLY NONLINEAR WAVES

Kevin G. Lamb

*Department of Applied Mathematics, University of Waterloo
Waterloo, Ontario, Canada N2L 3G1*

Two formulations of shallow-water weakly nonlinear theory for internal waves are presented. The structure of solitary waves predicted by these two theories are compared with fully nonlinear solitary waves.

Introduction

In this talk two different formulations of shallow-water, weakly-nonlinear theory will be considered and the predicted structure of solitary waves will be compared with fully nonlinear solitary waves. The latter are computed numerically using an iterative method (1). The two formulations of the theory are obtained by using different sets of independent variables. For the Eulerian formulation the independent variables are (x, z, t) where x and z are the horizontal and vertical Cartesian coordinates and t is time (2,3). For the Euler-Lagrange formulation of the theory z is replaced by the Lagrangian coordinate $y = z - \eta(x, z, t)$

where $\eta(x, z, t)$ is the vertical displacement of the fluid particle at (x, z, t) from its rest position (4).

Eulerian Formulation

Making the incompressible and Boussinesq approximations, neglecting rotation and viscosity, the equations of motion in Cartesian coordinates are

$$\nabla^2 \psi_t - b_x = \psi_x \nabla^2 \psi_z - \psi_z \nabla^2 \psi_x, \quad (1a)$$

$$b_t + N^2(z) \psi_x = \psi_x b_z - \psi_z b_x, \quad (1b)$$

where ψ is the stream function for the velocity $(u, w) = (\psi_x, -\psi_z)$, $b = g\rho'/\rho_0$ where $g = 9.81 \text{ ms}^{-1}$ is the constant gravitational acceleration, ρ_0 is a constant reference density and $\rho'(x, z, t)$ is the density perturbation due to the wave, and ∇^2 is the Laplacian operator. The buoyancy frequency $N(z)$ is given by

$$N^2(z) = -g \frac{d\bar{\rho}}{dz} \geq 0, \quad (2)$$

where $\rho_0 \bar{\rho}$ is the undisturbed density field. For simplicity it is assumed that there is no background flow. The fluid is assumed to lie between two horizontal, rigid planes at $z=0, H$ so that the boundary conditions are $b = \psi_x = 0$ at $z=0, H$.

Under the assumption of small, long waves an asymptotic expansion of the above equations leads to a weakly-nonlinear solution of the form

$$\begin{aligned} \left(\frac{\psi}{N^2} \right) \sim & B \left(\frac{c\phi}{\phi} \right) + \epsilon \left\{ B^2 \left(\frac{c^2 \phi^{1,0}}{E^{1,0}} \right) + B_{zz} \left(\frac{c\phi^{0,1}}{E^{0,1}} \right) \right\} + \epsilon^2 \left\{ B^3 \left(\frac{c^3 \phi^{2,0}}{E^{2,0}} \right) \right. \\ & \left. + (BB_{zz} - \frac{1}{2}B_z^2) \left(\frac{c^2 \phi^{1,1}}{E^{1,1}} \right) + \frac{1}{2}B_z^2 \left(\frac{c^2 \phi_b^{1,1}}{E_b^{1,1}} \right) + B_{zzzz} \left(\frac{c\phi^{0,2}}{E^{0,2}} \right) \right\} + \dots \end{aligned} \quad (3)$$

Here $B = B(x, t)$ and the ϕ and E with the various indices are functions of z . ϵ is a parameter whose value we take to be one. Nondimensional equations would have the same form, in which case ϵ appears as a small parameter measuring the strength of the nonlinearity and dispersion. Here it is included to indicate the relative ordering of the various terms. The leading-order terms in (3) describe infinitesimal, long waves. These, together with the $O(\epsilon)$ terms, comprise first-order theory. Second-order theory includes the $O(\epsilon^2)$ terms. $\phi(z)$ and the linear long-wave propagation speed c are given by the eigenvalue problem

$$\mathcal{L}\phi \equiv \left(\frac{d^2}{dz^2} + \frac{N^2}{c^2} \right) \phi = 0 \quad (4)$$

with boundary conditions $\phi(0) = \phi(H) = 0$. Only mode-1 waves are considered so c is the largest eigenvalue of (4) with ϕ the corresponding eigenfunction. The E_q^{ij} can be expressed in terms of the $\phi_q^{i,j}$ which are determined by equations of the form

$$\mathcal{L}\phi_a^{i,j} = -r_{ijq} \frac{2N^2}{c^3} \phi + S_q^{i,j} \quad (5)$$

where $S_q^{i,j}$ is a known function of the lower-order vertical structure functions. The general solution includes an undetermined constant multiple of ϕ (see 3). The constants r_{ijq} are determined by the solvability conditions $2r_{ijq} \int_0^H N^2 \phi^2 dz = c^3 \int_0^H \phi S_q^{i,j} dz$. The first-order constants r_{10} and r_{01} are given by

$$Ir_{10} = -\frac{3}{2} \int_0^H \phi^3 dz, \quad Ir_{01} = -c \int_0^H \phi^2 dz. \quad (6)$$

where

$$I = 2 \int_0^H \phi'^2 dz. \quad (7)$$

The second order constants are

$$\begin{aligned} Ir_{20} &= - \int_0^H \left\{ \frac{8}{3} r_{10} \phi' \phi_z^{1,0} + 3 \phi'^2 \phi_z^{1,0} \right\} dz, \quad Ir_{02} = - \int_0^H \left\{ c \phi \phi^{0,1} + 2 r_{01} \phi' \phi_z^{0,1} - \frac{3}{2} r_{01} \phi'^2 \right\} dz, \\ Ir_{11a} &= - \int_0^H \left\{ 4 r_{01} \phi_z^{1,0} \phi' + 2 c \phi \phi^{1,0} + 4 r_{10} \phi' \phi_z^{1,0} + 3 \phi_z^{0,1} \phi'^2 - 5 \frac{r_{01}}{c} \phi'^3 \right\} dz, \\ Ir_{11b} &= - \int_0^H \left\{ 6 c \phi \phi^{1,0} + 12 r_{10} \phi' \phi_z^{0,1} + 3 \phi_z^{0,1} \phi'^2 - \frac{25}{2} \frac{r_{01}}{c} \phi'^3 \right\} dz. \end{aligned} \quad (8)$$

The theory also yields an evolution equation for $B(x,t)$, namely

$$\begin{aligned} B_t &= -c B_x + \epsilon (2 r_{10} c B B_x + r_{01} B_{xxx}) \\ &\quad + \epsilon^2 (3 r_{20} c^2 B^2 B_x + r_{11a} c B B_{xxx} + r_{11b} c B_x B_{xx} + r_{02} B_{xxxxx}) + \dots \end{aligned} \quad (9)$$

To $O(\epsilon)$ this is the KdV equation.

Euler-Lagrange Formulation

To use the Lagrangian coordinate $y = z - \eta(x, z, t)$ as the independent variable instead of z we must be able to solve $z = z(x, y, t)$ for y . This requires that $\eta_z < 1$ and in particular rules out waves with overturning isopycnals. The governing equations (1a)-(1b) are replaced by

$$z_t = -\Psi_x, \quad (10a)$$

$$\Theta_t = -\frac{\Psi_y}{z_y} \Theta_x - N^2(y) \frac{z_x}{z_y}, \quad (10b)$$

where Ψ and Θ are the streamfunction ψ and vorticity $\nabla^2 \psi$ expressed as functions of (x, y, t) .

Solutions of (10a)-(10b) have the form

$$\begin{aligned} \begin{pmatrix} \zeta \\ \Psi \\ \Theta \end{pmatrix} &\sim G \begin{pmatrix} Z \\ P \\ T \end{pmatrix} + \epsilon \left\{ G^2 \begin{pmatrix} Z^{1,0} \\ P^{1,0} \\ T^{1,0} \end{pmatrix} + G_{xx} \begin{pmatrix} Z^{0,1} \\ P^{0,1} \\ T^{0,1} \end{pmatrix} \right\} + \epsilon^2 \left\{ G^3 \begin{pmatrix} Z^{2,0} \\ P^{2,0} \\ T^{2,0} \end{pmatrix} \right. \\ &\quad \left. + (G G_{xx} - \frac{1}{2} G_x^2) \begin{pmatrix} Z_a^{1,1} \\ P_a^{1,1} \\ T_a^{1,1} \end{pmatrix} + \frac{1}{2} G_x^2 \begin{pmatrix} Z_b^{1,1} \\ P_b^{1,1} \\ T_b^{1,1} \end{pmatrix} + G_{xxxx} \begin{pmatrix} Z^{0,2} \\ P^{0,2} \\ T^{0,2} \end{pmatrix} \right\} + \dots \end{aligned} \quad (11)$$

where $\zeta = \eta(x, z(x, y, t), t)$ is the isopycnal displacement written as a function of y , $G = G(x, t)$, and Z, P and T with the various indices are functions of y . $G(x, t)$ satisfies (9) with identical values for the coefficients. Z and ϕ satisfy the same eigenvalue problem so, if they are both scaled to have a maximum value of 1, they are identical. In that case we can take $B=G$. The remaining vertical structure functions can be expressed in terms of the $\phi_q^{i,j}(y)$

Comparisons with fully-nonlinear waves

The theoretical approximations are now compared with fully nonlinear waves. Two different density profiles are considered in a fluid of depth $H=100$ m. The first,

$$\bar{\rho}_1(z) = 1 + 0.01 \left(\frac{1 - e^{\frac{z-H}{10}}}{1 - e^{\frac{-H}{10}}} \right), \quad (12)$$

has an exponentially increasing stratification. The second,

$$\bar{\rho}_2(z) = 1.005 - 0.005 \tanh\left(\frac{z-80}{5}\right), \quad (13)$$

has a well defined pycnocline 20 m below the surface. The bottom to surface density difference is 0.01 in both cases. For both stratifications the wave half-widths are approximately 100 m for the largest waves. Comparisons of the isopycnal displacement along the vertical line through the centre of a number of waves are shown in figures 1 and 2. Solid curves are profiles from the fully nonlinear waves. Dashed curves are the theoretical profiles. In the Euler-Lagrange formulation the leading order isopycnal displacement is $\zeta = GZ(y)$. For the Eulerian formulation the isopycnal displacement is obtained by expanding

$\bar{\rho}(z) + \rho'(x, z, t) = \bar{\rho}(z - \eta(x, z, t))$ which gives $\eta = B\phi(z)$ at leading-order. Since $Z(y) = \phi(y)$ both expression have the identical form however there is a crucial difference between the two. In the Eulerian expression η is the vertical displacement of an isopycnal as a function of the displaced isopycnal height. In the Euler-Lagrange expression the vertical displacement of an isopycnal is given as a function of the rest height of the isopycnal. In figure 1 it can be seen that for density 1 the Eulerian description is much better than the Euler-Lagrange description while figure 2 shows that the opposite is true for density 2. Using first-order theory the theoretical isopycnal profiles obtained using the Eulerian formulation are almost indistinguishable from the fully-nonlinear wave profiles. This is remarkable as the largest wave considered is very close to breaking (i.e., $\max \eta_z$ is close to 1). Use of first-order theory for density 2 also reduces the error significantly but the agreement is not as good. For density 2 the largest wave is far from breaking.

In figures 3 and 4 vertical profiles of the horizontal velocity through the centre of the waves are shown. Solid curves are the profiles for the fully-nonlinear waves. Dashed profiles are the theoretical results. In figure 3 leading- and first-order Eulerian approximations are shown for density 1. In figure 4 leading- and first-order Euler Lagrange approximations are shown for density 2. For the Eulerian formulation the first-order velocity is given by

$$u = B\phi' + \epsilon(B^2 c^2 \phi_z^{1,0} + B_{zz} c \phi_z^{0,1}). \quad (14)$$

For the Euler-Lagrange formulation u is given, at first-order, by

$$u = \frac{Bc\phi' + \epsilon(B^2 P_y^{1,0} + B_{xx} P_y^{0,1})}{1 + \epsilon B\phi'}. \quad (15)$$

For leading-order theory the $\mathcal{O}(\epsilon)$ terms are dropped. For the first-order expressions for u the value of B_{xx} is needed in the centre of the wave. For this the well-known solitary wave solution $B = b_o \operatorname{sech}^2(\theta)$ of the KdV equation is used to express $B_{xx}(0,0)$ in terms of b_o . Here $\theta = (x - Vt)/\lambda = 0$ at the wave centre. For the vertical profiles the second-order coefficients r_{20} , r_{11a} , r_{11b} and r_{02} are not required, however for horizontal profiles they are required to calculate $\mathcal{O}(\epsilon)$ corrections to λ and to the expression for B .

For density 1 the theoretical estimate is very good for even the largest wave. For density 2 the magnitude of the velocities is underestimated for the larger waves well below the pycnocline. The theory does correctly predict a minimum in u immediately below the pycnocline, something that is not predicted by leading-order theory. The Eulerian formulation incorrectly predicts a subsurface maximum in u for the largest 2 waves (not shown).

These results show that the best formulation of shallow-water weakly-nonlinear theory for solitary internal waves is stratification dependent. Comparisons for more complicated stratifications taken from oceanographic observations will be shown.

References

- (1) Turkington, B., Eydeland, A., and S. Wang, *Stud. Appl. Math.*, **85**, 93-127, 1991.
- (2) Benney, D. J., *J. Math. Phys.*, **45**, 52-63, 1966.
- (3) Lamb, K. G., and L. Yan, *J. Phys. Oceanogr.*, **26**, 2712-2734, 1996.
- (4) Gear, J. A., and R. Grimshaw, *Phys. Fluids*, **26**, 14-29, 1983.

- [Figures ...](#)
- [About this document ...](#)

[Next](#) [Up](#) [Previous](#)

Next:[Figures ...](#)

1998-09-17

K. G. Lamb, Theoretical descriptions ... Figures

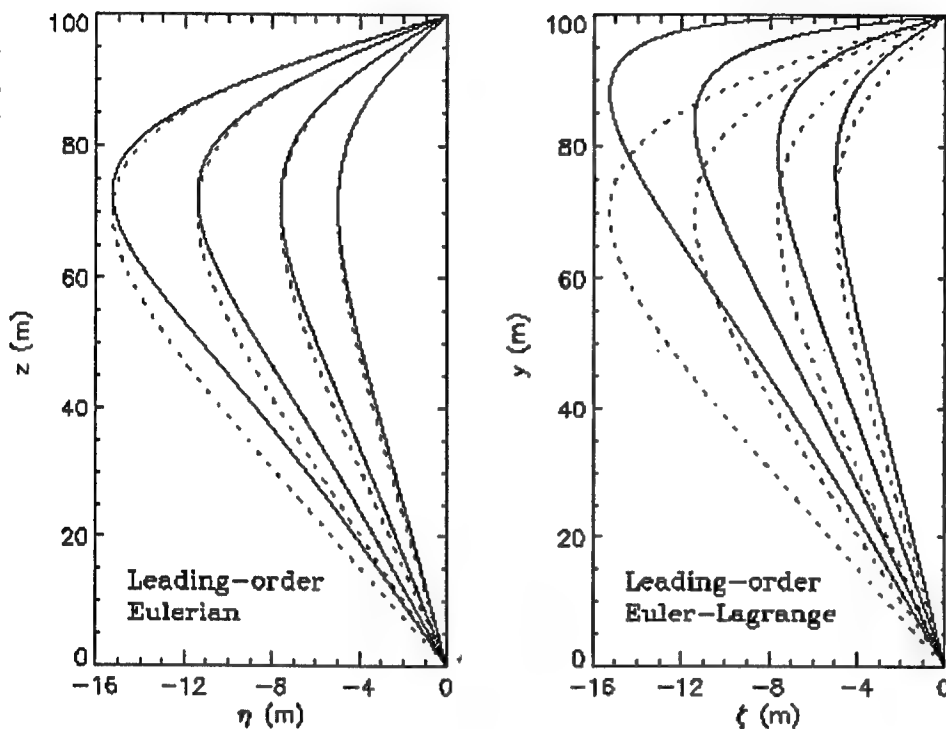


Figure 1. Isopycnal displacements for density 1. Comparison of leading-order Eulerian and Euler-Lagrange theories (dashed) with fully nonlinear waves (solid).

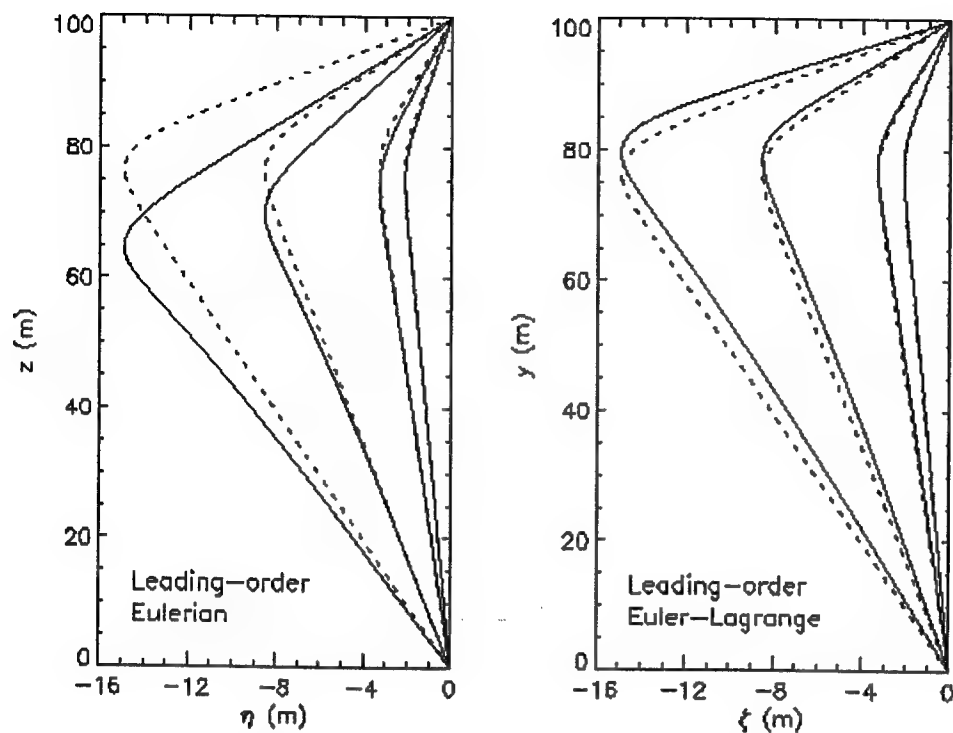


Figure 2. Isopycnal displacements for density 2. Comparison of leading-order Eulerian and Euler-Lagrange theories (dashed) with fully nonlinear waves (solid).

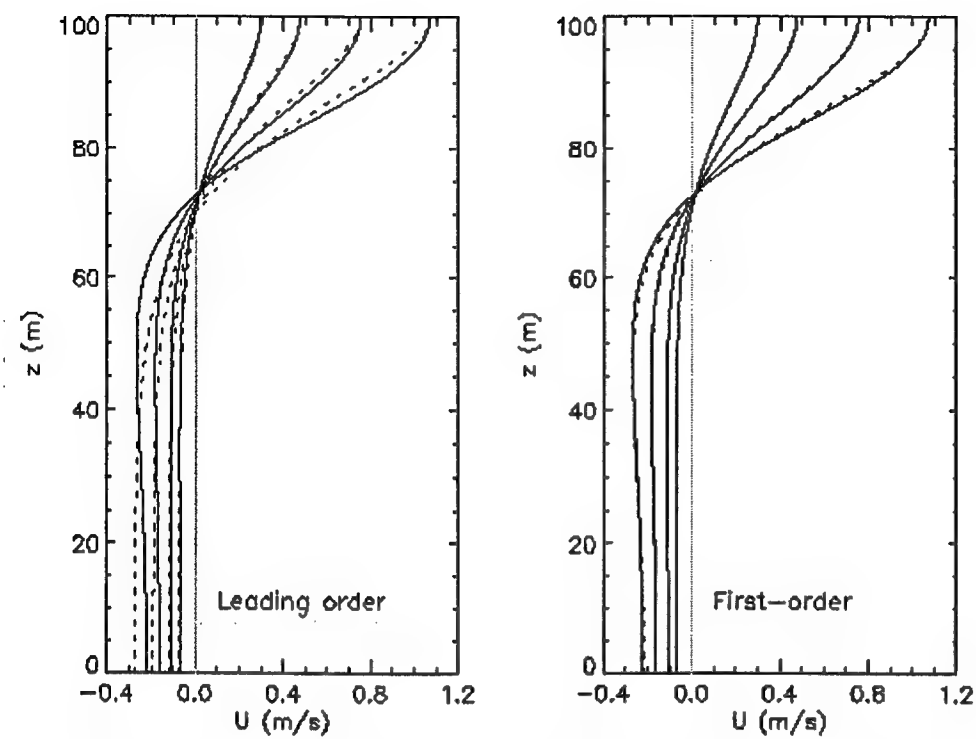


Figure 3. Horizontal velocity profiles. Density 1. Comparison of leading- and first-order Eulerian approximations (dashed) with fully nonlinear waves (solid).

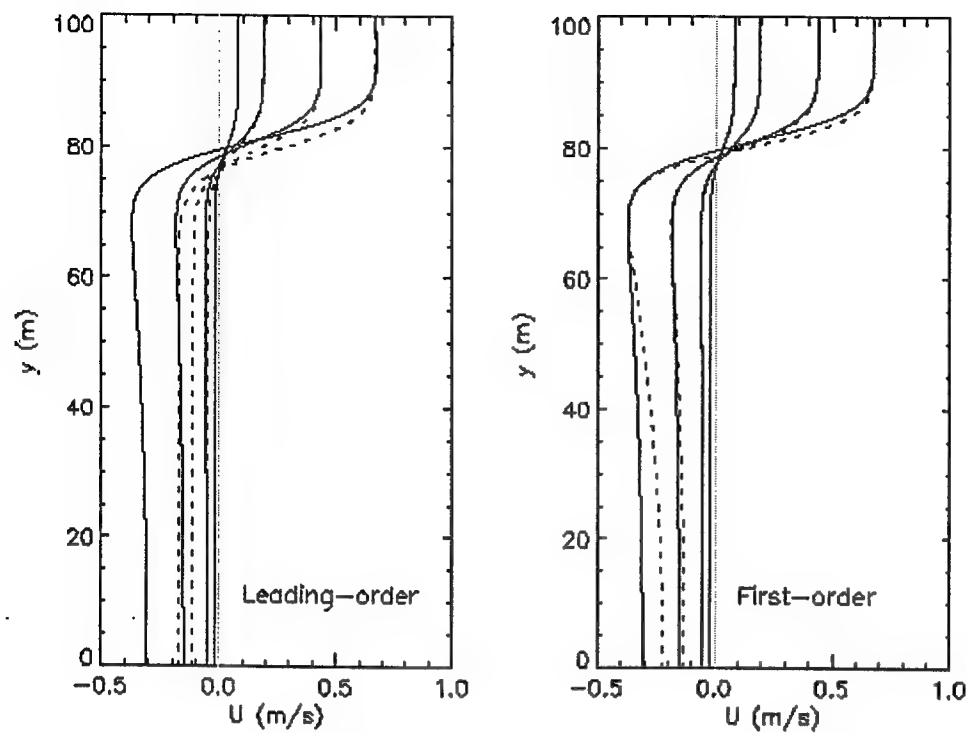


Figure 4. Horizontal velocity profiles. Density 2. Comparison of leading- and first-order Euler-Lagrange approximations (dashed) with fully nonlinear waves (solid).

1998-09-09

Numerical modeling of internal wave-wave interactions

Patrick Lynett and Philip L.-F. Liu

School of Civil and Environmental Engineering
Cornell University
Ithaca, NY

Internal waves have been observed in different parts of the world. For example, Ziegenbein (1969) and Lacombe & Richez (1982) measured eastward propagating internal waves in the Strait of Gibraltar. LaViolette & Arnone (1988) presented further measurements of internal waves in the Strait, together with simultaneous visual observations from aircraft and the space shuttle. The internal waves are believed to be generated by the tidal flow over Camarinal Sill at the western end of the Strait. While the tidal flow over the sill is westward, an internal lee wave or a hydraulic jump is formed on the westward side of the sill. As the westward component of the flow relaxes and eventually reverses to an eastward flow, the lee wave disturbance evolves into a train of nonlinear internal waves propagating eastward into the Strait.

Gargett (1976) studied internal waves observed in the Strait of Georgia, British Columbia. She attributes their generation to abrupt changes in current speed, characteristics of the tidal flow within the passes between islands to the south of the strait.

Farmer & Smith (1978) measured trains of large amplitude, nonlinear internal waves in Knight Inlet, a long and narrow fjord in British Columbia. These waves typically had amplitudes in excess of 10 meters and wavelengths of 70 to 100 meters. They traveled on the pycnocline, whose depth was typically 15 to 30 meters in the 400 meters deep water.

Osborne & Burch (1980) recorded the observation of internal waves in the Andaman Sea, offshore Thailand. Their measurements indicated a connection with the semidiurnal tide and suggested that the Nicobar Island chain and northern Sumatra were likely candidate for potential source regions. Osborne & Burch (1980) noted that knowledge of internal wave behavior would be necessary for the design of deepwater offshore production facilities.

More recently, using the ERS-1 and ERS-2 SAR images, Liu et al. (1998) reported many observations of internal waves in China Sea. They attribute the frequent generation of internal waves in the region of northwest of Taiwan to the upwelling induced by the Kuroshio intrusion (major western boundary current of the Pacific) at the Shelf break. They also showed the evidences of strong wave-wave interactions in both Yellow Sea and East China Sea.

Most of existing analyses on the propagation of internal waves have been based on the Korteweg de Vries (KdV) equation, neglecting two-dimensional and reflection effects (Lee & Beardsley 1974, Farmer 1978, Maxworthy 1979, Apel et al. 1985, Liu 1988), or the Kadomtsev-Petviashvili (KP) equation, which includes weak two-dimensional effects (Pierini 1989, Tomasson 1991, Chen & Liu 1995). However, the observations made in China Sea clearly indicated strong wave-wave interactions and the diffraction and refraction of internal waves by bathymetry and islands (Liu et al. 1998).

Therefore, two-dimensional and reflection effects can not be ignored.

Tomasson (1991) derived a set of Boussinesq equations for a two-layer fluid system. In the dimensionless form these equations can be written as:

$$\frac{\partial \eta}{\partial t} + \frac{\partial u}{\partial x} + \frac{\partial v}{\partial y} = O(\alpha^3, \beta^2)$$

$$\begin{aligned} \frac{\partial u}{\partial t} + \frac{\partial \eta}{\partial x} + \alpha \left[\frac{1}{h_2} - \frac{1}{h_1} \right] \left[2u \frac{\partial u}{\partial x} + \frac{\partial(vu)}{\partial y} - \eta \frac{\partial u}{\partial t} \right] + \alpha^2 \left[\frac{1}{h_2^2} - \frac{1}{h_2 h_1} + \frac{1}{h_1^2} \right] \left[\frac{\partial(\eta^2 u)}{\partial t} - \frac{\partial(\eta u^2)}{\partial x} - 2\eta v \frac{\partial u}{\partial y} - uv \frac{\partial \eta}{\partial y} \right] \\ - \beta \frac{h_1 h_2}{3} \left[\frac{\partial^3 u}{\partial x^2 \partial t} + \frac{\partial^3 u}{\partial y^2 \partial t} \right] = O(\alpha^3, \beta^2) \end{aligned}$$

$$\begin{aligned} \frac{\partial v}{\partial t} + \frac{\partial \eta}{\partial y} + \alpha \left[\frac{1}{h_2} - \frac{1}{h_1} \right] \left[2v \frac{\partial v}{\partial y} + \frac{\partial(vu)}{\partial x} - \eta \frac{\partial v}{\partial t} \right] + \alpha^2 \left[\frac{1}{h_2^2} - \frac{1}{h_2 h_1} + \frac{1}{h_1^2} \right] \left[\frac{\partial(\eta^2 v)}{\partial t} - \frac{\partial(\eta v^2)}{\partial y} - 2\eta u \frac{\partial v}{\partial x} - uv \frac{\partial \eta}{\partial x} \right] \\ - \beta \frac{h_1 h_2}{3} \left[\frac{\partial^3 v}{\partial x^2 \partial t} + \frac{\partial^3 v}{\partial y^2 \partial t} \right] = O(\alpha^3, \beta^2) \end{aligned}$$

in which h_1 and h_2 are the dimensionless thickness of the upper and lower layer, respectively, (u, v) represents the flux in the lower layer, eta denotes the interfacial displacement. These equations are derived under the assumption of weak nonlinearity, alpha $\ll O(1)$, and weak dispersion, beta $\ll O(1)$. It is also assumed that $O(\alpha^2) = O(\beta)$. Note that for completeness, both quadratic nonlinearity and cubic nonlinearity have been kept in the equations.

If the cubic nonlinear terms are ignored in the above equations can be simplified to the well-known KdV equation, which has the dimensional solitary wave solution,

$$\eta(x, t) = \alpha * \operatorname{sech}^2 \left(\frac{x - ct}{l} \right)$$

where

$$\begin{aligned}
 \mathbf{a} &= \text{wave amplitude,} \\
 c &= c_o * (1 + (a + (h_2 - h_1)) / (2 * h_1 * h_2)) \\
 c_o &= \sqrt{g * h_o * \Delta p} \\
 \mathbf{g} &= \text{gravity,} \\
 \Delta p &= \text{density difference,} \\
 h_o &= h_1 * h_2 / (h_1 + h_2)
 \end{aligned}$$

and

$$l = 2 * h_1 * h_2 / \sqrt{3 * a * (h_1 - h_2)}$$

The analytical solution has been plotted in Figure 1.

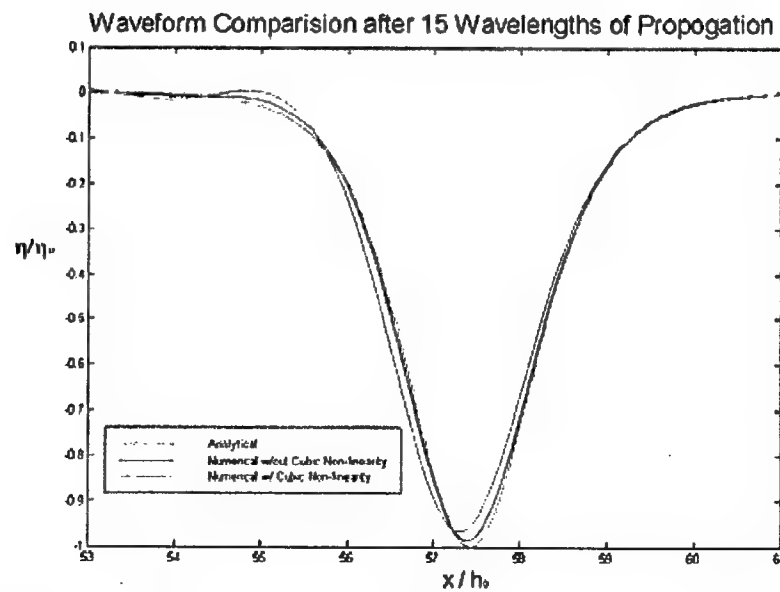


Figure 1. Solitary waveform comparison ($\alpha=0.1$, $\beta=0.008$) showing analytical (blue), numerical without cubic non-linearity (green), and numerical with cubic non-linearity (red)

A numerical algorithm has been developed to solve the Boussinesq equations as an initial boundary-value problem. As a test case the solitary wave solutions are used as the initial condition and computations are carried out with and without the cubic nonlinearity. As shown in Figure 1, after a propagation distance of 15 wavelengths, the numerical solitary wave solutions, without including the cubic nonlinearity, remain very similar to the analytical solutions. However, when the cubic nonlinearity is included, the wave amplitude is reduced slightly and the waveform is also dispersed. In Figure 2, the evolution of a solitary wave propagating onto a shelf is displayed. In this case the thickness of the lower layer has been decreased gradually; the initially depressed (negative) soliton degenerates into a series of oscillatory waves with a leading depression wave.

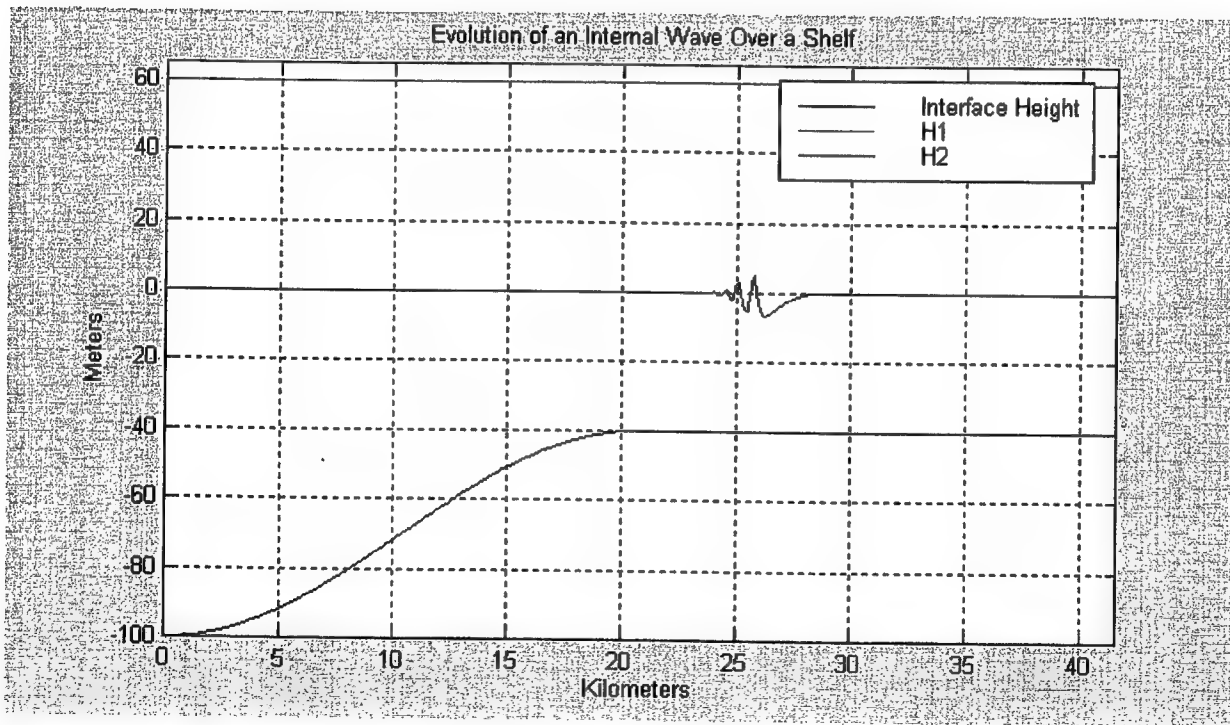


Figure 2. Internal solitary wave ($\alpha=0.27$, $\beta=0.012$) propagation over a shelf

The numerical model has also been used to investigate the wave-wave interactions. As shown in Figure 3 and 4, two solitons propagate obliquely at 45 and 20 degree angles, respectively. For the small incident angle case, stem waves are generated in both surface and internal waves

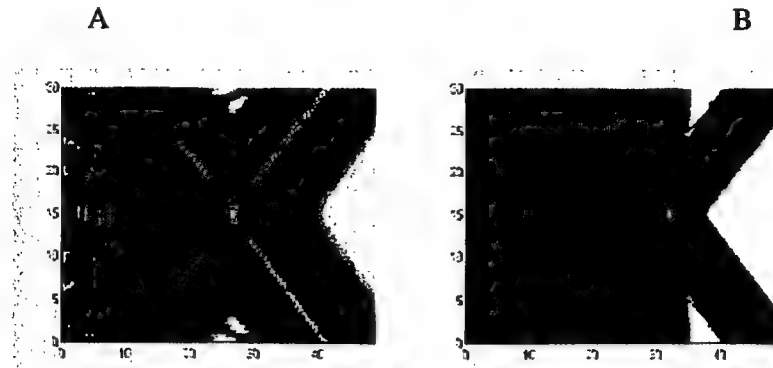


Figure 3. Wave-wave interactions for two 45 degree oblique solitary surface waves (alpha=0.1)[A] and internal waves (alpha=0.1,beta=0.008)[B]

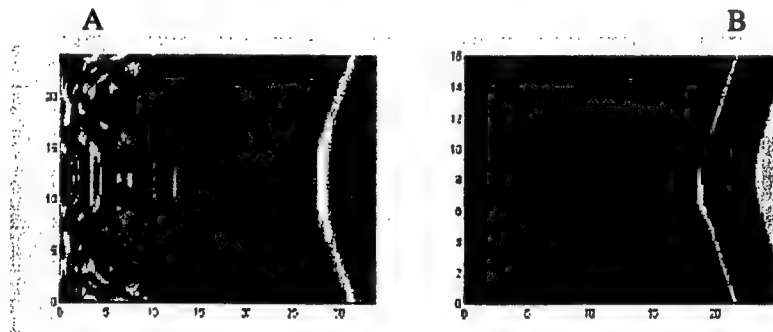


Figure 4. Wave-wave interactions for two 20 degree oblique solitary surface waves (alpha=0.1)[A] and internal waves (alpha=0.1,beta=0.008)[B]

From the above figures, it is evident that there are small, but clear differences between surface and internal wave-wave interactions. The presented numerical model will be extended to study internal wave interaction with islands and varying topography.

References:

Chen, Y. & Liu, P. L.-F. 1995 "The unified Kadomtsev-Petviashvili equation for interfacial waves", *J. Fluid Mech.*, **288**, 383-408.

Farmer, D. M. 1978 "Observations of long nonlinear internal waves in a lake", *J. Phys. Oceanography*, **8**, 63-73.

Lacombe, H. & Richez, C. 1982 "The regime of the Strait of Gibraltar," in *Hydrodynamics of semi-enclosed seas*, 13-73, Elsvier.

LaViolette, P. E. & Arnone, R. A. 1988 "A tide-generated internal waveform in the western approaches to the Strait of Gibraltar," *J. Geophys. Res.*, **93**, 15,653-667.

Lee, C-Y. & Beardsley, R. C. 1974 "The generation of long nonlinear internal waves in a weakly stratified shear flow," *J. Geophys. Res.*, **79**, 453-462.

Liu, A. K 1988 "Analysis of nonlinear internal waves in the New York Bight," *J. Geophys. Res.* **93**, 12,317-329.

Liu, A. K., Chang, Y.S., Hsu, M. K. & Liang, N. K., 1998 "Evolution of nonlinear internal waves in East and South China Seas", *J. Geophys. Res.*, **103**, 7995-8008.

Maxworthy, T. 1979 "A note on the internal solitary waves produced by tidal flow over a three-dimensional ridge", *J. Geophys. Res.*, **84**, 338-346.

Osborne, A. R. & Burch, T. L. 1980 "Internal solitons in Andaman Sea," *Science*, **208**, 451-460.

Pierini, S. 1989 "A model for the Alboran Sea internal solitary waves," *J. Phys. Oceanography*, **19**, 755-722.

Tomasson, G. G. 1991 *Nonlinear waves in a channel: Three-dimensional and rotational effects*. Doctoral Thesis, M.I.T.

Ziegenbein, J. 1969 "Short internal waves in the Strait of Gibraltar", *Deep Sea Res.*, **16**, 479-487.

How to Describe Strong Internal Waves in Coastal Areas

Lev A. Ostrovsky

*University of Colorado, CIRES; NOAA ETL
Boulder, CO, USA.*

Abstract

Model evolution equations for strongly nonlinear internal waves in the ocean are discussed in application to recent field experiments including COPE. For the cases considered, a commonly used Korteweg-de Vries (KdV) equation is inapplicable, and modified models with adding higher-order terms are needed (CombKdV equation). A most adequate and physically substantiated model uses an "exact" (for very long waves) nonlinearity and nonlinear dispersion. Theoretical results are compared with observational data. Some problems are discussed in conclusion.

Introduction

There exists a relatively large body of literature concerning observations and theoretical models of nonlinear internal waves (IW) in shelf areas (see, e.g., the review paper [1]). A common tool for description of these processes is the Korteweg-de Vries (KdV) equation that is applicable to relatively small-amplitude waves. However, in some cases really strong nonlinear waves are observed. A recent example is the Coastal Ocean Probe Experiment (COPE), which has been carried out in September 1995 in the Oregon Bay. Its data clearly indicated the presence of extremely strong trains of tidally-generated internal waves [2],[3]. The isotherm depressions consisted of solitary pulses (we shall call them solitons independently of how strict this definition could be) with amplitudes of thermocline displacements typically of order 10-20 m, and sometimes reaching 30 m. Even more important is the fact that they propagate into the background of a very shallow, 5-7m depth, pycnocline. This testifies for an extremely strong nonlinearity of the process (a high "Mach number," using the gas dynamic terminology). Thus, the problem of creating an adequate theoretical model of these processes is evidently actual.

KdV model

As mentioned, the models of shallow-sea solitons are commonly based on the classical Korteweg-de Vries equation

$$\frac{\partial \eta}{\partial \tau} + (c + \alpha \eta) \frac{\partial \eta}{\partial x} + \beta \frac{\partial^3 \eta}{\partial x^3} = 0, \quad (1)$$

where η is the displacement of an isopycnal surface, and c is the phase velocity of a long wave

corresponding to a given mode. This parameter is defined as an eigenfunction of the corresponding linear boundary problem for long-wave limit. Here we shall consider a simplified model of stratification in which the fluid consists of two layers: upper, of thickness h_1 and density ρ_1 and lower, with h_2 and $\rho_2 > \rho_1$, respectively. In this case, the parameters of (1) are

$$c = \sqrt{\frac{g\Delta\rho}{\rho} \frac{h_1 h_2}{h_1 + h_2}}, \quad \alpha = \frac{3c(h_2 - h_1)}{2h_1 h_2}, \quad \beta = \frac{ch_1 h_2}{6} \quad (2)$$

(all these expressions suggest that $\Delta\rho = \rho_2 - \rho_1 \ll \rho_{1,2}$ which is always true in the ocean). This equation has a family of well known solitary solutions. Such a model works well for a number of IW observations but is inapplicable for the cases considered here.

CombKdV model

The next-level model which may be tried takes into account the higher degree on nonlinearity; it is so-called CombKdV equation [1]:

$$\frac{\partial\eta}{\partial\tau} + (c + \alpha\eta + \alpha_1\eta^2) \frac{\partial\eta}{\partial x} + \beta \frac{\partial^3\eta}{\partial x^3} = 0, \quad (3)$$

The parameters c , α , and β are the same as for the KdV equation, for $\alpha_1 = 0$. The cubic nonlinearity parameter α_1 , for a two-layer model, is

$$\alpha_1 = \frac{3c}{h_1^2 h_2^2} \left[\frac{7}{8} (h_1 - h_2)^2 - \left(\frac{h_1^3 + h_2^3}{h_1 + h_2} \right) \right]. \quad (4)$$

Note that always $\alpha_1 < 0$, whereas the sign of α depends on the position of the interface (pycnocline). In our case $h_1 < h_2$, and $\alpha < 0$ as well, so that in the solitary wave, $\eta < 0$ (a depression). Moreover, there exist a critical value of displacement η , for which the nonlinearity tends to zero, namely:

$$\eta_m = -\alpha/\alpha_1.$$

The equation (3) is known to be completely integrable. It also has a solution in the form of a soliton. Its amplitude η_0 is limited by the value $\eta_{cr} = \alpha/\alpha_1$. If η_0 is sufficiently small, the wave is close to that defined by the KdV equation, but for larger solitons, the wave is broadening and when η_0 approaches η_{cr} , it acquires almost rectangular shape.

Comparison with the experimental data shows that the CombKdV model gives a much better agreement than the usual KdV model.

An equation with “exact” nonlinearity and nonlinear dispersion.

A more consistent approach can be developed based on the expression for “exact” nonlinear term obtained as an analog of the shallow-water theory for the surface waves. We suggest to use the equation

$$\frac{\partial \eta}{\partial t} + c(\eta) \frac{\partial \eta}{\partial x} + \frac{\partial}{\partial x} \left(\beta(\eta) \frac{\partial^2 \eta}{\partial x^2} \right) = 0 \quad (5)$$

with the same $c(\eta)$ and $\beta(\eta)$ depending on the local pycnocline displacement: in particular,

$$\beta = \frac{c(\eta)}{6} (h_1 + \eta) (h_2 - \eta). \quad (6)$$

In case of a thin upper layer most of wave energy is concentrated in this layer, and the local long-wave velocity is

$$c(\eta) = \sqrt{g'} (3\sqrt{h_1 + \eta} - 2\sqrt{h_1}); \quad g' = g(\Delta\rho/\rho). \quad (7)$$

For arbitrary relationship between h_1 and h_2 , the local wave velocity must be found from differential equations (D. Pelinovsky):

$$c = H^{-1} \left[\frac{(h_2 - \eta)^2 - (h_1 + \eta)^2}{(h_2 + \eta)} u + \sqrt{g' H (h_1 + \eta) (h_2 - \eta) - \frac{H^2 (h_1 + \eta)}{h_2} u^2} \right], \quad (8)$$

$$\frac{du}{d\eta} = \frac{c(\eta) + u}{h_1 + u} \quad (9)$$

The equation (5) also has a family of solitons which fit the COPE data quite well. It is notable that there exist a rather wide intermediate range where the soliton duration is almost independent of its amplitude; this agrees well with observational data [2].

Conclusions

These results show that even for strongly nonlinear waves, one-dimensional evolution equations, albeit not strictly derived from the basic hydrodynamic equations, can provide a satisfactory description of real processes in a broad range of their parameters. Now we are continuing to actively study evolution equations with nonlinear dispersion.

It appears that strongly nonlinear internal waves are a rather typical phenomenon for some shelf areas during spring tides; note that the PRIMER experiment performed by WHOI near the East coast, also demonstrated the presence of strong IWs. These areas deserve a special attention of oceanographers as those of especially active mixing, transport of biomasses and pollutants, etc. Regarding the theory, it is very desirable, along with further studies of model equations, to supplement these studies with direct numerical modeling of hydrodynamic equations.

- [Bibliography](#)
- [About this document ...](#)

[Next](#) | [Up](#) | [Previous](#)

Next:Bibliography
1998-10-08

[Next](#) | [Up](#) | [Previous](#)

Next:About this document ... Up:How to Describe Strong... Previous:How to Describe Strong...

Bibliography

- 1 L. A. Ostrovsky and Yu. A. Stepanyants, 1989. Do internal solitons exist in the ocean? *Rev. Geophys.*, **27**, 293-310.
- 2 T. P. Stanton and L. A. Ostrovsky, 1998. Observations of highly nonlinear internal solitons over the continental shelf. Accepted for *Geophys. Res. Lett.*
- 3 R. A. Kropfli, L. A. Ostrovsky, T. P. Stanton, E. A. Skirta, A. N. Keane, and V. Irisov, 1998. Relationships between strong internal waves in the coastal zone and their radar and radiometric signatures. Accepted for *J. Geophys. Res.*

1998-10-08

Numerical modelling of the evolution of internal bores and generation of internal solitons at the Malin Shelf

Efim Pelinovsky and Tatjana Talipova

Department of Applied Hydrodynamics and Nonlinear Acoustics,
Institute of Applied Physics, Russian Academy of Sciences,
Nizhny Novgorod, Russia

Justin Small

Defence Evaluation Research Agency,
Winfirth, Dorset, UK

1. Introduction

The SESAME experiment (Small et al, this workshop) at the Malin shelf-edge provided a number of observed examples of internal bore evolution both over the continental slope and on the shelf. This process is important to understand as a generator of internal solitons. Further, knowledge of the evolution of bores and waves may allow prediction forward from observations at a fixed point to distant points. Here the observations have been numerically simulated with the extended Korteweg-de-Vries type equations. Results indicate close agreement in the cases studied for single sources.

2. Observations of bore evolution

On the 13th August 1996 during the Shelf Edge Study Acoustic Measurement Experiment (SESAME) a number of ship tows across the Malin shelf-edge were conducted. The ship towed a thermistor chain and carried a hull-mounted ADCP. The thermistor chain resolved the internal waves well, with a 20 second sub-sampling from the original 1 Hz sampling, but the ADCP, averaging over 2 minutes, often smoothed out the high frequency waves. Figure 1 illustrates a set of four thermistor chain surveys which clearly show the evolution of an internal bore (marked ?A?) in the first survey into a set of large amplitude (~ 30 m) internal waves during the last two surveys. The bore was seen to move on-shelf with a phase speed close to that of the linear first mode phase speed of 0.3 ms^{-1} . The following sections interpret the evolution in terms of the extended Korteweg-de-Vries equation.

3. Theoretical Model

Taking into account the large amplitude of the internal waves and the relatively short period of the waves (compared with the tidal period) the extended Korteweg - de Vries equation incorporating quadratic and cubic nonlinear terms (Lamb & Yan, 1996; Talipova et al, 1997; Holloway et al, 1998) was chosen as the basic model for numerical simulation of the evolution of the internal bore. This equation has a form

$$\frac{\partial \eta}{\partial t} + (c + \alpha \eta + \alpha_1 \eta^2) \frac{\partial \eta}{\partial x} + \beta \frac{\partial^3 \eta}{\partial x^3} = 0, \quad (1)$$

where $\eta(x, t)$ is the wave profile function, which in the small amplitude, long-wave limit, gives the maximum vertical isopycnal displacement for the first mode, x is a horizontal co-ordinate and t is time. All coefficients of the extended Korteweg - de Vries equation are

$$\alpha^2 = \frac{c}{2} \frac{\int \Phi^2 dz}{\int (d\Phi/dz)^2 dz}, \quad \alpha' = \frac{3c}{2} \frac{\int (d\Phi/dz)^3 dz}{\int (d\Phi/dz)^2 dz}, \quad (2)$$

$$\alpha_1 = -\frac{\alpha^2}{c} + 3c \frac{\int [(d\Phi/dz)^4 - (N^2 \Phi^4/c)^2] dz}{\int (d\Phi/dz)^2 dz} +$$

$$+ 3c \frac{\int [c(d\Phi/dz)^2 + (N^2 \Phi^2/c) - (2\alpha/3)(d\Phi/dz)] (dT/dz) dz}{\int (d\Phi/dz)^2 dz}, \quad (3)$$

where $T(z)$ is a solution of the ordinary differential equation

$$\frac{d^2 T}{dz^2} + \frac{N^2}{c^2} T = \frac{c^2 N^2}{c^4} \Phi + \frac{\frac{d}{dz}(N^2)}{c^3} \Phi^2, \quad (4)$$

and the linear modal structure of the internal wave is described by

$$\frac{d^2 \Phi}{dz^2} + \frac{N^2(z)}{c^2} \Phi = 0 \quad (5)$$

with the zero boundary conditions for both equations. With the needed accuracy the vertical displacement is presented as

$$\eta(x, z, t) = \eta(x, t) \Phi(z) + \eta^2(x, t) T(z). \quad (6)$$

The normalised condition $T(z_{\max}) = 0$, where $\Phi(z_{\max}) = 1$ is used so that the wave function $\eta(x, t)$ describes the maximal vertical isopycnal displacement, or more exactly, the displacement in the maximum of the linear mode. The extended equation (1) is an integrable model like the Korteweg - de Vries equation. It posses steady-state solutions in the form of the solitary wave (soliton) and dissipativeless shock waves (kinks) which interact between them elasticity. The dynamics of the large-amplitude solitons in the frame of the extended Korteweg - de Vries equation recently was studied by Pelinovsky & Slunayev (1998).

The effect of variable depth and the horizontal variability of the density stratification at the Malin Shelf Edge can be included also in the model. The next modification of the equation (1) should be used if the horizontal variability is slow: (Pelinovsky et al, 1994; Zhou & Grimshaw, 1989; Holloway et al, 1998).

$$\frac{\partial^2 \xi}{\partial t^2} - \left(\frac{\alpha Q}{c^2} \xi + \frac{\alpha_1 Q^2}{c^2} \xi^2 \right) \frac{\partial \xi}{\partial t} - \frac{\beta}{c^4} \frac{\partial^2 \xi}{\partial t^2} = 0, \quad (7)$$

where

$$\xi(t, x) = \frac{\eta(t, x)}{Q(x)}, \quad t = t - \int \frac{dx}{c(x)}, \quad x = x, \quad (8)$$

$$Q = \sqrt{\frac{c_0^2 \int (c_0 - U) (d\Phi_0 / dz)^2 dz}{c^2 \int (c - U) (d\Phi / dz)^2 dz}} \quad (9)$$

and values with index "0" are the values at any fixed point x_0 (it usually corresponds to the deepest water station). Equation (7) is solved by finite difference.

The coefficients of the variable-coefficient extended Korteweg - de Vries equation (7), c , β , α , α_1 , Q , for the conditions of the Malin Shelf Edge were calculated for the four locations where internal waves were registered, they are presented in Table 1. Parameter Q is constant practically. Averaged values and standard deviations of the coefficients of the generalised Korteweg - de Vries equation are given in the last row of Table 1. These values of the coefficients of the basic model may be used to estimate the possible soliton parameters for conditions at the Malin Shelf Edge. As it is known, the exact soliton solution of the extended Korteweg - de Vries equation is (Kakutani, Yamasaki, 1978; Miles, 1981; Pelinovsky & Slunyaev, 1998)

$$\eta = \frac{6\alpha^2}{\alpha'} \frac{1}{1 + \sqrt{1 + \frac{6\alpha_1\alpha'^2}{\alpha^2} \cosh(\Gamma(x - Vt))}}, \quad V = c + \alpha'^2 \quad (10)$$

Here Γ^{-1} is a parameter characterised the effective width of the solitary wave, which varies from zero to

$$\Gamma = \sqrt{\frac{\alpha^2}{6|\alpha_1|\beta}} \quad (11)$$

The soliton polarity is negative. Spatial structure of the solitary wave profiles for different values of the parameter Γ are shown in Figure. 2. As it can be seen, the characteristic length of the solitary wave depends on the soliton amplitude and it varies from 1 km (for the wave amplitude 10 m) to 2 km and more for the wave amplitude close to the limiting value (30.8 m).

4. Numerical simulation

Data from the temperature time series for eight depths of the thermistor chain tow with the Doppler shift removed were transformed into time series of the vertical isopycnal displacement using the mean temperature gradient. Assuming that wave displacements are of the first mode only, the formula (6) can be used to calculate the vertical displacement in the maximum of linear mode η . Accuracy of this procedure for the

point of 160 m is demonstrated by Fig. 3, where the mean value of $\eta(t)$ and its deviation calculated from data in eight depths are presented. Vertical displacement in the maximum of the linear mode $\eta(t)$ is an input for the numerical simulation of the internal wave evolution. Results of comparison between computing and observations for each point are shown in Fig. 4. It can be seen that the model explains the observed leading solitary wave (amplitude and form) very well for every point in its formation and development. The agreement between the computed and the observed following large-amplitude waves is not so good in amplitude (but relatively good in phase), and the model predicts weaker waves than the observed ones. Possibly, this disagreement is related with some inaccuracy in the calculation of the vertical displacement from the thermistor chain data (averaged temperature gradient may change action of strongly nonlinear waves). Further, the calculation of the waveform assumes a constant speed across ground for each survey, to remove the Doppler shift, and this assumption does not include the possibility of different waves having different phase speeds, as expected from non-linear theory.

It is important to note that the amplitude of the largest solitary wave reaches approximately 30 m. Because this amplitude is comparable with the limited value for the soliton amplitude (30.8 m), the role of the cubic nonlinearity term should be significant. To demonstrate this, the same process was performed with no cubic nonlinearity in the frame of the "classic" Korteweg - de Vries equation. In this simplified variant, the amplitude of the leading soliton is higher (approximately 38 m). Therefore, the cubic nonlinearity is important for the internal waves at the Malin Edge Shelf, and it leads to limit for the soliton amplitude.

5. Conclusion

The evolution of an internal bore at the Malin Shelf Edge has been simulated with a numerical Korteweg - de Vries model which deals with quadratic (first order) and cubic (second order) nonlinearity. The simulations were done for the conditions of the 13th August 1996 during SESAME II. Using measured buoyancy profiles at the Malin Shelf Edge, the coefficients of the generalised Korteweg - de Vries equation have been calculated and interpolated onto intermediate points. Real thermistor chain data for 13th August 1996 have been transformed into vertical displacements at each depth, and then the wave displacement at the maximum of the linear mode has been calculated, using the assumption of a linear modal vertical structure. These data were used for numerical simulation and interpretation of the observed data. Calculations have confirmed the observed picture of the bore transformation into a group of solitary waves: the model correctly predicts the 30 m amplitudes of the leading large-amplitude solitary waves, but underpredicts the amplitudes of the following waves which were observed between 20 and 30 m. The 30 m amplitude coincides with the theoretical limited value of the soliton amplitude (30.8 m), and therefore, the cubic nonlinearity is important for the description of the nonlinear internal wave evolution at the Malin Shelf Edge. Model simulations without cubic non-linearity (i.e. the basic Korteweg - de Vries equation) showed larger amplitudes than observed.

References

Holloway, P.E, Pelinovsky, E., Talipova, T., and Barnes, B. A nonlinear model of internal tide transformation on the Australian North West Shelf. *J. Phys. Oceanogr.*, 1997, v. 27, No. 6, 871 - 896.

Holloway, P.E., Pelinovsky, E., and Talipova T., A generalised Korteweg - de Vries model of internal tide transformation in the coastal zone. *J. Geophys. Res.*, 1998, submitted.

Kakutani, T., and Yamasaki, N., Solitary waves on a two-layer fluid. *J. Phys. Soc. Japan*, 1978, v. 45, 674 - 679.

Lamb, K., and Yan, L., The evolution of internal wave undular bores: comparisons of a fully nonlinear numerical model with weakly nonlinear theory. *J. Phys. Oceanogr.*, 1996, v. 26, No. 12, 2712 - 2734.

Miles, J.W., On internal solitary waves. II. *Tellus*, 1981, v. 33, 397 - 401.

Pelinovsky, E., Stepanyants, Yu., and Talipova, T., Modelling of the propagation of nonlinear internal waves in horizontally inhomogeneous ocean. *Izvestiia, Atmos. Oceanic Physics*, 1994, v. 30, 79 - 85.

Pelinovsky, E., and Slunyaev, A., Generation and interaction of the solitary waves of large amplitudes. *JETP Letters*, 1998, 67, N. 9, 655 - 661

Small, J., Sawyer, T., and Scott, J., The evolution of an internal bore at the Malin shelf edge, *Annales Geophysicae*, 1998, accepted

Small, J., Internal solitons in the ocean: prediction from SAR, this Workshop Proceedings.

Talipova, T., Pelinovsky, E., Lamb, K., Grimshaw, R., and Holloway, P., Effects of cubic nonlinearity on the dynamics of internal waves. *Transactions of Russian Academy of Sciences, Earth Section* (accepted); *Annales Geophysicae*, 1997, v. 15, Suppl. 2, Pt. 2, C575.

Zhou, X., and Grimshaw, R., The effect of variable currents on internal solitary waves. *Dynamics Atm. Oceans*, 1989, v. 14, 17 - 39.

Table 1.
Coefficients of the basic equation for conditions of the Malin Shelf Edge

depth, m	c, m/s	β , m^3/s	$\alpha, (10^{-3}) \text{s}^{-1}$	$\alpha_1, (10^{-4}) \text{m}^{-1}\text{s}^{-1}$	Q
160	0.4340	473	-7.67	-2.38	1
156	0.4309	452	-7.44	-2.38	1
151	0.4208	406	-7.85	-2.62	1.02
150	0.417	396	-7.99	-2.65	1.03
mean value 154± 4	0.42± 0.01	432± 37	-7.7± 0.2	-2.5± 0.1	

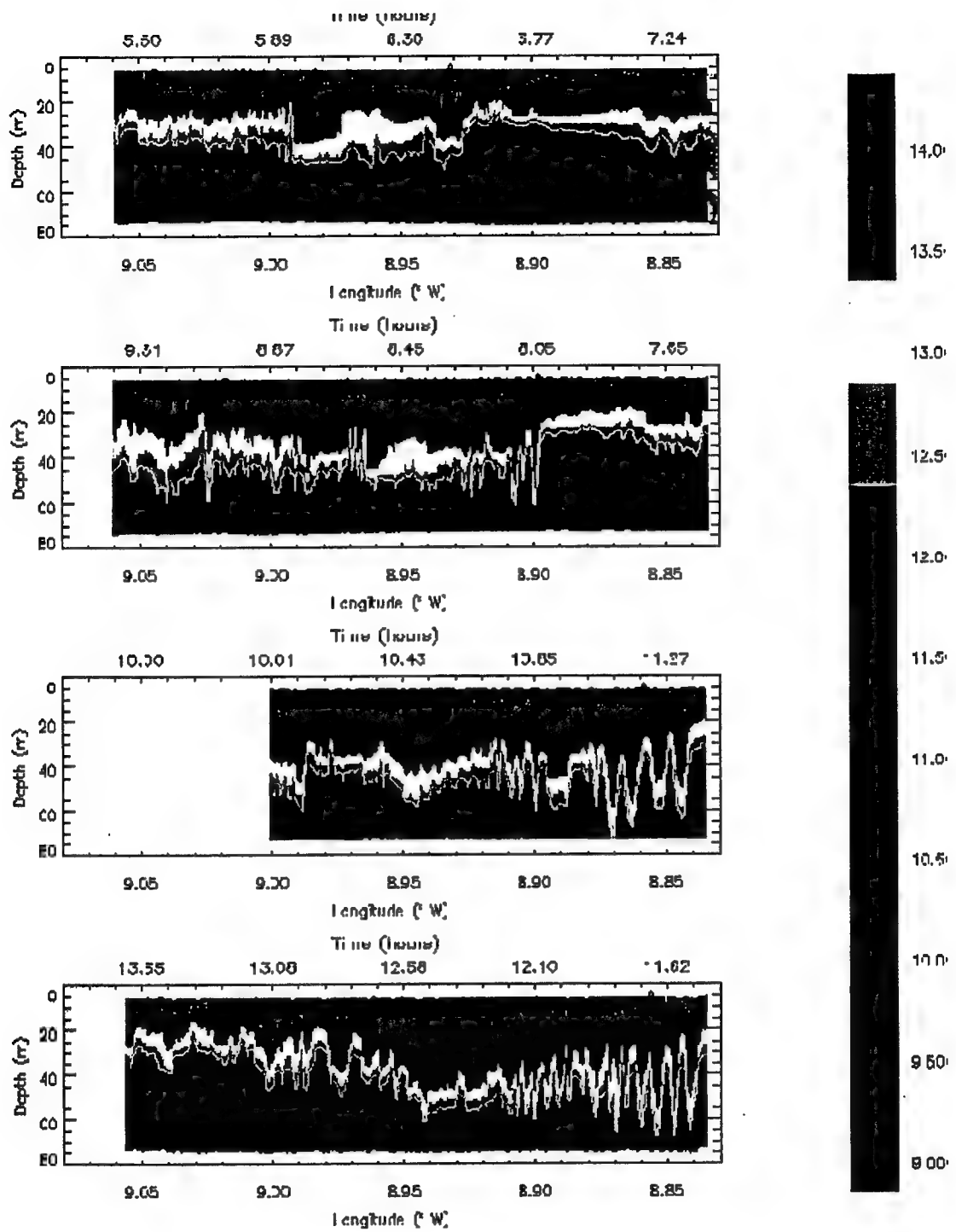


Figure 1. Temperature (°C) vertical cross-sections from thermistor chain, 13th August 1996. The four plots show four surveys across the shelf edge, with the time in hours at the top, and longitude at bottom, of the plot. The internal bore feature marked 'A' in each plot can be seen to move eastwards (on-shelf) between each plot, and evolve into internal waves.

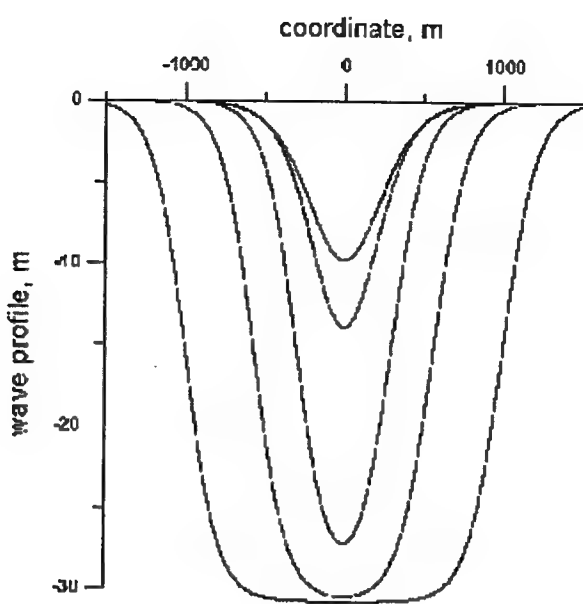


Figure. 2. Spatial structure of the soliton

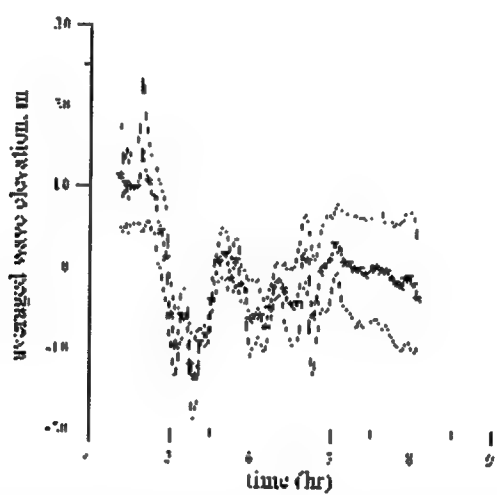


Figure 3. Mean value $\eta(t)$ (solid line with symbols) and $\eta(t) \pm \delta\eta(t)$ for the point of 150 m.

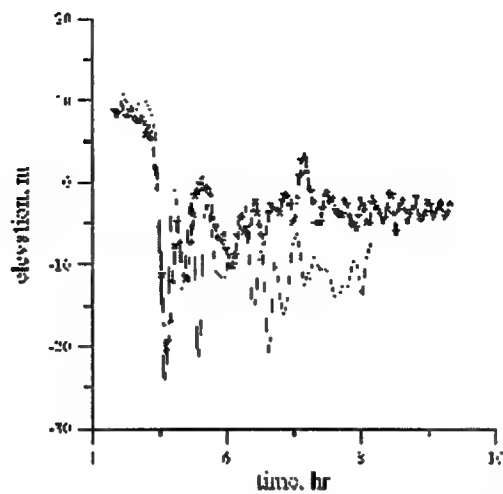


Figure 4. Comparison of the computed (solid line with symbols) and observed wave records. Depth 156 m.

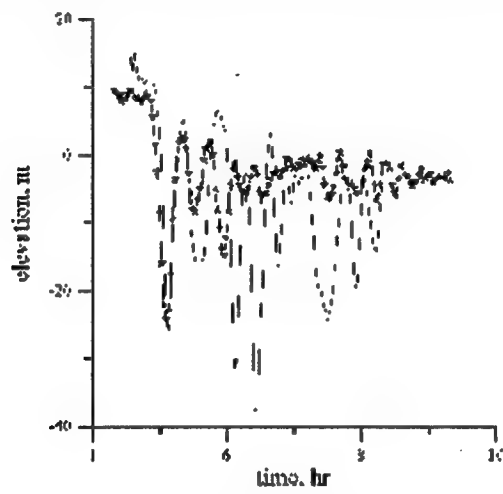


Figure 4 (continued). Depth 151 m

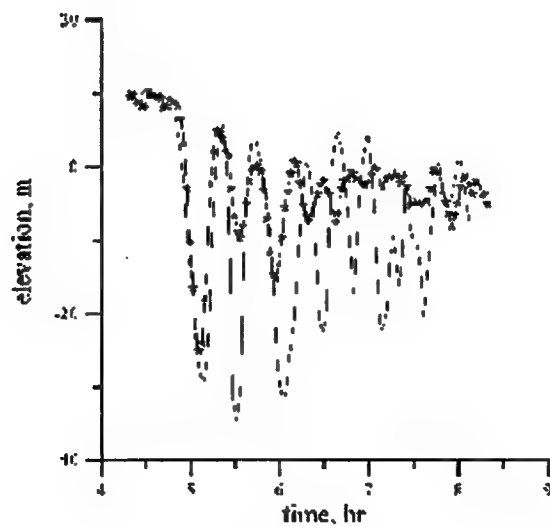


Figure 4 (continued). Depth 150 m

Cross-Shelf Mass Transport by Non-Linear Internal Waves

G. I. Shapiro¹, M. E. Inall² and T. J. Sherwin²

¹P. P. Shirshov Institute of Oceanology, Moscow

²University of Wales, Bangor, UK

It is well known that progressive non-linear surface waves generate a residual mass transport in the direction of their propagation (the Stokes' drift). This paper considers the similar problem for tidally generated internal waves in the case of approximately two-layer stratification. Such waves are an ubiquitous feature of the world's continental margins and are thought to play an important role in shelf sea/open ocean exchange. Theoretical expressions are consistent with the Kortweg de Vries wave equation and derived specifically to allow for comparison to be made with fixed point measurements. The theory expresses mass transports in terms of a time-varying interface displacement and can be applied to other forms of data, such as those from thermistor chains. Provided the barotropic flow is small compared to the phase speed of the waves, velocities and transports can be estimated from the interface displacement without a direct knowledge of the non-linear phase speed. Careful analysis of moored acoustic doppler current profiler data from a site 5 km shoreward of the edge of the Malin Shelf, west of Scotland, gives a value of 1.6 m² s⁻¹ for the mass transport in each layer. Presented theory account for approximately 70% of the observed transport.

It is generally accepted that in the ocean shelf, break regions are particularly dynamic places (see e.g. Huthnance, 1995). They attract large-scale phenomena such as ocean currents, their attendant eddies and frictional boundary layers and upwelling filaments are driven from them. Their sloping topography makes them prone to wave activity, and internal waves of all frequencies (from the order of minutes to the order of days) can be found there. Despite the degree of dynamic activity, shelf breaks also provide a barrier to exchange between shelf seas and the ocean due to the rotational constraint on geostrophic flows to follow contours of f/H . However, a contribution to ocean-shelf exchange is made by all ageostrophic processes including non-linear internal waves (NIWs), the subject of this investigation. Indeed non-linearly generated mean currents (e.g. averaged over a tidal cycle) may be important for long-term water fluxes between shelves and deep ocean, and the movement of fish larvae and sea-floor sediments (e.g. Lamb, 1997; Friedrichs and Wright, 1995; Shanks and Wright, 1987; Huthnance, 1981).

The NIWs of interest are large amplitude, short wavelength internal waves which are often found on continental shelves, within about 50 km of the break, propagating toward the coast in packets. The maximum number of waves in a packet is governed by the balance between dispersion, nonlinearity and dissipation (Barenblatt et al., 1985). Individual waves may have a length scale of order 500 m, a phase speed of order 1 m s⁻¹ and period of order 10 minutes; within a packet the waves tend to be rank ordered with the largest (and fastest) wave leading.

A comprehensive discussion of observations reported worldwide is inappropriate here but see, for example, Ostrovsky and Stepanyants (1989). However, along the Atlantic edge of the European Shelf they have been observed in several locations; on La Chapelle Bank in the Celtic Sea waves with an amplitude of 50 m and propagation speed of 70 cm s⁻¹ have been observed (see e.g. Pingree and Mardell, 1985, Pingree and New, 1995, and many other papers by these authors). In the Strait of Gibraltar waves up to 60 m deep have been recorded, (Watson and Robinson, 1990), whilst on the

Portuguese Shelf they have an amplitude approaching 50 m and phase speed of 50 cm s⁻¹ (Jeans, 1997).

Internal waves may significantly contribute to cross-shelf exchange. Kinder (1984) estimated the average mass transport from observations of NIWs in the strait to be 3.7 m² s⁻¹. However, there appear to be no direct estimates of the contribution of NIWs to shelf-edge exchange through mass transport. Huthnance (1995) suggests a value for a surface layer of order 1 m² s⁻¹ which makes NIWs comparable to many of the other processes mentioned in the first paragraph, in particular Ekman drainage of the slope current and upwelling filaments. It is possible that NIWs make an important contribution to mixing and exchange at the shelf edge but that, whilst they are relatively easy to measure, they are very difficult to model in general circulation models, requiring further work on the theoretical understanding of the waves.

Present work focuses on mass transport onto the shelf. Estimation of mass transport by NIWs using nonlinear KdV type theory is developed and compared with observations. Given that, in general, most observations are made by in situ Eulerian instruments, the theory avoids terms involving the horizontal spatial derivative, which is not easy to measure in the sea.

References

- [1] Barenblatt, G. I., M. A. Ivanov, and G. I. Shapiro, 1985: On the structure of wave fronts in nonlinear dissipative media. *Arch. Ration. Mech. Anal.*, 87(4), 293-303.
- [2] Friedrichs, C. T., and L. D. Wright, 1995: Resonant internal waves and their role in transport and accumulation of fine sediment in Eckernforde Bay, Baltic Sea. *Cont. Shelf Res.*, 15, 1697-1721.
- [3] Huthnance, J. M., 1981: On mass transport generated by tides and long waves. *J. Fluid Mech.*, 102, 367-387.
- [4] Huthnance, J.M., 1995: Circulation, exchange and water masses at the ocean margin: the role of physical processes at the shelf edge. *Progress in Oceanography*, 35, 353-431.
- [5] Jeans, D. R.G., 1997: *A nonlinear internal tide on the Portuguese shelf*. Ph.D. thesis, UCES, School of Ocean Sciences, University of Wales Bangor.
- [6] Kinder, T. H., 1984: Met mass transport by internal waves near the strait of Gibralter, *Geophys. Res. Lett.*, 11(10), 978-990.
- [7] Lamb, K. G., 1997: Particle transport by nonbreaking, solitary internal waves. *J. Geophys. Res.*, 102, 18641-18660.
- [8] Ostrovsky, L. A., and Y. A. Stepanyants, 1989: Do internal solitons exist in the ocean? *Rev. Geophys. Space Phys.*, 27(3), 293-310.
- [9] Pingree, R. D., and G. T. Mardell, 1985: Solitary internal waves in the Celtic sea. *Progress in Oceanography*, 14, 431--441.
- [10] Pingree, R. D., and A. L. New, 1995: Structure, seasonal development and sunglint spatial

coherence of the internal tide on the Celtic and Armorian shelves and in the Bay of Biscay. *Deep-Sea Res.*, 42, 245-283.

[11] Shanks, A. L., and W. G. Wright, 1987: Internal-wave-mediated shoreward transport of cyprids, megalopae, and gammarids and correlated longshore differences in the settling rate of internal barnacles. *J. Exp. Mar. Biol. Ecol.*, 114, 1-13.

[12] Watson, G., and I. S. Robinson, 1990: A study of internal wave propagation in the strait of Gibralter using shore based marine radar images. *J. Phys. Oceanogr.*, 20, 374-395.

AN INVESTIGATION OF THE TEMPORAL VARIABILITY OF A NON-LINEAR INTERNAL WAVE FIELD ON THE PORTUGUESE SHELF

Toby J. Sherwin and D.R. Gus Jeans*

Unit for Coastal and Estuarine Studies
UWB Marine Science Laboratories
Menai Bridge
Anglesey, LL59 5EY, UK
tjs@uces.bangor.ac.uk

*Present Address: Fugro-Geos
Gemini House
Hargreaves Rd
Swindon, Wiltshire, SN2 5AZ, UK
jeans@geos.co.uk

Summary

Observations of non-linear internal waves were made at about 41° N on the Portuguese Shelf in the summer of 1994 as part of the EU MAST II MORENA project into mixing and exchange at the shelf edge. The location was in an upwelling region close to the base of an off shore filament. Intensive ship-borne measurements were made from the University of Bergen's R V Håkon Mossby between 9th and 14th August using a yo-yoing CTD, the ship's ADCP, and a light weight temporary thermistor chain mooring that was deployed for up to 10 hours as a packet of waves propagated past. The location of the work is shown in Fig. 1 along with an outline of an ERS1 SAR image that was taken at the start of the cruise (see also da Silva et al., 1997). On one occasion the same wavepacket was measured three times as it propagated towards the coast, about 50 km from the shelf break (Stas 14 to 16 in Fig. 1). In addition a thermistor chain was deployed at the shelf break between 27th July and 28th August (Sta. M in Fig. 1). The work is described in detailed in Jeans (1998).

The leading wave was characterised by a sudden non-linear isotherm depression of up to 45 m and lasting between 10 and 35 minutes (Fig. 2), accompanied by current surges of up to 0.45 m s⁻¹ and shears of up to 0.7 m s⁻¹ over 60 m depth. The waves propagated on shore with a phase speed of about 0.57 m s⁻¹ in water that was typically 100 to 160 m deep. They were noted to be significantly wider than would be suggested by classical second order KdV theory, probably due to their large amplitude.

At Sta. M, a wavepacket appeared each semi-diurnal tidal cycle within the trough of the thermocline oscillations of the ?linear? internal tide. However, contrary to linear expectations, there was very poor correlation between the amplitude of the non-linear waves and tidal range, although a slightly better correlation was found between wave amplitude and upper layer thickness, which varied in response to upwelling winds (see Figs 3 and 4). The arrival time of the waves varied between 4.9 h and 10.8 h after HW Oporto. An investigation of the likely explanation of this variability showed a strong correlation between the lag and the northerly component of the wind, although good correlation was also found between the arrival time, t_a , and upper layer thickness. However, the size of the variations was greater than could be reasonably expected using a simple Ekman drift velocity that is uniform along the coast, and a better comparison was found when an estimate of the current in the offshore filament, v_{Ef} was taken into account (Fig. 5). This correlation suggested that the waves originated from a point about 8.2

km west of Sta M at a time of about 2.5 h after HW Oporto.

However, both the extent of the variability in the arrival time of the waves and the size of the waves relative to the amplitude of the local barotropic currents, throw doubt on their precise source. Linear and KdV like modelling exercises (see Jeans, 1998) suggest that, given their size, the waves could not originate from the shelf break and further investigations of this problem are being conducted elsewhere. One candidate source region is the Oporto Seamount, which lies approximately 50 km WSW of the observation region, although this location seems to conflict with the analysis given above

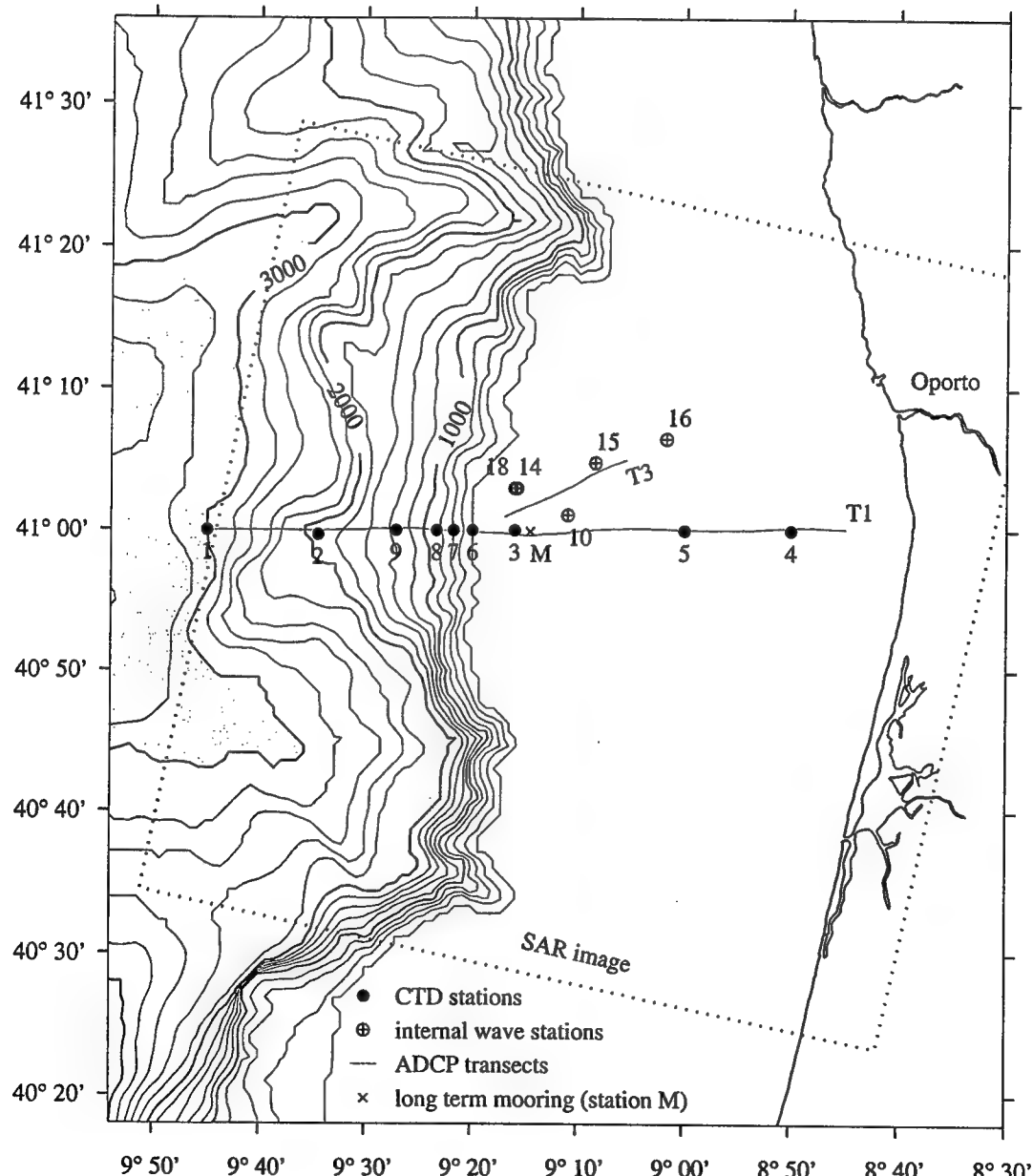


Figure 1. Location of the field measurements on the Portuguese Shelf. (Fig. 1 postscript)

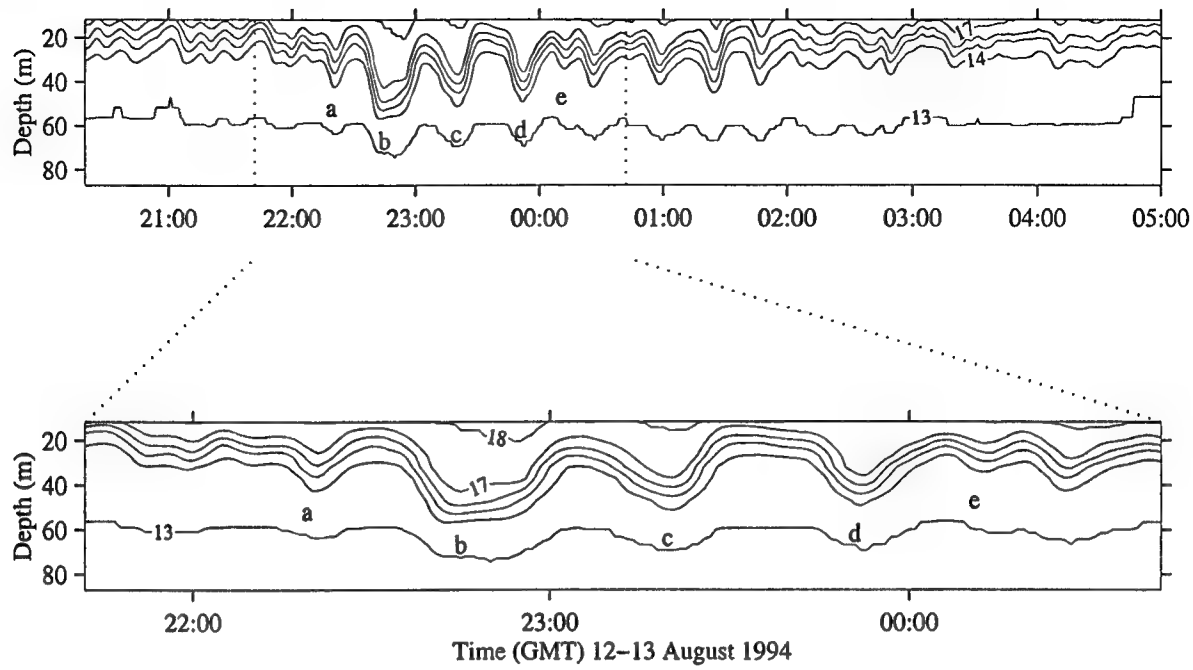


Figure 2. Thermistor chain observation of a non-linear internal wave train passing Sta. 16.
The letters a to e indicate different troughs in the train. (Fig. 2 postscript)

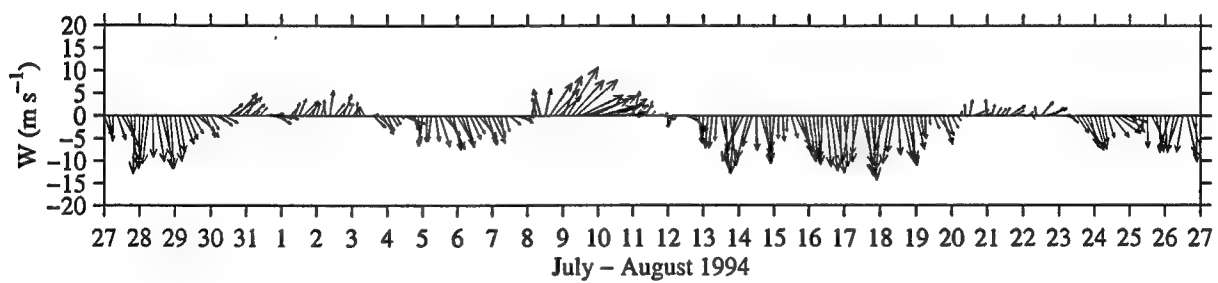


Figure 3. Winds in the region predicted from the UK Met Office European model. (Fig. 3 postscript)

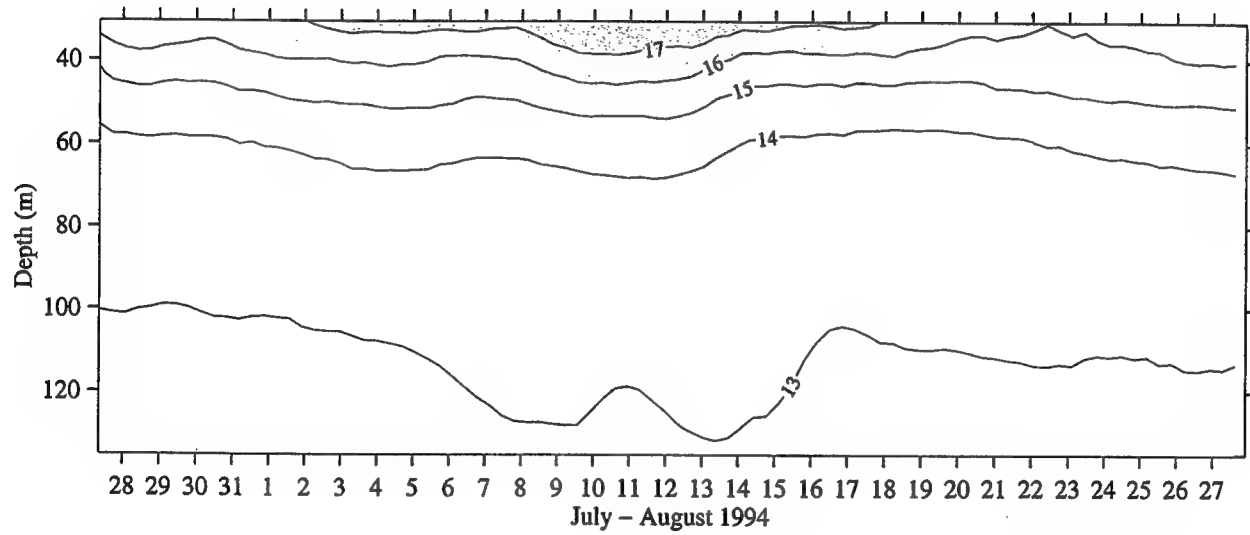


Figure 4. Low pass filtered temperature time series from Sta. M. (Fig. 4 postscript)

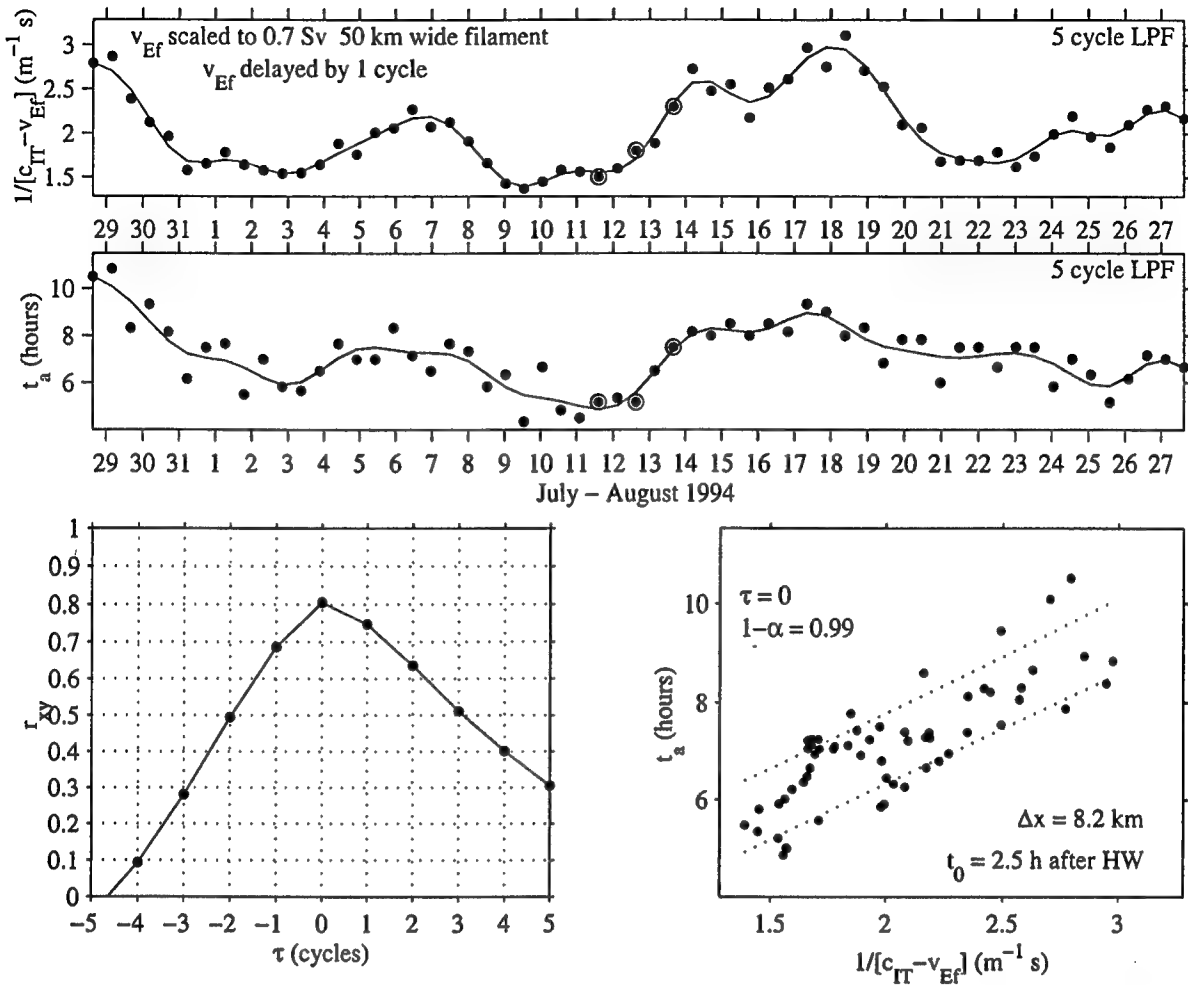


Figure 5. Time series of $1/(c_{IT} - v_{Ef})$ and t_a for each tidal cycle, with their cross correlation and scatter plot observed at Sta. M. In the upper plots the ringed circles correspond to times when the ship also observed the waves. The curve shows a low pass filter of the data points. The linear internal tide phase speed is c_{IT} . Error lines on the scatter plot have a confidence level of 0.99. The typical wave is estimated to have been at a position delta x west of Sta. M at time t_0 . (Fig. 5 postscript)

References

da Silva J.C., D.R.G. Jeans, I.S. Robinson and T.J. Sherwin (1998). The application of near real-time ERS-1 SAR data to the prediction of the location of internal waves at sea. *Int. J. Remote Sensing*, 18, 3507-3517.

D.R.G. Jeans (1998). A Non-Linear Internal Tide on the Portuguese Shelf. PhD Thesis, University of Wales, Bangor, School of Ocean Sciences. pp 136. [submitted].

Acknowledgement

This work constitutes part of the EU MAST II supported MORENA project, contract

MAST2-CT93-0065. We are grateful for the support of the officers and crew on the R V Håkon Mossby during the MORENA 3B cruise.

1998 WHOI/IOS/ONR Internal Solitary Wave Workshop Attendees

John Apel
Global Ocean Associates

Laurence Armi
Scripps Institution of Oceanography

Peter Baines
CSIRO Atmospheric Research, Australia

Tim Boyd
Oregon State University

Mel Briscoe
Office of Naval Research

David A. Cacchione
Aubrey Consulting, Inc.

Grace Chang
University of California, Santa Barbara

Ching-Sang Chiu
Naval Postgraduate School

Joan S. Cleveland
Office of Naval Research

John Colosi
Woods Hole Oceanographic Institution

Patrick Cummins
Institute of Ocean Sciences, Canada

Eric D'Asaro
Applied Physics Laboratory, U. Washington

Warren Denner
EOS Research Associates

Richard Dewey
University of Victoria, United Kingdom

Tommy Dickey
University of California, Santa Barbara

Timothy Duda
Woods Hole Oceanographic Institution

Alan Evans
University of Kent, United Kingdom

David Farmer
Institute of Ocean Sciences, Canada

Steven Finette
Naval Research Laboratory

Louis Goodman
Office of Naval Research

Roger Grimshaw
Monash University, Australia

John Grue
University of Oslo, Norway

Karl Helfrich
Woods Hole Oceanographic Institution

Myrl Hendershott
Scripps Institution of Oceanography

Frank Henyey
Applied Physics Laboratory, U. Washington

Peter Holloway
Australian Defence Force Academy, Canberra

Gus Jeans
Fugro GEOS, United Kingdom

Frans-Peter A. Lam
TNO Physics & Electronics Lab, The Netherlands

Kevin Lamb
University of Waterloo, Canada

Cleridy Lennert-Cody
Scripps Institution of Oceanography

James Lerczak
Scripps Institution of Oceanography

Murray Levine
Oregon State University

Ming Li
Institute of Ocean Sciences, Canada

Antony K. Liu
National Aeronautics & Space Administration

Philip L.-F. Liu
Cornell University

James F. Lynch
Woods Hole Oceanographic Institution

Neil S. Oakey
Bedford Institute of Oceanography, Canada

Marshall Orr
Naval Research Laboratory

Alfred Osborne
Università di Torino, Italy

Rich Pawlowicz
University of British Columbia, Canada

Efim Pelinovsky
Institute of Applied Physics, Russia

Jesús Pineda
Woods Hole Oceanographic Institution

Rob Pinkel
Scripps Institution of Oceanography

David L. Porter
Johns Hopkins University, APL

Larry Redekopp
University of Southern California

Alberto Scotti
Woods Hole Oceanographic Institution

Er-Chang Shang
NOAA/Environmental Technology Laboratory

Georgiy Shapiro
Shirshov Institute of Oceanology, Russia

Toby Sherwin
University of Wales, Bangor, United Kingdom

Jeff Simmen
Office of Naval Research

Justin Small
Defence Evaluation Research Agency, U.K.

Tim P. Stanton
Naval Postgraduate School

Timothy K. Stanton
Woods Hole Oceanographic Institution

Patrick Sullivan
Oceanit Laboratories, Inc.

Chris Tiemann
Scripps Institution of Oceanography

Mark Trevorrow
Institute of Ocean Sciences, Canada

Alex Warn Varnas
Naval Research Laboratory

Peter Worcester
Scripps Institution of Oceanography

DOCUMENT LIBRARY

Distribution List for Technical Report Exchange – July 1998

University of California, San Diego
SIO Library 0175C
9500 Gilman Drive
La Jolla, CA 92093-0175

Hancock Library of Biology & Oceanography
Alan Hancock Laboratory
University of Southern California
University Park
Los Angeles, CA 90089-0371

Gifts & Exchanges
Library
Bedford Institute of Oceanography
P.O. Box 1006
Dartmouth, NS, B2Y 4A2, CANADA

NOAA/EDIS Miami Library Center
4301 Rickenbacker Causeway
Miami, FL 33149

Research Library
U.S. Army Corps of Engineers
Waterways Experiment Station
3909 Halls Ferry Road
Vicksburg, MS 39180-6199

Marine Resources Information Center
Building E38-320
MIT
Cambridge, MA 02139

Library
Lamont-Doherty Geological Observatory
Columbia University
Palisades, NY 10964

Library
Serials Department
Oregon State University
Corvallis, OR 97331

Pell Marine Science Library
University of Rhode Island
Narragansett Bay Campus
Narragansett, RI 02882

Working Collection
Texas A&M University
Dept. of Oceanography
College Station, TX 77843

Fisheries-Oceanography Library
151 Oceanography Teaching Bldg.
University of Washington
Seattle, WA 98195

Library
R.S.M.A.S.
University of Miami
4600 Rickenbacker Causeway
Miami, FL 33149

Maury Oceanographic Library
Naval Oceanographic Office
Building 1003 South
1002 Balch Blvd.
Stennis Space Center, MS, 39522-5001

Library
Institute of Ocean Sciences
P.O. Box 6000
Sidney, B.C. V8L 4B2
CANADA

National Oceanographic Library
Southampton Oceanography Centre
European Way
Southampton SO14 3ZH
UK

The Librarian
CSIRO Marine Laboratories
G.P.O. Box 1538
Hobart, Tasmania
AUSTRALIA 7001

Library
Proudman Oceanographic Laboratory
Bidston Observatory
Birkenhead
Merseyside L43 7 RA
UNITED KINGDOM

IFREMER
Centre de Brest
Service Documentation - Publications
BP 70 29280 PLOUZANE
FRANCE

REPORT DOCUMENTATION PAGE		1. REPORT NO. WHOI-99-07	2.	3. Recipient's Accession No.
4. Title and Subtitle The 1998 WHOI/IOS/ONR Internal Solitary Wave Workshop: Contributed Papers			5. Report Date July 1999	6.
7. Author(s) Timothy F. Duda and David M. Farmer, Editors			8. Performing Organization Rept. No. WHOI-99-07	
9. Performing Organization Name and Address Woods Hole Oceanographic Institution Woods Hole, Massachusetts 02543			10. Project/Task/Work Unit No.	11. Contract(C) or Grant(G) No. (C) N00014-95-1-0633 (G) N00014-99-1-0126
12. Sponsoring Organization Name and Address Office of Naval Research			13. Type of Report & Period Covered Technical Report	
			14.	
15. Supplementary Notes This report should be cited as: Woods Hole Oceanog. Inst. Tech. Rept., WHOI-99-07.				
16. Abstract (Limit: 200 words) A workshop entitled <i>Internal Solitary Waves in The Ocean: Their Physics and Implications for Acoustics, Biology, and Geology</i> was held during October, 1998 in Sidney, British Columbia, Canada. It was jointly organized by the Woods Hole Oceanographic Institution (MA, USA), the Institute of Ocean Sciences (Sidney, BC, Canada), and the U.S. Office of Naval Research. More than 60 scientists from seven countries attended. Participants contributed papers prior to the meeting which were published on the internet at the Woods Hole web site. Those papers are reproduced here.				
17. Document Analysis a. Descriptors solitary waves internal waves wave workshop				
b. Identifiers/Open-Ended Terms				
c. COSATI Field/Group				
18. Availability Statement Approved for public release; distribution unlimited.		19. Security Class (This Report) UNCLASSIFIED	21. No. of Pages 251	
		20. Security Class (This Page)	22. Price	